Numerical simulation of soil creep with hypoplasticity

Shun Wang

Department of Civil Engineering and Natural Hazards

Universität für Bodenkultur Wien

This dissertation is submitted for the degree of

Doctor of Philosophy

Institut für Geotechnik

April 2017

Numerical Simulation of Soil Creep With Hypoplasticity

Shun Wang

Betreuer:

Univ.-Prof. Dr.-Ing. Wei Wu

Declaration

I hereby declare that except where specific reference is made to the work of others, the contents of this dissertation are original and have not been submitted in whole or in part for consideration for any other degree or qualification in this, or any other university. This dissertation is my own work and contains nothing which is the outcome of work done in collaboration with others, except as specified in the text and Acknowledgments.

Shun Wang
April 2017

Acknowledgements

This dissertation would not be possible to obtain the final result without the help and support from many professors, research staffs, graduate students, colleagues, and my family. It is my great pleasure to express my gratefulness to whom have given me guidance, help, and encouragement.

First of all, I would like to express the deepest appreciation to Univ. Prof. Dr.-Ing. Wei Wu for his constant guidance, personal attention, suggestions, endless encouragement, and full support during the last four years of my study in Vienna. He gave me opportunities to participate in many interesting workshops and scientific exchanges, and to work with many talented research staffs from different countries.

Besides my supervisor, my special appreciation goes to Prof. Wei Xiang, who recommended me to pursue a doctorate in the Institute of Geotechnical Engineering, Boku, and gave me invaluable advice and support, for which i am extremely grateful.

I would like to express my sincere appreciation to Prof. Zhen-yu Yin, who offered me many useful advises and remarks in writing my dissertation and whose enthusiasm in scientific research has a lasting effect on me. My thanks also go to Dr. Yin-fu Jing, who gave me enormous valuable discussions, technical support, and hands-on help in many aspects of my research work when I was in TongJi University as an exchange student.

I would like to thank the China Scholarship Council (CSC) for the financial support to my research work for the last four years. During my study, many colleagues and friends gave me supports. Special thanks to my colleagues from the Institute of Geotechnical Engineering. Especially: Chong Peng, Miguel, Barbara, Rick, Gregor, Guo-ping Lei, Jia Lin and Guo-fang Xu for their help, motivation, and fruitful discussions.

Last but not the least, special thanks to my family: my parents, my brother, and sister for their spiritual support throughout the time of my study and research, and my life in general. My deepest appreciation is expressed to them for their love, understanding, and inspiration. Without their blessings and encouragement, I would not have been able to finish this work.

Abstract

In geotechnical engineering, the evaluation of the long-term performance of construction greatly depends on the time-dependent behavior of geotechnical materials. It is well-known that, depending on the time and loading state, most geotechnical materials exhibit both Coulomb type frictional behavior and rheological behavior. For proper modeling the time-dependent behavior of geomaterials, it is essential to develop a numerical model, which takes into account the contributions of both the frictional and the viscous effects. Additionally, the development of improved integration techniques is essential in numerical computation. Hence, this dissertation focuses attention on the development of such a model and an appropriate integration method for this model.

First, a new constitutive model for modeling the viscous behavior of soils is proposed. This model consists of two components (the frictional part and the viscous part) representing respectively the frictional and the viscous stresses in soil. The frictional part is accounted for using a rate-independent hypoplastic constitutive model, which is enhanced by incorporating a simple critical state based formulations. The viscous part is considered using a viscous formulation, which contains a high-order term denoting strain acceleration. The performance of the proposed model is examined by simulating different elementary tests on granular materials.

Second, a comprehensive study on the finite element implementation of the simple critical state hypoplastic constitutive model (the frictional part) is presented. Several commonly used integration methods, including explicit and implicit methods, are enhanced by a stress correction scheme to avoid the drifted stresses lying outside the yield surface of the hypoplastic constitutive model. These integration methods have been examined using triaxial compression tests, stress response envelopes, and several typical boundary value problems. The results indicate that, in terms of accuracy, efficiency, and robustness, the adaptive explicit methods are the best choices for constitutive integration of hypoplastic models, while the stress correction scheme can stabilize the numerical computation, especially, in the simulation of slope failure. Based on the above study, an

adaptive explicit method with stress correction scheme is adopted to implement the visco-hypoplastic constitutive model. This implementation is validated by modeling some simple boundary value problems. The numerical evidence indicates that this integration method can significantly reduce the integration error produced during the computational time.

Finally, an in-situ direct shear creep test on the coarse-graded soil in slope is carried out. On the basis of this test, a finite element simulation using the proposed visco-hypoplastic model is performed. All comparisons of the experimental and numerical results indicate that the visco-hypoplastic model is able to predict the time-dependent behavior of soil.

Zusammenfassung

Die Beurteilung des Langzeitverhaltens von geotechnischen Konstruktionen hängt stark vom zeitabhängigen Verhaltens des Untergrunds ab. Es ist bekannt, dass, abhängig vom Zeit- und Lastzustand, die meisten geotechnischen Materialien sowohl ein Coulomb'sches Scherverhalten als auch ein rheologisches Verhalten aufweisen. Für die korrekte Modellierung des zeitabhängigen Verhaltens von Geomaterialien ist die Entwicklung eines numerischen Modells notwendig, welches das Scherverhalten als auch viskose Effekte berücksichtigt. Weiters ist die Entwicklung verbesserter Integrationstechniken essentiell für die numerische Berechnung. Darum liegt der Fokus dieser Dissertation auf der Entwicklung eines solchen Modells.

Zuerst wird ein konstitutives Modell für die Modellierung des viskosen Verhaltens vorgeschlagen. Dieses Modell setzt sich aus einer Reibungs- und viskoser Komponente zusammen, um die Scherspannungen und viskosen Spannungen im Boden abzubilden. Die Reibungskomponente macht sich eines ratenunabhängigen hypoplastischen Stoffgesetzes zu nutze, welches durch die Einbindung einer einfachen Critical-State Formulierung erweitert wird. Die Formulierung des viskosen Parts nutzt einen Terminus höherer Ordnung um Dehnungsbeschleunigungen anzugeben. Die Performance des aufgestellten Modells wird durch die Simulation von unterschiedlichen Elementtests mit granularem Material getestet.

Danach wird eine umfangreiche Studie über die Finite-Elemente Implementierung des einfachen hypoplastischen Critical-State Stoffgesetzs (Reibungspart) präsentiert. Einige gängige Integrationsverfahren, inklusive explizite und implizite Methoden, werden durch ein Model der Spannungskorrektur verbessert, um das Abdriften von Spannungen über die Grenzfläche des hypoplastischen Modells hinaus zu verhindern. Diese Integrationsverfahren wurden mit triaxialen Kompressionsversuchen, spannungsabhängige Hüllkurven, und anderen typischen Grenzwertproblemen getestet. Die Ergebnisse deuten an, dass, in Bezug auf Genauigkeit, Effizienz, und Robustheit, die Adaptive-Explicit-Methoden

die beste Wahl für die konstitutive Integration des hypoplastischen Modells sind, während das Model der Spannungskorrektur die numerische Berechnung stabilisiert, insbesondere bei der Simulierung von Hangrutschungen. Basierend auf dieser Studie wird eine Adaptive-Explicit-Methode mit Spannungskorrektur in das visko-hypoplastische Stoffgesetz implementiert. Dieses wird durch die Modellierung einfacher Grenzwertproblemen validiert. Es zeichnet sich ab, dass das Integrationsverfahren den über die Zeit akkumulierten Integrationsfehler signifikant reduzieren kann.

Zum Schluss wird ein in-situ Direktscher-Kriechversuch an einem grobkörnigen Böschungsboden durchgeführt. Auf der Basis dieses Tests wird eine Finite Elemente Simulation mit dem entwickelten visko-hypoplasitschen Modells durchgeführt. Alle Vergleiche der experimentellen und numerischen Ergebnisse weisen darauf hin, dass das entwickelte Modell im Stande ist das zeitabhängige Verhalten des Bodens vorherzusagen.

Contents

List of Figures

List of Tables

Nomenclature

In the following, the usual sign convention of soil mechanics (compression positive) is adopted throughout. All stresses are effective stresses, unless otherwise stated. Bold letter (e.g., $\boldsymbol{N}$) is used to denote second-order tensors and matrices. Calligraphic letters are used to represent fourth-order tensors (e.g., $\mathscr{L}$).

Abbreviations

CN	Crank-Nicolson Method
CNs	Crank-Nicolson with stress correction scheme
CPU	Center Processing Unit
DTCT	Drained Triaxial Compression Test
DST	Direct Shear Test
ME	Modified Euler Method
MEs	Modified Eulert method with stress correction scheme
NSFS	Nonstationary Flow Surface
FEM	Finite Element Method
FDM	Finite Difference Method
FE	Forward Euler Method
FEs	Forward Euler with stress correction scheme
FTOL	Error Tolerance for Failure Function
HB	Herschel-Bulkley model
REsec	Richardson Extrapolation method with substepping and error control
RKF23sec	Runge-Kutta-Fehlberg 2-3 order method with substepping and error control
RKF23secs	RKF23sec method with stress correction scheme
RKF45sec	Runge-Kutta-Fehlberg 4-5 order method with substepping and error control
ORC	Over-consolidation ratio
STOL	Error Tolerance for Local Stress Integration
SRE	Stress Response Envelope
SST	Simple Shear Test
UTCT	Undrained Triaxial Compression Test
UMAT	User Defined Material Model

Symbols

A	[-]	The assembly operator
$\dot{\boldsymbol{a}}$	[-]	The generalized nodal velocity vector
α	[-]	The parameter of the proposed hypoplastic model
β	[-]	The parameter of the proposed hypoplastic model
$\vec{\boldsymbol{B}}$	[-]	The hypoplastic flow rule
$\mathcal{B}$	[-]	The function of a bound surface
$C_{1,2,3,4}$	[-]	Parameters of a hypoplastic model
D_r	[-]	The reference creep rate
$\boldsymbol{D}$	[-]	The tangent stiffness of the hypoplastic model
$\boldsymbol{\delta}_{ij}$	[-]	The Kronecker delta
E	[N]	Young's modulus of soil
e_i	[-]	The loosest void ratio
e_{crt}	[-]	The critical void ratio
e_d	[-]	The densest void ratio
$\vec{\dot{\boldsymbol{\varepsilon}}}$	[-]	The direct of the stress rate tensor
$\boldsymbol{\varepsilon}$	[%]	Strain tensor
$\dot{\boldsymbol{\varepsilon}}$	[%/s]	Strain rate tensor
$\dot{\boldsymbol{\varepsilon}}^v$	[%/s]	Viscous strain rate tensor
$\dot{\varepsilon}_{ij}$	[%/s]	Strain rate tensor
$\ddot{\boldsymbol{\varepsilon}}$	[%/s^2]	Strain acceleration tensor
$\mathring{\boldsymbol{\varepsilon}}$	[-]	Jaumann stretching-rate tensor
$\dot{\varepsilon}^e_{ij}$	[%/s]	Elastic strain rate tensor
$\dot{\varepsilon}^{vp}_{ij}$	[%/s]	Visco-plastic strain rate tensor
$\boldsymbol{f}^e_{int}$	[-]	The internal nodal force vector
$\boldsymbol{f}^e_{ext}$	[-]	The external nodal force vector
$f_{1,2}$	[-]	The shear deformation in a simple shear test
f_d	[-]	Dynamic yield surface
f_s	[-]	Static yield surface
f_b	[-]	The barotropy function
f_v	[-]	Viscosity factor
$\phi(F)$	[-]	Scaling function
ϕ	[-]	Internal friction angle
ϕ_c	[-]	Critical internal friction angle
ψ	[-]	The dilatancy angle
$\boldsymbol{H}$	[-]	The tangent stiffness of the visco-hypoplastic model
$\eta_{1,2}$	[-]	Viscous parameters
I_1	[-]	First stress invariant
I_e	[-]	The critical state function
I_{se}	[-]	The stiffness function

$\boldsymbol{\mathscr{I}}$	[-]	Fourth-order unity tensor
I_v	[-]	Viscosity index
$\boldsymbol{J}$	[-]	The Jocobian matrix in Abaqus
J_2	[-]	Second deviatoric stress invariant
$\boldsymbol{K}$	[-]	The Tangent stiffness
K_0	[-]	Earth pressure
k_v	[-]	Coefficient of viscosity
κ_s	[-]	Hardening Parameter of the static yield surface
l	[%]	The length of strain path
l_a	[%]	The length of acceleration path
$\boldsymbol{\mathscr{L}}$	[-]	Fourth-order tensor for the linear part of the hypoplastic model
m	[-]	The slope of a line in the log$\dot{\varepsilon}$-log$t$ diagram
$\boldsymbol{N}$	[-]	Second-order tensor for the nonlinear part of the hypoplastic model
$\boldsymbol{\omega}$	[-]	The stretching and spin tensor
$\partial\Omega_v$	[-]	The Dirichlet boundary
$\partial\Omega_t$	[-]	The Neumann boundary
p_e	[Pa]	The equivalent pressure
p'_e	[Pa]	The current effect mean pressure
R_f	[-]	The failure stress ratio
$\dot{\gamma}$	[%]	Engineering shear strain rate
$\ddot{\gamma}$	[%]	Engineering shear acceleration
$\boldsymbol{\sigma}$	[Pa]	Cauchy stress tensor
$\boldsymbol{\sigma}_h$	[Pa]	Frictional stress tensor
$\boldsymbol{\sigma}_v$	[Pa]	Viscous stress tensor
$\boldsymbol{\sigma}^*$	[Pa]	Deviatoric stress tensor
$\hat{\boldsymbol{\sigma}}$	[Pa]	Cauchy stress ratio tensor
σ_{ij}	[Pa]	Cauchy stress tensor
$\dot{\boldsymbol{\sigma}}$	[Pa/s]	Cauchy stress rate tensor
$\dot{\boldsymbol{\sigma}}_h$	[Pa/s]	Frictional stress rate tensor
$\dot{\boldsymbol{\sigma}}_v$	[Pa/s]	Viscous stress rate tensor
$\dot{\sigma}_{ij}$	[Pa/s]	Cauchy stress rate tensor
$\mathring{\boldsymbol{\sigma}}$	[-]	Jaumann stress rate tensor
$\bar{\boldsymbol{t}}$	[-]	The force traction vectors in FEM
t_f	[-]	The creep failure time
τ_{xy}	[Pa]	The shear stress component
$\bar{\boldsymbol{v}}$	[-]	The line velocity in FEM
$\boldsymbol{v}$	[-]	The velocity of a material
$\mathscr{V}$	[-]	The trial functions in FEM
$\upsilon_{i,f}$	[-]	The initial and failure Poisson ratio
W^{vp}	[J]	Visco-plastic work
$\mathscr{W}$	[-]	The variations in FEM
χ	[-]	The parameter of the visco-hypoplastic model
$\boldsymbol{z}$	[-]	The outward normal of the bound surface
$\boldsymbol{\nabla}$	[-]	The Gradient Operator
$\Vert - \Vert$	[-]	The Euclidean norm of a tensor
$\otimes$	[-]	The outer product between two tensors.

Chapter 1

Introduction

1.1 Statement of problems

In geotechnical engineering, the time-dependent behavior of geotechnical materials is of importance to the evaluation of the long-term performance of construction. It is well-known that both clayey soil and granular soil exhibit time-dependent behavior. Clayey soil, usually referred to as isotach material, follows a classic viscous behavior with time. However, granular soil does not obey this classic viscous behavior and is considered as non-isotach material (Augustesen et al., 2004; Karimpour and Lade, 2010; Tatsuoka et al., 2001). Experimental results show that the creep strains are not negligible and can reach up to 10% of the monotonic loading strain, usually understood as the elastoplastic strain. In addition, when loading after creep and relaxation periods, the residence response is more rigid than if the time-dependent processes have not occurred (Tatsuoka et al., 2000). Due to this significance, the viscous effects have been studied extensively over the last decades, including both experimental and theoretical investigations. The latter includes constitutive modeling and application. From a mathematics point of view, the time-dependent deformation of a material depends on its elastic, plastic, and viscous properties. Therefore, the description of the deformation of a material often becomes an insurmountable task. Hence, the time-dependent deformation of a material is often described by mathematical models that concern the predominant characteristic with some assumption for simplification. From the experimental investigations, the time-dependent behavior can be directly measured and understood. Meanwhile, some useful empirical closed-formed equations may be obtained and used directly in practice. However, to accurately predict the behavior of geotechnical structures or a slope with more complex boundary conditions, it is essential to perform numerical modeling using a proper constitutive model that accounts for the time dependency of the stress–strain–strength properties of soils.

Although numerous constitutive models have been proposed for soil creep, the problem is far from being solved. On the one hand, most models describe either the elastoplastic behavior, or the viscous behavior of soil, which concerns solid-like material and fluid-like material, respectively. However, it is common knowledge that there are many import kinds of materials which cannot be classified under either aspect. Some of these materials exhibit both frictional and viscous properties. They may show elastoplastic deformation under the influence of statical stresses, but under dynamic stresses, their deformations can transfer from static regime to dynamic flow state. On the other hand, in any numerical scheme employed for the analysis of the boundary value problems, it eventually becomes necessary to integrate the constitutive equations governing the material behavior. Whereas, the numerical performance relies highly on the methods we choose, and inappropriate choices can easily lead to unsuccessful computations, unreliable results, or unacceptably long analysis times. Hence, it is essential to investigate the integration methods for the practical implementation of the proposed model.

In this thesis, a novel constitutive model for modeling the time-dependent behavior of soil is proposed, which takes into account the contribution of both the frictional and the viscous effects in soils. Furthermore, by using an adaptive explicit integration method with stress correction scheme, this model has been successfully implemented into finite element code for some boundary value problems.

1.2 Experimental observations in clay and sand

Comprehensive reviews of the time-dependent behavior of soils, and the models characterizing of this behavior have recently been presented in the literature Augustesen et al. (2004); Liingaard et al. (2004). The essence of these reviews claims that clay and sand behave differently with respect to time. A brief introduction of this view concerns the different time-dependent behavior of clay and sand is presented as follow.

In order to visualize the observed creep behavior in triaxial conditions, the creep test data is plotted in log$\dot{\varepsilon}$-log t diagrams. When the data is presented in such diagrams, the creep behavior can be analyzed by the parameter m, which is the slope of a straight line in the log$\dot{\varepsilon}_1$-log t diagram. However, upon initiated observation, it may be quite complex to imagine the consequences of varying m values. For that reason, the characteristics of three different m values are illustrated in Fig. 1.1. m is given by Eq. 1.1 and $\dot{\varepsilon}$ is taken as the axial strain rate, $\dot{\varepsilon}_1$, in this section concerning triaxial conditions.

$$m = -\frac{\log \dot{\varepsilon}_1}{\log t} \tag{1.1}$$

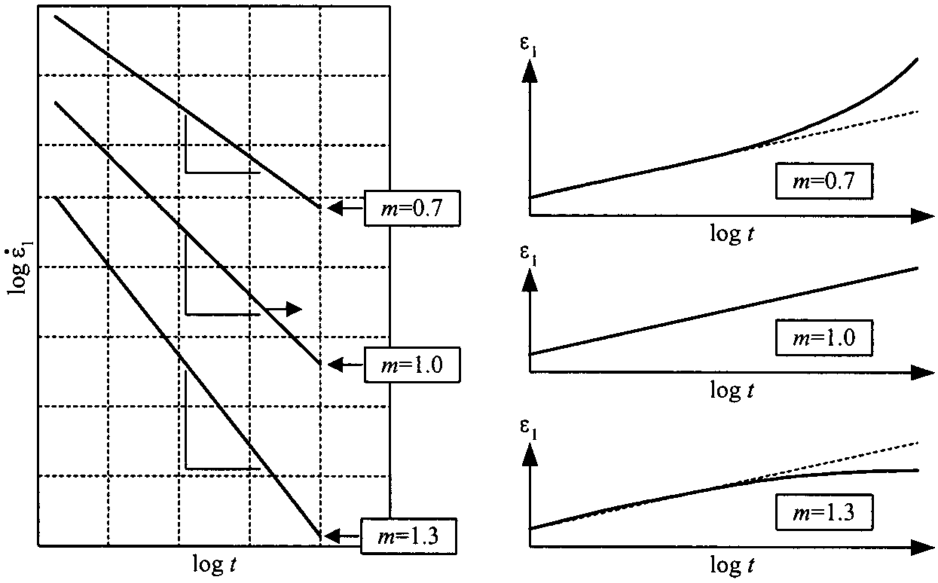

Figure 1.1 (a) Creep characteristics for three different m values. (b) The strain-time curves for the m values are shown to the right. $m = 1$ corresponds to a straight line in the $\dot{\varepsilon}_1 - logt$ diagram. $m \neq 1$ corresponds to curved lines in $\dot{\varepsilon}_1 - logt$ diagrams.

In one of the first studies of creep under drained and undrained triaxial conditions on various normal consolidated clay, Sing and Mitchell (1968) found that the parameter m varied between 0.75 and a value slightly greater than 1.0, with most values less than 1.0. They also suggested that the value of m was independent of the deviatoric stress level for a given soil. In other words, the creep lines for different deviatoric stress levels had the same slope in the log$\dot{\varepsilon}_1$-log t diagram. Sing and Mitchell (1968) also found that the creep strain rate increased with applied deviatoric stress. These characteristics have also been found in sand. The general opinion was that creep behavior in sand for various stress levels was similar to that of clay. For that reason, some researchers have investigated the creep behavior by means of the m parameter. Fig. 1.2(a) shows the creep behavior of Toyoura sand at different stress levels, as reported by Murayama et al. (1984), while Fig. 1.2(b) shows creep tests on Tailings sand for various stress levels, as presented by Mejia et al. (1988).

In the tests by Murayama et al. (1984), the axial effective stress was applied by a loading lever, which corresponded to constant load creep, while Mejia et al. (1988) applied a static load that was periodically adjusted to maintain constant stress. However, creep was allowed for only 20 minutes at each stress levels. The tests results showed that the strain rates increased with the applied deviatoric stress as expected. The strain-time relation in Fig. 1.2(a) seem to be semilogarithmic at low-stress levels, indicated by m values approximately equal to 1.0. The m values at low stresses in Fig. 1.2(b) were approximately 0.9. The results by Mejia et al. (1988) indicated an initial low slope for deviatoric stresses at $q =$

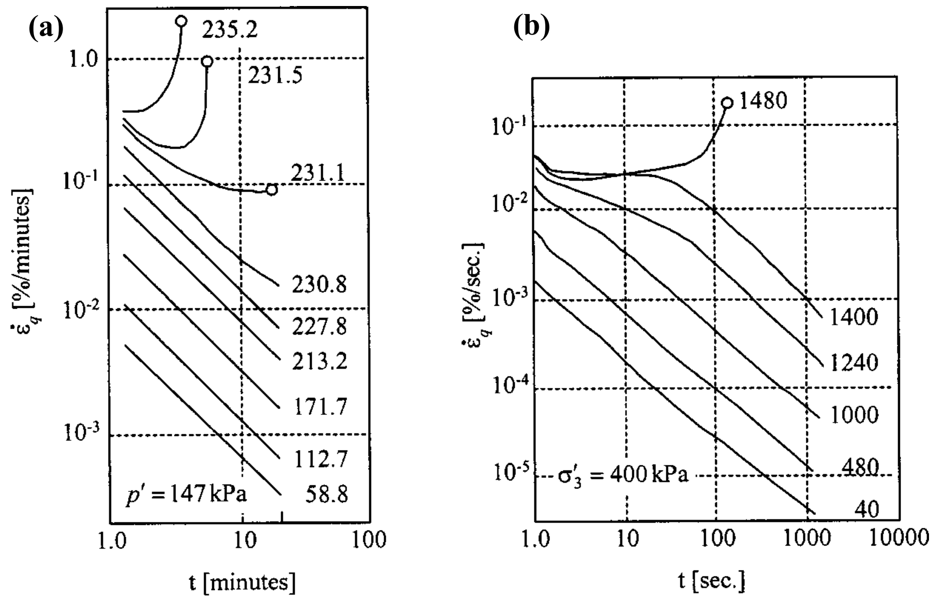

Figure 1.2 (a) Shear strain rate-time response for Toyoura sand at different deviatoric stresses (b)Shear strain rate-time response for Tailing sand at different deviatoric stresses

51,240 kPa and 1,400 kPa. After approximately 10 s, the slopes increased and became similar to the slopes for creep at lower stress levels. In both test series, creep failure was observed at high-stress levels. Mejia et al. (1988) and Murayama et al. (1984) reported that the stress levels at which creep failure occurred corresponded to the stress level at failure for the usual triaxial compression tests at the same confining pressure, i.e., creep rupture was, therefore, inevitable. A systematic study of long-term creep of sands has been presented by (Lade and Liu, 1998; Lade et al., 1997, 2009). These experimental investigations included experimentation with different strain rates, loading along different stress paths, and loading with different time intervals. The strain rate effect, the creep behavior, and the cause of creep in granular soils were largely demonstrated. The strain rate had distinct effects on sand and clay, as highlighted in the schematic stress difference-axial strain diagrams in Fig. 1.3. They showed that strain rate had an important influence on the stress-strain behavior of clay shown in Fig. 1.3(a), while widely different strain rates produce the same stress-strain relation for sand shown in Fig. 1.3(c), as seen in experiments presented by Murayama (1983), and also observed by AnhDan et al. (2006); Di Benedetto et al. (2002); Kiyota and Tatsuoka (2006); Kuwano and Jardine (2002); Matsushita (1999); Tatsuoka et al. (2002, 2008). Changes in strain rate had permanent effects in clay, where changes from one to another stress-strain curve occurred in response to changes in strain rate, see Fig. 1.3(b). Only temporary changes occurred in the stress-strain relations for sand as shown in 1.3(d)

The observed behavior by Augustesen et al. (2004) showed that the phenomena of creep

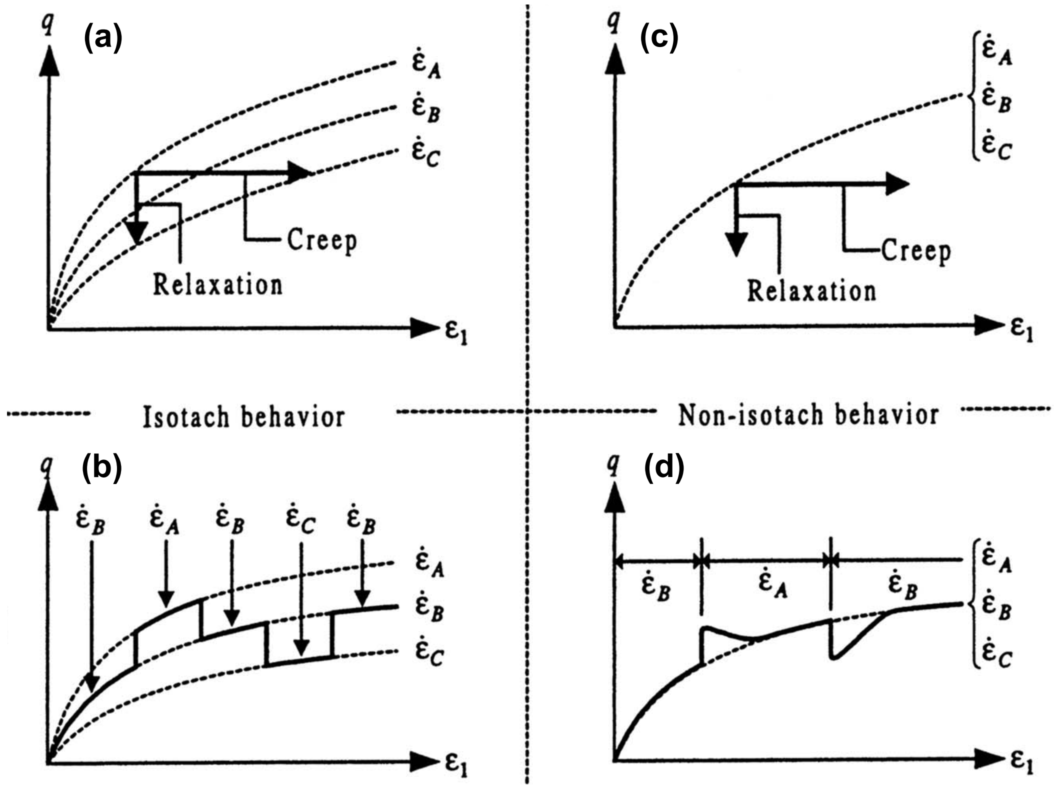

Figure 1.3 Isotach behavior observed in clay for: (a) creep and relaxation; (b) stepwise chance in strain rate. Non-isotach behavior observed in sand for (c) creep and relation; and (d) stepwise change in strain rate

and stress relaxation were also different in clay and sand. For clay, creep and relaxation properties could be obtained from a constant rate of strain tests, and vice versa. The fact that creep, relaxation, and strain rate effects are governed by the same basic mechanism referred to as isotach behavior. Isotach behavior, usually observed in clay, implies that a unique stress-strain-time rate relation exists for a given soil. Isotach behavior is shown in Fig. 1.3(a) and (b). On the other hand, an investigation of strain rate effects in dense Cambria sand under drained and undrained conditions at high pressures performed by Yamamuro and Lade (1993) showed no significant rate effects on the strain-stress relations. The Hostun and Toyoura sands tested by Matsushita (1999) exhibited noticeable amounts of creep and relaxation with no strain rate effects. The experimental results led to one of the main conclusions: the phenomena of creep and relaxation cannot be predicted based on results of constant rate of strain tests. This is because the changes in stress-strain relations due to changes in strain rate are temporary, as shown in Fig. 1.3(d). This behavior of sand does not correspond to the observed rate effects in clay. For sand, this behavior is labeled as nonisotach behavior. The non-isotach behavior is illustrated in Fig. 1.3(c) and (d).

1.3 Constitutive models for time-dependent behavior of soil

Various types of models have been developed to capture time effects in soils Liingaard et al. (2004). Empirical and rheological models have been mostly employed for one-dimensional time effects, while general three-dimensional stress-strain-time models based on nonlinear material behavior have been extensively used in practical engineering projects. In the later models, the viscous behavior is often coupled to an existing elastic-plastic model, e.g. overstress theory by Perzyna (1963, 1966) and the non-stationary flow surface theory by (Olszak and Perzyna, 1966b). In this section, the mentioned models will be briefly introduced. More details can be referred to in (Liingaard et al., 2004)

1.3.1 Empirical models

Empirical models are mainly obtained by fitting experimental results from creep, stress relaxation, and constant rate of strain tests. These constitutive relations are generally given by closed-form solutions or differential equations. In addition, they are strictly limited to a specific boundary and loading conditions (e.g., one specific model for creep and another for relaxation) and frequently involve natural time. That is, the relations are not general. However, these models are quite useful in several ways. They often reflect the real behavior of the soils, and, despite their limited applicability and sometimes theoretical inconsistency, they provide a basis for developing more sophisticated constitutive models. They may also provide practical solutions to engineering problems, as long as the boundary conditions comply with the laboratory experiments. The empirical models are categorized as empirical primary relations and secondary semi-empirical relations.

(1) **Empirical Primary Relations**

Primary empirical relations are obtained by directly fitting the observed test data with simple mathematical functions. They reflect actual observed soil behavior and are often restricted to specific phenomena The empirical models described below are: (I) The semilogarithmic law for creep, (II) Singh and Mitchell's creep model, (III) Lacerda and Houston's relaxation model, (IV) Prevost's model, and (V) Strain-rate approach.

Based on above concept, different primary empirical models have been proposed, e.g. relations for predicting creep by Yin (1999); The three parametric creep model by Sing and Mitchell (1968); relaxation model for clay and sand by Lacerda and Houston (1973); relaxation model based on undrained triaxial tests by Prevost (1976); viscous model for rate-dependency based on strain rate approach by Leroueil et al. (1985); and viscous model proposed by Yin et al. (2011) for time-dependent behavior of structural clay, which was also extended to three-dimensional form for general engineering practices

(2) **Secondary Semi-empirical Relations**

Secondary semi-empirical models are classified as models obtained by combining one or more of the primary models. The models can, to some extent, be used as stress-strain-time or stress-strain-strain-rate models that yield solutions for creep as well as relaxation within one particular model. These models are recognized as closed-form solutions for the different phenomena, such as creep and relaxation, contrary to the elastic/viscoplastic models reviewed herein, which are presented as rate formulations in incremental form.

The semi-empirical models explained below are: (I) Kavazanjian and Mitchell's approach, (II) Tavenas' approach, (III) Bjerrum's model, and (IV) Yin and Graham's model. For example, Kavazanjian and Mitchell (1977) proposed a general stress-strain-time model based on the decomposition of strain into volumetric strain and deviatoric strain. The similar approach has been used by Tavenas et al. (1978) for creep deformation of over-consolidated clay. On the other hand, Bjerrum (1973) proposed a concept for settlement analysis of normally and lightly overconsolidated clay. Moreover, based on one-dimensional creep test, an equivalent time concept have been proposed by Yin et al. (1994) for time-dependent of clay.

1.3.2 Rheological model

Rheological models were typically developed for metals, steel, and fluids, but they were, to some extent, used in the study of time effects in geomaterials. The terminology rheological models is often used when describing linear viscoelastic behavior of materials. However, in the rheology of soils the term rheological model includes plastic behavior as well. The rheological models are usually divided into three categories, the differential approach, engineering theories of creep, and the hereditary approach.

(1) **The differential approach**

The differential approach is also referred to as the method of mechanical rheological models. The constitutive relations are constructed by combining different elementary material models, such as the Hookean, Saint-Vernant's, Newtonian materials the Bingham model, and the Herschel-Bulkley model. It is noteworthy that a modified form of the Herschel-Bulkley model is combined with a hypoplastic model to describe the viscous behavior of granular materials in this thesis. Therefore, special attention will be paid to the Herschel-Bulkley model.

The Herschel-Bulkley model is a purely empirical curve-matching model. It is applicable to viscometer test results by using the following equation:

$$\tau = \tau_y + k_v(\dot{\gamma})^n \tag{1.2}$$

where k_v (consistent coefficient) and n (flow index) are constant fitting parameters. The model can be characterized by two components, i.e. time-independent component and time-dependent component. The time-independent component consists of the spring with spring constant E, denoting the elastic element. The time-dependent component consists of the dashpot with coefficient of viscosity, k_v, and the slider with a threshold stress τ_y combined in parallel, denoting the viscoplastic element. Since the elastic and viscoplastic elements are connected in series, the total shear strain rate $\dot{\gamma}$ may be additively decomposed with respect to the two groups. The slider along with the viscoplastic element are inactive as long as $\tau > \tau_y$. Therefore, it is only the difference $\tau - \tau_y$ that gives rise to viscoplastic strains. The Herschel-Bulkley model can be expressed by the decomposition of the strain rate.

$$\dot{\varepsilon} = \begin{cases} \dot{\varepsilon}^e + \dot{\varepsilon}^{vp} = \frac{\dot{\sigma}}{E} + \sqrt[n]{(\sigma - \sigma_y)/k_v} & \text{for } \sigma > \sigma_y \\ \dot{\varepsilon}^e = \frac{\dot{\sigma}}{E} & \text{for } \sigma \leqslant \sigma_y \end{cases} \tag{1.3}$$

where $\dot{\varepsilon}$ is total strain rate, $\dot{\varepsilon}^e$ and $\dot{\varepsilon}^{vp}$ are strain rates in the elastic and viscoplastic elements, respectively. The assumptions of the Herschel-Bulkley model are similar to those of the Bingham model for relatively high-viscosity fluids with laminar flow (Huang and Garcia, 1998). Chen et al. (2004) recommended that this model can be use for finer-grained soils

The basic theory behind the Herschel-Bulkley model is similar to the Bingham model. Their major difference lies in the formulation of the viscous part, i.e. the Bingham rheology is linear, while the Herschel-Bulkley rheology is nonlinear in the description of the viscous flow. Therefore, the Herschel-Bulkley model can, to some extent, reflect the highly nonlinear elastic and plastic behavior of soil. However, there are some shortcomings to different approaches of rheological models. The constitutive relationships for the rheological models are formulated for uniaxial compression conditions. The generalization of rheological models from one into three dimensions is possible, but practical calibration and application seem to be difficult. In principle, rheological models can only describe the viscous behavior of the material because the inviscid behavior is represented by a threshold stress τ_y. These are apparently not correct assumptions for soils. It is well-known that soil exhibit both frictional and viscous behavior. In most cases, these two contributions coexist and simultaneously influence the macro mechanics of soil. Hence, an inviscid part, which can describe the frictional behavior of materials is needed if we want to extend the rheological models.

Moreover, the accelerated creep cannot be modeled after rheological models.

(2) **Engineering theories of creep**

General theories for determining the inelastic creep response of solids are widely applied in the mechanics of concrete and metal. The mathematical structures of empirical models are varieties of this approach. Three sub-classes can be characterized as: (I)Total strain model, in which the total strain is assumed consists of an instantaneous elastic and a viscid creep component; (II) Time-hardening model, in which the hardening function is dependent on time; and (III) Strain-hardening model, in which the hardening function is dependent on creep strain.

(3) **The hereditary approach**

The hereditary approach is also known as the method of integral representation. In this approach, the time-dependent creep strain or stress is defined by a creep or relaxation function, which is a hereditary memory function describing the historic dependence of strains or stresses.

1.3.3 General stress-strain-time models

General stress-strain-time models are usually refereed to as three-dimensional models. They are often given in the incremental form. Therefore, they are readily adaptable to numerical implementation suitable for a finite element procedure. The models are not limited to the boundary conditions from which they are calibrated, i.e., in principle, all possible stress paths can be simulated. Special attention is paid to elastoviscoplastic models, which combine inviscid elastic and time-dependent plastic behavior. Elastic-viscoplastic models can be divided into three classes: (I) Elastoviscoplastic models based on the concept of overstress, they are denoted overstress models and the theory is called the overstress theory, (II) elastoviscoplastic models based on the concept of a nonstationary flow surface. they are denoted nonstationary flow surface (NSFS) models and the theory is called the NSFS theory, and (III) others.

(1) **Overstress Theory**

The concept of the overstress theory by Perzyna (1963, 1966) is widely used to develop three-dimensional elasto-viscoplastic constitutive models. A key assumption in relation to Perzyna's overstress theory is that the viscous effects are negligible in the elastic region, i.e., no viscous strains can occur within the static yield surface, which corresponds to the traditional yield surface associated with time-independent plasticity. In other words, the elastic strains are time independent whereas the inelastic strains are time dependent. The total strain rate is additively composed of the elastic and viscoplastic strain rates:

$$\dot{\varepsilon}_{ij} = \dot{\varepsilon}_{ij}^{e} + \dot{\varepsilon}_{ij}^{vp} \tag{1.4}$$

where $\dot{\varepsilon}_{ij}$ denotes the i, j component of the total strain rate tensor; and the superscripts e and vp stand for the elastic and the inelastic components, respectively.

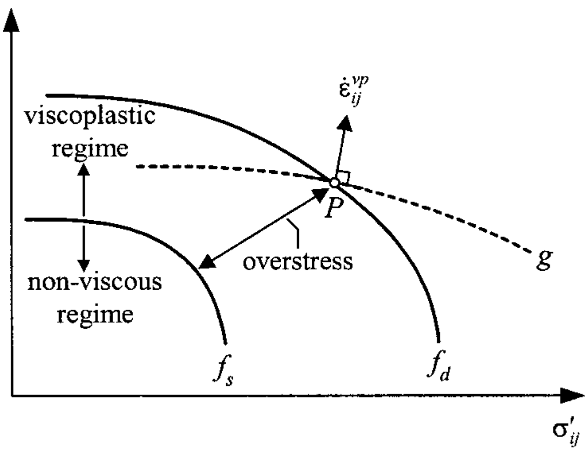

Figure 1.4 Stress state P is part of the dynamic yield surface f_d and overstress F is defined as the distance between P and the static yield surface f_s . Furthermore, the viscoplastic strain rate vector is perpendicular to the plastic potential surface g.

According to the theory of elasto-viscoplasticity, the inelastic strain rate represents both the viscous and plastic effects. The elastic strain rate $\dot{\varepsilon}_{ij}^{e}$ in Eq. (1.4) is assumed to conform to the generalized Hooke's law, while the viscoplastic strain-rate $\dot{\varepsilon}_{ij}^{vp}$ is assumed to conform to the following non-associated flow rule:

$$\dot{\varepsilon}_{ij}^{vp} = \gamma\phi(F)\frac{\partial g}{\partial \sigma'_{ij}} \tag{1.5}$$

where γ is fluidity parameter; ϕ is viscous nucleus; **F** is overstress function; g is potential function; and σ'_{ij} is effective stress state. The overstress function can be expressed as:

$$F(\sigma'_{ij}, W^{vp}) = \frac{f_d(\sigma'_{ij}, W^{vp})}{\kappa_s(W^{vp})} - 1, \text{ where } \kappa_s = \kappa_s(\int_0^{\dot{\varepsilon}_{ij}^{vp}} \sigma'_{ij}\varepsilon_{ij}^{vp}) \tag{1.6}$$

In Eq. (1.6), the function f_d depends on the stress state and the viscoplastic work W^{vp}. The function f_d describes the dynamic loading surface on which the current stress state P

is located, as shown in Fig. 1.4. κ_s is the hardening parameter of the static yield surface. $F=0$ when $f_d(\sigma'_{ij}, W^{vp}) = \kappa_s(W^{vp})$ which implies that κ_s must be an expression for the static yield surface f_s . The overstress theory differs from general elasto-plasticity in the sense that the consistency rule is not used in the derivation of the theory. This implies that inelastic strains in the overstress model are related to the current stress point rather than the stress history, while the inelastic strains are related to the stress rate in elasto-plasticity. Furthermore, by assuming the invalidity of the consistency rule, the stress state is allowed to be on, within or outside the static yield surface. This is used in the definition of overstress F. F is defined as the distance in stress space between the current stress state P and the static yield surface f_s , as illustrated in Fig. 1.4. $F > 0$, $F < 0$, and $F = 0$ when the state of stress P is outside, within, or on f_s . Therefore, according to the key assumption and the flow rule, the following constraints apply to the scaling function ϕ:

$$\langle \phi(F) \rangle = \begin{cases} 0 & \text{for } F \leqslant 0 \\ \phi(F) & \text{for } F > 0 \end{cases} \tag{1.7}$$

Eq. (1.7) can be considered as the loading criterion for inelastic deformations. The direction of $\dot{\varepsilon}^{vp}_{ij}$ in Eq. (1.5) is normal to the potential surface g at the current stress point P, as shown in Fig. 1.4. The magnitude of $\dot{\varepsilon}^{vp}_{ij}$ is given by γ and the scaling function $\langle \phi(F) \rangle$. Different scaling functions have been proposed for soils, as summarized by Yin et al. (2010a) in Table.1.1. The term $f_d - \kappa_s$ in the original expression by Adachi and Oka (1982) has been replace by $f_d/\kappa_s - 1$ in order to keep the same normalized term f_d/κ_s.

Table 1.1 Scaling functions for viscoplasticity based on the overstress theory of Perzyna

No.	Type	Scaling function $\phi(F)$	Reference
1	Expo 1	$\exp[N(f_d - \kappa_s)]$	Adachi and Oka (1982)
2	Expo 2	$\exp\left[N(\frac{f_d}{\kappa_s} - 1)\right] - 1$	Fodil et al. (1998)
3	Power 1	$(\frac{f_d}{\kappa_s})^n$	Rowe and Hinchberger (1998)
4	Power 2	$(\frac{f_d}{\kappa_s})^n - 1$	Hinchberger and Rowe (2005)
5	Power 3	$(\frac{f_d}{\kappa_s} - 1)^n$	Shahrour and Meimon (1995)

In a conventional overstress model, the material is assumed to behave elastically during the sudden application of a strain increment, which brings the stress state temporally beyond the yield surface. After when viscoplastic strain occurs, the yield surface expands due to strain hardening and simultaneously cause stress relaxation due to the reduction of elastic strain. Based on the conventional overstress model, the viscoplastic strain will not occur when the stress state is located within the static yield surface. However, experimental results have indicated that the viscoplastic strain always occurs, implying that the static yield surface never exists. Thus, the fundamental hypothesis of the conventional overstress model is in conflict with the experimental interpretations.

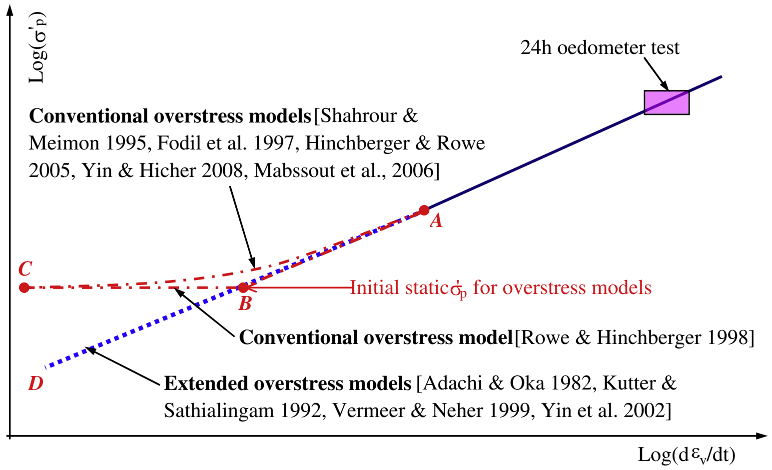

Figure 1.5 Schematic plot for the relationship between the strain-rate and the apparent preconsolidation pressure by different assumptions of models (Yin et al., 2010b)

To overcome the shortcoming, Yin et al. (2010b) proposed the extended overstress concept. The concept is graphically illustrated in Fig. 1.5. The double log plot of $\sigma'_p - d\varepsilon_v/dt$ is schematically plotted in Fig. 1.5. For conventional overstress models by Fodil et al. (1998); Hinchberger and Rowe (2005); Shahrour and Meimon (1995); Yin and Hicher (2008), a limiting initial static yield σ'_p was assumed at a very low strain-rate (point C), corresponding to the initial equilibrium state. Within the region of low strain-rate, the path A-C is nonlinear. The viscosity parameters can be back-calculated from a strain-rate test or 24 hours standard oedometer test. The viscosity parameters strongly depend on the assumed value of the initial static yield stress σ'_p, which is somehow arbitrary. This deficiency can be overcome by assuming the linear line is extended indefinitely (see the path A-D as shown in Fig. 1.5). In this way, the initial static yield stress does not exist. Therefore, there is no need to assume the initial value of static yield stress. The conventional overstress model is then extended and able to produce viscoplastic strains indefinitely in time. It also implies that viscoplastic strains may occur in the elastic region.

There are many elastoviscoplastic models based on the concept of overstress in literature. For example, the Adachi/Okano model for fully saturated and normally consolidated clay (Adachi and Oka, 1982); a viscoplastic cap model proposed by Katona (1984); Katona and Mulert (1984) for a wide range of geological materials, especially soils and rocks;

the models proposed by di Prisco and his co-workers (Di Prisco and Imposimato, 1996; Di Prisco et al., 2000) for time effects in loose sand; and a viscoplastic model by Desai and Zhang (1987) for description of the viscoplastic behavior of geologic material such as sand and rock salt.

(2) **Nonstationary Flow Surface Theory**

The concept of the NSFS theory has been introduced and developed by Naghdi and Murch (1962); Olszak and Perzyna (1966a) based on the yield surface of elastoplasticity. The NSFS theory is a result of the further development of the inviscid theory of elastoplasticity. That is, the NSFS theory is based on the basic concepts of inviscid elastoplasticity. The major difference between the NSFS theory and classical elastoplasticity lies in the definition of the yield condition. According to the latter, the yield condition for an isotropic hardening material is given by:

$$f(\sigma'_{ij}, \varepsilon^{p}_{ij}) = 0 \tag{1.8}$$

where σ'_{ij} ε^{p}_{ij} are effective stress state and plastic strains, respectively. According to Eq. 1.8, the yield condition does not change with time when the plastic strains are held constant. In that sense, the yield surface can be denoted as stationary. In contrast, the yield condition associated with the NSFS theory depends on time:

$$f(\sigma'_{ij}, \varepsilon^{vp}_{ij}, \beta) = 0 \tag{1.9}$$

where ε^{vp}_{ij} and β are viscoplastic strains and a time-dependent function, respectively. It can be concluded from Eq. 1.9 that the yield surface changes every moment even though the viscoplastic strains are held constant. In that sense, the flow surface can be denoted nonstationary. The difference between the yield surface defined in connection with classical elastoplasticity and NSFS theory is illustrated in Fig. 1.6 For an elastoviscoplastic material, the yield surface corresponding to any given viscoplastic strain will be reached at different points A, A_1, or A_2 dependent on time β. For an elastoplastic material, the yield surface corresponding to a given viscoplastic strain will for a given load path be reached at the same point (for example A) independently of time β. Like the overstress theory, the total strain rate $\dot{\varepsilon}$ associated with the NSFS theory can be decomposed into an elastic $\dot{\varepsilon}^{e}$ and a viscoplastic $\dot{\varepsilon}^{vp}$ part in the following way:

$$\dot{\varepsilon}_{ij} = \dot{\varepsilon}^{e}_{ij} + \dot{\varepsilon}^{vp}_{ij} \tag{1.10}$$

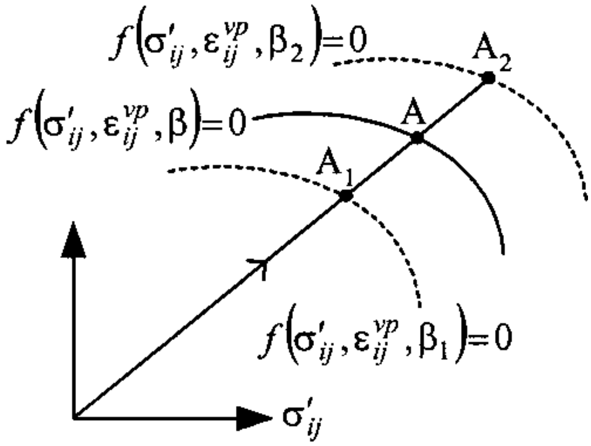

Figure 1.6 Loading path and yield surfaces of the NSFS model .

The elastic strain rate is determined by Hooke's generalized law, and the viscoplastic strain rate is defined according to the flow rule:

$$\dot{\varepsilon}^{vp}_{ij} = \langle \Lambda \rangle \frac{\partial g}{\partial \sigma'_{ij}} \tag{1.11}$$

where Λ is non-negative multiplier; and g is viscoplastic potential. $< \quad >$ is MacCauley's brackets. That is, MacCauley's brackets ensure that viscoplastic strains occur when loading from a plastic state and, in all other cases, the viscoplastic strains are zero. The expression for Λ yields:

$$\Lambda = -\frac{\frac{\partial f}{\partial \sigma'_{ij}} \dot{\sigma}'_{ij} + \frac{\partial f}{\partial \beta} \dot{\beta}}{\frac{\partial f}{\partial \varepsilon^{vp}_{ij}} \frac{\partial g}{\partial \sigma'_{ij}}} \tag{1.12}$$

where Λ in Eq. 1.12 can be decomposed into two parts:

$$\Lambda = \Lambda_1 + \Lambda_2 = -\frac{\frac{\partial f}{\partial \sigma'_{ij}} \dot{\sigma}'_{ij}}{\frac{\partial f}{\partial \varepsilon^{vp}_{ij}} \frac{\partial g}{\partial \sigma'_{ij}}} - \frac{\frac{\partial f}{\partial \beta} \dot{\beta}}{\frac{\partial f}{\partial \varepsilon^{vp}_{ij}} \frac{\partial g}{\partial \sigma'_{ij}}} \tag{1.13}$$

The parameter Λ_1 is identical to the plastic multiplier λ defined in connection with classical elastoplasticity, and Λ_2 controls the viscoplatic strain.

Many elastoviscoplastic models based on the NSFS theory have been proposed (Dragon and Mróz, 1979; Nova, 1982; Sekiguchi, 1977). The shortcoming of the NSFS theory lies on that it cannot account for the viscoplastic deformation if the stress state lies inside the yield surface. Therefore, it is inadequate to model creep and relaxation in this case. Due to this theoretical shortcoming, very few researches related to the application of this type of model have been reported in recent years.

1.3.4 Time dependent hypoplastic model

The above models are based on the combination of classic elastoplastic theory with overstress concept. An alternative way to incorporate the time-dependency of soil is hypoplasticity. Recently, some visco-hypoplastic models based on various theories, e.g. the theory of overstress or hydromechanics, have been proposed.

Wu 1993

Wu et al. (1993) proposed several concepts for the visco-hypoplastic constitutive models. The first concept for visco-hypoplasticity is to violate the restriction that the hypoplastic equation is homogeneous in $\boldsymbol{\sigma}$ i.e. with $\lambda > 0$, if $\mathbf{H}(\boldsymbol{\sigma}, \lambda\dot{\boldsymbol{\varepsilon}}) \neq \lambda\mathbf{H}(\boldsymbol{\sigma}, \dot{\boldsymbol{\varepsilon}})$, then, rate dependent is inevitable. Based on this concept, an extended model has been proposed , it reads:

$$\mathring{\boldsymbol{\sigma}} = \mathscr{L}(\boldsymbol{\sigma}) : \dot{\boldsymbol{\varepsilon}} - \boldsymbol{N}(\boldsymbol{\sigma})(\alpha\|\dot{\boldsymbol{\varepsilon}}\| + \beta), \tag{1.14}$$

where α and β are scale function of stress, strain and strain rate.

$$\alpha = \frac{1}{log(10 + \alpha_1\|\boldsymbol{\varepsilon}\|^{\alpha_2})}, \text{ and } \beta = \alpha_3 \exp(-\alpha_4 l) \tag{1.15}$$

where α_1 ,α_2 , α_3 and α_4 are constants, and the l denotes the length of the strain path and can be expressed in the following:

$$l = \int_0^t \|\boldsymbol{\varepsilon}\| dt \tag{1.16}$$

With an appropriate choice of the constants, the Eq. (1.14) can describe creep, relaxation, and rate-dependent behavior of normally consolidated cohesive soils.

Another concept of visco-hypoplasticity is based on the theory of overstress by (Perzyna, 1963, 1966). This formulation adopts the classical visco-plasticity to the hypoplastic constitutive equation by introducing a characteristic viscous strain rate $\dot{\boldsymbol{\varepsilon}}^v$ that depends on the stress and possibly some structure tensors, yet not on their rates. The viscous strain rate enters the constitutive equation in the following matter:

$$\mathring{\boldsymbol{\sigma}} = \mathscr{L}(\boldsymbol{\sigma}) : (\dot{\boldsymbol{\varepsilon}} - \dot{\boldsymbol{\varepsilon}}^v) - \boldsymbol{N}(\boldsymbol{\sigma})(\|\dot{\boldsymbol{\varepsilon}} - \dot{\boldsymbol{\varepsilon}}^v\|), \tag{1.17}$$

where $\mathscr{L}$ and $\boldsymbol{N}$ denote the linear and nonlinear operators, respectively. The direct of the viscous flow is

$$f_v = \frac{\dot{\boldsymbol{\varepsilon}}^v}{\|\dot{\boldsymbol{\varepsilon}}^v\|} \tag{1.18}$$

which is equal to the direction of the plastic flow in a limit state ($\mathring{\boldsymbol{\sigma}} = 0$). Hence, the viscous flow can be expressed by the linear and nonlinear operators.

$$f_v = \frac{\mathscr{L}^{-1} : \boldsymbol{N}}{\|\mathscr{L}^{-1} : \boldsymbol{N}\|} \tag{1.19}$$

In other words, the direction of the plastic flow corresponds to such a strain rate in the limited state that causes no changes in stress. A yield function f_d is introduced to describe the intensity of viscous flow:

$$\dot{\boldsymbol{\varepsilon}}^v = \gamma \phi(F) f_v \tag{1.20}$$

where γ is the fluidity parameter; and the viscous nucleus is expressed as $\phi(F) = (f_d/f_s)^n$ with f_d and f_s being the dynamic yield surface and the static yield surface. Although some concepts of visco-hypoplasticity have been outlined by Wu et al. (1993), no specific constitutive equation have been proposed. However, these concepts lead to some advanced visco-hypoplastic constitutive models, which will be described in the following subsections.

Niemunis 2003

Based on experimental observations on oedometer tests (Niemunis and Krieg, 1996) and Olszak and Perzyna's overstress theory (Olszak and Perzyna, 1966b), a noteworthy work by Niemunis (Niemunis, 2003a,b; Niemunis et al., 2009) has forwarded the viscohypoplastic models into many practical engineering projects. The rate type equation of the visco-hypoplstic model is expressed in the following form:

$$\mathring{\boldsymbol{\sigma}} = \mathscr{L} : (\dot{\boldsymbol{\varepsilon}} - \dot{\boldsymbol{\varepsilon}}^v), \tag{1.21}$$

Noted that the above equation only keeps the linear tensor as shown in Eq. (1.17).

The stiffness tensor $\mathscr{L}$ from hypoplasticity (Wolffesdorff, 1996) was modified for the visco-hypoplastic model in order to reduce the change of volume when the deviator stress increase. The tensor $\mathscr{L}$ for the visco-hypoplastic equation is: with the linear term

$$\mathscr{L} = f_b (F^2 \mathscr{I} + a^2 \hat{\boldsymbol{\sigma}} \otimes \hat{\boldsymbol{\sigma}}) \tag{1.22}$$

where $\boldsymbol{I}$ is a second-order unity tensor $\mathscr{I}_{ijkl} = 0.5(\boldsymbol{I}_{ik}\boldsymbol{I}_{jl} + \boldsymbol{I}_{il}\boldsymbol{I}_{jk})$, and

$$a = \frac{\sqrt{3}(3-\sin\phi_c)}{2\sqrt{2}\sin\phi_c} \tag{1.23}$$

The factor F for adapting the deviatoric yield curve to Matsuoka–Nakai is

$$F = \sqrt{\frac{1}{8}\tan^2\psi + \frac{2-\tan^2\psi}{2+\sqrt{2}\tan\psi\cos3\theta}} - \frac{1}{2\sqrt{2}}\tan\psi \tag{1.24}$$

with

$$\tan\psi = \sqrt{3}\|\hat{\boldsymbol{\sigma}}^*\|, \text{and} \quad \cos3\theta = -\frac{\sqrt{6}\hat{\boldsymbol{\sigma}}^{*3}}{\left(\mathrm{tr}\hat{\boldsymbol{\sigma}}^{*2}\right)^{3/2}} \tag{1.25}$$

The new barotropy function f_b is supposed to describe the volume changes at the absence of creep, i.e. $\dot{\boldsymbol{\varepsilon}}^v \neq 0$. The barotropy factor is defined according to the condition of the experiment. For isotropic conditions yields:

$$f_b = -\frac{\mathrm{tr}\boldsymbol{\sigma}}{(1+a^2/3)\kappa} = -\beta_b\mathrm{tr}\boldsymbol{\sigma}, \tag{1.26}$$

and for oedometric conditions

$$f_b = -\frac{\mathrm{tr}\boldsymbol{\sigma}}{\left[1+a^2/(1+2K_0)\right]\kappa^0} = -\beta_b\mathrm{tr}\boldsymbol{\sigma}, \tag{1.27}$$

The parameters κ and κ_0 are the unloading or reloading slope of the isotropic and oedometric test respectively. The parameter K_0, defined as the earth pressure coefficient, is calculated as:

$$K_0 = \frac{-2-a^2+\sqrt{36+36a^2+a^4}}{16} \tag{1.28}$$

As a matter of fact, the intensity of the viscous strain rate $\dot{\boldsymbol{\varepsilon}}^v$ can be expressed in different ways. A similar way to Norton's creep law is adopted:

$$\dot{\boldsymbol{\varepsilon}}^v = -D_r\vec{\boldsymbol{B}}\left(\frac{1}{ORC}\right)^{1/I_v}, \tag{1.29}$$

where $\vec{\boldsymbol{B}}$ is the hypoplastic flow rule, D_r is the reference creep rate, I_v is the viscosity index of Leinenkugel (1976), and OCR is the over-consolidation ratio, which can be calculated from $OCR = p_e/p'$ with p' and p_e representing the current effective mean stress and the equivalent isotropic pressure, respectively. This visco-hypoplastic constitutive model has been shown to enable a remarkably good description of creep and relaxation(Gudehus, 2004). Future extension for anisotropic pre-consolidation surface and structured soils can be found in literatures(Niemunis et al., 2009). Additionally, by making use of the Niemunis' visco-hypoplastic model, numerical simulations of footing (Qiu and Grabe, 2011), creeping slope (Van Den Ham et al., 2006, 2009), viscous behavior of Pampean Loess (Lizcano et al., 2007), and structured soils (Fuentes et al., 2010) have been conducted. These works have proved that the theory of visco-hypoplastic constitutive model is an attractive approach to account for the time-dependent behavior of soil.

Gudehus 2004

It is worth noting that the new barotropy function f_b in Niemunis' viscous model is modified according to Cam clay theory. This approach is also adopted by Mašín (2005) for a hypoplastic constitutive model for clay. Therefore, a modified viscous hypoplastic model is proposed by replacing the Cam clay part with the genuine hypoplasticity Gudehus (2004).

Formally viscosity is introduced into hypoplasticity by replacing the factor $\|\dot{\boldsymbol{\varepsilon}}\|$ by $f_v\dot{\boldsymbol{\varepsilon}}_r$. Hence, the generalized form of the visco-hypoplastic constitutive equation reads:

$$\mathring{\boldsymbol{\sigma}} = \mathscr{L}(\boldsymbol{\sigma}, e) : \dot{\boldsymbol{\varepsilon}} - \boldsymbol{N}(\boldsymbol{\sigma}, e) f_v \dot{\boldsymbol{\varepsilon}}_r \tag{1.30}$$

The same linear and nonlinear operators as Bauer (1996) are adopted:

$$\mathscr{L} = f_b(a^2\mathscr{I} + \hat{\boldsymbol{\sigma}} \otimes \hat{\boldsymbol{\sigma}}), \quad \boldsymbol{N} = f_b f_d a(\hat{\boldsymbol{\sigma}} + \hat{\boldsymbol{\sigma}}^*) \tag{1.31}$$

where $\boldsymbol{I}$ is a second-order unity tensor, $\mathscr{I}_{ijkl} = 0.5(\boldsymbol{I}_{ik}\boldsymbol{I}_{jl} + \boldsymbol{I}_{il}\boldsymbol{I}_{jk})$. and $\hat{\boldsymbol{\sigma}} = \boldsymbol{\sigma}/\mathrm{tr}\boldsymbol{\sigma}$ is the normalized stress tensor. However, different scale function f_d and f_b are adopted in this version. The argotropic density factor f_d depends on the density index I_d via

$$f_d = (1 - I_d)^{\alpha_p} = \Big(\frac{e - e_d}{e_c - e_d}\Big)^{\alpha_p} \tag{1.32}$$

where e_i, e_c, and e_d are the pressure-dependent loosest, densest, and the critical void ratios given by

$$\frac{e_i}{e_{i0}} = \frac{e_d}{e_{d0}} = \frac{e_c}{e_{c0}} = \exp\Big[-\Big(\frac{-\mathrm{tr}\boldsymbol{\sigma}}{h_s}\Big)^n\Big] \tag{1.33}$$

and h_s is granulate stiffness given by

$$h_s/h_{sr} = \begin{cases} 1 + I_v \mathrm{In}(\dot{\boldsymbol{\varepsilon}}/\dot{\boldsymbol{\varepsilon}}_r) & \text{if } \dot{\boldsymbol{\varepsilon}} \geqslant \dot{\boldsymbol{\varepsilon}}_0 \\ \alpha_r & \text{if } \dot{\boldsymbol{\varepsilon}} < \dot{\boldsymbol{\varepsilon}}_0 \end{cases} \tag{1.34}$$

with a bound $\dot{\boldsymbol{\varepsilon}}_0$ outlined below. $\dot{\boldsymbol{\varepsilon}}_r$ is a reference rate, conveniently taken as $10^{-6}s^{-1}$, which could be replaced by a physically objective value. The viscosity index I_v renages from 0.02 to 0.06. The lower bound for h_s/h_{sr} in Eq. (1.34) is called the relaxation factor α_r. It is fixed as $\alpha_r = 0.5$ and secures that h_r does ot vanish for $\dot{\boldsymbol{\varepsilon}} < \dot{\boldsymbol{\varepsilon}}_0$. In addition, the exponent α_p in Eq. (1.32) lies in the range from 0.10 to 0.25. For the rate $\dot{\boldsymbol{\varepsilon}} < \dot{\boldsymbol{\varepsilon}}_r$, α_p determines the peak angles of friction and dilatancy as in non-viscous hypoplasticity.

The factor f_b is determined by calculating an isotropic compression with constant strain rate in the following equation:

$$f_s = \frac{h_s}{n}\left(\frac{e_i}{e}\right)^{\beta}\frac{1+e_i}{e_i}\left(\frac{-\mathrm{tr}\boldsymbol{\sigma}}{h_s}\right)^{1-n}\left[3/a^2+1-\sqrt{3}/a\left(\frac{e_{i0}-e_{d0}}{e_{c0}-e_{d0}}\right)^{\alpha}\right]^{-1} \tag{1.35}$$

The constant β usually lies in the range between 1.0 and 2.0, and $\beta = 1.2$ accounting for soft soil.

The viscosity factor f_v depends on the over-consolidation ratio by

$$f_v = \begin{cases} \exp\left(\frac{p'/p_e-1}{I_v}\right) & \text{if } p'/p_e \geqslant \alpha_r \\ 0 & \text{if } p'/p_e < \alpha_r \end{cases} \tag{1.36}$$

where p_e is the equivalent pressure defined as

$$p_e = \frac{1}{3}h_{sr}[-\mathrm{In}(ef_\tau/e_{c0})]^{1/n} \tag{1.37}$$

with a factor

$$f_\tau = \frac{e_{c0}}{e_{d0}} - \left(\frac{e_{c0}}{e_{d0}}-1\right)\cdot\left(-\frac{\lambda_\sigma}{\lambda_c}\right) \tag{1.38}$$

with λ_σ being a ratio of stress invariants.

Other approaches

An alternative approach to rate dependence has been proposed by Kolymbas (1988). It assumes that the total stress can be decomposed into two independent parts: the frictional part for rate-independent behaviour, and viscous part for rate-dependent behavior,*viz.*

$$\boldsymbol{\sigma} = \boldsymbol{\sigma}_h + \boldsymbol{\sigma}_v, \quad \dot{\boldsymbol{\sigma}} = \dot{\boldsymbol{\sigma}}_h + \dot{\boldsymbol{\sigma}}_v \tag{1.39}$$

The frictional part can be represented by any rate-independent hypoplastic constitutive mode, which can be written out in terms of $\boldsymbol{\sigma}_h$ and $\dot{\boldsymbol{\varepsilon}}$ as follows

$$\dot{\boldsymbol{\sigma}}_h = \mathrm{H}(\boldsymbol{\sigma}_h, \dot{\boldsymbol{\varepsilon}}), \tag{1.40}$$

The visco-hypoplastic model is a combination of a rate-independent hypoplastic mode and a rheological model. This kind of model is assumed to describe both solid-like and fluid-like behaviors of geomaterials, especially in dynamic flow .

One of the viscous parts by Kolymbas (1988) is accounted for by including the second stretching tensor, which is similar to the Rivlin-Ericksen tensor (Truesdell and Noll 1965) in the following manner

$$\dot{\boldsymbol{\sigma}}_v = \eta_1 \frac{\ddot{\boldsymbol{\varepsilon}}}{\sqrt{\eta_2^2 + \mathrm{tr}\dot{\boldsymbol{\varepsilon}}^2}}, \tag{1.41}$$

and another candidate by Wu (2006) is

$$\dot{\boldsymbol{\sigma}}_v = \eta_1 \sqrt{\eta_2^2 + \mathrm{tr}\dot{\boldsymbol{\varepsilon}}^2}\, \ddot{\boldsymbol{\varepsilon}}, \tag{1.42}$$

where $\ddot{\boldsymbol{\varepsilon}}$ is the second stretching and η_1 and η_2 are materials parameters. The above formulation can be crudely likened to a description of an accelerating motion, with the second stretching being the acceleration. The above framework has been adopted to describe the rate-dependent behavior of granular Wu (2006) and debris flow (Guo et al., 2016). More details will be illustrated in this thesis. In addition, Fang (2008) proposed a visco-hypoplastic model for granular mass flow based on the theory of granular flow.

1.4 Outline of the study

The objective of this research is to provide a detailed demonstration of a unified constitutive model combining a simple critical state hypoplastic model and a viscous model. The proposed model contributes to the analysis of time-dependent behavior, especially the creep behavior of soil. The scope of this thesis is to numerically implement this unified constitutive model with the Finite Element Method which allows the simulation of the time-dependent behavior in soils up to the critical state of creep rupture.

In section 2, a simple critical state hypoplastic constitutive model for soil has been outlined. In this model, there is no clear boundary between elastic and plastic deformations in the hypoplastic model. The explicit formulations of the yield and bound surfaces of this model are derived. Then, this model is used to simulate the behavior of sandy soil and cohesive soil. It should be noted that the model in section 2 is rate-independent, thus it cannot account for the loading rate effects and rheological properties of sandy soil. With this consideration, a rate-dependent hypoplastic constitutive model named as a visco-hypoplastic constitutive model is developed in section 3. This viscous model is obtained by dividing the stress rate into a frictional and a viscous part, which are formulated by the rate-independent model in section 2 and a high order rheological model with respects to strain acceleration, respectively. Then, the versatility of the viscous model is examined by simulating some stepwise compression tests at the abrupt change of loading rates and some creep tests at different creep stresses. In section 4, a comprehensive study of the numerical integration methods for the rare independent model is carried out. Several explicit and implicit integration methods together with a stress correction scheme have been involved. The performance of different integration methods was examined by performing triaxial compression tests, stress response tests, and some boundary value problems. In order to get proper results in numerical computation, the stress correction scheme is necessary for the implementation of the hypoplastic model. On the basis of the numerical study of the rate-independent model, the visco-hypoplastic model is successfully implemented into a finite element code. The detailed integration strategies of the proposed visco-hypoplastic model are given in section 5. The implementation is examined by performing some numerical tests. Finally, an in-situ direct shear creep test is carried out, and this test is modeled using the proposed visco-hypoplastic constitutive model. In section 6, conclusions of this study are listed, followed by some open-ended questions and remarks on this study.

Chapter 2

A simple critical state hypoplastic constitutive model

2.1 Introduction

Understanding and modeling of the mechanical response of soils, particularly fine-grained materials, has been the subject of several studies, one of which is the development of suitable constitutive models to mathematically describe soil properties. To achieve this aim, many constitutive models based on the theory of elastoplastic have been developed for geomaterials during the last decades, e.g., Cam-Clay and Mohr-Coulomb model, in which the elastic and plastic deformations need to be distinguished and different material parameters are required. Moreover, in order to account for the non-linear behavior of soil, different approaches such as kinematic hardening plasticity (Wallin et al., 2003), bounding surface plasticity (Dafalias and Herrmann, 1986) and generalized plasticity (Pastor et al., 1990) have been incorporated with conventional elastoplastic models. These models are able to predict soil behaviors with good performance.

An alternative approach to model the soil non-linearity is the theory of hypoplasticity, which is a particular class of incrementally non-linear constitutive models (Mašín and Khalili, 2008a). Unlike elastic-plastic models, there is no clear boundary between elastic and plastic deformations in a hypoplastic model. Moreover, explicit pre-definition of yield and potential surfaces are not needed, which have been proved to be by-produced of the particular assumptions for their constitutive equation (Wu and Bauer, 1994). The predictive capabilities of hypoplastic models compete with those of advanced models based on elasto-plastic frameworks, yet they only require a nonlinear tensorial equation, which holds equally for loading and unloading, and a single set of parameters. This, together with the availability of robust algorithms for their implementation into numerical codes, makes hypoplasticity a promising approach for use in practical applications (Mašín and Khalili, 2008b).

Early versions of the hypoplastic constitutive models (Chambon et al., 1994; Wu and Bauer, 1994), albeit their simplicity, are able to reasonably capture some silent features of granular materials, such as sands or gravels. It is well-known that the mechanical behavior granular material is dependent on the void ratio, stress level and their interaction. An important step forward in developing constitutive was the implementation of this important feature for soil behavior. Wu et al. (1996) proposed a critical state hypoplastic constitutive model, which took account the effect of void ratio and stress level using very simple formulation. The later versions of hypoplasticity gained this capacity by sacrificing the simplicity(Bauer, 1996; Gudehus, 2000; Herle and Kolymbas, 2004; Mašín, 2005; Von Wolffersdorff, 1996). Another important aspect of the behavior of geomaterials marks the cohesion. Though the hypoplasticity is originally developed for granular materials rather than clay-like soils, sands and clay-like soils possess many common properties. Therefore, arose the idea to develop the hypoplastic model to clay. Recently, hypoplastic models have been extended to a wide range of geomaterials, such as soils with a low friction angle and clays (Herle and Kolymbas, 2004) and rockfill material (Bauer, 2009). Furthermore, hypoplastic constitutive models have been successfully applied to solve some boundary value problems, e.g. retailing wall, shallow foundation, pile foundation, shear band formation and site response analysis.

The primary purpose of the present chapter is to introduce a simple critical state hypoplastic constitutive model. The chapter is organized as follows: section 2.2 is devoted to the presentation of the framework of hypoplasticity and a reference hypoplastic model for granular materials. Section 2.3 epitomizes an updated hypoplastic constitutive model, including failure surface, bound surface and parameter calibration. Section 2.4 presents two important extension of this model. i.e. the extensions for critical state concept and cohesion. In section 2.5, the performance of this critical state model is outlined by performing a series of triaxial compression tests. Finally, the main contents of this chapter is summarized in section 2.6.

2.2 Framework of Hypoplasticity

2.2.1 General remarks

The basic idea of hypoplasticity can be traced back to the pioneering work of Kolymbas on description the behavior of an elastic material by using nonlinear tensorial function of the rate-type (Kolymbas, 1977, 1985). Since then different versions of hypoplasticity have been independently established for an alternative description of the soil behavior, without an explicit definition of yield and potential surfaces

The original hypoplastic equation given by Kolymbas (1977) in 1977 is too complex (at those days the name of hypoplasticity is not introduced). Later some improved versions have been presented (Bauer, 1996; Wu and Bauer, 1994; Wu and Kolymbas, 1990). The general hypoplastic constitutive equation is presented by Wu and Kolymbas (1990) in 1990. Based on the general hypoplastic constitutive equation, a simple hypoplastic constitutive model is proposed by Wu and Bauer (1994) in 1994. Recent hypoplastic models include the concept of critical states (Wu et al., 1996) to account for the effects of density and stress level (Wu and Bauer, 1993). However, this model shows excessive contraction (volume reduction) in triaxial extension. In order to remedy this, the constitutive model is updated by including a new term into the constitutive model (Wang, 2009) and the updated model has been successfully used in some computations of boundary value problems within Finite Different method (FDM) code(Wang, 2009) and the smoothed particle hydrodynamics code(SPH) as well (Peng et al., 2015). More recently, the updated constitutive incorporated with micropolar theory has been successfully developed (Lin et al., 2015), which can be used to model the evolution of shear band in granular material.

We recapitulate the main ingredients of hypoplasticity and begin with a fairly general formulation by assuming that there exists a tensor-valued function $\mathbf{H}$ such that:

$$\mathring{\boldsymbol{\sigma}} = \mathbf{H}(\boldsymbol{\sigma}, \dot{\boldsymbol{\varepsilon}}), \tag{2.1}$$

where $\boldsymbol{\sigma}$ is the Cauchy stress tensor, $\dot{\boldsymbol{\varepsilon}}$ is the stretching tensor, $\mathring{\boldsymbol{\sigma}}$ is the Jaumann rate of the Cauchy stress tensor defined in terms of the time-deriviative of the Cauchy stress tensor $\dot{\boldsymbol{\sigma}}$ and the spin tensor $\boldsymbol{\omega}$

$$\mathring{\boldsymbol{\sigma}} = \dot{\boldsymbol{\sigma}} + \boldsymbol{\sigma} \cdot \boldsymbol{\omega} - \boldsymbol{\omega} \cdot \boldsymbol{\sigma}, \tag{2.2}$$

The stretching and spin tensors are related to the velocity gradient tensor through

$$\dot{\boldsymbol{\varepsilon}} = \frac{1}{2}(\nabla \boldsymbol{v} + \boldsymbol{v} \nabla), \quad \boldsymbol{\omega} = \frac{1}{2}(\nabla \boldsymbol{v} - \boldsymbol{v} \nabla) \tag{2.3}$$

where $\boldsymbol{v}$ is the velocity, ∇ is *Gradient Operator*. It should be noted that the function $\mathbf{H}$ in Eq. (2.1) is required to be not differentiable in and only in $\dot{\boldsymbol{\varepsilon}} = 0$

In order to be able to obtain a concrete formulation, some restrictions are imposed on the constitute equation (2.1). Some of these restrictions are based on the general principles of continuum mechanics, while the others are based on experimental observation.

The first restriction follows directly from the definition of hypoplasticity (Wu et al., 1996). According to the definition, the natural time should not appear in the constitutive equation and the behavior to be described is assumed to be rate independent. For constitutive equation (2.1), rate independence is equivalent to the following statement.

Restriction 1. For rate independence the function $\mathbf{H}$ should be positively homogeneous of the first degree in $\dot{\boldsymbol{\varepsilon}}$

$$\mathbf{H}(\boldsymbol{\sigma}, \lambda \dot{\boldsymbol{\varepsilon}}) = \lambda \mathbf{H}(\boldsymbol{\sigma}, \dot{\boldsymbol{\varepsilon}}). \tag{2.4}$$

where λ is a positive but otherwise arbitrary scalar.

The second requirement states the objectivity of the constitutive equations under rigid rotations. The objectivity requirement is fulfilled if the function (2.1) is isotropic.For this requirement, it equivalent to:

Restriction 2.The function of $\mathbf{H}$ should fulfill the following condition of objectivity

$$\mathbf{H}(\mathbf{Q}\boldsymbol{\sigma}\mathbf{Q}^{\mathbf{T}}, \mathbf{Q}\dot{\boldsymbol{\varepsilon}}\mathbf{Q}^{\mathbf{T}}) = \mathbf{Q}\mathbf{H}(\boldsymbol{\sigma}, \dot{\boldsymbol{\varepsilon}})\mathbf{Q}^{\mathbf{T}}, \tag{2.5}$$

in which $\mathbf{Q}$ is an orthogonal tensor.

The requirement of objectivity is satisfied if the function $\mathbf{H}$ is formulated according to the representation theorems for isotropic tensor-valued functions. In the most general case, the representation theorem for an isotropic tensor-valued function of two symmetric tensors can be written out as follows (Wang, 1970):

$$\begin{aligned} \mathring{\boldsymbol{\sigma}} = \alpha_0 \boldsymbol{\delta}_{ij} + \alpha_1 \boldsymbol{\sigma} + \alpha_2 \dot{\boldsymbol{\varepsilon}} + \alpha_3 \boldsymbol{\sigma}^2 + \alpha_4 \dot{\boldsymbol{\varepsilon}}^2 + \alpha_5 (\boldsymbol{\sigma}\dot{\boldsymbol{\varepsilon}} + \dot{\boldsymbol{\varepsilon}}\boldsymbol{\sigma}) \\ + \alpha_6 (\boldsymbol{\sigma}^2 \dot{\boldsymbol{\varepsilon}} + \dot{\boldsymbol{\varepsilon}}\boldsymbol{\sigma}^2) + \alpha_7 (\boldsymbol{\sigma}\dot{\boldsymbol{\varepsilon}}^2 + \dot{\boldsymbol{\varepsilon}}^2 \boldsymbol{\sigma}) + \alpha_8 (\boldsymbol{\sigma}^2 \dot{\boldsymbol{\varepsilon}}^2 + \dot{\boldsymbol{\varepsilon}}^2 \boldsymbol{\sigma}^2), \end{aligned} \tag{2.6}$$

where $\boldsymbol{\delta}_{ij}$ is Kronecker delta.The coefficient $\alpha_j (j = 0, 1 \ldots, 8)$ are functions of the invariants and joint invariants of $\boldsymbol{\sigma}$ and $\dot{\boldsymbol{\varepsilon}}$:

$$\alpha_j = \tilde{\alpha}_j(\mathrm{tr}\boldsymbol{\sigma}, \mathrm{tr}\boldsymbol{\sigma}^2, \mathrm{tr}\boldsymbol{\sigma}^3, \mathrm{tr}\dot{\boldsymbol{\varepsilon}}, \mathrm{tr}\dot{\boldsymbol{\varepsilon}}^2, \mathrm{tr}\dot{\boldsymbol{\varepsilon}}^3, \mathrm{tr}(\boldsymbol{\sigma}\dot{\boldsymbol{\varepsilon}}), \mathrm{tr}(\boldsymbol{\sigma}^2\dot{\boldsymbol{\varepsilon}}), \mathrm{tr}(\boldsymbol{\sigma}\dot{\boldsymbol{\varepsilon}}^2), \mathrm{tr}(\boldsymbol{\sigma}^2\dot{\boldsymbol{\varepsilon}}^2)). \tag{2.7}$$

in which tr represents the trace of a tensor. Note that the isotropy of the tensorial function does not necessarily mean that the response is also isotropic. The representation theorem yields plenty of possibilities, so one needs several additional restrictions and assumptions to construct a concrete formula of hypoplasticity.

The third restriction is based on the experimental observation by Goldscheider (1984) with a true triaxial apparatus on dry sand: *A proportional strain (stress) path starting from a nearly stress-free and undistorted state gives rise to a proportional stress (strain) path.* This observation is of fundamental importance for developing constitutive equations, which can be mathematically expressed by the flowing restriction.

Restriction 3. The function $\mathbf{H}$ should be homogeneous in $\boldsymbol{\sigma}$, e.g.,

$$\mathbf{H}(\lambda\boldsymbol{\sigma},\dot{\boldsymbol{\varepsilon}}) = \lambda^n \mathbf{H}(\boldsymbol{\sigma},\dot{\boldsymbol{\varepsilon}}) \tag{2.8}$$

where λ is an arbitrary scalar and n denotes the degree of homogeneity. This restriction implies that the tangential stiffness and strength is proportional to the n^{th} power of the stress level, which is represented by the trace of the stress tensor $(\mathrm{tr}\boldsymbol{\sigma})^n$,so that experiments conducted under different stress levels can be normalized by $(\mathrm{tr}\boldsymbol{\sigma})^n$.

In hypoplasticity, the constitutive Eq. (2.1) is written in two parts, representing respectively reversible and irreversible behaviors of soils. Within the framework of Eq. (2.1) the general formulation for the hypoplastic rate-independent constitutive equation by Wu and Kolymbas (1990) can be written as the sum of linear and nonlinear terms of the strain rate $\dot{\boldsymbol{\varepsilon}}$.

$$\mathring{\boldsymbol{\sigma}} = \mathscr{L}(\boldsymbol{\sigma}) : \dot{\boldsymbol{\varepsilon}} - \boldsymbol{N}(\boldsymbol{\sigma})\|\dot{\boldsymbol{\varepsilon}}\| \tag{2.9}$$

where the term $\mathscr{L}$and $\boldsymbol{N}$ denote the linear and nonlinear components in tensor $\dot{\boldsymbol{\varepsilon}}$,which are isotropic tensor-valued functions consisted by the terms from the representation theorem in Eq. (2.6) and (2.7). Here $\mathscr{L}(\boldsymbol{\sigma})$ is a fourth-order tensor. $\|\dot{\boldsymbol{\varepsilon}}\| = \sqrt{\mathrm{tr}\dot{\boldsymbol{\varepsilon}}^2}$ stands for the Euclidean norm of the stretching tensor. The colon : denotes an inner product between two tensors.

Owing to the non-differentiable term containing $\|\dot{\boldsymbol{\varepsilon}}\|$ the constitutive equation (2.9) is incrementally nonlinear, which can be brought to light by recasting Eq. (2.9) in a more convenient form with virtue of Euler's theorem for homogeneous functions (Wu et al., 1996).

$$\mathring{\boldsymbol{\sigma}} = (\mathscr{L} - \boldsymbol{N} \otimes \vec{\dot{\boldsymbol{\varepsilon}}}) : \dot{\boldsymbol{\varepsilon}} \tag{2.10}$$

where $\vec{\dot{\boldsymbol{\varepsilon}}} = \dot{\boldsymbol{\varepsilon}}/\|\dot{\boldsymbol{\varepsilon}}\|$ stands for the direction of strain; and the symbol $\otimes$ denotes an outer product between two tensors.

The two terms in the brackets in Eq. (4.30) represents the tangential stiffness, which depends not only on stress but also on the direction of strain rate. Noted that Eq. (2.9) can describe the relation of stress rate and strain rate without using additional notions introduced by elastoplasticity such as yield surface, plastic potential or decomposition of deformation into elastic and plastic parts, since they are implied by the constitutive equation. Moreover, the distinction between loading and unloading is of unimportance for the constitutive equation, because the nonlinear part of the equation works for both for loading and unloading. For details please refer to literature (Wu and Niemunis, 1997; Wu et al., 1996). Some more advanced hypoplastic constitutive models can be find in Appendix III

2.2.2 Reference constitutive model

Base on the above concept, a simple hypoplastic constitutive equation for granular materials by Wu and Bauer (1994) has been proposed to solve some boundary value problems, which is composed of two linear and two non-linear terms in stretching tensor $\dot{\boldsymbol{\varepsilon}}$.

$$\mathring{\boldsymbol{\sigma}} = C_1(\mathrm{tr}\boldsymbol{\sigma})\dot{\boldsymbol{\varepsilon}} + C_2\frac{\mathrm{tr}(\boldsymbol{\sigma}\dot{\boldsymbol{\varepsilon}})}{\mathrm{tr}\boldsymbol{\sigma}}\boldsymbol{\sigma} + (C_3\frac{\boldsymbol{\sigma}^2}{\mathrm{tr}\boldsymbol{\sigma}} + C_4\frac{\boldsymbol{\sigma}^{*2}}{\mathrm{tr}\boldsymbol{\sigma}})\|\dot{\boldsymbol{\varepsilon}}\| \tag{2.11}$$

where C_i $(i = 1,2,3,4)$ are dimensionless parameters. The deviatoric stress tensor $\boldsymbol{\sigma}^*$ in the Eq. (2.11) is defined through

$$\boldsymbol{\sigma}^* = \boldsymbol{\sigma} - \frac{1}{3}(\mathrm{tr}\boldsymbol{\sigma})\boldsymbol{\delta}_{ij}, \tag{2.12}$$

where $\boldsymbol{\delta}_{ij}$ is Kronecker delta.

The four parameters can be identified with single triaxial compression test. Details of calibration procedure using the initial tangential stiffness E_i, the initial Poisson ratio υ_i, the internal friction angle ϕ and the dilatancy angle ψ to identify the material parameters can be found in the work by Wu and Bauer (1994).

The salient merits of the constitutive equation are the predictive capacity and the formulative simplicity, which make this equation particularly appealing for problems with simple loading. For complex loading, however, Eq. (2.11) is not well suited. Additionally, the feature of this constitutive model such as failure criterion, flow rule, and mechanical performance are demonstrated in great detail in literature (Wu et al., 1996). The critical state concept has been incorporated into Eq. (2.11) to account for the influence of density changes (Wu et al., 1996) and stress level by Wu and Bauer (1993).

2.3 An updated constitutive model

2.3.1 Constitutive equation

It was found out by Bauer (1996) that constitutive equation 2.11 predicts critical state (defined by $\mathring{\boldsymbol{\sigma}} = 0$ and $\mathrm{tr}\dot{\boldsymbol{\varepsilon}} = 0$) for any paths only if the two parameters in the nonlinear term of Eq. (2.11) satisfy:

$$C_3 = -C_4, \tag{2.13}$$

As a consequence of Eq. (2.13), the number of parameters in Eq. (2.11) reduces to three. This changing, however, restricts the predictive capability of this model. For instances, The initial Poisson ratio cannot be varied, which consequently results in another shortcoming that the volumetric strain cannot be changed in the critical state of a specimen with a initial void ratio near critical (Wu and Kolymbas, 2000). To resolve this problem, a new term $(\mathrm{tr}\dot{\boldsymbol{\varepsilon}})\boldsymbol{\sigma}$ introduced by Wang (2009) is added to the constitutive equation (2.11), and thus, the number of material parameters regains four. The modified constitutive equation can be rewritten out in full.

$$\mathring{\boldsymbol{\sigma}} = C_1(\mathrm{tr}\boldsymbol{\sigma})\dot{\boldsymbol{\varepsilon}} + C_2(\mathrm{tr}\dot{\boldsymbol{\varepsilon}})\boldsymbol{\sigma} + C_3\frac{\mathrm{tr}(\boldsymbol{\sigma}\dot{\boldsymbol{\varepsilon}})}{\mathrm{tr}\boldsymbol{\sigma}}\boldsymbol{\sigma} + C_4(\boldsymbol{\sigma}+\boldsymbol{\sigma}^*)\|\dot{\boldsymbol{\varepsilon}}\|, \tag{2.14}$$

Without causing confusions the same notations for the four parameters are retained in the above equation. The new term $\mathrm{tr}\dot{\boldsymbol{\varepsilon}}$ maintains the critical state for all paths, since it vanishes in a critical state ($\mathrm{tr}\dot{\boldsymbol{\varepsilon}} = 0$).

In the constitutive equation (2.14), the former three terms describe the reversible behavior of material which are responsible for the stress increase during deformation, and the last term describes the irreversible behavior that enables a stiffer behavior at unloading. Some practical applications have been conducted based on the updated constitutive model. Recently, micropolar theory has been successfully incorporated into this updated constitutive model to model evaluation of shear band (Lin et al., 2015). Also, it has been implemented into the smoothed particle hydrodynamics code (SPH) for debris flow materials (Peng et al., 2015).

2.3.2 Failure surface, flow rule

The failure surface and flow rule of hypoplasticity are known as by-products of its constitutive equation (Wu and Bauer, 1994; Wu et al., 1996). Hence, the failure surface and flow rule of constitutive equation (2.14) can be explicitly expressed using the flowing failure definition. A material element is considered to be at failure if, for a given stress $\boldsymbol{\sigma}$, there exists at least one strain rate $\dot{\boldsymbol{\varepsilon}} \neq 0$ resulting in vanishing stress rate. A straightforward way of the statement is given in the following:

$$\mathring{\boldsymbol{\sigma}} = \mathscr{L}(\boldsymbol{\sigma}) : \dot{\boldsymbol{\varepsilon}} - \boldsymbol{N}(\boldsymbol{\sigma})\|\dot{\boldsymbol{\varepsilon}}\| = 0 \tag{2.15}$$

The direction of strain rate at failure can be readily obtained from Eq.(2.15):

$$\frac{\dot{\boldsymbol{\varepsilon}}}{\|\dot{\boldsymbol{\varepsilon}}\|} = \mathscr{L}^{-1} : \boldsymbol{N} \tag{2.16}$$

By making using of the fact that $(\dot{\boldsymbol{\varepsilon}}/\|\dot{\boldsymbol{\varepsilon}}\|) : (\dot{\boldsymbol{\varepsilon}}/\|\dot{\boldsymbol{\varepsilon}}\|) = 1$, the failure criterion can be derived:

$$f^s = \boldsymbol{N}^{\mathrm{T}} : (\mathscr{L}^{\mathrm{T}})^{-1} : \mathscr{L}^{-1} : \boldsymbol{N} - 1 = 0 \tag{2.17}$$

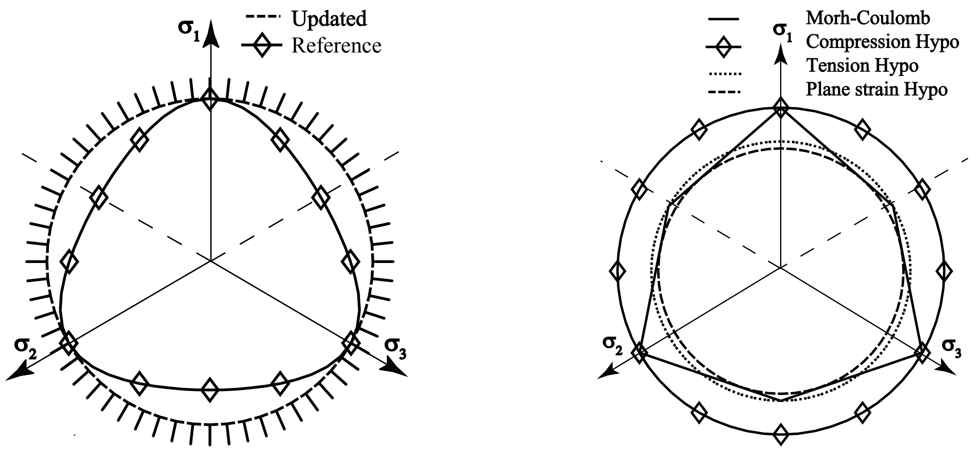

Figure 2.1 (a) The failure surfaces of the the reference model and the updated model in π plane. (b) The failure surfaces of the updated model in π plane for triaxial compression test, triaxial tension test, and plate strain response,respectively

The explicit formula of the failure surface can be readily obtained using the symbolic computational program *Mathematica*, which gives rise to the failure surface in the following form:

$$f(\boldsymbol{\sigma}) = \sqrt{J_2} + \varsigma(C_i)I_1 = 0, \tag{2.18}$$

where J_2 and I_1 are respectively the second deviatoric stress invariant and the first stress invariant. ς is a constant determined by the dimensionless parameters C_i $(i = 1,2,3,4)$, which may be expressed as:

$$\varsigma = \sqrt{\frac{a-b}{12C_3^2(3C_1^2 - C_4^2)}}, \tag{2.19}$$

in which

$$a = -18C_1^3C_3 + 9C_2^2C_4^2 + 6C_2C_3C_4^2 + C_3^2C_4^2 + 6C_1(6C_2 + C_3)C_4^2 - 6C_1^2(3C_2C_3 + C_3^2 - 6C_4^2)$$
$$b = C_4(6C_1 + 3C_2 + C_3)\sqrt{-36C_1^3C_3 + 36C_1C_2C_4^2 + (3C_2 + C_3)^2C_4^2 - 36C_1^2(C_2C_3 - C_4^2)}$$

It is worth to mention that the constant ς is only related to C_1 and C_4 if the dilatancy angle ψ = 0 (see next section), and it takes the following form:

$$\varsigma = \frac{C_1}{\sqrt{2}C_4} \tag{2.20}$$

Further parameters studies show that the parameter ς is only dependent on the internal friction angle of materials, and it takes the formula as:

$$\varsigma = \frac{2sin\phi}{\sqrt{3}(3 - sin\phi)} \tag{2.21}$$

Apparently, the Eq. (2.18) is coincident with the failure formula proposed by Bardet (1990), which encompassed two widely used failure condition of Matsuoka and Nakai (1974) and lade (Lade, 1977; Lade and Duncan, 1975).

To compare the updated model with the reference model, the failure surface of both models are presented in Fig. 2.1(a), which shows that the failure surface of the reference model in π-plane is a cone, whereas the failure surface of the updated model is a circle, and it encloses the failure surface of the reference model. Therefore, the updated model possesses the same yield limit for both compression and extension. Eq. (2.16) denotes the direction of the strain rate, that is flow rule, in hypoplasticity, which is also plotted in Fig. 2.1(a) with short radial line. The direction of the strain rate is not usually normal to the failure surface, which suggests that the flow rule is non-associated.

2.3.3 Material parameters

It is well-known that the Mohr-Coulomb yield surface is often expressed in terms of the cohesion (we assume $c = 0$) and the angle of internal friction (ϕ). If we assume that the hypoplastic yield surface circumscribes, middle circumscribes and inscribes the Mohr–Coulomb yield surface, the parameter ς in Eq. (2.18) can be expressed as:

$$\varsigma = \frac{2sin\phi}{\sqrt{3}(3 - sin\phi)}, \quad \varsigma = \frac{2sin\phi}{\sqrt{3}(3 + sin\phi)}, \text{and} \quad \varsigma = \frac{tan\phi}{\sqrt{3(3 + 4tan^2\phi)}} \tag{2.22}$$

The above three equations correspond to triaxial test(compression and tension) response and plate strain response, respectively. Correspondingly, the yield surface of the updated model circumscribes, middle circumscribes, and inscribes the Mohr-Coulomb yield surface in the π plane is presented in Fig. 2.1(b).

According to the above equations, we can easily match the hypoplastic parameters with the Mohr-Coulomb parameters in the triaxial compression state. To identify the four material parameters in Eq. (2.14) with a single triaxial compression test under constant confining pressure, we need to consider two specific stress states, namely the initial hydrostatic state and the stress state at failure. The stress rate, stress and strain rate tensors at the initial state and the failure state are $(\mathring{\boldsymbol{\sigma}}_i, \boldsymbol{\sigma}_i, \dot{\boldsymbol{\varepsilon}}_i)$ and $(\mathring{\boldsymbol{\sigma}}_f, \boldsymbol{\sigma}_f, \dot{\boldsymbol{\varepsilon}}_f)$, respectively.

$$\begin{gathered}
\mathring{\boldsymbol{\sigma}}_i = \begin{pmatrix} \dot{\sigma}_i & 0 & 0 \\ 0 & 0 & 0 \\ 0 & 0 & 0 \end{pmatrix}, \quad \boldsymbol{\sigma}_i = \begin{pmatrix} \sigma_i & 0 & 0 \\ 0 & \sigma_i & 0 \\ 0 & 0 & \sigma_i \end{pmatrix}, \quad \dot{\boldsymbol{\varepsilon}}_i = \begin{pmatrix} \dot{\varepsilon}_{i1} & 0 & 0 \\ 0 & \dot{\varepsilon}_{i3} & 0 \\ 0 & 0 & \dot{\varepsilon}_{i3} \end{pmatrix} \\
\mathring{\boldsymbol{\sigma}}_f = \begin{pmatrix} 0 & 0 & 0 \\ 0 & 0 & 0 \\ 0 & 0 & 0 \end{pmatrix}, \quad \boldsymbol{\sigma}_f = \begin{pmatrix} \sigma_f & 0 & 0 \\ 0 & \sigma_i & 0 \\ 0 & 0 & \sigma_i \end{pmatrix}, \quad \dot{\boldsymbol{\varepsilon}}_f = \begin{pmatrix} \dot{\varepsilon}_{f1} & 0 & 0 \\ 0 & \dot{\varepsilon}_{f3} & 0 \\ 0 & 0 & \dot{\varepsilon}_{f3} \end{pmatrix}
\end{gathered} \tag{2.23}$$

Hence, in a triaxial compression test the constitutive equation (2.14) can be explicitly written out. According to Eq. (2.23), four independent equations can be obtained:

$$\begin{aligned}
\dot{\sigma}_i =& 3C_1\sigma_i\dot{\varepsilon}_{i1} + C_2(\dot{\varepsilon}_{i1} + 2\dot{\varepsilon}_{i3})\sigma_i + C_3\sigma_i(\dot{\varepsilon}_{i1} + 2\dot{\varepsilon}_{i3})/3 + C_4\sqrt{\dot{\varepsilon}_{i1}^2 + 2\dot{\varepsilon}_{i3}^2}\sigma_i \\
0 =& 3C_1\sigma_i\dot{\varepsilon}_{i3} + C_2(\dot{\varepsilon}_{i1} + 2\dot{\varepsilon}_{i3})s_i + C_3 s_i(\dot{\varepsilon}_{i1} + 2\dot{\varepsilon}_{i3})/3 + C_4\sqrt{\dot{\varepsilon}_{i1}^2 + 2\dot{\varepsilon}_{i3}^2}\sigma_i \\
0 =& C_1(\sigma_f + 2\sigma_i)\dot{\varepsilon}_{f3} + C_2(\dot{\varepsilon}_{f1} + 2\dot{\varepsilon}_{f3})\sigma_f + C_3(\sigma_f\dot{e}_{i1} + 2\sigma_i\dot{e}_{i3})/(\sigma_f + 2\sigma_i)\sigma_f \\
&+ C_4\sqrt{\dot{\varepsilon}_{f1}^2 + 2\dot{\varepsilon}_{f3}^2}[2\sigma_f - (\sigma_f + 2\sigma_i)/3] \\
0 =& C_1(\sigma_f + 2\sigma_i)\dot{e}_{f3} + C_2(\dot{\varepsilon}_{f1} + 2\dot{\varepsilon}_{f3})\sigma_f + C_3(s_f\dot{\varepsilon}_{1i} + 2\sigma_i\dot{\varepsilon}_{3i})/(\sigma_f + 2\sigma_i)\sigma_i \\
&+ C_4\sqrt{\dot{\varepsilon}_{1f}^2 + 2\dot{\varepsilon}_{3f}^2}[2\sigma_i - (\sigma_f + 2\sigma_i)/3]
\end{aligned} \tag{2.24}$$

Apparently, the first two equations in equation array (2.24) stand for the initial hydrostatic stress state, and the last two equations denote the stress state at failure, respectively. For the sake simplicity, four material parameters measured in a triaxial test are used, e.g., the initial tangential stiffness:

$$E_i = \frac{\dot{\sigma}_{i1}}{\dot{\varepsilon}_{i1}} \tag{2.25}$$

the initial Poisson ratio:

$$\upsilon_i = \frac{\dot{\varepsilon}_{i3}}{\dot{\varepsilon}_{i1}} \tag{2.26}$$

the failure stress ratio:

$$R_f = \frac{\sigma_{f1}}{\sigma_{i1}} = \frac{1 + \sin\phi}{1 - \sin\phi} \tag{2.27}$$

and the failure Poisson ratio:

$$\upsilon_f = \frac{\dot{\varepsilon}_{f3}}{\dot{\varepsilon}_{f1}} = \frac{1 + \tan\psi}{2} \tag{2.28}$$

where ϕ and ψ are the internal friction angle and the dilatancy angle. With the help of the above notations, equation array (2.24) can be simplified to:

$$\begin{aligned} E_i/\sigma_i &= 3C_1 + C_2(1+2\upsilon_i) + C_3(1+2\upsilon_i)/3 - C_4\sqrt{1+2\upsilon_i^2} \\ 0 &= 3C_1\upsilon_i + C_2(1+2\upsilon_i) + C_3(1+2\upsilon_i)/3 - C_4\sqrt{1+2\upsilon_i^2} \\ 0 &= C_1(R_f+2) + C_2(1+2\upsilon_f)R_f + C_3(R_f+2\upsilon_i)/(R_f+2)R_f - C_4\sqrt{1+2\upsilon_i^2}(5R_f-2)/3 \\ 0 &= C_1(R_f+2)\upsilon_f + C_2(1+2\upsilon_f) + C_3(R_f+2\upsilon_i)/(R_f+2) + C_4\sqrt{1+2\upsilon_i^2}(R_f-4)/3, \end{aligned} \tag{2.29}$$

As a consequence, the four hypoplastic parameters can be computed by solving the following matrix form equation.

$$\begin{pmatrix} \frac{E_i}{s_i} \\ 0 \\ 0 \\ 0 \end{pmatrix} = \begin{pmatrix} 3 & 1+2\upsilon_i & \frac{1+2\upsilon_i}{3} & -\sqrt{1+2\upsilon_i^2} \\ 3\upsilon_i & 1+2\upsilon_i & \frac{1+2\upsilon_i}{3} & -\sqrt{1+2\upsilon_i^2} \\ R_f+2 & (1+2\upsilon_i)R_f & \frac{R_f+2\upsilon_f}{R_f+2}R_f & -\sqrt{1+2\upsilon_i^2}\frac{5R_f+2}{3} \\ (R_f+2)\upsilon_f & 1+2\upsilon_i & \frac{R_f-2\upsilon_f}{R_f+2} & \sqrt{1+2\upsilon_i^2}\frac{R_f-4}{3} \end{pmatrix} \begin{pmatrix} C_1 \\ C_2 \\ C_3 \\ C_4 \end{pmatrix}, \tag{2.30}$$

Note that the four material parameters E_i, υ_i, ϕ and ψ are obtained under a specific confining pressure σ_3 under which the triaxial test is performed. In the ensuing sections all the parameters are assumed to be obtained from triaxial tests with confining pressure $\sigma_3 = 100$ kPa.

Table 2.1 Material parameters for Mohr-Coulomb yield criterion

Para.	E_i(Mpa)	υ_i	$\phi_c(/^\circ)$	$\psi(/^\circ)$
Value	20	0.33	20	0

Table 2.2 The matched parameters for the updated model and Drucker-Prager model

Para.	$\phi_{dp}(/^\circ)$	$\phi_{hypo}(/^\circ)$	C_1	C_2	C_3	C_4
Triaxial compression	37.6	20	-50.1	-541.7	-1135.2	-238.54
Triaxial tension	31.6	16.14	-50.1	-520.74	-1802.29	-300.57
Plane strain	30.2	15.33	-50.1	-505.8	-2014.8	-315.8

The parameters for triaxial compression test are provided, however, sometimes experimental data are not directly available for triaxial tension test or plane strain state, in which case we need to calculate the values for the parameters of the hypoplastic model to provide a reasonable match to Mohr-Coulomb model. It is noticed that the failure surface is only dependent on the internal friction angle, so it is reasonable to calculate the parameters by using Eq. (2.22). We assume the friction angle for triaxial compression test is ϕ_c, then the friction angle to calculate the parameters of the hypoplastic model in the case of triaxial tension and plane strain response can be obtained in the following:

$$\phi_t = \arctan\left[\frac{\tan\phi_c(3-\sin\phi_c)}{3+\sin\phi_c}\right], \qquad \phi_p = \arctan\left[\frac{\tan\phi_c(3-\sin\phi_c)}{2\cos\phi_c\sqrt{3+4\tan^2\phi_c}}\right] \tag{2.31}$$

For example, material parameters of a triaxial compression test are shown in Table 2.1, the friction angle is 20°, by using Eq.(2.31), the friction angle to calculate the parameters of the hypoplastic model is 16.14° for triaxial tension response and 15.33° for plane strain response. The corresponding hypoplastic parameters are shown in Table 2.2.

2.3.4 Bound surface

One of the key characteristics of the Eq. (2.11) is the presence of the bound surface in the stress space which encloses all accessible stress state (Wu and Kolymbas, 2000). The constitutive Eq. (2.14) do not explicitly incorporate the bound surface. However, it can be anticipated that the bound surface is predicted implicitly by the constitutive equation as a by-product of Eq. (2.14).

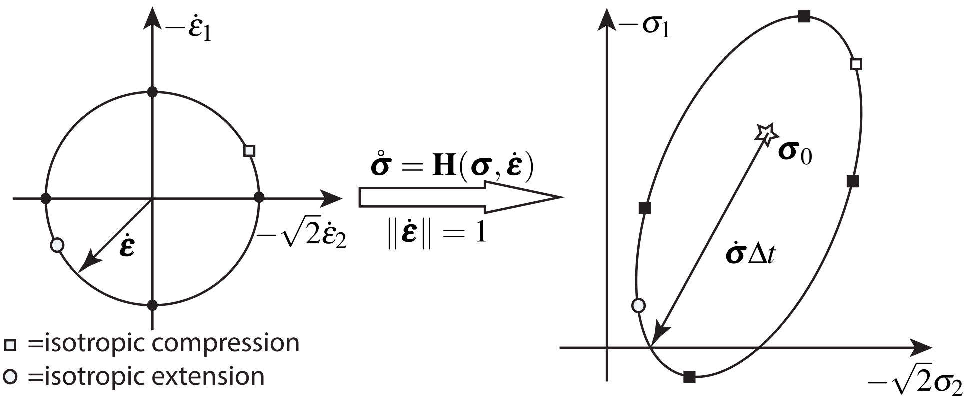

Figure 2.2 Principal sketch of response envelope on the $-\sqrt{2}\sigma_2, -\sigma_1$ plane

Before proceeding further about the bound surface, it is useful to introduce the concept of response envelop proposed in the seventies by Gudehus (2000) and Lewin and Burland (1970). General speaking, a response envelope is a polar diagram of stiffness plotted for different directions of stretching. It is an efficient approach to study the behavior of rate independent models. Usually stress states with cylindrical symmetry are considered. We start by choosing an initial stress state $\boldsymbol{\sigma}_0$ on the Rendulic place $(-\sqrt{2}\sigma_2, -\sigma_1)$. The response envelope is obtained as a plot of finial stresses $\dot{\boldsymbol{\sigma}}$ calculated from the corresponding probes of the stretching $\dot{\boldsymbol{\varepsilon}}$ with the same magnitude $\|\dot{\boldsymbol{\varepsilon}}\|$ (with $\|\dot{\boldsymbol{\varepsilon}}\|, \Delta\tau$ = const or $\|\dot{\boldsymbol{\varepsilon}}\| = 1$). A constitutive model may be regarded as a mapping that carried a circle plotted in the strain space $(-\sqrt{2}\dot{\varepsilon}_2, -\dot{\varepsilon}_1)$ to the stress space $(-\sqrt{2}\sigma_2, -\sigma_1)$, where it becomes an ellipse. The response envelop can be presented either in the space of stress rate or in the stress space by adding the stress increment to the initial stress $\boldsymbol{\sigma} = \boldsymbol{\sigma}_0 + \dot{\boldsymbol{\sigma}}\Delta t$, see Fig. 2.2.

The response envelopes of some stress paths of the updated model is presented in Fig. 2.3. As is shown in Fig. 2.3, some strain directions may lead to the limited stress states beyond the failure surface. This feature led to the discovery of the bound surface by Wu and Niemunis (1997). According to the theoretical analysis procedure of the bound surface for the hypoplastic constitutive model by Wu and Niemunis (1997), the bound surface of the updated model is derived.

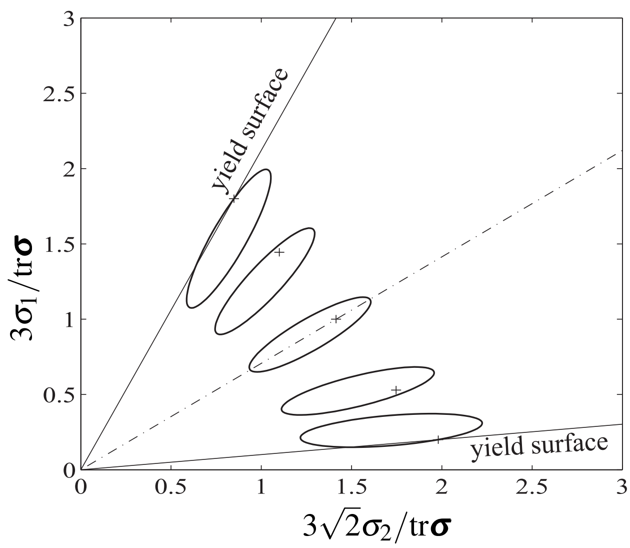

Figure 2.3 Response envelope of the updated constitutive model

Let $\mathcal{B}$ denote a bound surface, which possesses the definition $\mathcal{B}(\boldsymbol{\sigma}) = 0$, with $\mathcal{B}(\boldsymbol{\sigma})$ being an isotropic function of stress. We assume that stress $\boldsymbol{\sigma}^b$ happens to be on the surface, so that $\mathcal{B}(\boldsymbol{\sigma}^b) = 0$. The outward normal to the bound surface at $\boldsymbol{\sigma}^b$ can be expressed succinctly using the following relation

$$\boldsymbol{z} = \left.\frac{\partial \mathcal{B}(\boldsymbol{\sigma})}{\partial \boldsymbol{\sigma}}\right|_{\boldsymbol{\sigma}=\boldsymbol{\sigma}^b} \tag{2.32}$$

It is convenient to represent the $\boldsymbol{\sigma}^b$ by using its diagonal form. Hence, the outward normal $\boldsymbol{z}$ can be shown to be diagonal as well, that is $\boldsymbol{z} = diag(z_1, z_2, z_3)$.

By the definition, all stress rate $\mathring{\boldsymbol{\sigma}}$ calculated at $\boldsymbol{\sigma}^b$ must be directed to the interior of the bound surface. Therefore, for any strain rate $\dot{\boldsymbol{\varepsilon}}$ the corresponding stress rate must satisfy the inequality

$$\boldsymbol{z} : \mathring{\boldsymbol{\sigma}} \leqslant 0, \tag{2.33}$$

Obviously, if the stress state lies on the bound surface, then the maximum of the scalar product of $\boldsymbol{z}$ and $\mathring{\boldsymbol{\sigma}}$ must vanish, i.e.

$$Max(\boldsymbol{z} : \mathring{\boldsymbol{\sigma}})_{\boldsymbol{\sigma}=\boldsymbol{\sigma}^b} = 0, \tag{2.34}$$

Substituting constitutive Eq. (2.9) into Eq. (2.34) and differentiating the resulting equation after $\dot{\boldsymbol{\varepsilon}}$, then the maximizing of $\boldsymbol{z} : \mathring{\boldsymbol{\sigma}}$ can be obtained as follows

$$\frac{\partial[\boldsymbol{z} : \boldsymbol{\mathscr{L}} : \dot{\boldsymbol{\varepsilon}} + \boldsymbol{z} : \boldsymbol{N}\|\dot{\boldsymbol{\varepsilon}}\|]}{\partial \dot{\boldsymbol{\varepsilon}}} = \boldsymbol{z} : \boldsymbol{\mathscr{L}} + \boldsymbol{z} : \boldsymbol{N}\frac{\dot{\boldsymbol{\varepsilon}}}{\|\dot{\boldsymbol{\varepsilon}}\|} = 0, \tag{2.35}$$

Thus the above equation is formulated in term of $\dot{\boldsymbol{\varepsilon}}$. Since the constitutive equation (2.9) is of rate independence, we require $\|\dot{\boldsymbol{\varepsilon}}\| = 1$. The the maximizing of $\boldsymbol{z} : \mathring{\boldsymbol{\sigma}}$ can be obtained

$$D_{max} = -\frac{\boldsymbol{z} : \boldsymbol{\mathscr{L}}}{\boldsymbol{z} : \boldsymbol{N}} \tag{2.36}$$

Substitution of Eq.(2.36) to Eq. (2.34), we obtain the a condition for stress lying on the bound surface $\mathcal{B}(\boldsymbol{\sigma})$

$$\|\boldsymbol{z} : \boldsymbol{\mathscr{L}}\| = -\boldsymbol{z} : \boldsymbol{N} \tag{2.37}$$

Since the normal direction $\boldsymbol{Z}$ is unknown, the criterion (2.37) is not sufficient to determine the bound surface. If the stress $\boldsymbol{\sigma}^b$ lies on the bound surface, then due to stress positive homogeneity the proportional stress $\alpha\boldsymbol{\sigma}^b$ ($\alpha > 0$) also does. Thus $\mathcal{B}(\boldsymbol{\sigma}) = 0$ must represents a conical surface with the vertex in the origin of the stress space. From this property, the following condition of orthogonality between $\boldsymbol{\sigma}^b$ and $\boldsymbol{z}$ has been obtained:

$$\boldsymbol{\sigma}^b : \boldsymbol{z} = 0 \tag{2.38}$$

which can be regarded as an criterion condition to determine the bound surface.

The assumption the bound surface is an isotropic function of stress implies that for special stress states $\boldsymbol{\sigma}^s = diag(\sigma_1^b, \sigma_2^b, \sigma_3^b)$ with $\sigma_2^b = \sigma_3^b$, the respective partial derivatives z^2 and z^3 are also equal. Making use of the property under consideration of (2.39) the stress state on the bound surface $\mathcal{B}(\boldsymbol{\sigma}) = 0$ can be found by solving the following equation system:

$$\boldsymbol{\sigma}^b - \frac{\boldsymbol{\sigma}^b : \boldsymbol{\sigma}^b}{\mathrm{tr}\boldsymbol{\sigma}^b}\mathbf{1} = \boldsymbol{z}, \quad \|\boldsymbol{z} : \boldsymbol{\mathscr{L}}\| = -\boldsymbol{z} : \boldsymbol{N}. \tag{2.39}$$

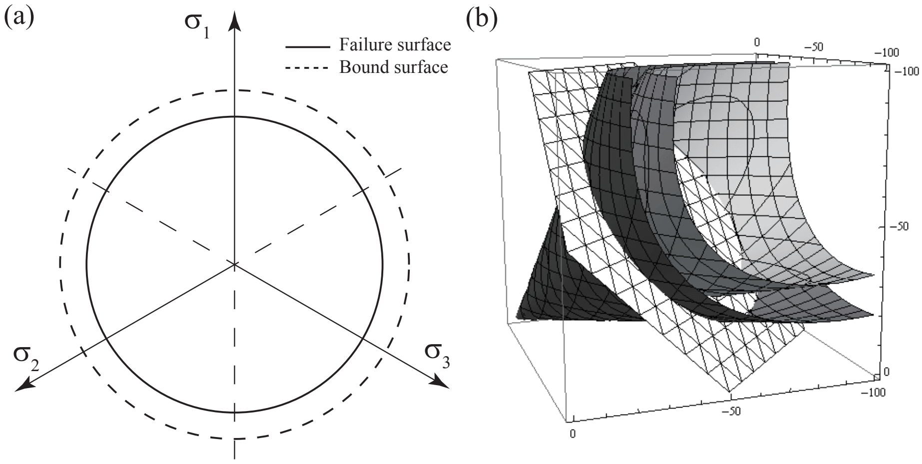

Figure 2.4 (a)The failure surface and bound surface of the updated model in the π-plane, and (b) view of (a) from a point in principal stress space.

For the updated constitutive equation (2.14), the bound surface is obtained. The explicitly form of the bound surface is expressed in the following :

$$\mathcal{B}(\boldsymbol{\sigma}) = \sqrt{J_2} - \frac{C_1}{\sqrt{C_4^2 - 3C_1^2}} I_1 = 0, \tag{2.40}$$

With the help of Eq.(2.18) and (2.40), it is easy to plot the failure surface and bound surface of the updated model in the π-plane , shown as Fig. 2.4(a) the cross-sections of the bound and failure surfaces in π-plane, and Fig. 2.4(b) in the principal stress space. As is known that the failure surface of the updated model is a cone with its apex at the origin in the principal stress space. The bound surface possesses similar geometry as the failure surface, whereas it lies slightly outside the failure surface.

Normally, the stress state is constrained inside the failure surface. However, some strain directions may lead to stress state lying between the between the failure surface and the bound surface. The distance between these two surface, to some extent, indicates the integration error in numerical computation. Let us consider two stress states $\boldsymbol{\sigma}_f$ and $\boldsymbol{\sigma}_b$ with the same lode angle lying on the failure and bound surface, respectively. Thus, the stress ratios can be obtained:

$$\frac{\sigma_{f1} - \sigma_{f3}}{\sigma_{f1} + \sigma_{f3}} = \sin\phi_{cf}, \quad \frac{\sigma_{b1} - \sigma_{b3}}{\sigma_{b1} + \sigma_{b3}} = \sin\phi_{cb}, \tag{2.41}$$

where σ_1 and σ_3 are maximum principal stress and minimum principal stress, respectively. The stress ratio yields a critical friction angle ϕ_c.

Contrary to Mohr-Coulomb yield criterion, the critical friction angle ϕ_c is various for different lode angles for the updated constitutive model. Additionally, the critical friction angle obtained from $\boldsymbol{\sigma}_f$ and $\boldsymbol{\sigma}_b$ are different. Fig. 2.5 shows the two critical friction angles ϕ_{cf} and ϕ_{cb} for different MC friction angle (ϕ). For triaxial compression stress state (lode angle is zero) with ϕ being 20^o, we obtain $\phi_{cf} = 20°$ and $\phi_{cb} = 21.4°$, while for triaxial tension stress state (lode angle is 60^o) , $\phi_{cf} = 26.3°$ and $\phi_{cb} = 28.8°$. In addition, the difference between ϕ_{cf} and ϕ_{cb} largely increase with increasing of ϕ , as depicted in Table 2.3.

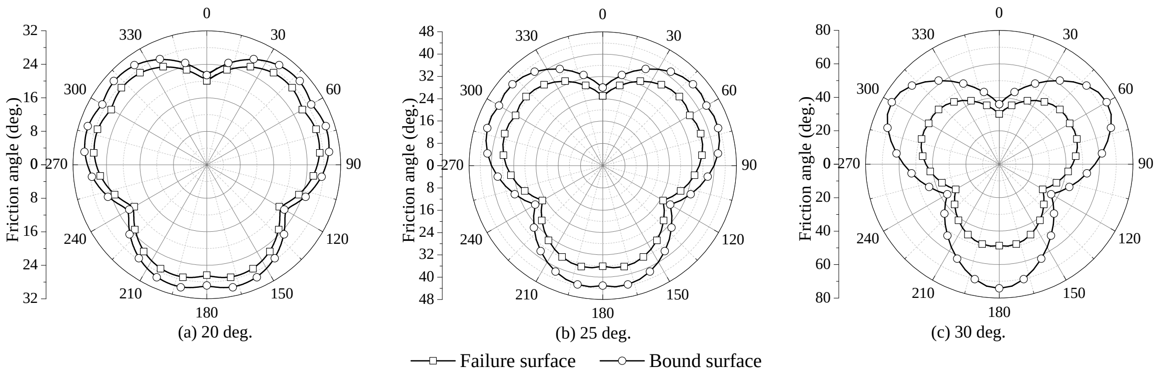

Figure 2.5 The critical fiction angle ϕ_{cf} and ϕ_{cb} for different ϕ (a) $\phi = 20°$, (b) $\phi = 25^o$, and (c) $\phi = 30°$

Table 2.3 The critical friction angle ϕ_{cf} and ϕ_{cb} for $\phi = 20°$

Stress state	Triaxial conpression[/°]			Triaxial tension[/°]		
ϕ_{cf}	20.0	25.0	30.0	26.3	36.8	43.6
ϕ_{cb}	21.4	28	35.9	28.8	49.2	73.2

The bound surface is an intrinsic property of the updated hypoplastic constitutive Eq. (2.14), which gains a great advantage in numerical integration comparison with most conventional constitutive models. For constitutive equation (2.14), the stress states lying outside the bound surface, e.g., as a result of too large time increment, will be automatically corrected in the next time step (Wu and Niemunis, 1997). However, the stress state can also lie between the failure and bound surface for some strain paths, which can result in a considerable error for large MC friction angle, e.g., $\phi = 30°$. Hence, stress correction algorithm (Lee and Fenves, 2001) is needed to correct the drift of stress during numerical integration, considering the large difference between ϕ_{cf} and ϕ_{cb}.

2.3.5 Numerical examples

To give an overall assessment of the performance of the updated model, a set of elementary tests, including drained triaxial compression tests and simple shear tests, are carried out. The numerical results of the updated model and two conventional elastoplastic models, i.e. Mohr-Coulomb model and Druck-Prager model, are compared.

Drained triaxial compression tests

Let us consider the drained triaxial compression test (DTCT). Due to the symmetry, we have $\sigma_2 = \sigma_3$ and $\dot{\varepsilon}_2 = \dot{\varepsilon}_3$ in the whole loading process. Then the stress rate , stress and strain rate and for triaxial test can be expressed in the matrix form:

$$\mathring{\boldsymbol{\sigma}} = \begin{pmatrix} \dot{\sigma}_1 & 0 & 0 \\ 0 & \dot{\sigma}_3 & 0 \\ 0 & 0 & \dot{\sigma}_3 \end{pmatrix}, \boldsymbol{\sigma} = \begin{pmatrix} \sigma_1 & 0 & 0 \\ 0 & \sigma_3 & 0 \\ 0 & 0 & \sigma_3 \end{pmatrix}, \dot{\boldsymbol{\varepsilon}} = \begin{pmatrix} \dot{\varepsilon}_1 & 0 & 0 \\ 0 & \dot{\varepsilon}_3 & 0 \\ 0 & 0 & \dot{\varepsilon}_3 \end{pmatrix}$$

The governing differential equations for drained triaxial compression test is obtained by substituting the above matrix into constitutive equation (2.14):

$$\dot{\sigma}_1 = C_1(\sigma_1 + 2\sigma_3)\dot{\varepsilon}_1 + C_2(\dot{\varepsilon}_1 + 2\dot{e}_3)\sigma_1 + C_3\frac{\sigma_1\dot{\varepsilon}_1 + 2\sigma_3\dot{\varepsilon}_3}{\sigma_1 + 2\sigma_3}\sigma_1 + C_4(\sigma_1 + \sigma_1^*)\sqrt{\dot{\varepsilon}_1^2 + 2\dot{\varepsilon}_3^2} \tag{2.42}$$

$$\dot{\sigma}_3 = C_1(\sigma_1 + 2\sigma_3)\dot{\varepsilon}_3 + C_2(\dot{\varepsilon}_1 + 2\dot{\varepsilon}_3)\sigma_3 + C_3\frac{\sigma_1\dot{\varepsilon}_1 + 2\sigma_3\dot{\varepsilon}_3}{\sigma_1 + 2\sigma_3}\sigma_3 + C_4(\sigma_3 + \sigma_3^*)\sqrt{\dot{\varepsilon}_1^2 + 2\dot{\varepsilon}_3^2} \tag{2.43}$$

In the drained triaxial compression numerical tests, the constant confining pressure is 100 kPa, and the test starts from a hydrostatic stress state. The parameters for Mohr-Coulomb model in Table 2.1, and corresponding parameters for the updated hypoplastic and Druck-Prager model in Table 2.2 are used in this simulation. The numerical results of the axial strain-stress relation and axial strain-volumetric strain relation are presented in Fig. 2.6.

It can be observed from the numerical results in Fig. 2.6(a) that the numerical tests give rise to the same failure deviatoric stress regardless of the model it used, while the test using hypoplastic model gains a nonlinear strain-stress response. The results in 2.6(b) reveals that different model results in various volumetric response. The hypoplastic model and Druck-Prager model give contractive volume change, and the volume change vanishes at limited state. However, the Mohr-Coulomb model gives a slight vilumetric dilatancy in the

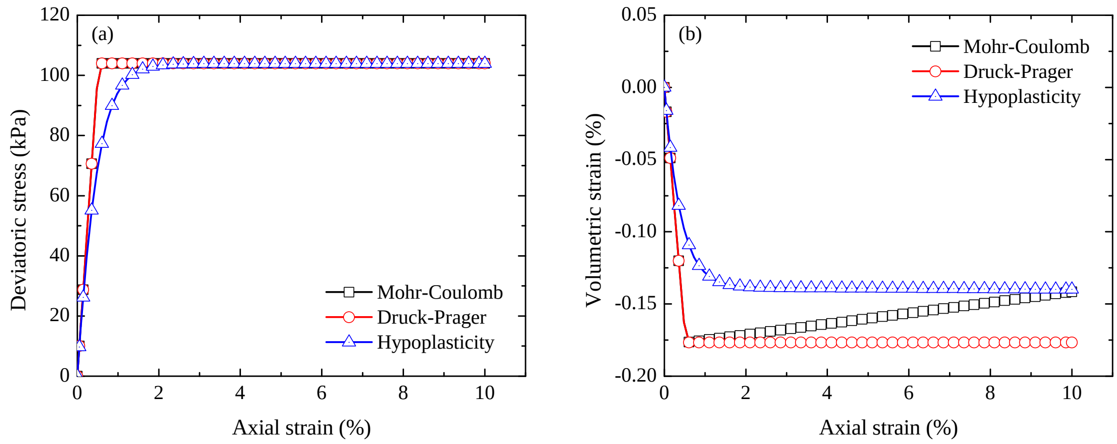

Figure 2.6 Numerical simulation of the drained triaxial compression test using different constitutive models (a) axial strain-stress relation, and (b) axial strain- volumetric strain relation(confining pressure $\sigma_3 = 100$ kPa)

simulation. The difference in the volumetric response can be attribute to the definition of the tangential stiffness in the three models,i.e., the initial Young's modulus for the hypoplastic model is stress dependent, while the initial Young's modulus of Mohr-Coulomb and Druck-Prager model is stress independent.

Simple shear test

The simple shear test (SST) is particularly relevant to the situations where failure is expected to occur along the thin shear zone. In the laboratory, The simple shear test can be performed using direct simple shear (DSS) apparatus. In this test, the soil specimen is commonly subjected to K0-consolidation stress, and drained or undrained conditions can be considered. The undrained condition is simulated by continuously adjusting the vertical stress so that the specimen height is kept constant (thereby keeping constant volume). The change in vertical stress is assumed to be equal to the change in pore water pressure that would have occurred during a truly undrained test. Beside the practical significance, the simple shear test plays an important role in developing constitutive models as well. To numerically perform the simple shear test, we write out the stress rate, stress, strain rate, and spin rate for the simple shear test can be expressed in the matrix form.

$$\mathring{\boldsymbol{\sigma}} = \begin{pmatrix} \mathring{\sigma}_{11} & \mathring{\sigma}_{12} & 0 \\ \mathring{\sigma}_{12} & \mathring{\sigma}_{22} & 0 \\ 0 & 0 & \mathring{\sigma}_{33} \end{pmatrix}, \boldsymbol{\sigma} = \begin{pmatrix} \sigma_{11} & \sigma_{12} & 0 \\ \sigma_{12} & \sigma_{22} & 0 \\ 0 & 0 & \sigma_{33} \end{pmatrix}, \dot{\boldsymbol{\varepsilon}} = \begin{pmatrix} \dot{\varepsilon}_{11} & \dot{\varepsilon}_{12} & 0 \\ \dot{\varepsilon}_{12} & \dot{\varepsilon}_{22} & 0 \\ 0 & 0 & 0 \end{pmatrix}, \dot{\omega} = \begin{pmatrix} 0 & \dot{\omega}_{12} & 0 \\ \dot{\omega}_{12} & 0 & 0 \\ 0 & 0 & 0 \end{pmatrix}$$

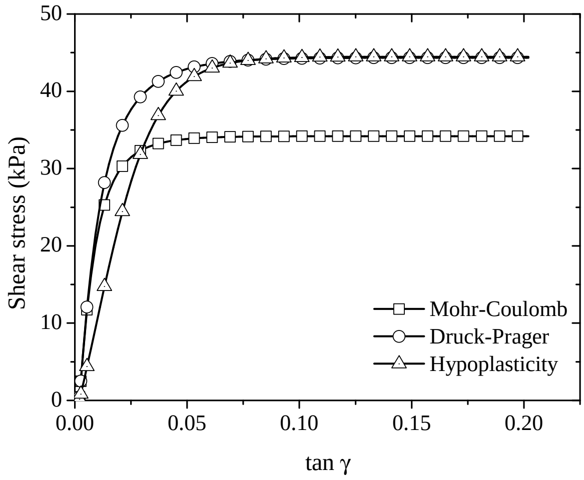

Figure 2.7 Numerical simulation of simple shear test using the triaxial compression test matched parameters for the updated model, Druck-Prager model, and Mohr-Coulomb model(confining pressure $\sigma_3 = 100$ kPa)

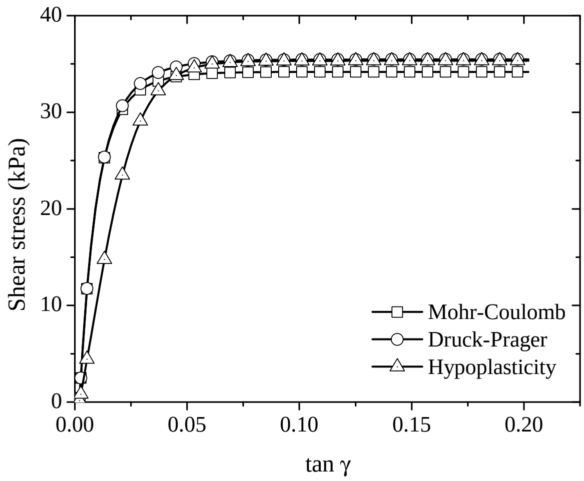

Figure 2.8 Numerical simulation of simple shear test using the triaxial tension test matched parameters for the updated model, Druck-Prager model, and Mohr-Coulomb model(confining pressure $\sigma_3 = 100$ kPa)

Compared with the matrices representing of the triaxial test, the spin tensor ($\dot{\omega}$) does not vanish in the simple shear test. To simulate the simple shear tests numerically, let us consider the motion described by the following expressions:

$$x_1 = X_1 + X_2 f_1(t), \quad x_2 = X_2 + X_2 f_2(t), \quad x_3 = X_3 \tag{2.44}$$

f_1 and f_2 in Eq. (2.44) represent the shear deformation and the volume change, respectively. For simple shear test with constant volume(undrained), we have $f_2 = 0$. The strain rate and

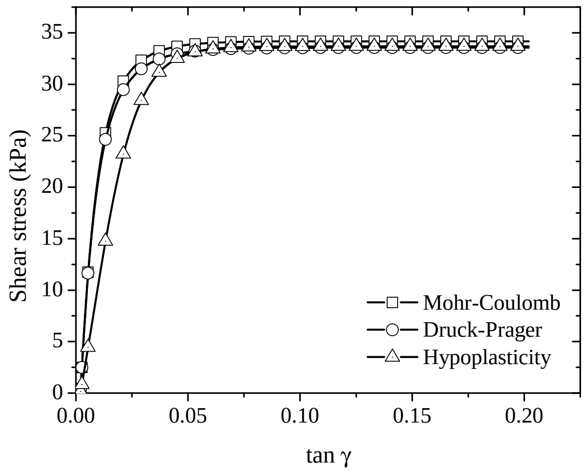

Figure 2.9 Numerical simulation of simple shear test using the plane strain response matched parameters for the updated model, Druck-Prager model, and Mohr-Coulomb model(confining pressure $\sigma_3 = 100$ kPa)

the spin tensors can be obtained from Eq. (2.44):

$$\dot{\boldsymbol{\varepsilon}} = \frac{1}{2(1+f_2)}\begin{pmatrix} 0 & \dot{f}_1 & 0 \\ \dot{f}_1 & 2\dot{f}_2 & 0 \\ 0 & 0 & 0 \end{pmatrix}, \quad \dot{\omega} = \frac{1}{2(1+f_2)}\begin{pmatrix} 0 & \dot{f}_1 & 0 \\ -\dot{f}_1 & 0 & 0 \\ 0 & 0 & 0 \end{pmatrix}, \tag{2.45}$$

In the simple shear test, the material time rate of stress $\dot{\sigma}$ rather than the Jaumann stress rate $\mathring{\sigma}$ should be added to the stress in each time step. According to Eq. (2.2) and making using of Eq. (2.45), the relation between $\dot{\sigma}$ and $\mathring{\sigma}$ can be explicitly expressed:

$$\begin{pmatrix} \dot{\sigma}_{11} & \dot{\sigma}_{12} & 0 \\ \dot{\sigma}_{12} & \dot{\sigma}_{22} & 0 \\ 0 & 0 & \dot{\sigma}_{33} \end{pmatrix} = \begin{pmatrix} \mathring{\sigma}_{11} & \mathring{\sigma}_{12} & 0 \\ \mathring{\sigma}_{12} & \mathring{\sigma}_{22} & 0 \\ 0 & 0 & \mathring{\sigma}_{33} \end{pmatrix} + \frac{\dot{f}_1}{2(1+f_2)}\begin{pmatrix} 2\sigma_{12} & \sigma_{22}-\sigma_{11} & 0 \\ \sigma_{22}-\sigma_{11} & -2\sigma_{12} & 0 \\ 0 & 0 & 0 \end{pmatrix} \tag{2.46}$$

The governing differential equations for simple shear test can be obtained by substituting the corresponding stress and strain rate matrices into constitutive equation (2.14). The parameters for Mohr-Coulomb model in Table are used in this simulation. Correspondingly, the parameters mached from the triaxial compression test, triaxial tension test, and plane strain test are used for comparison. The relation between the shear stress and the shear angle γ using parameters matched for triaxial compression response, triaxial tension response, and plane strain response are respectively presented in Fig. 2.7, Fig.2.8, and Fig. 2.9. It is observed that the simulation using the parameters matched from plane strain test give the closest results, while there is great difference in the simulation using the parameters matched from the triaxial compression test. This result suggests that it is better to choose the parameters matched from plane strain test in some situation, where failure is expected to occur in a shin shear zone, e.g. direct shear test.

2.4 Extensions of the updated constitutive model

Both the constitutive Eq. (2.11) and (2.14), albeit their mathematical simplicity, are capable of capturing the salient features of granular materials, e.g. nonlinearity, failure and dilatancy (Wang, 2009; Wu and Bauer, 1994). However, some behaviors such as cohesion of soils, and the effect of void ratio and stress level cannot be taken into account. These shortcomings may restrict the application of hypoplasticity. Fortunately, the inherent shortcomings can be remedied by through extension of the hypoplastic constitutive equation. In the following subsection, the updated model is enhanced by a simple critical state formulation, and furthermore, a simple way to account the cohesion of soil is introduced. These extensions can broaden the piratical adoption of the hypoplastic model.

2.4.1 Critical state of granular material

The response of constitutive equation (2.14) is governed by the interaction between the linear and nonlinear terms. The linear term can be viewed as constructive, whereas the nonlinear term can be considered as destructive. Any perturbation either on the linear term or on the nonlinear term can unbalance the hypoplastic equation, i.e., enhancing the nonlinear term causes the constitutive response to be contractive, resembling loose material behavior; diminishing it causes the constitutive response to be dilatant, resembling dense material behavior Wu et al. (1996). Therefore, we can describe both dense and loose material behavior with the same constitutive equation by enhancing or diminishing the nonlinear part with density. Following the idea proposed in Wu and Niemunis (1996); Wu et al. (1996), we introduce a multiplier I_e into the nonlinear term as a perturbation that incorporates the effect of critical state on the constitutive response. The multiplier has the value $I_e = 1$ at the critical state, greater than 1 for a loose state, and less than 1 for a dense state. In the framework of Eq.(2.9), the general form of the extended model reads

$$\mathring{\boldsymbol{\sigma}} = \mathscr{L}(\boldsymbol{\sigma}) : \dot{\boldsymbol{\varepsilon}} - \boldsymbol{N}(\boldsymbol{\sigma})\|\dot{\boldsymbol{\varepsilon}}\|\, I_e, \tag{2.47}$$

In the framework of Eq. (2.14), the consecutive equation including the critical state concept reads

$$\mathring{\boldsymbol{\sigma}} = C_1(\mathrm{tr}\boldsymbol{\sigma})\dot{\boldsymbol{\varepsilon}} + C_2(\mathrm{tr}\dot{\boldsymbol{\varepsilon}})\boldsymbol{\sigma} + C_3\frac{\mathrm{tr}(\boldsymbol{\sigma}\cdot\dot{\boldsymbol{\varepsilon}})}{\mathrm{tr}\boldsymbol{\sigma}}\boldsymbol{\sigma} + C_4(\boldsymbol{\sigma}+\boldsymbol{\sigma}^*)\|\dot{\boldsymbol{\varepsilon}}\|I_e \tag{2.48}$$

There are several forms for I_e in literature (Lin et al., 2015; Wu et al., 1996). In the present work, a different formulation for the critical state function I_e is proposed:

$$I_e = (\frac{e}{e_{crt}})^{\alpha} \tag{2.49}$$

in which e and e_{crt} refer to the current void ratio and critical state void ratio, respectively. α is a constitutive constant, which controls the degree of strain softening, as shown in Fig. 2.10(a). Li and Wang (1998) suggested a formulation for the location of critical state line (CSL) in the $e-p$ space that has a considerable range of applicability. A slightly modified form is used in this work:

$$e_{crt} = e_{co}\exp\left[-\lambda(\frac{p}{p_a})^{\xi}\right] \tag{2.50}$$

where e_{co}, λ, ξ are parametric constants, and $p = \mathrm{tr}\boldsymbol{\sigma}/3$ and p_a stands for the confining pressure and atmospheric pressure for normalization, respectively. Due to the incorporation of critical state function, the dilatancy angle ψ, which controls the dilatancy and contraction, should equal to zero. It is noteworthy that the original structure of I_e in (Guo et al., 2016; Lin et al., 2015; Peng et al., 2016; Wu et al., 1996) has seven parameters. However, only four parameters are needed in the present form. Note that constitutive equation (2.48) is homogeneous of the first degree in stress. This implies that the tangential stiffness is proportional to the stress level. By making use of this feature, the tangential stiffness can be altered by multiplying Eq. (2.48) as a whole with a scale function, called the stiffness function, without changing the critical state. From Eq. (2.47) it can be easily observed that multiplying the whole constitutive with a scale function does not effect the failure criterion. The stiffness function proposed by Wu (1999) is adopted:

$$I_{se} = \frac{\exp[\beta(e_{crt}-e)]}{(1+r)^2} \tag{2.51}$$

where β is a material parameters and r denotes the stress ratio $\|\boldsymbol{\sigma}^*\|/\mathrm{tr}\boldsymbol{\sigma}$. The dependence of the initial tangential stiffness on the initial void ratio is accounted for by the exponential function in the numerator. The potential function in the denominator is introduced to modulate the shape of the stress-strain curve, since constitutive equation 2.48 gives rise to a too stiff stress-strain response at small strain.

The modified constitutive model can be written as follow:

$$\mathring{\boldsymbol{\sigma}} = I_{se}\left[C_1(\mathrm{tr}\boldsymbol{\sigma})\dot{\boldsymbol{\varepsilon}} + C_2(\mathrm{tr}\dot{\boldsymbol{\varepsilon}})\boldsymbol{\sigma} + C_3\frac{\mathrm{tr}(\boldsymbol{\sigma}\cdot\dot{\boldsymbol{\varepsilon}})}{\mathrm{tr}\boldsymbol{\sigma}}\boldsymbol{\sigma} + C_4(\boldsymbol{\sigma}+\boldsymbol{\sigma}^*)\|\dot{\boldsymbol{\varepsilon}}\|I_e\right], \tag{2.52}$$

with the stiffness function $I_{se}(\boldsymbol{\sigma}, e)$ in Eq. (2.49) and the critical state function I_e in Eq.

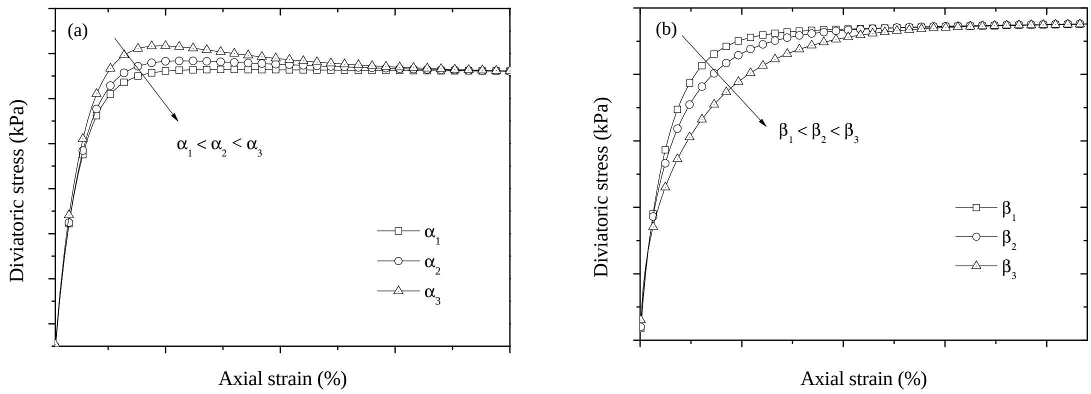

Figure 2.10 Strain-stress relations under drained triaxial condition:(a) the effect of parameter α,and (b) the effect of parameter β.

(2.51). The effect of β on the tangential stiffness is presented in Fig 2.10(b). It can be observed from this figure that the tangential stiffness decrease with increasing β. Therefore, the shortcoming that the constitutive equation (2.52) leads to too stiff of strain-stress response with small strain is resolved by the stiffness function I_{se}.

Owing to the critical state function, the yield function can be obtained according to Eq. (2.19) by multiplying C_i with the critical state function I_e and the stiffness function I_{se}, i.e.

$$C_1' = I_{se}C_1, \quad C_2' = I_{se}C_2, \quad C_3' = I_{se}C_3, \quad C_4' = I_{se}I_eC_4 \tag{2.53}$$

in Eq.(2.18), which then can model the effect of strain softening and hardening. Consequently, the hypoplastic model Eq. (2.52) is an attracting choice for describing rate-independent behaviors of granular soils.

2.4.2 Extension for cohesive soils

Through a review of the development in hypoplasticity by Wu and Kolymbas (2000), one can find that the attempt to specifically develop hypoplasticity to clay has been less successful. An alternative approach to account for the cohesion of soil is to extend the hypoplastic model by adding a structure tensor to the Cauchy stress. For instance, Bauer and Wu (1995) extended the constitutive Eq.(2.11) by adding the intrinsic pressure, which depends on stress level and void ratio, to the actual stress to account for cohesion and the effect of strain history. In a similar way, a structure tensor with respect to stress-like internal parameter was introduced to model behavior of clay with sets of material parameters for various states of consolidation (Weifner and Kolymbas, 2007).

Another approach is to combine the critical state soil mechanics with hypoplaticity. According to this approach, a hypoplastic model for clay was proposed by Mašín (2005) on the basis of a constitutive equation suggested by Herle and Kolymbas (2004), which combines hypoplasticity principles with the traditional critical state soil mechanics. Moreover, Huang et al. (2006) suggested a hypoplastic model based on the constitutive model proposed for sands by Gudehus (2000) and Bauer (1996), which incorporates the critical state and is able to capture the undrained behavior of normally consolidated clay. It is worth noting that the aim of this work is to develop a visco-hypoplastic model to account for creep soils, therefore, a complex treatment of cohesion behavior of soils may weak the potential model's capacity of presenting the rheological characteristic of soils. Among these extensions of hypoplasticity for cohesive soils, the adding of a structure tensor to the actual stress seems simple for a sophisticated model.

Let us look at a simple way to extend the constitutive Eq. (2.14) to cohesive soils. The constitutive Eq. (2.14) is originally proposed for granular materials, which are usually cohesionless soil. As is discussed above, the limit state of Eq. (2.14) leads to a conical surface with its apex in the conical origin of the principal stress space. Therefore, the Eq. (2.14) is not able to account for tensile stress. Inspired by the similarities between the failure surface of the updated model and Drucker-Prager model. The parameter k_ϕ can be introduced into Eq. (2.18) to account for cohesion, then the yield surface reads:

$$f^s = \sqrt{J_2} - \chi I_1 - k_\phi = 0 \tag{2.54}$$

For the updated constitutive Eq. (2.14), the same effect can be achieved by simply replacing the stress tensor $\boldsymbol{\sigma}$ with the following translated stress tensor (Wang, 2009)

$$\boldsymbol{\sigma_c} = \boldsymbol{\sigma} - p_c \mathbf{1} \tag{2.55}$$

where p_c is related to cohesion c and friction angle ϕ of Mohr-coulomb yield criterion. With this approach, the apex of the circle cone was translated to point $\sigma(p_c, p_c, p_c)$ in the principal stress space. Substitution of the stress point $\sigma(p_c, p_c, p_c)$ into equation (2.54) yields the magnitude of $p_c = c\ /\tan\phi$. Thus, the constitutive Eq. (2.14) can be extended in the following form:

$$\mathring{\boldsymbol{\sigma}} = C_1(\mathrm{tr}\boldsymbol{\sigma}_c)\dot{\boldsymbol{\varepsilon}} + C_2(\mathrm{tr}\dot{\boldsymbol{\varepsilon}})\boldsymbol{\sigma}_c + C_3\frac{\mathrm{tr}(\boldsymbol{\sigma}_c \cdot \dot{\boldsymbol{\varepsilon}})}{\mathrm{tr}\boldsymbol{\sigma}_c}\boldsymbol{\sigma}_c + C_4(\boldsymbol{\sigma}_c + \boldsymbol{\sigma}_c^*)\|\dot{\boldsymbol{\varepsilon}}\| \tag{2.56}$$

For cohesive soils, the magnitude of p_c can be regarded as the cohesion of soils, which can be obtained from triaxial compression test. However, it should be noted that different chemical or physical causes for cohesion give rise to a different material behavior. In this study, the evolution equation for p_c is focused on cohesive soils like clay, the soft clayey soil where cohesion is assumed to depend on the physical-chemical effects of clay particles. The effects of granulometry of the particles and the change of water content are not taken into account. The effect of cohesion is demonstrated using two numerical triaxial compression tests on a cohesionless and cohesive soil with . The material parameters presented in Table 2.1 for Eq. (2.56) are used for the numerical simulations. The cohesion is $c = 11.5$ kPa and the confining pressure is $\sigma_3 = 100$ kPa. The result is presented in Fig.2.11. The test result reveals that the cohesive can influence the strain- stress response, i.e., increase the deviatoric stress, while it cannot influence the volumetric response.

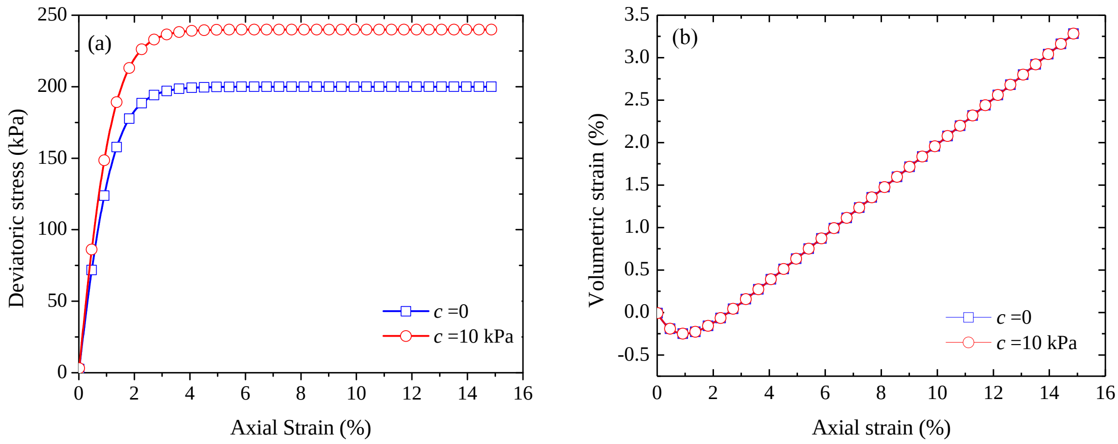

Figure 2.11 Numerical simulation of triaxial compression test with or without cohesion (confining pressure σ_3 =100 kPa,c =0 kPa/11.5 kPa)

2.5 Constitutive model performance

The results from two types of soil, representing the cohesionless and cohesive soils, are used to validate the model: Toyoura sand, whose calibration procedure has been illustrated earlier, and a rockfill material. Toyoura sand has been studied extensively by different researchers in Japan. Here, the series of triaxial compression test results from Toyoura sand with different confining pressures and void ratios are used for the calibration under both drained and undrained conditions. In addition, a cohesive soil for rockfill dam is used to validate the effect of cohesion. The rockfill material contains both fine-graded particles and a large proportion of coarse-graded particles. Owing to the existence of the fined-graded particles, the selected soil exhibit cohesive behavior. Therefore, these simulations are used to validate the capacity of the model for both cohesionless and cohesive soils.

2.5.1 Cohesiveless soil

Toyoura sand is a uniform fine quartzitic sand consisting of sub-rounded to sub-angular particles, which is the standard cohesionless soil reported in the Japanese soil mechanics literature (Miura and Yamanoucm, 1975; Norihiko et al., 1984; Verdugo and K, 1996). Verdugo and K (1996) have conducted a complete set of monotonic drained and undrained triaxial tests on isotropically consolidated samples of Toyoura sand with a mean diameter D_{50} = 0.17 mm and a uniformity coefficient C_u = 1.7. These tests have been conducted on a wide range of void ratios and confining pressures. To demonstrate the performance of the hypoplastic constitutive model, this set of data has been again used in this work. The parameters used for constitutive equation (2.52) in these simulations are given in Table 2.6 and Table 2.5 for drained and undrained conditions, respectively.

Table 2.4 Material parametets for simulation of drained triaxial tests on Toyoura sand

Para.	C_1	C_2	C_3	C_4	e_{co}	λ	ξ	α	β
Value	-47.2	-152	-398.1	-137.1	0.947	0.022	0.057	1.5	15

Table 2.5 Material parametets for simulation of undrained triaxial tests on Toyoura sand

Para.	C_1	C_2	C_3	C_4	e_{co}	λ	ξ	α	β
Value	-47.2	-150.4	-220.3	-102	0.947	0.022	0.057	1.8	0

In the drained tests, two different confining pressures of 100 and 500 kPa were used. Samples with three different void ratios e_i =0.81, 0.917 and 0.996, which respectively corresponded to a relative density of 18%, 33%, and 52%, were used in the tests. Fig. 2.12 compares the results of the simulation and the experimental results. Fig. 2.12 (a) and (c) makes the comparison in terms of variations of axial strain with shear stress and void ratio, respectively, for the loose, medium and dense samples of Toyoura sand with the initial confining pressure of 100 kPa. Similarly, Fig. 2.12 (b) and (d) compares the data and simulations of drained triaxial tests with the initial confining pressure of 500 kPa. In particular, Fig. 2.12 (e) and (f) does the same in terms of variations of variations of void ratio with shear stress.

The undrained tests were conducted at a confining pressure ranging from p = 100 to 3000 kPa at three different void ratios e_i = 0.907,0.833, and 0.735 that corresponded to a relative density of 16, 38, and 64%, respectively. Fig.2.13 compares the data and simulations for undrained triaxial compression (UTCT) tests on isotropically consolidated samples of

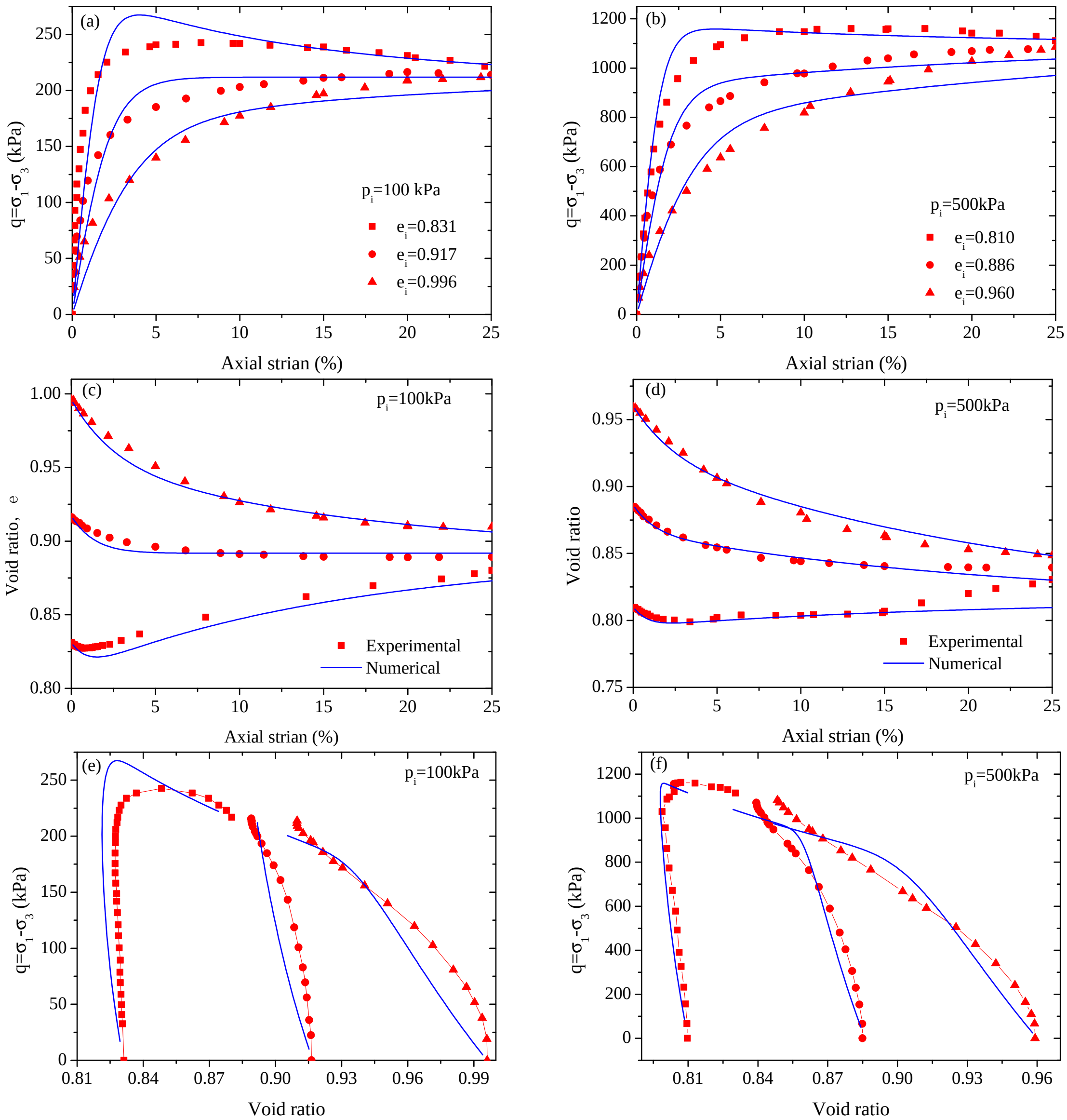

Figure 2.12 Comparison of data and simulations for drained triaxial compression tests on isotropically consolidated samples of Toyoura sand (p_i =100 and 500 kPa)

Toyoura sand. In particular, Fig. 2.13 (a) makes the comparison in terms of stress-strain response , while Figure 11(b) does the same in terms of effective stress paths for the loose samples ($e_i = 0.907$) with initial confining pressures in the range of 100 to 2000 kPa. Similar comparison between data and simulations at medium dense (e_i = 0.833) and dense (e_i = 0.735) samples are presented in Fig. 2.13 (c)–(f), respectively.

The dramatically different responses that result from different combinations of confining pressure and the void ratio in drained and undrained condition can be all successfully captured by using a unique set of model constants. The response varied from highly dilatant in

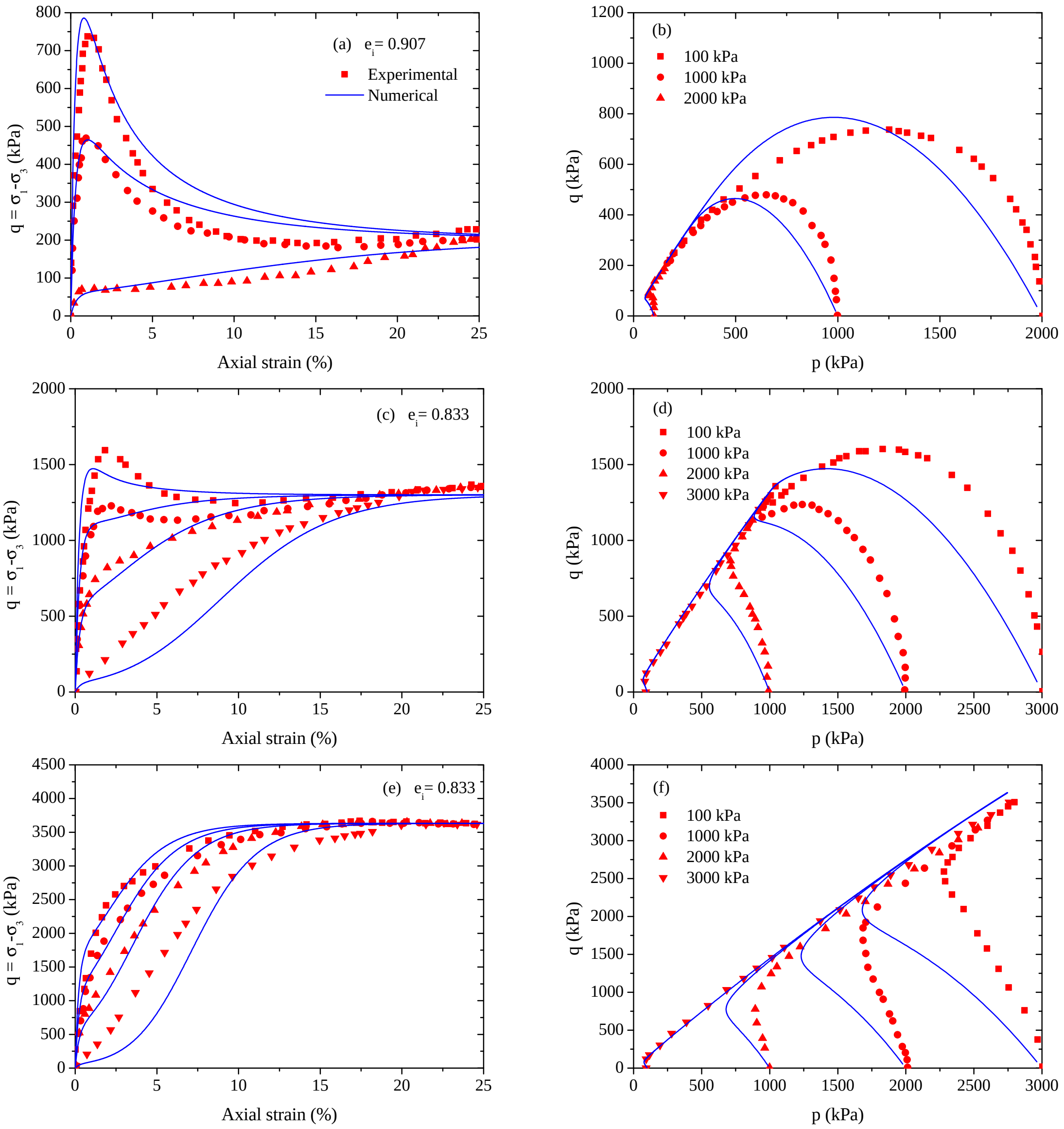

Figure 2.13 Comparison of data and simulations for undrained triaxial compression tests on isotropically consolidated samples of Toyoura sand (e_i =0.907, 0.83, and 0.735)

higher densities and lower confining pressures to highly contraction in lower densities and higher confining pressures. The key to this achievement lies function I_e. Very good match has been achieved in simulations of the void ratio along with axial strain in the drained condition; however, one can observe a comparative shortcoming of the model in accurately capturing the stress-strain relations. To be more specific, the simulations have overestimated the strain softening of the densest samples in drained conditions. This could be solved by choosing slightly higher initial void ratios for simulations, however, this will affect the evolution of the void ratios. On the other hand, the stain-stress response in undrained condition can be well caricatured, while simulated stress paths do not agree very well with the experimental results. To be specific, the effective mean pressures degrade too fast in the undrained condition. Nevertheless, the strain hardening and softening behavior, together with the critical state, can be depicted using the hypoplastic constitutive model.

2.5.2 Cohesive soil

A series of drained triaxial tests on rockfill material are used to validate the effect of cohesion. The tested rockfill material is a crushed weakly-weathered granite from Nuozhadu rockfill dam in Yunnan, China (Wu et al. 2015). Selected properties of the original granite block are: density is 2.63 g/cm^3, saturated compression strength σ_c = 85 Mpa. The hydrophilic softening coefficient, defined as the ratio of two uniaxial compression strengths measured respectively under saturated and dry conditions, is $\eta_c = 0.76$. The rockfill material can be characterized as a coarse-grained soil, which to some extent exhibits cohesive behavior under very dense condition. The parameters for Eq. (2.56) used in this simulation are calibrated with triaxial compression tests of rockfill soil. as shown in Table.2.6.

Table 2.6 Material parameters for simulation of the drained triaxial test on rockfill material

Para.	E_i(Mpa)	υ_i	$\phi(/^o)$	$\psi(/^o)$	$c(kPa)$	C_1	C_3	C_3	C_4
Value	200	0.1	46	0	20	60.6	-95.12	-228.45	-117.67

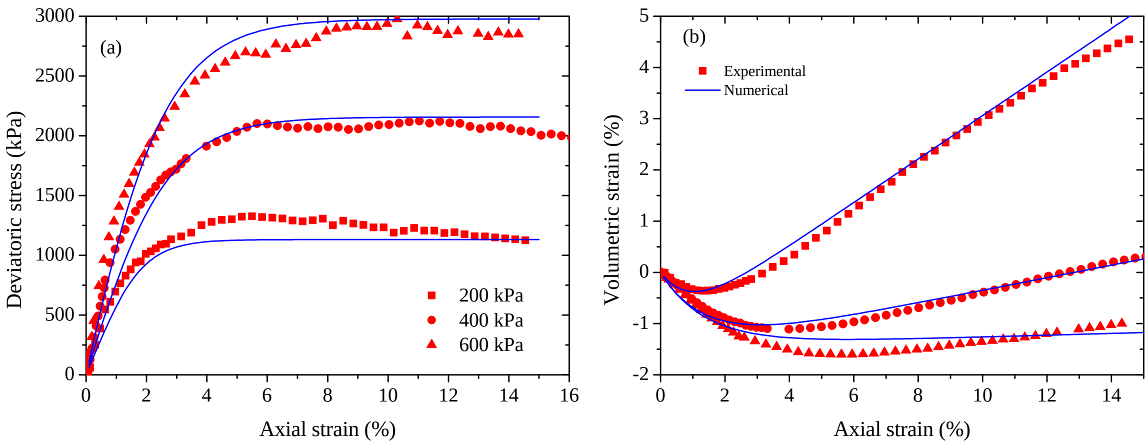

Figure 2.14 (a)Stress-strain behavior, and (b) Volumeric strainaxial strain behavior of a rockfill material

Fig. 2.14(a) presents the strain-stress relations of the rockfill material under three confining pressures, i.e., 200 kPa, 400 kPa, and 600 kPa. The numerical stress-strain result is compared with the experimental data. Reasonable agreement of stress-strain response is noted in this simulation. It should be noted that the dilative behavior in the volumetric strain versus axial strain cannot be captured with the same dilation angle. Different dilation angles for different confining stress are needed for capturing the dilative phenomenon better. As shown in Fig. 10(b), the dilation angle is 23°, 7° and 1° for confining pressure of 200 kPa, 400 kPa, and 600 kPa, respectively.

2.6 Conclusion

This chapter discusses a simple critical state hypoplastic constitutive model. The main conclusions of this chapter are drawn in the following:

Firstly, a simple hypoplastic constitutive is presented. Based on this model a comprehensive study on the failure surface and bound surface is carried out. This simple hypoplastic model has a Drucker-Prager type failure surface with its apex in the conical origin, and circumscribes the Mohr-Coulomb yield surface in the principal stress space. Its bound surface possesses the same geometry as the failure surface, while lies slightly outside the failure surface. Normally, the stress state is constrained inside the failure surface. However, some strain directions may lead to stress state lying between the between the failure surface and the bound surface. The distance between these two surfaces, to some extent, indicates the integration error in numerical computation. Furthermore, this distance increase with increasing the friction angle. Therefore, stress correction algorithm should be considered during the stress integration for numerical analysis.

Secondly, the critical state concept and cohesion are incorporated into the hypoplastic constitutive equation (2.14). The performance of the model is validated using triaxial tests on Toyoura sand under both drained and undrained conditions. The strain hardening and softening behavior, together with the critical state of Toyoura sand, can be depicted using the hypoplastic constitutive model. On the other hand, the cohesion is described by a translated tensor, which is added to the Cauchy tensor in the hypoplastic model to account for the effect of cohesion. The magnitude of the translated tensor is connected to the Mohr-Coulomb parameter constants: cohesion c and friction angle ϕ.

Chapter 3

Modeling the viscous behavior of granular material

3.1 Introduction

Geotechnical structures such as embankments, bridge abutments, retaining walls, slopes, etc., have been extensively observed with significant deformation and settlement with time (Karstunen and Yin, 2010; Komornik et al., 1972; Lade et al., 2009). These long-time deformations are largely due to the time-dependent behavior of soils. It is well known that both clayey and granular soils exhibit time-dependent behavior. Clayey soil, usually referred to isotach material, follows a classic viscous behavior with time (Kim and Leroueil, 2001; Kimoto and Oka, 2005; Yin and Graham, 1989). However, granular soil does not obey this classic viscous behavior and is considered as non-isotach material (Augustesen et al., 2004; Karimpour and Lade, 2010; Tatsuoka et al., 2001). Many experimental investigations reveal that the effect of strain rate is insignificant on the stress-strain relationships of sand in the constant strain rate tests (Lade and Liu, 1998; Lade et al., 1997, 2009; Yamamuro and Lade, 1993) , whereas the stress-strain relationship temporarily overshoots the unique relationship owing to the accelerated loading in the stepwise rate of strain tests (Di Benedetto et al., 2002; Kuwano and Jardine, 2002; Matsushita, 1999). Granular soils, other than clay, to some extent is acceleration dependent. The practical significance of this viscous behavior in granular material is increasingly evident. For instance, driven or displacement piles in sand often demonstrate a significant increase in the shaft capacities with time (Bowman and Soga, 2005; Chow et al., 1998; Jardine et al., 2006). Creep settlement contributes a large proportion of the overall movements of the foundations constructed on granular soil regions (Burland and Burbridge, 1985; Morsy et al., 1995). Hence, it is essential to consider the time-dependent behavior of granular material in engineering design.

The constitutive equations for time-dependency of granular soil, which govern how the material moves over time are still a matter of debate. One reason is that, depending on the time and loading condition, a granular soil exhibits both frictional and viscous behaviors, but most of the models focus on frictional behavior. To model the viscous effects in granular soil, different approaches can be classified as: (1)some empirical models (Lacerda and Houston, 1973; Murayama, 1983) by closed-form solutions or differential equations, which can be applied only to problems of specific boundary conditions (Liingaard et al., 2004); (2) granular rheology models, such as Herschel-Bulikley and Bingham based models (Atapattu et al., 1995; Chen and Lee, 2002) and models (Jop et al., 2006; Tankeo et al., 2013) in which the viscous deformation takes place if the shear stress exceeds the yield value and difficult to be determined; (3) general elasto-viscoplastic models based on theories of Perzyna (Perzyna, 1963, 1966), such as Di Prisco and Imposimato (1996) and Di Prisco et al. (2000), which describe the constant rate of viscoplastic flow, but not relating to acceleration; and (4) models considering acceleration effect by Tatsuoka (Tatsuoka et al., 2002)], in which the frictional component was too simple to describe the nonlinear stress-strain of sand, and the viscous component was too complicated for use. An alternative approach is to model the frictional and viscous behaviors of granular material in the framework of hypoplasticity. Owing to the predictive capacity and the formulative simplicity, hypoplastic models have enabled the unified description of frictional and viscous behaviors of granular material much easier. Recently, rate-dependency has been incorporated into hypoplasticity to describe the creep of frozen soil (Xu et al., 2016), debris flow (Guo et al., 2016; Peng et al., 2016), creep of clay (Niemunis, 2003b). However, up to now there is no report on such models describing acceleration effect of granular material. Nevertheless, the development of well-established constitutive equations describing both the viscous and inviscid behaviors of granular soils is still an ongoing undertaking.

In the present paper, a new constitutive model for modeling viscous behavior of granular materials is proposed. The model consists of two components (frictional part and viscous part) representing respectively the frictional and viscous stresses in granular media. The frictional part is accounted for using a rate-independent hypoplastic constitutive model, which is enhanced by incorporating simple critical state based formulations. The viscous part is implemented by a high order term considering the effect of strain acceleration. The performance of the proposed model is examined by simulating different tests on granular materials, i.e. a stepwise strain-rate triaxial test, creep tests under different stress levels on Toyoura sand, and a stepwise strain rate triaxial test on Chiba gravelly soil.

3.2 Constitutive model framework

Two main mechanisms that govern the behaviors of granular materials are friction and viscosity. In the quasi-static regime, the interparticle frictional forces give rise to rate-independent Coulomb-type plastic behavior. On the other hand, in the dynamic flow state, a notable part of stress comes from the particle collision (Peng et al., 2016). In this work, we, therefore, make the fundamental assumption, as in (Di Benedetto et al., 2002; Wu, 2006; Xu et al., 2016), that the frictional and the viscous stresses coexist in the granular viscous response. Direct addition of the two stress contributions gives the following form of granular stress:

$$\boldsymbol{\sigma} = \boldsymbol{\sigma}_h + \boldsymbol{\sigma}_v \tag{3.1}$$

where $\boldsymbol{\sigma}_h$ and $\boldsymbol{\sigma}_v$ denote frictional stress (time-independent) and viscous stress (time-dependent), respectively. As illustrated in the above model, the frictional and the viscous stresses take effect simultaneously. This mathematical structure corresponds to the fact that the soil exhibits both frictional and the vicious behaviors.

To obtain a concrete formulation, some fundamental restrictions should be imposed on the constitutive equation (3.1). Firstly, the resulting constitutive relation should able to capture the salient behaviors of granular material in the quasi-static frictional regime. Secondly, the formulation for the viscous stress part should consider the influences of strain rate and strain acceleration. Additionally, in poorly graded sands such as Hostun and Toyoura sands, viscous stresses decay with an increase in the strain path. As a result, in granular soils, viscous stresses depend not only on the strain rate and strain acceleration but also on the recent strain path. Consequently, the influence of strain path also needs to be considered. Thirdly, the proposed model should be able to describe the whole process of creep failure including primary creep, secondary creep, and tertiary creep in a unified way, which is realized by the coupled evolution of the two stress parts.

In the present work, the critical state hypoplastic constitutive model presented in previous chapter and a rate form of HB rheology are employed to formulate the new constitutive model. The rate form of the new model is expressed as follows:

$$\dot{\boldsymbol{\sigma}} = \dot{\boldsymbol{\sigma}}_h + \dot{\boldsymbol{\sigma}}_v \tag{3.2}$$

where $\dot{\boldsymbol{\sigma}}$, $\dot{\boldsymbol{\sigma}}_h$ and $\dot{\boldsymbol{\sigma}}_v$ denote the Cauchy, hypoplastic frictional and HB viscous stress rates, respectively.

3.3 Structure of viscous models

The mathematical theories of viscous behaviors developed independently from that of frictional behaviors. Traditionally, the rheological models are based on a superposition principle. This indicates that the response (i.e., strain) at any time is directly proportional to the value of the initiating signal (i.e., stress). In the linear theory of viscoelasticity, the differential equations are linear, and the coefficients of the time differentials are constant as well. Following the above concept, we can write down a general differential equation for linear viscoelasticity as follows:

$$\boldsymbol{\sigma}+\mu_1\frac{\partial\boldsymbol{\sigma}}{\partial t}+\mu_2\frac{\partial^2\boldsymbol{\sigma}}{\partial t^2}+...+\mu_n\frac{\partial^n\boldsymbol{\sigma}}{\partial t^n}=\eta_0\boldsymbol{\varepsilon}+\eta_1\frac{\partial\boldsymbol{\varepsilon}}{\partial t}+\eta_2\frac{\partial^2\boldsymbol{\varepsilon}}{\partial t^2}+...+\eta_m\frac{\partial^m\boldsymbol{\varepsilon}}{\partial t^m} \tag{3.3}$$

where $n=m$ or $n=m-1$, μ_i $(i=1,...,n)$ and η_j $(j=1,...,m)$ are time differentials constants. These constants are material parameters, such as viscosity coefficient and rigidity modulus. $\boldsymbol{\sigma}$ and $\boldsymbol{\varepsilon}$ are the Cauchy stress tensor and the strain tensor, respectively. However, other types of deformation could be included without difficulties, with the stress and strain referring to that particular deformation process. For example, the stress tensor and strain tensor can be replaced in terms of shear stress τ and shear strain γ, respectively, relevant to a simple shear test.

The basic fluid-like behavior of a material can be expressed in terms of uniaxial models or mechanical elements, one of the simplest case, Hookean model, is the spring element, which is capable of representing the elastic characteristic of the continuous medium. In Eq. (3.3), if η_1 is the only non-zero parameter, we have:

$$\boldsymbol{\sigma}=\eta_1\dot{\boldsymbol{\varepsilon}}, \tag{3.4}$$

in our notation, this represents Newtonian viscous flow, with $\dot{\boldsymbol{\varepsilon}}$ being the stretching tensor and η_1 being the viscosity coefficient. The above equation can be regarded as the simplest rheological model for fluid-like behavior. Let us then consider some other basic rheological models based on the general Eq. (3.3). in which if η_0 and η_1 are both non-zero, whilst the other constants are zero, Kelvin model, one of the basic rheological models, can be obtained:

$$\boldsymbol{\sigma}=\mu_0\boldsymbol{\varepsilon}+\mu_1\dot{\boldsymbol{\varepsilon}}, \tag{3.5}$$

where η_0 a modulus of elasticity. Kelvin model, also known as Voigt model, represents a viscoelastic material having the properties both of elasticity and viscosity. It can be regarded as a combination of the Hookean model and the Newtonian model as well.

Another very simple model is so-called Maxwell model. The differential equation of the model is obtained by making μ_1 and η_1 the only non-zero parameters

$$\boldsymbol{\sigma} + \mu_1 \dot{\boldsymbol{\sigma}} = \eta_1 \dot{\boldsymbol{\varepsilon}} \tag{3.6}$$

With strain rate $\dot{\boldsymbol{\varepsilon}}$ in Eq.(3.6) being zero, equation (3.6) represents a relaxation test. Therefore, the meaning of μ_1 can be identified as relaxation time. Noted that the hypoplastic Eq.(2.1) has a similar construction with Maxwell viscous flow.

The next level of complexity in the framework of Eq.(3.3) is to make three of the material parameters non zero. More specifically, if μ_1, η_1 and η_2 are taken to be non-zero, the Jeffreys model has been obtained. In the present notation, the equation is presented in the following form.

$$\boldsymbol{\sigma} + \mu_1 \dot{\boldsymbol{\sigma}} = \eta_1 \dot{\boldsymbol{\varepsilon}} + \eta_2 \ddot{\boldsymbol{\varepsilon}}, \tag{3.7}$$

It is worth to note that the Kelvin model and Maxwell model and can be regarded as special cases of the Jeffreys model. We note with interest that Jeffreys model has been used for a dilute suspension of solid elastic spheres in a viscous liquid by Fröhlich and Sack (1946) and a dilute emulsion of incompressible viscous liquid by Oldroyd (1953).

3.4 Extended H-B model for viscous behaviors

The Jeffreys's model can be decomposed into two parts, with one part denoting the Newtonian flow, and the other part denoting the contribution of strain acceleration. The later part can be formally regarded as the time differentiation of the former part provided the viscosity coefficient η_2 is constant. In this work, we need to consider the contribution of the strain acceleration to the viscous behaviors of granular materials, so that the later part is chosen as a possible candidate for the viscous model. Hence, the constitutive equation for the viscous part can be expressed by the following isotropic function:

$$\mathring{\boldsymbol{\sigma}}_v = H(\dot{\varepsilon}, \mathring{\varepsilon}) = \eta \mathring{\boldsymbol{\varepsilon}} \tag{3.8}$$

where $\mathring{\boldsymbol{\varepsilon}}$ is the Jaumann stretching-rate tensor and can be obtain according to the scheme in Eq. (2.2).

$$\mathring{\boldsymbol{\varepsilon}} = \ddot{\boldsymbol{\varepsilon}} + \dot{\boldsymbol{\varepsilon}} \cdot \boldsymbol{\omega} - \boldsymbol{\omega} \cdot \dot{\boldsymbol{\varepsilon}}, \tag{3.9}$$

The constant η is defined as functions of strain rate in the following form

$$\eta = \tilde{\alpha}_i(I_{\dot{\varepsilon}}, II_{\dot{\varepsilon}}, III_{\dot{\varepsilon}}, \|\dot{\boldsymbol{\varepsilon}}\|...), \qquad i = 1, ..., m \tag{3.10}$$

where I, II III are invariants of strain rate tensor defined as $I_{\dot{\varepsilon}} = \mathrm{tr}(\dot{\boldsymbol{\varepsilon}})$, $\quad II_{\dot{\varepsilon}} = [\mathrm{tr}(\dot{\boldsymbol{\varepsilon}})^2 - \mathrm{tr}(\dot{\boldsymbol{\varepsilon}}^2)]/2$, and $III_{\dot{\varepsilon}} = det\dot{\boldsymbol{\varepsilon}}$.

Note that the inclusion of high temporal derivative of strain rate tensor in Eq. (3.8) requires the specification of an initial value for $\dot{\boldsymbol{\varepsilon}}$. This can be compared to the specification of the initial speed in an accelerated motion. Before considering in depth the complete form of the fluid model, let us turn back to consider the normal stress effects. We assume that the following terms may be used to compile a workable constitutive equation.

$$\mathring{\boldsymbol{\sigma}}_v = \eta_1 \mathring{\boldsymbol{\varepsilon}} + \eta_2(\dot{\boldsymbol{\varepsilon}}\mathring{\boldsymbol{\varepsilon}} + \mathring{\boldsymbol{\varepsilon}}\dot{\boldsymbol{\varepsilon}}), \tag{3.11}$$

In order to demonstrate the normal-stress effects, we consider a steady simple shear flow where the rectangular components of $\dot{\boldsymbol{\varepsilon}}$ takes the following form:

$$\dot{\boldsymbol{\varepsilon}} = \begin{bmatrix} 0 & \dot{\gamma} & 0 \\ \dot{\gamma} & 0 & 0 \\ 0 & 0 & 0 \end{bmatrix}, \tag{3.12}$$

Making use of Eq.(3.9), we obtained the terms $\mathring{\boldsymbol{\varepsilon}}$ and $\dot{\boldsymbol{\varepsilon}}\mathring{\boldsymbol{\varepsilon}} + \mathring{\boldsymbol{\varepsilon}}\dot{\boldsymbol{\varepsilon}}$ as follows:

$$\mathring{\boldsymbol{\varepsilon}} = \begin{bmatrix} 0 & \ddot{\gamma} & 0 \\ \ddot{\gamma} & 0 & 0 \\ 0 & 0 & 0 \end{bmatrix} + 2\begin{bmatrix} -\dot{\gamma}^2 & 0 & 0 \\ 0 & \dot{\gamma}^2 & 0 \\ 0 & 0 & 0 \end{bmatrix}, \quad \dot{\boldsymbol{\varepsilon}}\mathring{\boldsymbol{\varepsilon}} + \mathring{\boldsymbol{\varepsilon}}\dot{\boldsymbol{\varepsilon}} = 2\begin{bmatrix} \dot{\gamma}\ddot{\gamma} & 0 & 0 \\ 0 & \dot{\gamma}\ddot{\gamma} & 0 \\ 0 & 0 & 0 \end{bmatrix} \tag{3.13}$$

Therefore, the relevant stress distribution for Eq.(3.11) can be expressed in terms of shear stress :

$$\tau_{xy} = \tau = \phi_1 \ddot{\gamma}, \quad \tau_{xz} = \tau_{yz} = 0, \tag{3.14}$$

and normal stress differences N_1 and N_2 :

$$N_1 = \tau_{xx} - \tau_{yy} = -4\phi_1\dot{\gamma}^2, \quad N_2 = \tau_{yy} - \tau_{zz} = -2(\phi_1\dot{\gamma}^2 + \phi_2\dot{\gamma}\ddot{\gamma}) \tag{3.15}$$

It is clear that the first normal stress is proportional to quadratic in shear rate, and the second normal stress is a function of shear rate and shear acceleration. Therefore, both the terms $\mathring{\boldsymbol{\varepsilon}}$ and $\dot{\boldsymbol{\varepsilon}}\mathring{\boldsymbol{\varepsilon}} + \mathring{\boldsymbol{\varepsilon}}\dot{\boldsymbol{\varepsilon}}$ can give rise to normal stresses in a steady shear flow.

Before proceeding to the much more difficult subject of the viscous model, it is helpful to consider some viscous behaviors of granular materials subjected to large viscous flow. Nushimura et al. (2002) investigated the rate-dependency of natural sand using cyclic torsion shear tests under drained condition. Fig. 3.1(a) shows the relation between shear strain rate and viscosity coefficient obtained from tests on Toyoura sand under a confining pressure of 30 kPa. It is observed that the viscosity coefficient η decreases with the increase of shear strain rate in an exponential manner. This decrease of viscosity with respect to increasing shear strain rate is termed as shear thinning, which is a common property for natural soils (Lal and Shukla, 2004). Fig. 3.1(b) shows the results of viscous stress under different shear strain rates, strain levels and confining pressures. The results reveal that the viscous stress depends both on the strain and the strain rate, while the effects of confining pressure on viscosity are less significant at low confining pressure. In common occasions of viscous granular deformation such as creep and geophysical flow, the confining pressure is usually low. Therefore, it is rational to assume that the viscous stress rate depends only on strain rate and strain acceleration.

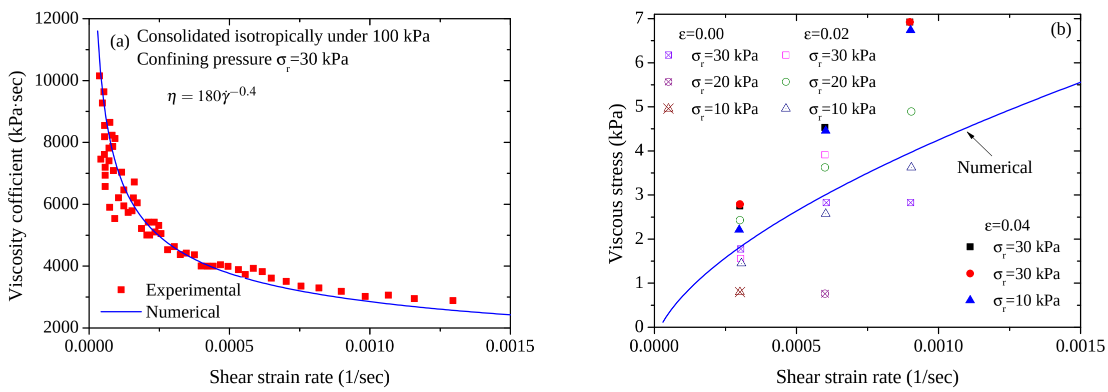

Figure 3.1 Relation between deviator strain rate and (a)viscosity coefficient,(b) viscous stress of Toyoura sand

Following the framework of Eq. (3.8), the form of the viscous coefficient is proposed as $\eta = k_v \dot{\gamma}^m$. Thus, the viscous stress rate defined by the strain rate and strain acceleration is obtained:

$$\dot{\tau}_v = k_v \dot{\gamma}^m \ddot{\gamma} \tag{3.16}$$

in which m is an index usually satisfying $m \leqslant 0$, k_v is the consistency index , which depends on the physical properties of the granular materials such as particle diameter, dry density and void ratio. Integration of Eq. (3.16) with respect to time, the total stress in terms of the frictional stress and strain rate can be obtained.

$$\tau = \tau_f + k_v \dot{\gamma}^{m+1} \tag{3.17}$$

This form of viscous model is known as Herschel-Bulkley model (H-B model), in which τ_f indicates the frictional stress. By using Eq. (3.17), the same tendency that viscous stress increases with increasing strain rate is shown in Fig. 3.1(b). The assumptions of the Herschel-Bulkley model are similar to those of the Bingham model for relatively high-viscosity fluids undergoing laminar flow (Huang and Garcia, 1998). Chen et al. (2004) recommended this model for use with fine-grained soils.

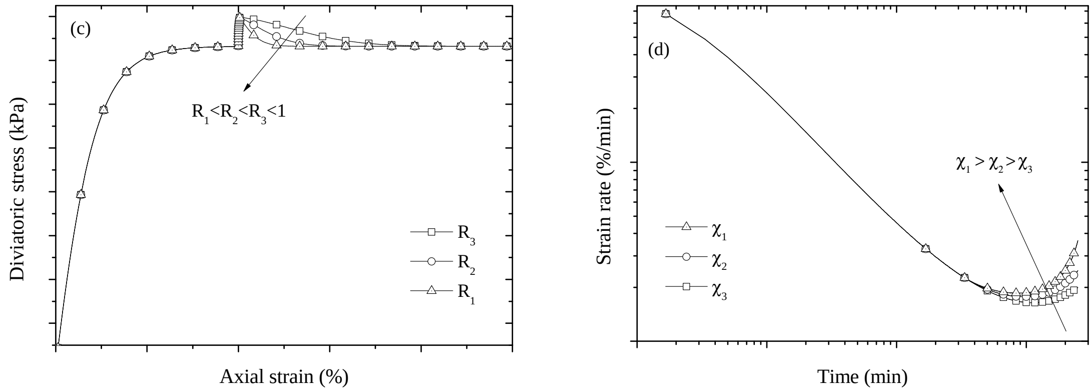

Figure 3.2 (a) The effect of decay factor R, and (b) the effect of parameter χ on the time of creep rupture

We extend the H-B model to three-dimensional to represent the viscous part of the new model. It takes the following formulation:

$$\mathring{\boldsymbol{\sigma}}_v = k_v \|\dot{\varepsilon}\|^m \mathring{\varepsilon} \tag{3.18}$$

Note that some poorly graded sands exhibit non-isotach behavior, that is the viscous stress decays with the increase in strain path. This behavior can be described by a decay factor. In this work, the viscous stress is assumed to decay with strain path when the acceleration vanishes. Thus, the viscous stress can be expressed as follows:

$$\boldsymbol{\sigma}_v = \begin{cases} k_v \int_{l_i}^{l} \|\dot{\varepsilon}\|^{(m)} \mathring{\varepsilon}\, d\tau & \text{if } \ddot{\varepsilon} \neq 0 \\ \boldsymbol{\sigma}_v^i R^{(l-l_i)} & \text{if } \ddot{\varepsilon} = 0 \end{cases} \tag{3.19}$$

in which the strain path l is defined by the the accumulated $\|\dot{\boldsymbol{\varepsilon}}\|$ with time: $l_i = \int_{t_0}^{t_i} \|\dot{\boldsymbol{\varepsilon}}\| d\tau$, and $\boldsymbol{\sigma}_v^i$ is the viscous stress that developed in the accelerated phase when strain path is l_i and then decayed until strain path is l. R is a positive constant smaller than unity. The decay factor R controls the speed of decaying of viscous stress at the constant strain rate test, , as observed in 3.2(a). Eq. (3.19) reveals that the viscous stress accumulates only in the process of non-uniform motion, such as soil creep and granular flow, in which the constant $R = 1$.

3.5 The new constitutive model and its formulation for creep

We combine Eq. (2.52) and Eq. (3.18). Thus, the complete form of the new model is obtained:

$$\mathring{\boldsymbol{\sigma}} = I_{se}\left[C_1 \mathrm{tr}(\boldsymbol{\sigma}_h)\dot{\boldsymbol{\varepsilon}} + C_2 \mathrm{tr}(\dot{\boldsymbol{\varepsilon}})\boldsymbol{\sigma}_h + C_3 \frac{\mathrm{tr}(\boldsymbol{\sigma}_h \cdot \dot{\boldsymbol{\varepsilon}})}{\mathrm{tr}\boldsymbol{\sigma}_h}\boldsymbol{\sigma}_h + C_4(\boldsymbol{\sigma}_h + \boldsymbol{\sigma}_h^*)\|\dot{\boldsymbol{\varepsilon}}\| I_e\right] + k_v(\|\dot{\varepsilon}\|)^m \mathring{\dot{\varepsilon}}, \quad (3.20)$$

Within the framework of Eq. (3.20), we consider the variation of deformation with vanishing stress rate ($\mathring{\boldsymbol{\sigma}} = 0$), namely creep, and we assume spin tensor $\boldsymbol{\omega}$ equal to zero at creep. Thus the creep acceleration can be obtained. Integrating of the creep acceleration with respect to time yields the integral form of the creep rate tensor:

$$\dot{\boldsymbol{\varepsilon}} = \int \frac{-I_{se}\|\dot{\varepsilon}\|^{-m}}{k_v}\left[C_1 \mathrm{tr}(\boldsymbol{\sigma}_h)\dot{\boldsymbol{\varepsilon}} + C_2 \mathrm{tr}(\dot{\boldsymbol{\varepsilon}})\boldsymbol{\sigma}_h + C_3 \frac{\mathrm{tr}(\boldsymbol{\sigma}_h \cdot \dot{\boldsymbol{\varepsilon}})}{\mathrm{tr}\boldsymbol{\sigma}_h}\boldsymbol{\sigma}_h + C_4(\boldsymbol{\sigma}_h + \boldsymbol{\sigma}_h^*)\|\dot{\boldsymbol{\varepsilon}}\| I_e\right] d\tau, \quad (3.21)$$

Constitutive parameters $C_i (i = 1, 2, 3, 4)$ and parameters related to the critical state factor I_e are first identified with triaxial compression test. The consistent coefficient k_v and flow index m can be identified by fitting tests as shown in Fig.3.1.

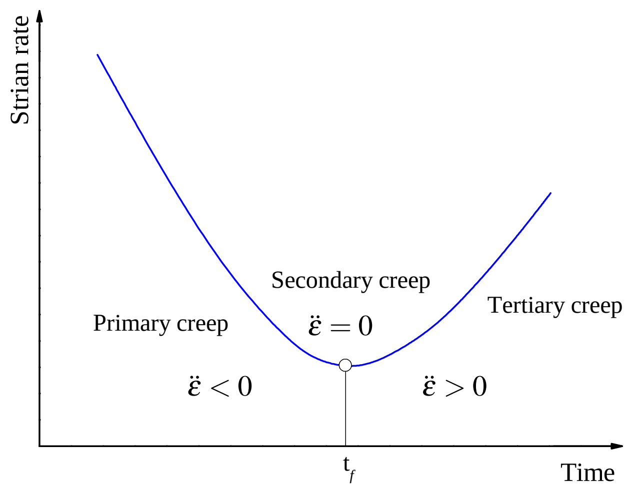

Figure 3.3 The evaluation of creep strain rate of sand over time, t_f denotes the creep failure time

It is known that the grains experience accelerated and decelerated motion over time at a creep. Although the interparticle velocity of grains is usually very slow, the interactions between individual particle display both Coulomb-type plastic and rheological deformation, and there is no evident phase transition from the frictional regime to viscous flow regime in the process of creep. Fig. 3.3 depicts the evaluation of strain rate over time during creep. As shown in Fig. 3.3 three stages of creep is characterized. In the primary stage, the strain rate decreases with negative strain acceleration. A very short secondary creep is defined as a point (also defined as creep failure point at the time (t_f) where the strain acceleration vanishes and the minimum creep strain rate $\dot{\varepsilon}_{min}$ is obtained. The tertiary creep starts when the strain acceleration becomes positive.

The viscous behaviors of granular materials can be attributed to several processes including progressive particle breakage due to intergranular contact stresses and the rearrangement of the grains with time due to micromechanical slip (Ghiabi and Selvadurai, 2009). Similar conclusions are reported by Di Prisco and Imposimato (1996); Gajo et al. (2000); Kuwano and Jardine (2002); Lade and Liu (1998), who also provide additional references. The creep rupture in the material can cause the decrease of the critical ratio as well. These processes become significant when the creep failure occurs in a material at accelerated creep stage. On the other hand, the accelerated creep can lead to the change of the critical state void ratio. Based on the microscopic description of the microstructure change of granular material in creep process, an additional parameter to account for the accelerated failure is introduced into Eq. (2.50)

$$e_{crt} = (e_0 - \chi l_a \frac{p}{p_a}) \exp\left[-\lambda (\frac{p}{p_a})^{\xi}\right] \tag{3.22}$$

where χ is a constitutive parameter, l_a is the acceleration path defined by the accumulated $||\ddot{\varepsilon}||$ after creep failure time, so it is activated only in the tertiary creep stage. The effect of χ on the creep rupture time is depicted in Fig. 3.2(b). It can be observed that the rupture time decrease with increasing χ. Since the critical state function I_e increases with decreasing critical void e_{crt}, both the increment of stress level and the acceleration path can contribute to the creep failure in the time-strain rate curve, as shown in Fig. 3.3.

3.6 Proposed model performance

In this section, the performance of the presented model is demonstrated. The viscous behaviors of granular materials including strain rate effects and creep are simulated using different tests on granular materials, e.g., a stepwise strain-rate triaxial test, creep tests under different stress levels on Toyoura sand, a stepwise strain rate triaxial test on Chiba gravelly soil.

3.6.1 Drained Stepwise strain rate tests

The abrupt change of strain in the stepwise strain rate tests is assumed to be achieved by an accelerated loading phase. Let us first consider the numerical form of the stepwise strain rate test with the hypoplastic constitutive model. Due to the symmetry, we have $\sigma_2 = \sigma_3$ and $\dot{\varepsilon}_2 = \dot{\varepsilon}_3$ in the whole loading and testing phase, and $\ddot{\varepsilon}_2 = \ddot{\varepsilon}_3$ in the loading phase. Then the stress rate, stress and strain rate and strain acceleration for triaxial test can be expressed in the matrix form:

$$\mathring{\boldsymbol{\sigma}} = \begin{pmatrix} \dot{\sigma}_1 & 0 & 0 \\ 0 & \dot{\sigma}_3 & 0 \\ 0 & 0 & \dot{\sigma}_3 \end{pmatrix}, \boldsymbol{\sigma} = \begin{pmatrix} \sigma_1 & 0 & 0 \\ 0 & \sigma_3 & 0 \\ 0 & 0 & \sigma_3 \end{pmatrix}, \dot{\boldsymbol{\varepsilon}} = \begin{pmatrix} \dot{\varepsilon}_1 & 0 & 0 \\ 0 & \dot{\varepsilon}_3 & 0 \\ 0 & 0 & \dot{\varepsilon}_3 \end{pmatrix}, \ddot{\boldsymbol{\varepsilon}} = \begin{pmatrix} \ddot{\varepsilon}_1 & 0 & 0 \\ 0 & \ddot{\varepsilon}_3 & 0 \\ 0 & 0 & \ddot{\varepsilon}_3 \end{pmatrix},$$

The simulation is carried out according to the following procedures: In the loading phase, the prescribed rate of strain is assumed to be achieved by conducting an acceleration process, in which the axial acceleration of strain is constant while the radial acceleration is various. So the governing differential equations for the triaxial test can be obtained by substituting the above matrix into constitutive Eq. (3.20):

$$\begin{aligned} \dot{\sigma}_1 = I_{se}\Big[&C_1(\sigma_{h1}+2\sigma_{h3})\dot{\varepsilon}_1 + C_2(\dot{\varepsilon}_1+2\dot{\varepsilon}_3)\sigma_{h1} + C_3\frac{\sigma_{h1}\dot{\varepsilon}_1+2\sigma_{h3}\dot{\varepsilon}_3}{\sigma_{h1}+2\sigma_{h3}}\sigma_{h1}+ \\ &I_eC_4(\sigma_{h1}+\sigma_{h1}^*)\sqrt{\dot{\varepsilon}_1^2+2\dot{\varepsilon}_3^2}\,\Big] + k_v(\sqrt{\dot{\varepsilon}_1^2+2\dot{\varepsilon}_3^2})^{m-1}\ddot{\varepsilon}_1 \end{aligned} \tag{3.23}$$

$$\begin{aligned} \dot{\sigma}_3 = I_{se}\Big[&C_1(\sigma_{h1}+2\sigma_{h3})\dot{\varepsilon}_3 + C_2(\dot{\varepsilon}_1+2\dot{\varepsilon}_3)\sigma_{h3} + C_3\frac{\sigma_{h1}\dot{\varepsilon}_1+2\sigma_{h3}\dot{\varepsilon}_3}{\sigma_{h1}+2\sigma_{h3}}\sigma_{h3}+ \\ &I_eC_4(\sigma_{h3}+\sigma_{h3}^*)\sqrt{\dot{\varepsilon}_1^2+2\dot{\varepsilon}_3^2}\,\Big] + k_v(\sqrt{\dot{\varepsilon}_1^2+2\dot{\varepsilon}_3^2})^{m-1}\ddot{\varepsilon}_3 \end{aligned} \tag{3.24}$$

The equation (3.23) and (3.24) contains six unkonwns, namely $\dot{\sigma}_1, \dot{\sigma}_3, \dot{\varepsilon}_1, \dot{\varepsilon}_3, \ddot{\varepsilon}_1$ and $\ddot{\varepsilon}_3$. We start the **accelerated phase** from an initial state $(\sigma_{i1}, \sigma_{i3})$,$(\dot{\varepsilon}_{i1}, \dot{\varepsilon}_{i3})$. For the stepwise strain rate test with constant confining pressure and acceleration of strain, three of the six unkonwns can be specified. So we have $\dot{\sigma}_3 = 0$ and $\ddot{\varepsilon}_1 = const.$, respectively. At the initial time t_i, the strain rate $\dot{\varepsilon}_1 = \dot{\varepsilon}_{i1}$, if we assume a time step Δt in the accelerated phase, the strain rate $\dot{\varepsilon}_1$ can be determined as $\dot{\varepsilon}_1 = \dot{\varepsilon}_{i1} + \ddot{\varepsilon}_1\Delta t$. Substitution of $\dot{\sigma}_3 = 0$ into equation (3.24), and integration of the acceleration of strain, we have the integral form of radial strain rate.

$$\dot{\varepsilon}_3 = \int_{t_i}^{t} \frac{-I_{se}(\sqrt{\dot{\varepsilon}_1^2+2\dot{\varepsilon}_3^2})^{-m}}{k_v}\Big[C_1(\sigma_{h1}+2\sigma_{h3})\dot{\varepsilon}_3 + C_2(\dot{\varepsilon}_1+2\dot{\varepsilon}_3)\sigma_{h3}+ \tag{3.25}$$

$$C_3\frac{\sigma_{h1}\dot{\varepsilon}_1+2\sigma_{h3}\dot{\varepsilon}_3}{\sigma_{h1}+2\sigma_{h3}}\sigma_{h3} + I_eC_4(\sigma_{h3}+\sigma_{h3}^*)\sqrt{\dot{\varepsilon}_1^2+2\dot{\varepsilon}_3^2}\,\Big]d\tau \tag{3.26}$$

The above equation can be integrated by assuming a time step Δt, then we obtain the radial acceleration of stain $\ddot{\varepsilon}_3$. The stretching tensor obtained in this way will be inserted into Eq.(3.23) to get the axial stress rate $\dot{\sigma}_1$. The frictional stresses and viscous stresses are then updated for the next time step. In general, the updating of stress for a time step Δt can be performed as follows:

$$\begin{aligned}\boldsymbol{\sigma}_f(t+\Delta t) &= \boldsymbol{\sigma}_f(t) + \int_t^{t+\Delta t} \dot{\boldsymbol{\sigma}}_f[\boldsymbol{\sigma}_f(\tau), \dot{\boldsymbol{\varepsilon}}(\tau)]d\tau \\ \boldsymbol{\sigma}_v(t+\Delta t) &= \boldsymbol{\sigma}_v(t) + \int_t^{t+\Delta t} \dot{\boldsymbol{\sigma}}_v[\dot{\boldsymbol{\varepsilon}}(\tau), \ddot{\boldsymbol{\varepsilon}}(\tau)]d\tau \\ \boldsymbol{\sigma}(t+\Delta t) &= \boldsymbol{\sigma}_f(t+\Delta t) + \boldsymbol{\sigma}_v(t+\Delta t)\end{aligned} \tag{3.27}$$

In accelerated phase, the viscous stress $\boldsymbol{\sigma}_v$ and the new strain rate $(\dot{\varepsilon}_1, \dot{\varepsilon}_3)$ for the constant strain rate test are obtained.

In the constant strain rate tests, we assume the strain acceleration vanishes, that is ($\ddot{\boldsymbol{\varepsilon}} = 0$), then the rate form Eq. (3.23) and (3.24) degrade to

$$\begin{aligned}\dot{\sigma}_{f1} = I_{se}\Big[&C_1(\sigma_{h1}+2\sigma_{h3})\dot{\varepsilon}_1 + C_2(\dot{\varepsilon}_1+2\dot{\varepsilon}_3)\sigma_{h1} + C_3\frac{\sigma_{h1}\dot{\varepsilon}_1+2\sigma_{h3}\dot{\varepsilon}_3}{\sigma_{h1}+2\sigma_{h3}}\sigma_{h1} + \\ &I_e C_4(\sigma_{h1}+\sigma_{h1}^*)\sqrt{\dot{\varepsilon}_1^2+2\dot{\varepsilon}_3^2}\,\Big]\end{aligned} \tag{3.28}$$

$$\begin{aligned}\dot{\sigma}_{f3} = I_{se}\Big[&C_1(\sigma_{h1}+2\sigma_{h3})\dot{\varepsilon}_3 + C_2(\dot{\varepsilon}_1+2\dot{\varepsilon}_3)\sigma_{h3} + C_3\frac{\sigma_{h1}\dot{\varepsilon}_1+2\sigma_{h3}\dot{\varepsilon}_3}{\sigma_{h1}+2\sigma_{h3}}\sigma_{h3} + \\ &I_e C_4(\sigma_{h3}+\sigma_{h3}^*)\sqrt{\dot{\varepsilon}_1^2+2\dot{\varepsilon}_3^2}\,\Big]\end{aligned} \tag{3.29}$$

The updating of stress for a time step Δt can be performed in the same way as illustrated above.

$$\boldsymbol{\sigma}(t+\Delta t) = \boldsymbol{\sigma}_f(t) + \int_t^{t+\Delta t} \dot{\boldsymbol{\sigma}}_f[\boldsymbol{\sigma}_f(\tau), \dot{\boldsymbol{\varepsilon}}(\tau)]d\tau + \boldsymbol{\sigma}_v \tag{3.30}$$

Due to the complexity of the constitutive equation, the above integral can be rarely performed analytically (Wu and Niemunis, 1996). Instead, a simple one-step, Euler forward scheme is adopted to integrate the above equation.

To investigate the rate effects of granular materials, Kiyota and Tatsuoka (2006) have carried out a series of drained triaxial tests on Toyoura sand. The specimen was consolidated up to an effective confining pressure equal to 400 kPa in the drained triaxial condition. The sample achieved an initial void ratio of $e_i = 0.912$ after the consolidation, then was subjected to a prescribed loading path. In these tests, the axial strain rate was stepwise changed many times during otherwise monotonic loading. The variated strain rates are taken as $\dot{\varepsilon}_0/10$, $\dot{\varepsilon}_0$, $10\dot{\varepsilon}_0$ and $20\dot{\varepsilon}_0$, with the strain rate $\dot{\varepsilon}_0 = 0.0125$ %/min in the monotonic loading. These strain rates are small enough to make sure that no excessive pore pressure is developed; thus, the drained condition is guaranteed.

In the stepwise strain rate tests, the viscous property is quantified mainly by changing stepwise the axial strain rate many times during otherwise monotonic loading at a con-

Table 3.1 The strain acceleration for simulation of stepwise strain rate tests on toyoura sand

Acc.($\%/sec^2$)	$\ddot{\varepsilon}_1$	$\ddot{\varepsilon}_2$	$\ddot{\varepsilon}_3$	$\ddot{\varepsilon}_4$	$\ddot{\varepsilon}_5$	$\ddot{\varepsilon}_6$
Value	-0.5	50.5	-50.5	0.5	-30.1	30.1

stant axial strain rate. In the simulation, we assume the samples experienced two different loading path. namely: (I) constant strain rate phase, and (II) accelerated strain rate phase. Correspondingly, the viscous stress increased nonlinearly, accompanied by the increase of frictional stress. Parameters presented in Table 2.6 are used for modeling the frictional stress. The other parameters for the viscous model are: $k_v = 180$ kPa·sec^m, $m = -0.4$ and $R = 0.12$. In addition, the second time derivative of strain in Eq. (3.18) is required to change the strain rate at each step. In this work, the strain accelerations presented in Table 4.5 are obtained by fitting the stepwise strain rate tests.

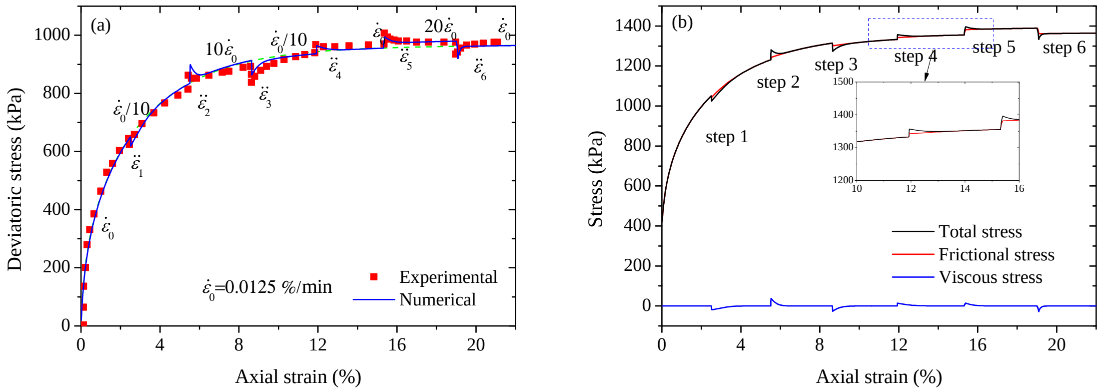

Figure 3.4 Comparison of data and simulations for stepwise monotonic loading drained triaxial tests on isotropically consolidated samples of Toyoura sand (p_i =400 kPa).

Together with the experimental results, the simulated stepwise strain rate tests on Toyoura sand are presented in Fig. 3.4. The experimental results show that the stress changes temporarily when the constant strain rate was changed stepwise. This feature is known as non-isotach behavior. The simulated strain-stress curve is in agreement with the experimentally measured curve except that the model underestimates the stress at the initial stage of the test. The constitutive predictions in Fig. 3.4(a) show that the model is capable of capturing the stress-strain relation under the drained condition and modeling the non-isotach strain effect, both in constant strain rate and accelerated strain rate conditions. The evolution of viscous, frictional and the total stresses with axial strain is presented in Fig. 3.4(b). The viscous stress decreases /increases in the deaccelerating/accelerating phase, and decay in the constant strain rate phase. The viscous stress change may influence the frictional stress.

In particular, as shown in step 5 with $20\dot{\varepsilon}$, the frictional stress experienced a big increase, while it drops when the strain rate decreases from $20\dot{\varepsilon}$ to $\dot{\varepsilon}$

Table 3.2 Values of material parametets for Chiba gravelly soil

Para.	C_1	C_2	C_3	C_4	e_0	λ	ξ	α	β	k_v	m	R
Value	-124	-410.4	-457.1	-238.1	0.24	0.019	0.071	0.5	50	205	-0.49	0.98

Table 3.3 Strain accelerations for simulating drained stepwise tests on Chiba gravelly soil

Acc.($\%/sec^2$)	$\ddot{\varepsilon}_1$	$\ddot{\varepsilon}_2$	$\ddot{\varepsilon}_3$	$\ddot{\varepsilon}_4$	$\ddot{\varepsilon}_5$	$\ddot{\varepsilon}_6$	$\ddot{\varepsilon}_7$	$\ddot{\varepsilon}_8$	$\ddot{\varepsilon}_9$	$\ddot{\varepsilon}_{10}$
Value	-1.1	20.5	-50.1	20.5	-15.5	-1.1	20.5	-50.1	15.5	-20.5

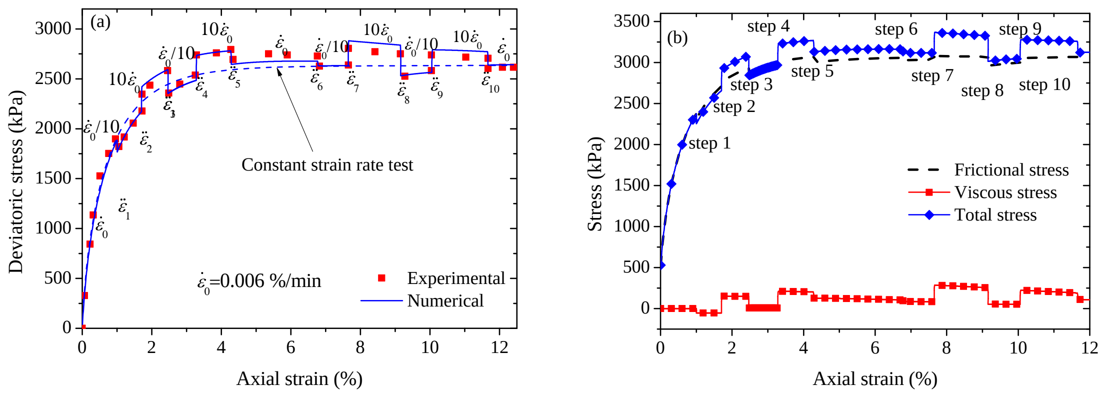

Figure 3.5 Comparison of data and simulations for stepwise monotonic loading drained triaxial tests on isotropically consolidated samples of gravelly soil (p_i =490 kPa).

In the previous sections, the present model has been evaluated by drained stepwise strain rate tests on Toyoura sand. Here, we further evaluate the model on gravelly soil by (AnhDan et al., 2006). A well-graded quarry gravelly soil of sandstone was used. The sample was prepared to achieve a high dry density in a range of 2.2-2.3 g/cm^3 and a void ratio of $e_i = 0.19$, which is close to typical field values of this type of gravelly soil. The parameters used in this simulation are given in Table 4.7. Likewise, a set of strain accelerations is required in this simulation, as shown in Table 3.3. Fig. (3.5) presents the numerical results along with the experimental data. It can be observed that the proposed model gives a good prediction of the strain rate effects for gravelly soil. Owing to the properties of the gravelly soils, the viscous stress does not decay during the constant strain rate period. Therefore, the presented model is capable of modeling both the isotach and non-isotach behavior of granular materials.

3.6.2 Drained triaxial creep tests with constant stress

The conventional drained triaxial creep tests can be conducted by applying a prescribed deviatoric stress on the confined sample. Usually, the process of achieving this prescribed stress state is not taken into account. From a constitutive modeling point of view, the prescribed stress state is applied instantaneously, the realistic process of applying this stress state is out of the scope of most constitutive models. In the numerical test, creep is referred to as the variation of deformation under vanishing stress rate($\dot{\boldsymbol{\sigma}} = 0$). According to this definition, we can give the expression of stress rate, stress and strain rate for drained triaxial creep test in the matrix form:

$$\dot{\boldsymbol{\sigma}} = \begin{pmatrix} 0 & 0 & 0 \\ 0 & 0 & 0 \\ 0 & 0 & 0 \end{pmatrix}, \boldsymbol{\sigma} = \begin{pmatrix} \sigma_1 & 0 & 0 \\ 0 & \sigma_3 & 0 \\ 0 & 0 & \sigma_3 \end{pmatrix}, \dot{\boldsymbol{\varepsilon}} = \begin{pmatrix} \dot{\varepsilon}_1 & 0 & 0 \\ 0 & \dot{\varepsilon}_3 & 0 \\ 0 & 0 & \dot{\varepsilon}_3 \end{pmatrix}, \ddot{\boldsymbol{\varepsilon}} = \begin{pmatrix} \ddot{\varepsilon}_1 & 0 & 0 \\ 0 & \ddot{\varepsilon}_3 & 0 \\ 0 & 0 & \ddot{\varepsilon}_3 \end{pmatrix}$$

Contrary to the conventional view, we assume that there is an accelerated loading phase to achieve the testing state, in which both the initial frictional and viscous stresses are accumulated. After the loading phase, the initial viscous stresses $(\sigma_{v1}, \sigma_{v2})$ and the initial strain rate $(\varepsilon_1, \varepsilon_3)$ are obtained. So the strain accelerations components in the drained triaxial creep tests can be obtained by substituting the above matrices into constitutive Eq. (3.20).

$$\ddot{\varepsilon}_i = \frac{-I_{se}(\sqrt{\dot{\varepsilon}_1^2 + 2\dot{\varepsilon}_3^2})^{-m}}{k_v} \dot{\sigma}_{hi} \tag{3.31}$$

where $\dot{\sigma}_{hi}$, $i = 1,3$ is the corresponding stress rate, which can be obtained by substituting the above matrices into Eq. (2.48). Integration of the Eq. (3.31) , both the axial and radial strain rate can be obtained. Correspondingly, the viscous stress rate can be obtained as well. Then the viscous and frictional stresses can be updated by using Eq. (3.1).

Matsushita (1999) performed a series of drained triaxial compression creep tests for a period of 20 minutes under a constant mean effective principal stress of 147.0 kPa. Remolded Toyoura sand was used in these tests after removing grains coarser than 0.297 mm and finer than 0.074 mm by sieving. The properties of the sand were as follows: effective diameter D_{10} = 0.14 mm, uniformity coefficient C_u = 1.47, specific gravity of solids G_s = 2.635. All samples for the creep tests were prepared in an attempt to have the same initial void ratio by applying the same isotropic pressure. The initial void ratio is e_i = 0.840. In the creep tests, the samples were subjected to several levels of deviatoric stresses under drained condition.

Since remolded Toyoura sand was used in the creep tests, a new set of parameters shown in Table 3.4 are used in this simulation. The material parameters are obtained from a triaxial

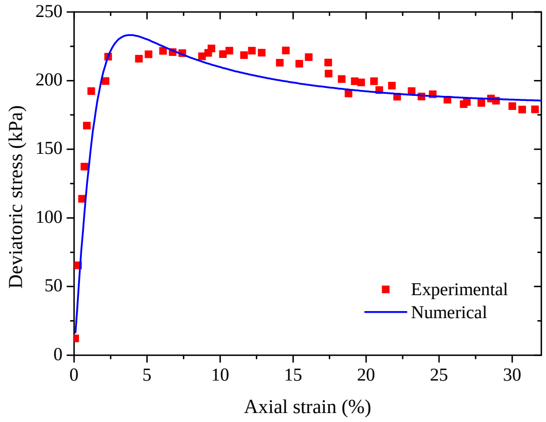

Figure 3.6 The strain-stress relationship of Toyoura sand in drained triaxial test (p_i =147 kPa)

Table 3.4 Values of material parameters for remolded Toyoyra sand

Para.	C_1	C_2	C_3	C_4	e_{co}	λ	ξ	α	β	k_v	m	χ
Value	-30.3	-93.8	-441.7	-115.7	0.947	0.022	0.51	1.0	10	35.5	-0.38	1.08

compression test, as shown in Fig.5.4. The exponent m and the consistency index k_v are obtained by fitting the creep tests. In addition, the the same strain acceleration $\ddot{\varepsilon} = 1.0 \times 10^{-4}$ $\%/sec^2$ is used in the simulation of loading phases.

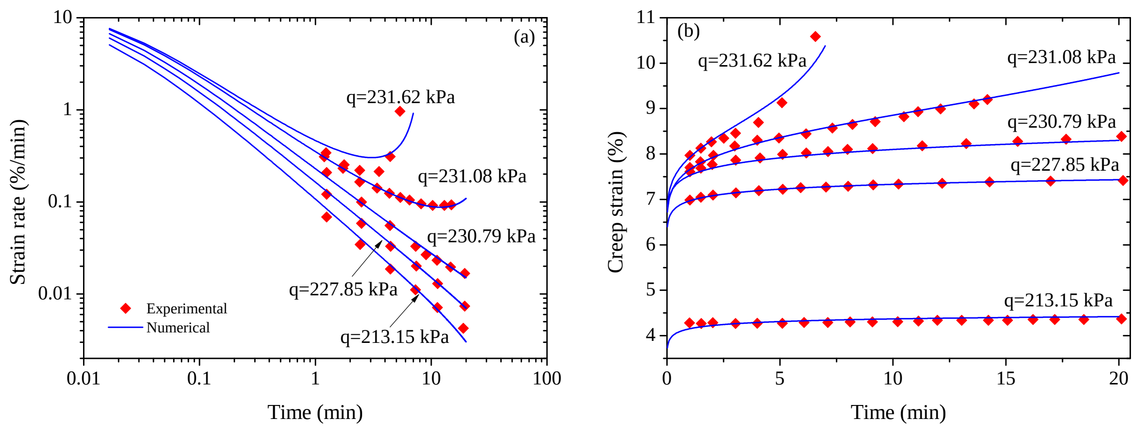

Figure 3.7 Comparison of data and simulations for drained creep triaxial tests on Toyoura sand (p_i =147 kPa)

Fig. 3.7 presents the creep strain rate and creep strain over time together with the numerical results. Both predicted creep rate (Fig. 3.7(a)) and creep strain (Fig. 3.7(b)) agree well with the experimental results. . In Fig. 3.7(a)), It can be observed that the relationships for different creep stresses are expressed as straight lines, except for the creep stresses greater than a certain value, such as deviatoric stress q =231.08 kPa and 231.62 kPa. At the outset of creep, the creep rates decay in a linear manner and all the lines are approximately parallel to each other. In other words, all the samples in this study exhibit a similar creep rate change, i.e., the same slope, which is controlled by the constant m. This can be compared to the constant defined by m defined by Sing and Mitchell (1968).

$$m = -(\frac{\Delta \log \dot{\varepsilon}}{\Delta \log t} - 1) \tag{3.32}$$

In addition, a higher deviatoric stress q applied during creep will give a greater creep rate. For the case, q =231.08 kPa, typical three stage creep of sand is characterized. The sand packing starts to creep with a primary creep, which is followed by a very short secondary creep and a tertiary creep. In the primary creep, the strain rate decreases continuously from the outset of creep until it reaches a minimum, where is usually defined as the time of creep failure. After creep failure, the strain rate increases dramatically until creep rupture. Accordingly, the creep strain increases rapidly, as shown in Fig. 3.7(b).

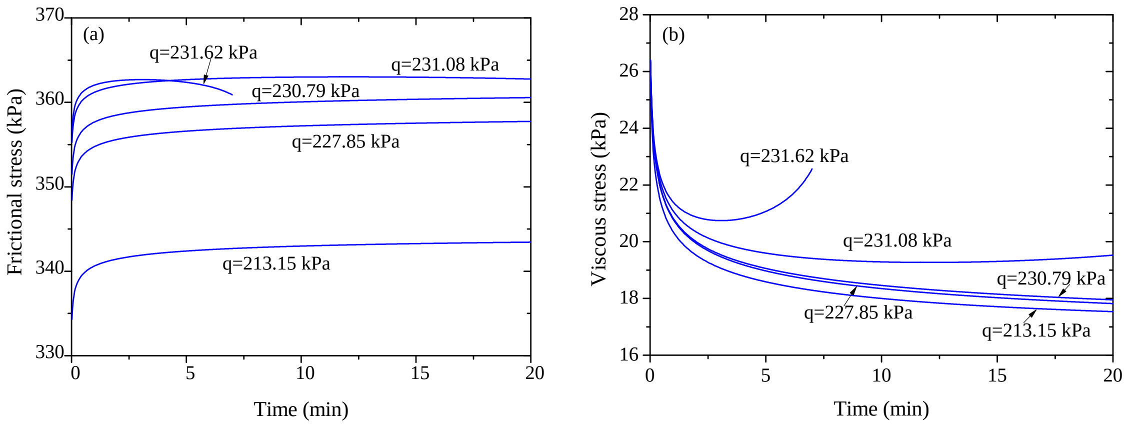

Figure 3.8 Simulation results with various levels deviatoric stresses: (a)the frictional and (b)viscous stresses over time

The evolution of the frictional stress and the viscous stress over time at different stress levels are shown in Fig. 7. For the case q =231.08 kPa, it can seem from 3.8(a) that the three stages, corresponding to the primary, secondary, and tertiary creep stage, are also recognizable. The frictional stresses increase at the primary creep stage. Then it reaches a maximum corresponding to the inflection point in the creep curve, which represents the second stage. Accordingly, in the third stage, the frictional stress decrease until the end of creep test when creep rupture occurs. For lower creep stress levels, for example, below 231 kPa, only the first stage of creep can be observed and the change of frictional stress after the onset of creep is negligible. However, the frictional stress continuously increases and gets infinitely close to a constant value. Correspondingly, the viscous stresses evaluate in a converse manner to the frictional stresses, as shown in 3.8(b). Obviously, the balance between the frictional and viscous stresses will maintain the total stress constant, which is required by the creep test.

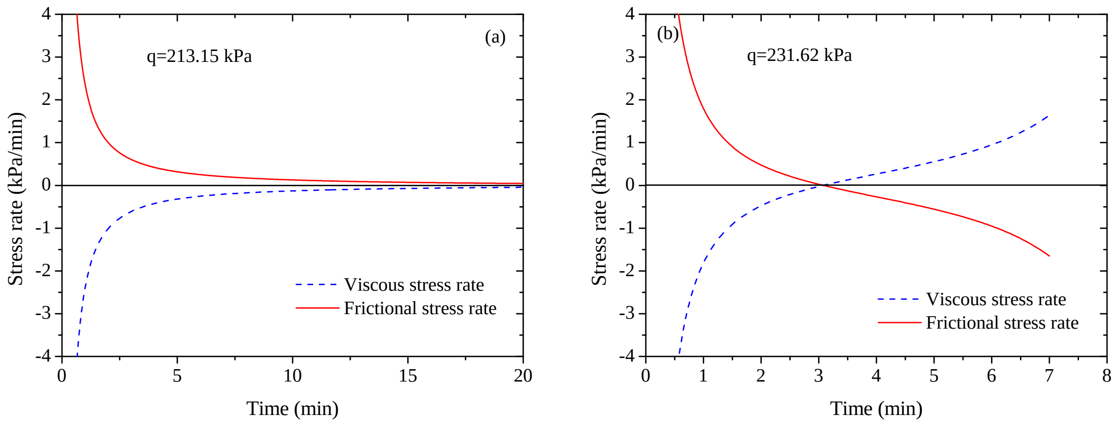

Figure 3.9 The evaluation of frictional and viscous stress rates over time (a) $q = 213.15$ kPa, and (b) $q = 231.62$ kPa

Because the total stress rate in the proposed model is composed of a frictional stress rate and a viscous stress rate, as shown in Eq. (3.2), the evaluation of the frictional and viscous stress rates can also be analyzed during the creep test. Fig. 8 presents the changes in frictional and viscous stress rates over time under creep stresses and q=231.62 kPa. As can seem from Fig. 3.9(a) that the frictional stress decrease throughout the three typical creep stage. Likewise, three stages of frictional stress rate can also be characterized. The frictional stress decrease from a positive value to null in the first stage, and an approximate null in the second stage, and then decrease from null to a negative value in the third stage. Fig. 3.9(b) depicts the change of frictional and viscous stress under creep stress q=213.15 kPa. For this case, there is no failure taking place in the sample, and the frictional stress decrease to approaches null. Fig. 3.9(a) and Fig. Fig. 3.9(b) also show that the change pattern of the viscous stress rate is opposite to that of the frictional stress rate. This will give rise to a vanishing total stress rate and remain the total stress constant at the creep.

The point of minimum creep rate, $\dot{\varepsilon}_{min}$ is also defined as the onset of tertiary creep hereinafter which the creep rate accelerates rapidly and the sample eventually undergoes creep rupture or creep failure. An alternative way to denote $\dot{\varepsilon}_{min}$ is the point where the strain acceleration $\ddot{\varepsilon} = 0$. Fig. 3.10 presents the evolution of the strain acceleration over time at different stress levels. The strain acceleration can be also evaluated from Eq. (3.31). Note that the frictional stress rate is positive at the onset of creep. Therefore, the strain accelerations are negative for all stress levels at the beginning of the creep tests. At the

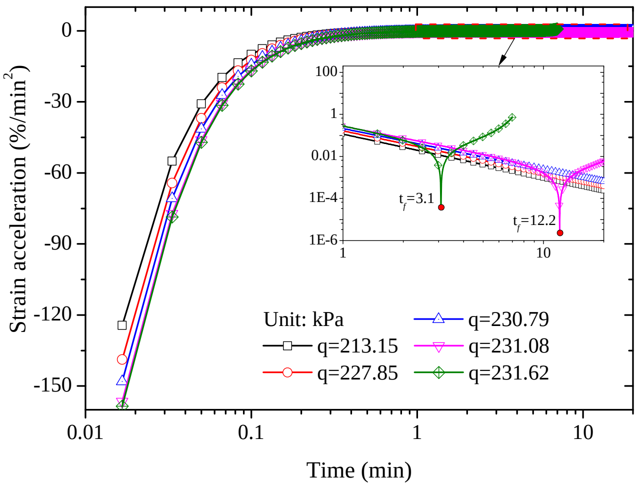

Figure 3.10 Simulation results with various levels deviatoric stresses: the creep acceleration over time. The absolute value of the strain acceleration is plotted in a log-log scale in which the creep failure time t_f is signed

beginning of creep tests, the strain accelerations increase conterminously. For relative low-stress levels, the strain acceleration will approach zero asymptotically but cannot exceed null. For example, at creep stress q=213.15 kPa, no matter how long the test last, creep failure will not occur. This can be evidenced by Fig. 3.7(a), in which the strain rate is concave-downward for q=213.15 kPa. For relative high creep stresses, such as q =231.06 kPa and 231.62 kPa, creep failures have occurred in the samples. It is observed that the strain accelerations surpass zero and become positive if we zoom into Fig. 3.10 and plot the absolute value of the strain accelerations in a log-log scale. In addition, the time to failure decrease from t_f = 12.2 min to t_f = 3.1 min with the creep stress level increase from q =231.06 kPa to 231.62 kPa, as shown in the log plot. According to Eq. (3.18), the positive strain accelerations will lead to increase of the viscous stress, and may eventually lead to creep rupture. It can be concluded that the coupling of viscous stress and frictional stress can give rise to strain acceleration in granular materials at the creep. In return, the evaluation of acceleration can affect the frictional and viscous stresses and results in the three stages of creep in granular materials.

3.7 Conclusion

A new constitutive model is proposed for modeling viscous behaviors of granular materials. The model consists of two components representing respectively the frictional and viscous stresses in granular media. The development of frictional stress is modeled using a critical state hypoplastic constitutive model, which is able to describe the friction-induced behaviors of granular materials. The viscous part is a differential form of the Herschel-Bulkley (HB) model with a high order term, which is used to account for the effect of strain acceleration.

Drained stepwise strain rate triaxial tests on Toyoura sand and gravelly soil and drained triaxial creep tests on Toyoura sand are modeled to evaluate the present model. Comparisons between experimental results and numerical results show that the capability of the model in describing both the strain rate effects and creep behaviors of granular materials. In the stepwise strain rate tests, The non-isotach behavior of granular can be successfully modeled by introducing the strain acceleration. Moreover, in the creep test, the coupling between the frictional stress and the viscous stress gives rise to the evolution of strain acceleration. As a consequence, three stages of creep including primary, secondary and tertiary creep can be described in a unified way.

It is worth to note that the proposed model can not only describe the creep behavior of the granular material but can also predict creep behavior of cohesive soil by introducing a cohesive-related structure tensor.

Chapter 4

Study on the numerical integrations of the hypoplastic model

4.1 Introduction

Hypoplasticity is a particular class of incrementally non-linear constitutive models (Mašín and Khalili, 2008a). Unlike elastic-plastic models, there is no clear boundary between elastic and plastic deformations in hypoplastic models. Moreover, explicit pre-definition of yield and potential surfaces are not needed, which have been proved to be by-produced of the particular assumptions for their constitutive equations (Wu and Bauer, 1994). The stress rate is related to the strain rate through a well-defined tensorial function, which is generally nonlinear in the strain rate. The predictive capabilities of hypoplastic models compete with those of advanced models based on elastoplastic frameworks, yet they only require a nonlinear tensorial equation, which holds equally for loading and unloading, and a single set of parameters. This, together with the availability of robust algorithms for their implementation into numerical codes, makes hypoplasticity a promising approach for modeling the non-linear behavior of soils (Mašín and Khalili, 2008b). However, due to their complex structure, hypoplastic models exhibit strongly non-linear behavior and thus require carefully-crafted algorithms to avoid unreliable results.

Though numerous references are available on the numerical implementation of conventional elastoplastic models, few works have been devoted to the hypoplastic constitutive models. Several numerical studies have been conducted to investigate the accuracy and efficiency of local integration schemes for hypoplastic models. Explicit Euler methods with constant step sizes were adopted in early works (Tejchman et al., 1999), while Roddeman (1997) discussed the θ-method for stress-strain integration. Later, Heeres and de Borst

(2000) considered implicit integration methods, and Fellin and Ostermann (2002); Fellin et al. (2009) proposed a method for generating the consistent tangent operator numerically. Tamagnini et al. (2000) systematically studied the behavior of explicit and implicit methods in the integration of CLoE hypoplastic models. A comparison of different integration schemes by Ding et al. (2015) concluded that the explicit methods with substepping and error control are the suitable ways for hypoplasticity.

It is well known that some hypoplstic models are characterized by the bound surface, which restricts the accessible stress state in a certain range and avoids unreasonable stress state occurring in the computation (Wu and Niemunis, 1997). Hence, it is usually assumed that there is no need to consider the crossing of the yield surface in an integration scheme. For a hypoplastic model, however, if the bound surface and the failure surface possess large difference, stress may surpass the yield surface and results in an accumulative error if there is no stress correction scheme. Thought the integration accuracy and efficiency can be enhanced using only explicit adaptive integration methods, the phenomenon that some stresses drift from the yield surface commonly exists in the analysis of boundary value problems using finite element method. Therefore, the adaptive explicit method must deal with the intersection of the yield surface to make sure that the updated stress states lie close to the yield surface. The intersection to some extent complicates the integration method, but it may cause significant errors if there is no dealing with the intersection.

In this chapter, the first key objective of the research is to study the stress integration methods for a simple constitutive model. Particularly, a stress correction is introduced to enhance these integration methods. The present chapter is therefore organized as follows. In section 4.2, the basic principles underlying the formulation of the constitutive equations for elastoplasticity and hypoplasticity are briefly outlined. Section 4.3 provides the detailed numerical equation and the strain stress integration of the hypoplastic constitutive model. Due to the intrinsic property of hypoplasticity, some stresses are accessible to surpass the yield surface. To overcome this shortcoming, a stress correction algorithms is adopted. In section 4.4, the performance of different integration methods as well as the stress correction scheme are demonstrated by performing a series of numerical simulation. Some concluding remarks and suggestions for further studies are finally given in section 4.5.

4.2 General finite element equation

4.2.1 Momentum balance and weak form

Let us consider a continuum Ω delineated by surface $\partial\Omega$ as shown in Fig.4.1. We assume that the boundary surface $\partial\Omega$ can be decomposed into two parts: Dirichlet and Neumann boundary $\partial\Omega_v$, where a velocity $\boldsymbol{v}$ is specified, and Neumann boundary $\partial\Omega_t$, where a surface traction $\boldsymbol{t}$ is prescribed. In addition, a body force $\boldsymbol{f}$ is specified in the whole body as well. We also assume the usual boundary can be expressed more succinctly by the following equations:

$$\partial\Omega = \overline{\partial\Omega_v \cup \partial\Omega_t}, \quad \Phi = \partial\Omega_v \cap \partial\Omega_t \tag{4.1}$$

where the superposed line denotes a closure.

For a body with given geometry, we know the applied loads, displacement boundary conditions, and material stress-strain law, the requirement for the finite element equations is to determine the displacement field for the body.

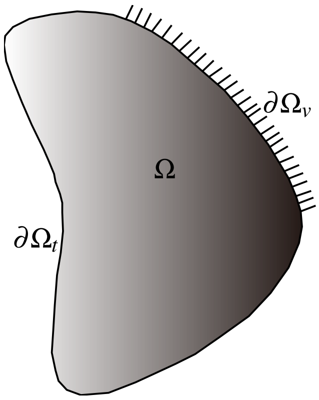

Figure 4.1 Definition of problem domain Ω , boundary $\partial\Omega_v$ and boundary $\partial\Omega_t$

For a linear continuum, the strong form consists of the balance of linear momentum and the traction boundary conditions. The balance of linear momentum takes the form:

$$\rho \frac{D\boldsymbol{v}}{Dt} - \boldsymbol{\nabla} \cdot \boldsymbol{\sigma} - \boldsymbol{f} = 0, \tag{4.2}$$

where D/Dt is the material time derivative, $\boldsymbol{v}$ is the solid velocity, $\boldsymbol{\sigma}$ is the Cauchy stress tensor, $\boldsymbol{f}$ is the body force , and $\boldsymbol{\nabla}$ is the symmetric component of the gradient operator. The relevant essential and natural boundary conditions are

$$\boldsymbol{v} = \bar{\boldsymbol{v}} \quad \text{on } \partial\Omega_v; \quad \boldsymbol{n} \cdot \boldsymbol{\sigma} = \bar{\boldsymbol{t}} \quad \text{on } \partial\Omega_t, \tag{4.3}$$

where $\boldsymbol{n}$ is the outward unit normal to boundary $\partial\Omega_t$, $\bar{\boldsymbol{v}}$ and $\bar{\boldsymbol{t}}$ are the prescribed line velocity and force traction vectors, respectively.

To develop the weak form of the momentum conservation laws, consider a set of trial functions

$$\mathscr{V} = \{\boldsymbol{v}|v_i \in H^1; \boldsymbol{v} = \bar{v} \quad \text{on } \partial\Omega_v\} \tag{4.4}$$

and a set of variations

$$\mathscr{W} = \{\boldsymbol{w}|w_i \in H^1; \boldsymbol{w} = 0 \quad \text{on } \partial\Omega_v\} \tag{4.5}$$

We want to find $\boldsymbol{v} \in \mathscr{V}$ such that for all $\boldsymbol{w} \in \mathscr{W}$,

$$\int_\Omega \boldsymbol{w} \cdot (\rho \frac{D\boldsymbol{v}}{Dt} - \boldsymbol{\nabla} \cdot \boldsymbol{\sigma} - \boldsymbol{f}) dV = 0, \tag{4.6}$$

Integrating by parts of the following term, we have

$$\int_\Omega \boldsymbol{w} \cdot (\boldsymbol{\nabla} \cdot \boldsymbol{\sigma}) dV = \int_\Omega \boldsymbol{\nabla} \cdot (\boldsymbol{\sigma}^{\mathrm{T}} \cdot \boldsymbol{w}) dV - \int_\Omega \boldsymbol{\sigma} : (\boldsymbol{\nabla} \boldsymbol{w}) dV \tag{4.7}$$

Using the divergence theorem and substituting Eq. (4.3), we have

$$\int_\Omega \boldsymbol{\nabla} \cdot (\boldsymbol{\sigma}^{\mathrm{T}} \cdot \boldsymbol{w}) dV = \int_{\partial\Omega_t} \boldsymbol{n} \cdot (\boldsymbol{\sigma}^{\mathrm{T}} \cdot \boldsymbol{w}) dA = \int_{\partial\Omega_t} \boldsymbol{w} \cdot \bar{\boldsymbol{t}} dA \tag{4.8}$$

By combination of the above three equations, we obtained the weak form for linear momentum

$$\int_\Omega \boldsymbol{w} \cdot \rho \frac{D\boldsymbol{v}}{Dt} dV + \int_\Omega (\boldsymbol{\nabla} \boldsymbol{w})^{\mathrm{T}} : \boldsymbol{\sigma} dV = \int_\Omega \boldsymbol{w} \cdot \boldsymbol{f} dV + \int_{\partial\Omega_t} \boldsymbol{w} \cdot \bar{\boldsymbol{t}} dA \tag{4.9}$$

where superscript T is a transposition operator.

For quasi-static loading the inertia terms drop out, and we are left with the equation.

$$\int_\Omega (\boldsymbol{\nabla} \boldsymbol{w})^{\mathrm{T}} : \boldsymbol{\sigma} dV = \int_\Omega \boldsymbol{w} \cdot \boldsymbol{f} dV + \int_{\partial\Omega_t} \boldsymbol{w} \cdot \bar{\boldsymbol{t}} dA \tag{4.10}$$

Let us consider an abstract three-dimensional finite element. Here, the only relevant kinematical variables are the line velocities v_x , v_y, and v_z at each nodes. Therefore, the generalized trial and weighting functions can be written in vector form as:

$$\boldsymbol{V} = \left\{ \begin{array}{c} v_x \\ v_y \\ v_z \end{array} \right\}, \quad \boldsymbol{W} = \left\{ \begin{array}{c} w_x \\ w_y \\ w_z \end{array} \right\} \tag{4.11}$$

For completeness, we also write the generalized trial function V in time-integrated form as

$$\boldsymbol{V} = \begin{Bmatrix} v_x \\ v_y \\ v_z \end{Bmatrix} \implies \boldsymbol{U} = \begin{Bmatrix} u_x \\ u_y \\ u_z \end{Bmatrix} \tag{4.12}$$

where $u_i (i = 1,2,3)$ are the nodal displacement components at each nodes. The generalized body and traction vectors can also be written as

$$\boldsymbol{F} = \begin{Bmatrix} f_x \\ f_y \\ f_z \end{Bmatrix}, \quad \boldsymbol{T} = \begin{Bmatrix} \bar{t}_x \\ \bar{t}_y \\ \bar{t}_z \end{Bmatrix}; \tag{4.13}$$

Whereas the generalized gradient of the weighting functions, as well as the force stresses, are written in the column form

$$\boldsymbol{Q} = \begin{Bmatrix} w_{x,x} \\ w_{y,y} \\ w_{z,z} \\ w_{x,y} \\ w_{y,z} \\ w_{z,x} \end{Bmatrix}, \quad \boldsymbol{\sigma} = \begin{Bmatrix} \sigma_{xx} \\ \sigma_{yy} \\ \sigma_{zz} \\ \tau_{xy} \\ \tau_{yz} \\ \tau_{zx} \end{Bmatrix} \tag{4.14}$$

Therefore, we can write the variational equation of the balance of linear momentum in the more compact form

$$\int_{\Omega} \boldsymbol{Q} \cdot \boldsymbol{\sigma} dV = \int_{\Omega} \boldsymbol{W} \cdot \boldsymbol{F} dV + \int_{\partial\Omega_t} \boldsymbol{W} \cdot \boldsymbol{T} dA \tag{4.15}$$

4.2.2 Finite element formulation

The finite element formulation for the linear continuum model follows the standard Galerkin approximation of the weak form. According to the Eq. (2.3), the strains rate can be written as

$$\dot{\boldsymbol{\varepsilon}} = \frac{1}{2}(\boldsymbol{\nabla} \boldsymbol{v} + \boldsymbol{v} \boldsymbol{\nabla}) \tag{4.16}$$

Therefore, the generalized strain rate vector are of the form

$$\dot{\boldsymbol{\varepsilon}} = \begin{Bmatrix} v_{x,x} \\ v_{y,y} \\ v_{z,z} \\ v_{x,y} \\ v_{y,z} \\ v_{z,x} \end{Bmatrix} \tag{4.17}$$

The similar structures of the generalized virtual strain vector $\boldsymbol{Q}$ and the generalized strain rate vector $\dot{\boldsymbol{\varepsilon}}$ leads to the standard Galerkin formulation of the finite element problem. Consider the following finite element interpolation of the trial function within the finite element domain Ω^e

$$\boldsymbol{V}|_{\Omega^e} = \boldsymbol{N}^e \dot{\boldsymbol{a}}^e, \quad \dot{\boldsymbol{\varepsilon}} = \boldsymbol{B}^e \dot{\boldsymbol{a}}^e \tag{4.18}$$

In the preceding equations, $[\boldsymbol{N}^e]$ is the element shape function matrix of the form

$$\boldsymbol{N}^e = [\boldsymbol{N}_1, \boldsymbol{N}_2, ..., \boldsymbol{N}_{i_n}], \qquad \boldsymbol{N}_i = N_i \begin{bmatrix} 1 & 0 & 0 \\ 0 & 1 & 0 \\ 0 & 0 & 1 \end{bmatrix} \tag{4.19}$$

where N_i is the local shape function associated with element node i, $\dot{\boldsymbol{a}}^e$ is the generalized element nodal velocity vector, and i_n is the number of element nodes. The gradient operator matrix $\boldsymbol{B}^e$ for three-dimensional elements has the following form

$$\boldsymbol{B}^e = [\boldsymbol{B}_1, \boldsymbol{B}_2, ..., \boldsymbol{B}_{i_n}], \qquad \boldsymbol{B}_i = \nabla \boldsymbol{N}_i = \begin{bmatrix} N_{i,x} & 0 & 0 \\ 0 & N_{i,y} & 0 \\ 0 & 0 & N_{i,z} \\ N_{i,y} & N_{i,x} & 0 \\ 0 & N_{i,z} & N_{i,y} \\ N_{i,z} & 0 & N_{i,x} \end{bmatrix} \tag{4.20}$$

In the Galerkin approximation , the trial solution $\boldsymbol{V}$ and weighting functions $\boldsymbol{W}$ are approximated using the same collection of shape functions. So the finite element interpolation of the weighting function can be written as

$$\boldsymbol{W}|_{\Omega^e} = \boldsymbol{N}^e \dot{\boldsymbol{c}}^e, \quad \boldsymbol{Q}|_{\Omega^e} = \boldsymbol{B}^e \dot{\boldsymbol{c}}^e \tag{4.21}$$

where $\dot{\boldsymbol{c}}^e$ is a vector of arbitrary constants. Therefore, the variational Eq. (4.15) can be expressed in terms of the global shape function matrix $\boldsymbol{N}$ and gradient operator $\boldsymbol{B}$

$$\underbrace{\int_{\Omega} \boldsymbol{B}^{\mathrm{T}} \cdot \boldsymbol{\sigma} dV}_{\boldsymbol{F}_{int}} = \underbrace{\int_{\Omega} \boldsymbol{N}^{\mathrm{T}} \cdot \boldsymbol{F} dV + \int_{\partial\Omega_t} \boldsymbol{N}^{\mathrm{T}} \cdot \boldsymbol{T} dA}_{\boldsymbol{F}_{ext}} \tag{4.22}$$

In practice, the internal and external nodal force vectors $\boldsymbol{F}_{int}$ and $\boldsymbol{F}_{ext}$ can be evaluated from assembling the contributions of the individual finite elements .

$$\boldsymbol{f}^e_{int} = \int_{\Omega^e} \boldsymbol{B}^{e\mathrm{T}} \cdot \boldsymbol{\sigma} dV, \quad \text{and} \quad \boldsymbol{f}^e_{ext} = \int_{\Omega^e} \boldsymbol{N}^{e\mathrm{T}} \cdot \boldsymbol{F} dV + \int_{\partial\Omega^e_t} \boldsymbol{N}^{e\mathrm{T}} \cdot \boldsymbol{T} dA, \tag{4.23}$$

Then assemble the contributions $\{\boldsymbol{f}^e_{int}\}$ and $\{\boldsymbol{f}^e_{ext}\}$ as follows

$$\boldsymbol{F}_{int} = \mathop{\mathsf{A}}_{e=1}^{n_{el}} \boldsymbol{f}^e_{int}, \quad \text{and} \quad \boldsymbol{F}_{ext} = \mathop{\mathsf{A}}_{e=1}^{n_{el}} \boldsymbol{f}^e_{ext}, \tag{4.24}$$

where A denotes an assembly operator.

For the hypoplastic formulation, it is more convenient to write the finite element equation in rate form,

$$\boldsymbol{K}\dot{\boldsymbol{a}} = \dot{\boldsymbol{F}}_{ext}, \tag{4.25}$$

where $\boldsymbol{K}$ is the tangent stiffness matrix. $\dot{\boldsymbol{a}}$ is the generalized nodal velocity vector. It is easy to show that $\boldsymbol{K}$ can simply be assembled from element stiffness matrices of the form

$$\boldsymbol{k}^e = \int_{\Omega^e} \boldsymbol{B}^{e\mathrm{T}} \boldsymbol{D} \boldsymbol{B}^e dV \quad \Longrightarrow \quad \boldsymbol{K} = \mathop{\mathsf{A}}_{e=1}^{n_{el}} \boldsymbol{k}^e \tag{4.26}$$

For the updated hypoplastic constitutive model, the generalized rate-constitutive equation is of the form

$$\dot{\boldsymbol{\sigma}} = \boldsymbol{D}\dot{\boldsymbol{\varepsilon}} + \boldsymbol{\sigma}_w, \tag{4.27}$$

where $\boldsymbol{\sigma}_w$ emanate from rigid-body rotation to satisfy objectivity. The next section develops an expression for the tangential matrices $\boldsymbol{D}$ for the updated hypoplastic model .

4.2.3 Implementation in Abaqus

The equations of motion together with the constitutive law form a coupled system consisting of an initial–boundary value problem and an ordinary differential equation (Fellin and Ostermann, 2002). A steady-state solution of this system is usually obtained by co-simulation: the equations of motion are solved with the help of a finite-element package, and the constitutive law by a solver for ordinary differential equations. As an example, we describe henceforth the situation for Abaqus. However, the ideas presented below are not at all based on Abaqus. This can be used with any co-simulation-based finite-element package. The relevant constitutive information is passed to Abaqus by a subroutine UMAT which is the user subroutine for defining a material's mechanical behavior in Abaqus and has to be supplied by the user. Thus various constitutive models can be implemented as alternatives to the built-in models. This function greatly increases the freedom of users dealing with various materials. The two main functions of UMAT are:

- Updating the stresses in the FE model due to the changes of strains which are provided by Abaqus at the start of each iteration;

- Providing a Jacobian matrix for formulating the global stiffness matrix in the FE model.

It should be noted that the Jacobian matrix provided by UMAT does not necessarily exactly reflect the true behavior of a material constitutive relations.

We describe the process of UMAT. Starting from an equilibrium at time t_i, Abaqus performs an (incremental) loading and provides the subroutine UMAT with the Cauchy stress tensor $\boldsymbol{\sigma}(t_i)$ at the beginning of the loading as well as with the time increment Δt and an initial guess $\Delta\boldsymbol{\varepsilon}_i$ for the strain increment. The subroutine UMAT has then to supply Abaqus with the new Cauchy stress tensor $\boldsymbol{\sigma}(t_i + \Delta t)$; updated according to the constitutive law as well as with the derivative of $\boldsymbol{\sigma}$ with respect to the strain increment. With this information, a new guess for the strain increment is calculated and the whole procedure is iterated until convergence. The precise information on the Jacobian

$$\boldsymbol{J} = \frac{\partial \Delta\boldsymbol{\sigma}}{\partial \Delta\boldsymbol{\varepsilon}} = \frac{\partial \boldsymbol{\sigma}(t_i + \Delta t)}{\partial \Delta\boldsymbol{\varepsilon}} \tag{4.28}$$

is essential to achieve fast (quadratic) convergence in the Newton-type iteration performed by Abaqus. With a poor approximation in Eq. (4.28), the speed of convergence can be very slow and might even demand Δt to be very small too. One problem of the co-simulation approach is that the equilibrium iterations performed by Abaqus are decoupled from the stress computations over a time window of length Δt. Information between the two subsystems is only exchanged at the beginning and at the end of this time window. Therefore, the temporal rate of the strain tensor is not known as a function of time. Only its mean value over the window

$$\dot{\boldsymbol{\varepsilon}} = \frac{\Delta\boldsymbol{\varepsilon}}{\Delta t} \tag{4.29}$$

is available for use in the constitutive law. Moreover, since our constitutive law is path dependent, the simulation results might slightly depend on the loading history, i.e. on the choice of Δt. This, of course, is rather a problem of the modeling than a problem of discretization. A remedy is to supply an upper bound on Δt at the price of a higher computing time.

4.3 Stress–strain integration algorithms

The Eq.(2.9) can be recast in a more convenient form with the virtue of Euler's theorem for homogeneous functions (Wu and Niemunis, 1996).

$$\mathring{\boldsymbol{\sigma}} = (\mathscr{L} - \boldsymbol{N} \otimes \vec{\dot{\boldsymbol{\varepsilon}}}) : \dot{\boldsymbol{\varepsilon}} = D^{hp}(\boldsymbol{\sigma}, e, \vec{\dot{\boldsymbol{\varepsilon}}}) : \dot{\boldsymbol{\varepsilon}} \tag{4.30}$$

where $\vec{\dot{\boldsymbol{\varepsilon}}} = \dot{\boldsymbol{\varepsilon}}/\|\dot{\boldsymbol{\varepsilon}}\|$ stands for the direction of strain; and the symbol $\otimes$ denotes an outer product between two tensors. It can be seen that the tangential stiffness tensor D^{hp} for the hypoplastic model depends on the stress variables $(\boldsymbol{\sigma}, e)$ as well as the direction of the strain rate $\vec{\dot{\boldsymbol{\varepsilon}}}$. Hence the constitutive equation can be regarded as an ordinary differential equation , for which the general time integration over an increment step $t \in [t_n, t_{n+1}]$ can be written as:

$$\boldsymbol{\sigma}_{n+1} = \boldsymbol{\sigma}_n + \int_{t_n}^{t_{n+1}} h(\boldsymbol{\sigma}, e, \dot{\boldsymbol{\varepsilon}}) d\tau = \boldsymbol{\sigma}_n + \boldsymbol{D}\Delta\boldsymbol{\varepsilon} + \boldsymbol{\sigma}_w \Delta t, \quad n = 1, 2, \ldots \tag{4.31}$$

where the subscript n denotes the n^{th} step of the analysis.

In the integration of the updated hypoplastic constitutive model, all stresses are evaluated at time t_n. so the rate form Eq.(2.14) effectively takes the form:

$$\mathring{\boldsymbol{\sigma}} = I_{se}\left[C_1(\mathrm{tr}\boldsymbol{\sigma}_n)\dot{\boldsymbol{\varepsilon}} + C_2(\mathrm{tr}\dot{\boldsymbol{\varepsilon}})\boldsymbol{\sigma}_n + C_3 \frac{\mathrm{tr}(\boldsymbol{\sigma}_n \dot{\boldsymbol{\varepsilon}}_n)}{\mathrm{tr}\boldsymbol{\sigma}_n}\boldsymbol{\sigma}_n + C_4(\boldsymbol{\sigma}_n + \boldsymbol{\sigma}_n^*)\|\dot{\boldsymbol{\varepsilon}}\| I_e\right] \tag{4.32}$$

where $\boldsymbol{\sigma}_n$ denotes the Cauchy stress tensor. It should be noted that, for cohesive material, the stress tensor $\boldsymbol{\sigma}$ should be replaced by the the cohesion-related stress tensor $\boldsymbol{\sigma}_c$ as demonstrated in Eq. (2.55).

The problem can be solved numerically in time by evaluating the tangent(dropping the time subscript n for brevity)

$$\frac{\partial \mathring{\sigma}_{ij}}{\partial \dot{\varepsilon}_{mn}} = I_{se}\left[C_1 \Theta \boldsymbol{I}_{ijmn} + C_2 \sigma_{ij}\delta_{mn} + C_3 \frac{\sigma_{ij}\sigma_{mn}}{\Theta} + C_4(\sigma_{ij} + \sigma_{ij}^*)\dot{\mathscr{E}}_{mn} I_e\right] = d_{ijmn} \tag{4.33}$$

where $\boldsymbol{I}_{ijmn}$ is a rank-four symmetric identity tensor with components

$$\boldsymbol{I}_{ijmn} = \frac{1}{2}(\delta_{im}\delta_{jn} + \delta_{jm}\delta_{in}) \tag{4.34}$$

and $\Theta = \mathrm{tr}\boldsymbol{\sigma}$, $\quad \dot{\mathscr{E}}_{mn} = \dot{\varepsilon}_{mn}/\|\dot{\varepsilon}\|$. Then the constitutive equation can be recast in the following form

$$\dot{s}_{ij} = d_{ijmn}\dot{\varepsilon}_{mn} - s_{ik}w_{kj} + w_{ik}s_{kj} \tag{4.35}$$

Thus, the tangential tensor $\boldsymbol{D}$ and the incremental contributions arising from the rigid-body rotation can be obtained in matrix forms

$$d_{ijmn} \rightarrow \boldsymbol{D}, \text{ and } (-\varepsilon_{ik}w_{kj} + w_{ik}\varepsilon_{kj}) \rightarrow \boldsymbol{\sigma}_w \tag{4.36}$$

The constitutive equation can be integrated by assuming a time step Δt:

$$\boldsymbol{\sigma}_{n+1} = \boldsymbol{\sigma}_n + \boldsymbol{D}\Delta\dot{\boldsymbol{\varepsilon}} + \boldsymbol{\sigma}_w\Delta t, \tag{4.37}$$

where $\Delta\boldsymbol{\varepsilon}|_{\Omega^e} = \boldsymbol{B}^e\Delta\dot{\boldsymbol{a}}^e$ is the increment of the generalized strain. The solution can be advanced step by step with different integration methods.

The evolution of the void ratio is related to the volumetric strain $\dot{\varepsilon}_v = \mathrm{tr}(\dot{\boldsymbol{\varepsilon}})$ and $\dot{\varepsilon} = (1+e)\cdot\dot{\varepsilon}_v$. A closed form of integration for the void ratio is therefore available:

$$e_{n+1} = (1+e_n)\cdot\exp(\Delta\varepsilon_v) - 1 \tag{4.38}$$

Various numerical integration methods for Eq. (4.31) are possible and a few commonly-used methods are discussed in the following.

In our implementation, three simple integration schemes, the explicit forward Euler method, the modified Euler method and the Crank-Nicolson method are examined. Additionally, several adaptive explicit methods are compared with the simple integration methods. Furthermore, a stress correction scheme is adopted as a supplementary, which will be introduced in the next section.

4.3.1 The theta method

The general form of the theta method, or generalized midpoint method (e.g. (Tamagnini et al., 2000)), can be written as:

$$\boldsymbol{\sigma}_{n+1} = \boldsymbol{\sigma}_n + \Delta t_{n+1}[(1-\theta)\cdot\dot{\boldsymbol{\sigma}}_n + \theta\dot{\boldsymbol{\sigma}}_{n+1}] \quad n = 1,2,... \tag{4.39}$$

Here $\Delta t_{n+1} = t_{n+1} - t_n$ is the time step increment, the parameter $\theta \in [0,1]$, and $\theta = 0$ and $\theta = 1$ correspond to an explicit forward Euler and an implicit backward Euler method, respectively. The Crank-Nicolson (mid-point or trapezoidal) method is obtained by setting $\theta = 0.5$.

4.3.2 Explicit method with substepping and error control

For a given integration method, the accuracy can be improved by reducing the size of the time increment. Thus, a simple way to increase the accuracy is to divide a given time step into k equal substeps. Choosing k empirically does not allow the error to be controlled to a specified tolerance, but this can be achieved using the procedure described in Wissmann and Hauck (1983) A more powerful scheme, which enables us to adjust the substep size automatically according to the local truncation error, was introduced by Sloan (1987). Studies have revealed that this approach has the merits of being efficient and robust for a wide range of constitutive models. In this paper, two explicit substepping methods, namely the Richardson extrapolation (RE) scheme and the Runge−Kutta−Fehlberg (RKF23) scheme, are implemented and compared. Following the method proposed by Fellin and Ostermann (2002); Fellin et al. (2009) , we collect all the stress components and state variables (if there are) in the vector $\boldsymbol{y}$ for integration of Eq.(4.31).

$$\boldsymbol{y} = \{\sigma_{11}, \sigma_{22}, \sigma_{33}, \sigma_{12}, \sigma_{13}, \sigma_{23}, v_1 \dots v_m\}^{\mathrm{T}} \tag{4.40}$$

where σ_{ij} are stress components and $v_i(i = 1...m)$ are additional state variables,if void ratio or strain softening related factor is included . Integration of Eq.(4.40), we have to solve the given initial value problem

$$\boldsymbol{y}'(t) = H(\boldsymbol{y}(t)), \quad \boldsymbol{y}'(0) = \boldsymbol{y}(0). \tag{4.41}$$

To compute the local error in each substep of the stress integration, two different approximate solutions with different orders of accuracy (p,q) are obtained and compared, if the two solutions are in close agreement, the approximation is accepted. Otherwise, the step size is reduced. If the difference of the two approximation is larger than a prescribed accuracy, then the step size is increased. For the generic substep k in the time interval $[t_n, t_{n+1}]$, with dimensionless size $\Delta T_k \in (0,1]$ given by the following equation,

$$\Delta T_k = (t_{k+1} - t_k)/(t_{n+1} - t_n) \leqslant 1 \quad \text{and} \quad \sum_{k=1}^{n_s} \Delta T_k = 1 \tag{4.42}$$

Two different approximate solutions of the evolution problem (4.41) are obtained simultaneously according to

$$\boldsymbol{y}_{k+1}^{(p)} = \boldsymbol{y}_k + \Phi_1(\boldsymbol{y}_k, \Delta\boldsymbol{\varepsilon}_{n+1}, \Delta T)\Delta(T_k)^{(p+1)} \tag{4.43a}$$

$$\boldsymbol{y}_{k+1}^{(q)} = \boldsymbol{y}_k + \Phi_2(\boldsymbol{y}_k, \Delta\boldsymbol{\varepsilon}_{n+1}, \Delta T)\Delta(T_k)^{(q+1)} \tag{4.43b}$$

The two function Φ_1 and Φ_2 are constructed as

$$\Phi_1 := \sum_{i=0}^{p} k_i^{(p)} h_i(\boldsymbol{y}_k, \Delta\boldsymbol{\varepsilon}_{n+1}, \Delta T) \tag{4.44a}$$

$$\Phi_2 := \sum_{i=0}^{q} k_i^{(q)} h_i(\boldsymbol{y}_k, \Delta\boldsymbol{\varepsilon}_{n+1}, \Delta T) \tag{4.44b}$$

where

$$h_i(\boldsymbol{y}_k, \Delta\boldsymbol{\varepsilon}_{n+1}, \Delta T) := h(\boldsymbol{y}_k + \Delta T \sum_{j=0}^{l-1} \vartheta_{lj} h_j, \Delta\boldsymbol{\varepsilon}_{n+1}) \tag{4.45}$$

For simplicity and speed, we usually set $q = p+1$. The constants $k_i^{(p)}$, $k_i^{(q)}$ and ϑ_{lj} are used to obtained the approximated solutions of order p and q, respectively. Then the local truncation error of the lower order method at time T_{k+1} can be obtained by using the difference of the above two approximate solution :

$$\boldsymbol{R}_{k+1} = \boldsymbol{y}_{k+1}^{(p)} - \boldsymbol{y}_{k+1}^{(q)}, \quad \text{and} \quad R_{k+1} = \frac{\|\boldsymbol{R}_{k+1}\|}{\|\boldsymbol{y}_{k+1}^{(q)}\|} \tag{4.46}$$

The integration over the k^{th} substep is assumed to be successful when, for a given stress error tolerance STOL:

$$R_{k+1} \leqslant \text{STOL}, \tag{4.47}$$

Then the new substep size can be estimated by using the following extrapolation formula:

$$\Delta T_{k+1} = \Delta T_k \left[\frac{\text{STOL}}{R_{k+1}}\right]^{1/(p+1)} \tag{4.48}$$

If the estimated error is less than the prescribed accuracy tolerance STOL, the step is accepted and we enlarge our step size according to

$$\Delta T_{k+1} = \Delta T_k \cdot \min\left\{1.1, 0.9\left[\frac{\text{STOL}}{R_{k+1}}\right]^{1/(p+1)}\right\} \tag{4.49}$$

Box 1. Adaptive method with substepping and error control

1. Initialize substep counter, vector $\boldsymbol{y}$, dimensionless time and time increment:
$$k = 1 \quad \boldsymbol{y}_k|_{k=1} = \boldsymbol{y}_n \quad T_k = 0 \quad \Delta T_k = 1$$
2. Check if integration process is complete:
$$\text{IF} \quad T_k = 1 \quad \text{GO TO 10}$$
3. Compute approximate solutions for $\boldsymbol{y}_{k+1}$:
$$\boldsymbol{y}_{k+1}^{(p)} = \boldsymbol{y}_k + \Phi_1(\boldsymbol{y}_k, \Delta\boldsymbol{\varepsilon}_{n+1}, \Delta T)\Delta(T_k)^{(p+1)}$$
$$\boldsymbol{y}_{k+1}^{(q)} = \boldsymbol{y}_k + \Phi_2(\boldsymbol{y}_k, \Delta\boldsymbol{\varepsilon}_{n+1}, \Delta T)\Delta(T_k)^{(q+1)}$$
4. Compute relative error:
$$R_{k+1} = \frac{\|\boldsymbol{R}_{k+1}\|}{\|\boldsymbol{y}_{k+1}^{(q)}\|} = \frac{\|\boldsymbol{y}_{k+1}^{(p)} - \boldsymbol{y}_{k+1}^{(q)}\|}{\|\boldsymbol{y}_{k+1}^{(q)}\|}$$
5. Skip if the step failed:
$$\text{IF} \quad R_{k+1} > \text{TOL} \quad \text{GO TO 9}$$
6. Update dimensionless time and vector $\boldsymbol{y}$:
$$T_{k+1} = T_k + \Delta T_k, \boldsymbol{y}_{k+1} = \boldsymbol{y}_{k+1}^{(q)}$$
7. Evaluate next substep size according to equations
$$\Delta T_{k+1} = min\left\{0.9\Delta T_k \left[\frac{\text{TOL}}{R_{k+1}}\right]^{1/(p+1)}, 1.1\Delta T_k\right\}$$
8. Make the substep size less than residual dimensionless time and start a new substep
$$\Delta T_{k+1} \leftarrow min\{\Delta T_{k+1}, 1 - T_k\}; k \leftarrow k+1; T_k \leftarrow T_{k+1}; \text{ and } \boldsymbol{y}_k \leftarrow \boldsymbol{y}_{k+1}$$
9. The step has failed; reduce substep size according to equations
$$\Delta T_{k+1} \leftarrow max\left\{0.9\Delta T_k \left[\frac{\text{TOL}}{R_{k+1}}\right]^{1/(p+1)}, 0.25\Delta T_k\right\} \quad \text{GO TO 3}$$
10. Integration process is complete, the new vector $\boldsymbol{y}$ is obtained:
$$\boldsymbol{y}_{n+1} = \boldsymbol{y}_{k+1}, \quad \text{EXIT}$$

If condition (4.47) is not satisfied, i.e. the k^{th} substep has failed, we have to reject this step and redo it with a new, smaller value for the step size ΔT_k^*:

$$\Delta T_k^* = \Delta T_k \cdot \max\left\{0.25, 0.9\left[\frac{\mathrm{STOL}}{R_{k+1}}\right]^{1/(p+1)}\right\} \tag{4.51}$$

Noting that the right side of Eq.(4.48) is multiplied by a safety factor to generate a new time step. This factor attempts to prevent later steps just failing because of slight inaccuracies in the prediction and is typically set to 0.9. Also, an upper bound 1.1 and a lower bound 0.25 are set for each new substep so that the extrapolation will not be carried too far. For more details about the substepping algorithm, please refer to literature (Abbo, 1997). After the integration process is complete, new stress tensor can be extracted from the super vector $\boldsymbol{y}$. The complete structure of the adaptive method is summarized in Box 1

4.3.3 Correction of Stresses to failure Surface

At the end of each increment in the integration process, the stresses may diverge from the yield condition so that $f(\boldsymbol{\sigma}) > FTOL$. The extent of this violation, which is commonly known as yield surface 'drift', depends on the accuracy of the integration scheme and the nonlinearity of the constitutive relations. Sloan (1987) suggests that, provided the integration is performed accurately, the extent of drift from the yield surface will tend to be small and no remedial action is required. Wu and Niemunis (1997) and Niemunis (2003b) , on the other hand, reported that some stress states are accessible to surpass the yield surface no matter how accurate the integration results are. In this case, the stress state is not satisfying the yield condition, and this effect is cumulative. Hence, some form of stress correction is advisable.

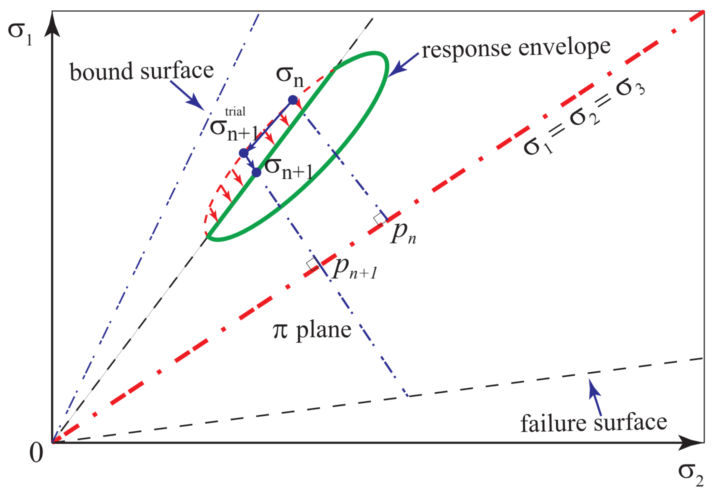

Figure 4.2 The sketch of correction of stresses to yield surface

Consider a point, which is lying outside the failure surface, defined by $\boldsymbol{\sigma}_n$ at $(n)^{th}$ step of analysis, no matter how accurate the integration method, the stress, defined by $\boldsymbol{\sigma}_{n+1}^{trial}$ at $(n+1)^{th}$ step of analysis, will violate the yield condition, as shown in Fig. 4.2, so that:

$$f(\boldsymbol{\sigma}_{n+1}^{trial}) = \sqrt{J_2(\boldsymbol{\sigma}_{n+1}^{*trial})} + \varsigma(C_i)I_1 > FTOL, \tag{4.52}$$

As any deviations from the yield condition are cumulative and may result in unacceptable errors in subsequent computations, the stresses should be corrected in an attempt to satisfy the current yield condition. In these circumstances, it is assumed that the correction is applied along the radial direction and the stress is forced back to the yield surface (Wu, 1990). With the radial return scheme, the corrected stress state takes the following form:

$$\boldsymbol{\sigma}_{n+1}^{*} = \lambda \boldsymbol{\sigma}_{n+1}^{*trial}, \quad p_{n+1} = p_{n+1}^{trial}, \tag{4.53}$$

where $p = 1/3I_1$ denotes the hydrostatic pressure, λ is an unknown multiplier. Using the definition of J_2, we have:

$$\frac{\boldsymbol{\sigma}_{n+1}^{*}}{J_2(\boldsymbol{\sigma}_{n+1}^{*})} = \frac{\boldsymbol{\sigma}_{n+1}^{*trial}}{J_2(\boldsymbol{\sigma}_{n+1}^{*trial})}. \tag{4.54}$$

In returning the stress state to the yield surface, it is desirable that the total strain increment, $\Delta\varepsilon$, remains unchanged, since this is consistent with the philosophy of the displacement finite element procedure. The corrected stress state in Eq.(4.53) is satisfying the consistency condition. Using Eq. (4.52) and (4.54), together with the assumption that departures from yield surface are small and that one return step is sufficient, we have the consistency condition expressed as:

$$f = \lambda \sqrt{J_2(\boldsymbol{\sigma}_{n+1}^{*trial})} + \varsigma(C_i)I_1 = 0, \tag{4.55}$$

which yields the unknown multiplier λ. After solution of the above equation , the stress is updated by Eq.(4.53). The return mapping scheme can be easily adopted to incorporate the effect of critical state and the cohesion. To this end, the constant ς can be obtained according to Eq.(2.19) and Eq.(2.53) for constitutive equation (2.56) and (2.52), respectively.

4.4 Numerical tests for different integration strategies

To give an overall assessment of the integration methods presented in Section 3, a comprehensive set of numerical tests is conducted for the constitutive model (2.52). Firstly, drained and undrained triaxial compression tests are modeled. Next, the influences of stress correction on the stress-strain relation in drained and undrained triaxial tests are evaluated. The relative error that denotes how much the stresses drift from the yield surface has been studied as well. Thirdly, incremental stress envelopes are calculated for various initial stress states and loading conditions. These kinds of numerical tests are conducted on the integration point level. The influence of the loading path, the direction of the strain increment, and the initial state on the accuracy and robustness of the methods are discussed. Finally, three particular boundary problems, namely a rigid footing test, a tunnel excavation in soil, and the safety factor of a homogeneous slope are solved using Finite Element Code Abaqus. The performance of the integration methods and correction of stress on these problems are compared in terms of their accuracy, efficiency, and robustness.

4.4.1 Triaxial compression tests

Performance of integration methods

Six integration methods are employed in the numerical triaxial compression tests: the forward Euler (FE) method, the modified Euler (ME) method, the Crank-Nicolson (CN) method and the Richardson extrapolation method with substepping and error control (REsec) and the Runge−Kutta−Fehlberg method with substepping and error control (RKF23sec and RKF45sec). The summary of different integration methods is given in Table 4.1.

To assess the numerical performance, an exact solution is obtained by using the RKF45 method with substeping and error control, in which the integration error tolerance is set to 10^{-9}. The relative error, which is calculated for every step as follows:

$$E_n = \frac{\|\boldsymbol{\sigma}^n_{exact} - \boldsymbol{\sigma}^n\|}{\|\boldsymbol{\sigma}^n_{exact}\|}. \qquad n = n^{th} \text{ step} \tag{4.56}$$

In the modeling of triaxial compression tests, an initial isotropic stress state with $\sigma_{11} = \sigma_{22} = \sigma_{33} = 100$ kPa is assumed. The initial void ratio is set to e_i = 0.78 for the drained triaxial test and e_i = 0.93 for the undrained triaxial test, and the tests are strain-controlled with a maximum axial (vertical) strain of $\dot{\varepsilon}_{22} = 10\%$ being applied. The parameters used in these simulations are shown in Table 4.2. In the numerical procedures, two kinds of increments are adopted. In the first calculation, the loading process is divided into 10 equal increments, which denotes large increment sizes scheme. In the second calculation, the loading process is divided into 20 equal increments, which denotes relative fine increment sizes scheme. For each kind of increment scheme, different substeps are performed for the explicit Euler method and the implicit CN method. Different STOLs are applied for the CN method. Likewise, the integration error tolerance STOL is various for the adaptive

Table 4.1 Different integration methods for generating estimated errors.

Method	Formulation	Error estimation
FE	$\sigma_{n+1} = \sigma_n + \Delta\sigma_{n+1}$	$R_{n+1} = \frac{\lVert\sigma_{n+1} - \sigma_n\rVert}{\sigma_{n+1}}$
ME	$\sigma^1_{n+1} = \sigma_n + \Delta\sigma^1_{n+1}$ $\sigma^2_{n+1} = \sigma_n + 0.5(\Delta\sigma^1_{n+1} + \Delta\sigma^2_{n+1})$	$R_{n+1} = \frac{\lVert\sigma^2_{n+1} - \sigma^1_n\rVert}{\sigma^2_{n+1}}$
RE	$\sigma^1_{n+1} = \sigma_n + \Delta\sigma^1_{n+1}$ $\sigma^2_{n+1} = \sigma_n + 0.5\Delta\sigma^1_{n+1}$ $\sigma^3_{n+1} = \sigma^2_n + 0.5\Delta t_{n+1}\mathbf{H}(\sigma^2_{n+1})$	$R_{n+1} = \frac{\lVert\sigma^3_{n+1} - \sigma^1_n\rVert}{\sigma^3_{n+1}}$
RKF$_{23}$	$\sigma^1_{n+1} = \sigma_n + 0.5\Delta\sigma^1_{n+1}$ $\sigma^2_{n+1} = \sigma_n - \Delta\sigma^1_{n+1} + 2\Delta\sigma^2_{n+1}$ $\sigma^3_{n+1} = \sigma_n + \Delta\sigma^2_{n+1}$ $\sigma^k_{n+1} = \sigma_n + \frac{1}{6}\Delta\sigma^1_{n+1} + \frac{2}{3}\Delta\sigma^2_{n+1} + \frac{1}{6}\Delta\sigma^3_{n+1}$	$R_{n+1} = \frac{\lVert\sigma^k_{n+1} - \sigma^3_n\rVert}{\sigma^k_{n+1}}$
RKF$_{45}$	$\sigma^1_{n+1} = \sigma_n + \frac{1}{4}\Delta\sigma^1_{n+1}$ $\sigma^2_{n+1} = \sigma_n + \frac{3}{32}\Delta\sigma^1_{n+1} + \frac{9}{32}\Delta\sigma^2_{n+1}$ $\sigma^3_{n+1} = \sigma_n + \frac{1932}{2197}\Delta\sigma^1_{n+1} - \frac{7200}{2197}\Delta\sigma^2_{n+1} + \frac{7296}{2197}\Delta\sigma^3_{n+1}$ $\sigma^4_{n+1} = \sigma_n + \frac{439}{216}\Delta\sigma^1_{n+1} - 8\Delta\sigma^2_{n+1} + \frac{3680}{513}\Delta\sigma^3_{n+1} - \frac{845}{4104}\Delta\sigma^4_{n+1}$ $\sigma^5_{n+1} = \sigma_n - \frac{8}{27}\Delta\sigma^1_{n+1} + 2\Delta\sigma^2_{n+1} - \frac{3544}{4104}\Delta\sigma^3_{n+1} + \frac{1859}{4104}\Delta\sigma^4_{n+1} - \frac{11}{40}\Delta\sigma^5_{n+1}$ $\sigma^k_{n+1} = \sigma_n + \frac{25}{216}\Delta\sigma^1_{n+1} + \frac{1408}{2565}\Delta\sigma^3_{n+1} + \frac{2197}{4104}\Delta\sigma^4_{n+1} - \frac{1}{5}\Delta\sigma^5_{n+1}$ $\sigma^z_{n+1} = \sigma_n + \frac{16}{135}\Delta\sigma^1_{n+1} + \frac{6656}{12825}\Delta\sigma^3_{n+1} + \frac{28561}{56430}\Delta\sigma^4_{n+1} - \frac{9}{50}\Delta\sigma^5_{n+1} + \frac{2}{55}\Delta\sigma^6_{n+1}$	$R_{n+1} = \frac{\lVert\sigma^k_{n+1} - \sigma^z_n\rVert}{\sigma^k_{n+1}}$

explicit method with error control strategies. For each method, the integration results will be accepted once convergence is obtained or the iteration number limit is reached.

The numerical results of drained and undrained triaxial tests obtained from various integration methods with 10 increments (2 substeps) and 20 increments (1 substeps) are shown in Fig. 4.3 and Fig. 4.4. The substeps and maximum error of each integration method during calculations are summarized in Table 4.3 and Table 4.4. The total substeps are the accumulative substeps in the total increments. Maximum stress error denotes the maximum stress error in the total increments.

As indicated by the data in the Table 4.3, the various integration strategies show very

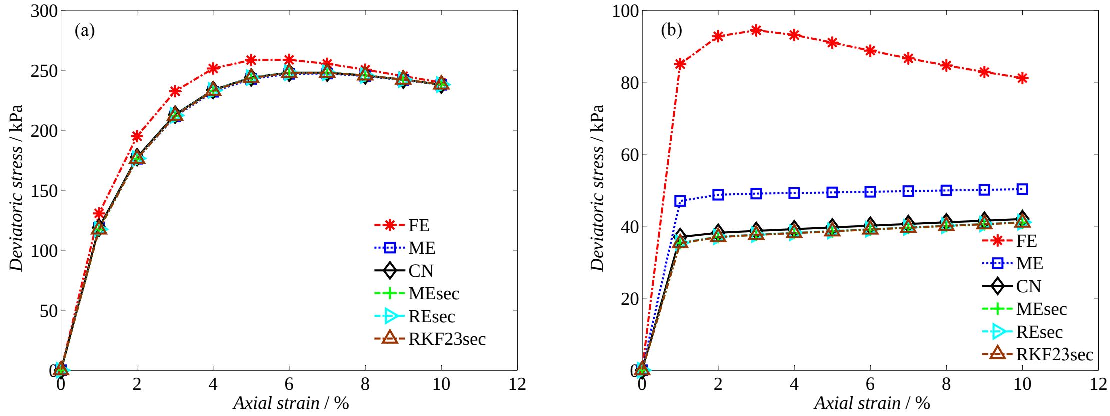

Figure 4.3 Stress-strain relations (10 increments, 2 substeps, STOL = 10^{-4}) (a)drained triaxial tests, and (b) undrained triaxial tests

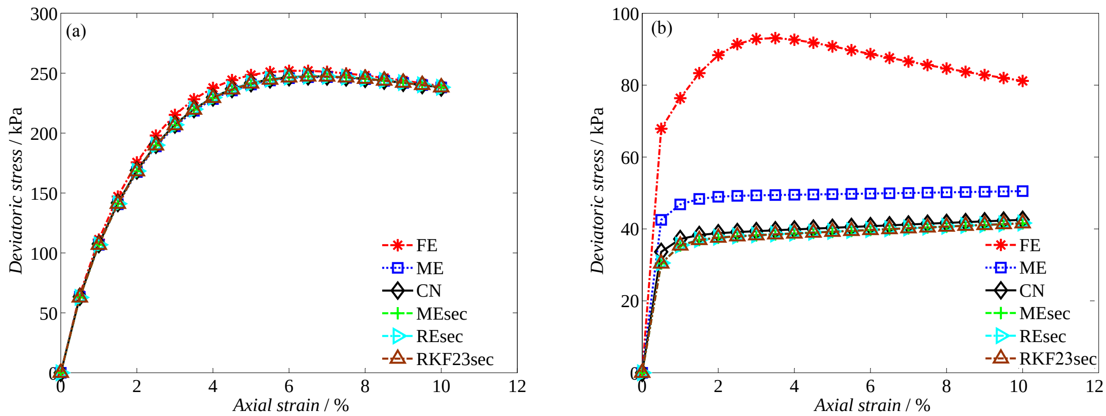

Figure 4.4 Stress-strain relations (20 increments, 1 substeps, STOL = 10^{-4}) (a)drained triaxial tests, and (b) undrained triaxial tests

Table 4.2 Parameters for numerical simulation of the drained triaxial test

Para.	C_1	C_2	C_3	C_4	e_0	λ	ξ	α	β
Value	-30.56	-90.93	-375.35	-107.09	0.957	0.022	0.061	1.5	1.0

different behavior. The simple forward Euler (FE) method with single substep gives the roughest estimation of the stress-strain response for both the drained and undrained triaxial test. Indeed, the relative error produced by this scheme reached 0.0365 and 1.344 for drained and undrained tests, respectively, which can easily lead to unacceptable results in finite element calculations due to error accumulation. With increasing the number of substeps, the relative error increase. However, the stress error in the undrained test is still not satisfactory.

Table 4.3 Performance of different integration methods for the triaxial test (10 increments))

	Drained test		**Undrained test**	
Method	Total substeps	Maximum Stress error	Total substeps	Maximum Stress error
FE				
2 substeps	20	3.6447×10^{-2}	20	1.3443
20 substeps	200	2.5379×10^{-3}	200	1.4907×10^{-2}
100 substeps	1000	4.9987×10^{-4}	1000	2.8393×10^{-3}
ME				
2 substeps	20	4.1771×10^{-3}	20	0.35299
20 substeps	200	1.1497×10^{-4}	200	6.095×10^{-4}
100 substeps	1000	4.5241×10^{-5}	1000	2.2028×10^{-5}
CN method (2 substeps)				
STOL = 10^{-1}	20	1.0168×10^{-2}	20	5.0406×10^{-2}
STOL = 10^{-2}	20	5.8278×10^{-3}	20	3.0047×10^{-2}
STOL = 10^{-3}	20	5.5931×10^{-3}	20	2.979×10^{-2}
STOL = 10^{-4}	20	5.5616×10^{-3}	20	2.9787×10^{-2}
CN method (20 substeps)				
STOL = 10^{-1}	200	3.7791×10^{-4}	200	9.8036×10^{-4}
STOL = 10^{-2}	200	6.9199×10^{-5}	200	3.1577×10^{-4}
STOL = 10^{-3}	200	5.7284×10^{-5}	200	2.6922×10^{-4}
STOL = 10^{-4}	200	5.6718×10^{-5}	200	2.6614×10^{-4}
MEsec method				
STOL = 10^{-1}	78	2.1806×10^{-3}	139	1.5462×10^{-2}
STOL = 10^{-2}	120	9.8354×10^{-4}	142	2.1586×10^{-3}
STOL = 10^{-3}	122	1.1362×10^{-4}	138	2.4943×10^{-4}
STOL = 10^{-4}	241	1.6432×10^{-5}	274	2.6199×10^{-5}
STOL = 10^{-6}	2178	1.2466×10^{-7}	1876	2.6876×10^{-7}
REsec method				
STOL = 10^{-1}	82	4.7348×10^{-2}	168	3.7314×10^{-2}
STOL = 10^{-2}	108	3.6243×10^{-3}	64	1.5343×10^{-2}
STOL = 10^{-3}	99	1.7921×10^{-3}	134	5.8378×10^{-3}
STOL = 10^{-4}	245	6.8076×10^{-4}	216	1.9108×10^{-3}
STOL = 10^{-6}	1569	9.2606×10^{-5}	1356	1.9587×10^{-4}
RKF23sec method				
STOL = 10^{-1}	155	1.1314×10^{-3}	104	2.5724×10^{-3}
STOL = 10^{-2}	88	1.1455×10^{-4}	122	4.8971×10^{-4}
STOL = 10^{-3}	106	6.7266×10^{-5}	152	1.7561×10^{-4}
STOL = 10^{-4}	119	2.2932×10^{-5}	155	2.0948×10^{-5}
STOL = 10^{-6}	219	2.6641×10^{-7}	264	2.2705×10^{-7}

Table 4.4 Performance of different integration methods for the triaxial test (20 increments))

Method	Drained test Total substeps	Drained test Maximum Stress error	Undrained test Total substeps	Undrained test Maximum Stress error
FE				
1 substeps	20	2.5674×10^{-2}	20	1.2743
10 substeps	200	2.373×10^{-3}	200	1.8918×10^{-2}
50 substeps	1000	4.7127×10^{-4}	1000	3.6557×10^{-3}
ME				
1 substeps	20	2.6538×10^{-3}	20	0.32113
10 substeps	200	6.202×10^{-5}	200	9.6345×10^{-4}
50 substeps	1000	2.4883×10^{-6}	1000	3.5063×10^{-5}
CN method (1 substeps)				
STOL = 10^{-1}	20	2.9048×10^{-3}	20	8.2816×10^{-2}
STOL = 10^{-2}	20	2.7617×10^{-3}	20	5.2308×10^{-2}
STOL = 10^{-3}	20	2.7315×10^{-3}	20	5.4467×10^{-2}
STOL = 10^{-4}	20	2.4501×10^{-3}	20	5.4769×10^{-2}
CN method (10 substeps)				
STOL = 10^{-1}	200	2.8223×10^{-4}	200	9.5735×10^{-4}
STOL = 10^{-2}	200	3.7108×10^{-5}	200	5.2871×10^{-4}
STOL = 10^{-3}	200	3.2723×10^{-5}	200	4.2185×10^{-4}
STOL = 10^{-4}	200	3.1086×10^{-5}	200	4.2975×10^{-4}
MEsec method				
STOL = 10^{-1}	187	1.322×10^{-4}	161	1.5476×10^{-2}
STOL = 10^{-2}	240	2.3702×10^{-4}	216	2.0051×10^{-3}
STOL = 10^{-3}	172	2.0073×10^{-4}	189	2.1432×10^{-4}
STOL = 10^{-4}	282	1.5749×10^{-5}	343	2.2663×10^{-5}
REsec method				
STOL = 10^{-1}	225	1.1674×10^{-2}	261	4.2371×10^{-2}
STOL = 10^{-2}	229	7.9004×10^{-3}	246	1.7145×10^{-2}
STOL = 10^{-3}	271	1.4684×10^{-3}	171	6.2644×10^{-3}
STOL = 10^{-4}	292	1.2891×10^{-3}	366	2.074×10^{-3}
RKF23sec method				
STOL = 10^{-1}	222	5.3623×10^{-5}	177	3.2024×10^{-3}
STOL = 10^{-2}	190	4.159×10^{-5}	227	4.5993×10^{-4}
STOL = 10^{-3}	190	2.6404×10^{-5}	188	1.2079×10^{-4}
STOL = 10^{-4}	222	2.5566×10^{-6}	261	1.4964×10^{-5}

Though better than the FE method, the performance of the simple Modified Euler (ME) method is also not very satisfactorily. The maximum error is obviously reduced compared with the FE method. The implicit Crank-Nicolson (CN) method with 2 substeps gives better accuracy than either of the above explicit methods. However, the total integration error for C–N method are not sensitive to STOL (here STOL means the error tolerance for local iteration in implicit methods). This implies that, for a small step size (20 substeps), the C–N method can result in very high accuracy.

Among the three explicit adaptive methods, the Modified Euler method and Rkf23 method with substepping and error control achieved the highest accuracy with relative errors around 10^{-5}, but the computation using REsec with STOL = 10^{-1} gives relative coarse accuracy. When STOL is decreased, all the adaptive explicit methods exhibit good accuracy. The stress errors continue to reduce as STOL is reduced, and the best accuracy is achieved when the error tolerance is set to 10^{-6}. The total number of substeps is also counted. As expected, these counts increase as STOL is tightened for the MEsec and REsec methods. Among these methods, the total substeps is dramatically increased as STOL is tightened to STOL = 10^{-6} For RKFsec methods, very fine accuracy can be achieved using relative fewer substeps. This implies the RKFsec methods performances the best both in accuracy and efficiency.

In the second calculation, whose results are shown in Table 4.4, a smaller increment size has been used (20 equal increments). The basic features of the results are similar to the results of the former case. In these two cases, the simple Euler methods and implicit method have the same total substeps but different global increments. However, the integration errors produced by the simple Euler methods and implicit method are reduced. This implies the global increment has the fundamental effect on the performance of different methods. The integration errors produced by adaptive explicit methods are reduced when the error tolerance is tightened, while the effect is not sensitive. Still, the REsec method gives the worst prediction both in drained and undrained tests. but the RKF23sec method performances very well. The results again confirm the accuracy and robustness of explicit RKF23 methods with substepping and an error control scheme. All in all, the numerical performance of integration methods in the drained tests are better than that in the undrained test, which implies all the integration methods can be strongly influenced by the stress path.

The effect of stresses Correction

To evaluate the effect of stress correction, three different initial isotropic stress states with $\sigma_{11} = \sigma_{22} = \sigma_{33} = 50/100/200$ kPa are assumed. The initial void ratio is set to e_i = 0.78 for the drained triaxial test and e_i = 0.95 for the undrained triaxial test, and the tests are strain-controlled with a maximum axial (vertical) strain of $\dot{\varepsilon}_{22} = 20\%$ being applied. The parameters used in these simulations are shown in Table 4.2. To eliminate the effect of integration methods, only the RKF23sec method with error control is employed in this simulation. The integration error tolerance STOL = 10^{-4}, which is sufficient fine to guarantee the accuracy of this simulation. The stress correction scheme is employed in each step to force the stress state to the yield surface.

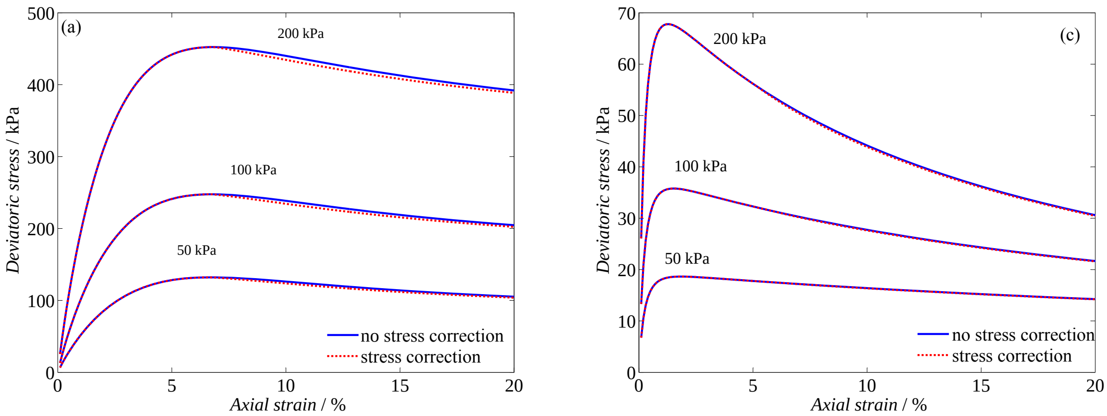

Figure 4.5 Results of stress correction in triaxial tests: Stress-strain relations of (a) drained triaxial test, (a) undrained triaxial test

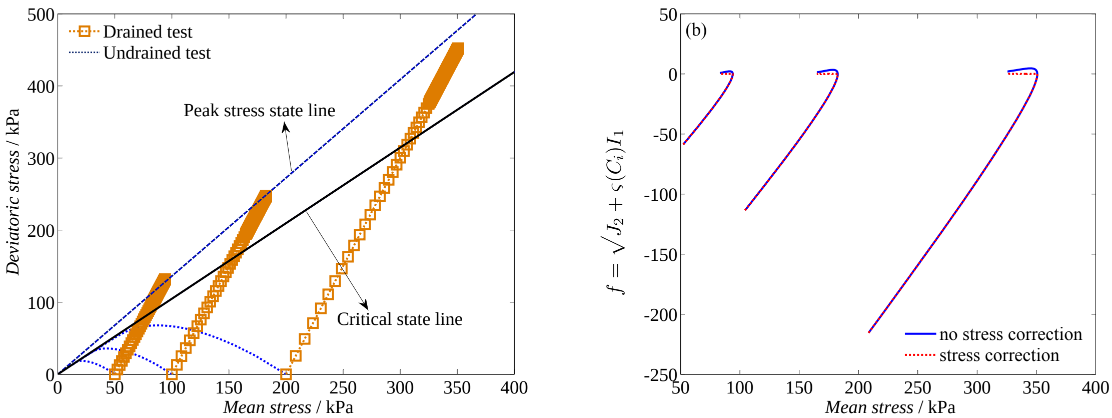

Figure 4.6 (a) stress path of triaxial tests (a) the velue of yield function f in drained triaxial test

Fig. 4.5 presents the results of stress correction in both drained and undrained triaxial tests. As can be observed from Fig. 4.5(a) the stress correction takes effect only after the peak is obtained in the stress-strain curve. This implies that the stresses may violate the yield surface if softening occurs. However, stress correction does not occur in the undrained test, as shown in Fig. 4.5(b). The stress path of both drained and undrained tests are presented in Fig. 4.6(a). It can be observed from Fig. 4.6(a) that the undrained stress paths do not

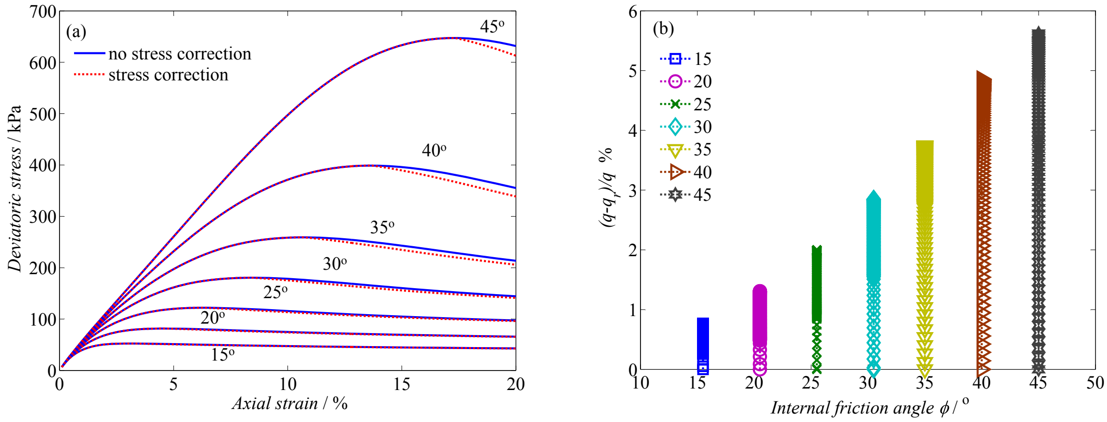

Figure 4.7 The effect of stress correction on drained triaxial tests (p = 50 kPa): (a) Stress-strain relation with various internal friction angle, and (b) relative error after stress correction

surpass the critical state line, while the drained stress paths exceed the critical state line and reach the peak stress state line. This reveals that the stress correction takes place in between the domain of critical state line and the peak stress state line. Fig. 4.6(b) shows the value of the yield function f in drained tests. It is clearly shown that the yield function $f > 0$ after the stress peak is obtained. With the stress correction scheme, the yield function f become null. Therefore, this stress correction scheme can guarantee the stress lying in or on the yield surface.

It has been discussed in Chapter 3 that the stress will lie out of the failure surface for some strain paths, especially for some materials with large friction angle, e.g., $\phi = 30^o$. The effect of stress correction for materials with various friction angle has been discussed. Fig. 4.6(a) shows the stress-strain relations for different friction angles. It can be observed from this figure that the magnitude of corrected stress increases with increasing the friction angle. Fig. 4.6(b) shows the relative error of the stress correction in drained triaxial tests. With increasing the friction angle, the relative error increase from 0.8% for $\phi = 15^o$ to 5.5% for $\phi = 45^o$. This further indicates the necessary of stress correction scheme in the numerical implementation of the hypoplastic constitutive model.

4.4.2 Stress response envelopes

It is well known that the numerical performance of an integration algorithm is influenced by the loading path (Ding et al., 2015; Tamagnini et al., 2000). In this section, the influence of the loading direction on the performance of the various algorithms is studied based on the Stress Response Envelope (SRE).

The concept of stress response envelope can be adapted to represent in an effective way the influence of loading direction on the algorithm performance. Tamagnini et al. (2000) and Ding et al. (2015) discussed the influence of the direction of the applied strain increment, instead of strain rates, on the integration methods for the CLoE hypoplastic model and Gudehus-Bauer hypoplastic model. The results reveal that the loading direction, as well as the strain increment size, can strongly influence the performance of integration algorithms, and the adaptive explicit methods show better accuracy and efficiency. Similar to their approach, the SREs for the updated hypoplastic model are computed to examine the influence of the strain increment direction. For the sake of simplicity, only three representative integration methods are considered: the Crank-Nicolson (CN) method, the Modified Euler method with substepping and error control (MEsec) and the Modified Euler method with substepping and error control and stress correction.

To obtain straightforward graphical representations of the SREs, two special loading cases are examined: Axisymmetric deformation and Simple shear loading. Each loading cases consider two initial stress states: isotropic stress and limited stress stats. The limited stress state represents the stresses on the failure surface. This stress state is adopted to study this stress correction algorithm.

(I) Axisymmetric deformation, $\Delta\varepsilon_{11} = \Delta\varepsilon_{33} = -\frac{1}{\sqrt{2}}\|\Delta\boldsymbol{\varepsilon}\|\cos\theta_\varepsilon$, $\Delta\varepsilon_{22} = -\|\Delta\boldsymbol{\varepsilon}\|\sin\theta_\varepsilon$

(a) Isotropic stress, p= -100 kPa, $\sigma_{11} = \sigma_{22} = \sigma_{33}$ = -100 kPa

(b) Limited state, p= -156.3 kPa, $\sigma_{11} = \sigma_{33}$ = -100 kPa, for σ_{22} =-275 kPa

(II) Simple shear, $\varepsilon_{12} = \varepsilon_{21} = -\frac{1}{\sqrt{2}}\|\Delta\boldsymbol{\varepsilon}\|\cos\theta_\varepsilon$, $\Delta\varepsilon_{22} = -\|\Delta\boldsymbol{\varepsilon}\|\sin\theta_\varepsilon$,

(c) Isotropic stress, p= -100 kPa, $\sigma_{11} = \sigma_{22} = \sigma_{33}$ = -100 kPa

(d) Limited state, p= -100 kPa, $\sigma_{11} = \sigma_{22} = \sigma_{33}$ = -100 kPa, and σ_{12} = 65 kPa

The norm of strain increment is constant ($\|\Delta\boldsymbol{\varepsilon}\|$ = 2.0 $\times$ 10^{-3}), $\theta_\varepsilon \in [0,\ 2\pi)$. The parameters used in these simulations are shown in Table 4.2. To compare the performance of the two methods, an exact solution is obtained using the MEsec method with a tight stress integration error tolerance of STOL = 10^{-6} . The CN and REsec methods are then used with the error tolerance STOL = 10^{-3} . As a supplement, another calculation was conducted using the CN method with STOL = 10^{-3} and strain increments divided into 100 equal substeps. Additionally, the MEsec method with stress correction is considered for the limited stress state. The results are plotted in the $\sqrt{2}\sigma_{11}/\mathrm{tr}\boldsymbol{\sigma}$: $\sigma_{22}/\mathrm{tr}\boldsymbol{\sigma}$ and $\sqrt{2}\sigma_{12}/\mathrm{tr}\boldsymbol{\sigma}$: $\sigma_{22}/\mathrm{tr}\boldsymbol{\sigma}$ planes, as shown in Fig. 4.8.

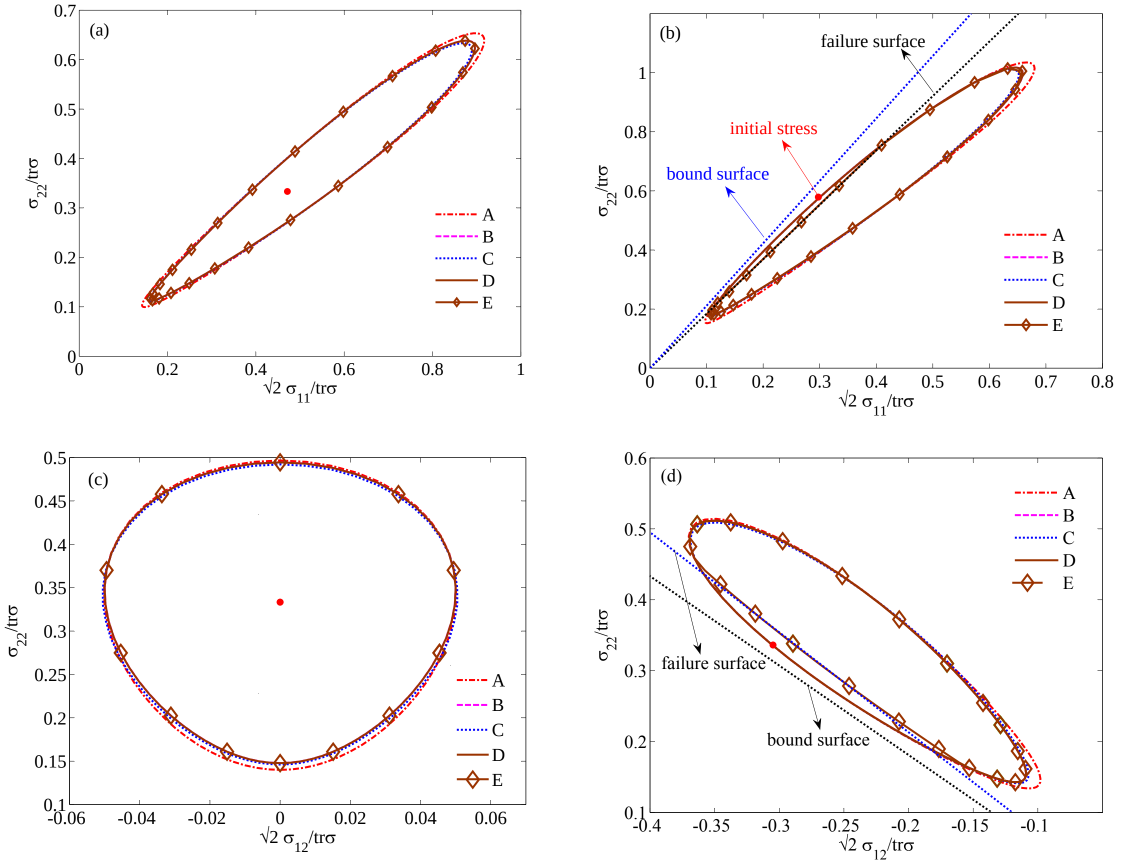

Figure 4.8 Stress response envelopes: (a) axisymmetric loading with isotropic stress state; (b) axisymmetric loading with axisymmetric stress state; (c) simple shear loading with isotropic stress sate; (d) simple shear loading with axisymmetric stress state. The numerical results are for A the CN method with STOL = 10^{-3} with single step; B the CN method with STOL = 10^{-3} with 100 equal substeps; C the MEsec method with STOL = 10^{-3}; D the MEsec method with STOL = 10^{-6}; E the REsec method with STOL = 10^{-6} and stress correction

As can be indicated from the above results, the numerical performance of the various schemes is influenced by the loading direction. The CN method with STOL = 10^{-3} and a single step produces the largest integration error in the extension direction for both axisymmetric loading and simple shear loading. The numerical results of the MEsec method with STOL = - 10^{-3}, and the CN method with STOL = 10^{-3} and 100 equal substeps, are very close to the exact solution. These results agree with the conclusions of Tamagnini et al. (2000) and Ding et al. (2015) for their numerical implementation of the CLoE hypoplastic model and Gudehus-Bauer hypoplastic model. Since the stresses lie within the failure surface for isotropic stress state for both axisymmetric loading and simple shear, the stress correction does not take place, see Fig. 4.8(a) and (c). On the other hand, for the limited stress state, the stress state lies between the bound surface and failure surface. The corrections of stress take effect for both axisymmetric loading and simple shear, and the stresses, which is beyond the failure surface, are corrected to the failure surface, see Fig. 4.8(b) and (d).

The results also indicate that the stress integration for a hypoplastic model is affected strongly by the step size, with much better performance being obtained when the step size is reduced. For a relatively large increment size and a certain loading direction, the implicit iteration may converge but give a significant error. The errors from the adaptive explicit methods, however, can be reduced easily by tightening the tolerance STOL and thus increasing the number of sub-increments. Although the stress states lying outside the bound surface will be automatically corrected in the next time step for the updated constitutive model. However, the stress will lie out of the failure surface for some strain paths, which would result in large errors in FEM analysis. Thus, in FEM analysis with complex loading conditions and large number of increments, some stresses lying outside the failure surface can be remedied by adopting the stress correction algorithm.

4.4.3 Typical boundary value problem tests

In this section, the discussion is extended to two typical boundary value problems: a rigid footing test and a tunnel excavation test. In the first boundary value problems, attention is focused not only on the accuracy and robustness, but also on the computational efficiency of the numerical schemes. As can be seen from subsection 4.4.1, the simple explicit methods and implicit method with large step sizes can produce large errors or unsuccessful computation. In a FEM calculation, to circumvent these risks, a widely used approach is to divide the applied step into several equal substeps. In our implementation, this kind of substepping is adopted for the forward Euler method (with 100 equal substeps), modified Euler method (with 100 equal substeps) and Crank-Nicolson method (with 20 equal substeps and 100 equal substeps). For Crank-Nicolson method, different stress tolerances are adopted and the maximum number of local iterations is set to 10000. The integration results are accepted once the error is tolerable or the maximum iteration number is reached.

In the second boundary value problems, the attention will be focused on the effect of stress correction strategy. Still, an exact solution is assumed to be obtained by using the RKF45sec method with STOL = 10^{-9}. Then the calculation obtained using ME method (10 substeps)and the ME method (10 substeps) with stress correction are compared. For the adaptive explicit methods, the maximum number of substep is less than 10000 and the minimum substeps size is less than 1.0×10^{-7} of the current increment size. To avoid numerical failure for positive (tensile) stresses, a cohesive is given to all elements. Therefore, the development of tensile stresses is allowed during the computations.

Rigid footing test

A further investigation of the above numerical methods is conducted for the boundary value problem of a rigid footing. The computation domain, as shown in Fig.4.9, is 4.0 m thick by 12 m wide and the width of the footing is w = 1.2 m with a depth of h = 0.38 m.

For the sake of simplicity, an asymmetric model was chosen for this numerical simulation. A total of 150 four node plane strain elements, involving 600 Gauss integration points, are used. The maximum vertical displacement is d = 0.5 m, at which the vertical force reaches its peak value, and the displacement loading process is divided into 100 equal increments. Prior to loading the footing, an initial geostatic stress (120 kPa) is applied to obtain negligible displacement for this model. The parameters shown in Table 4.5 are used in this simulation and the initial void ratio $e_i = 0.78$. As before, the results from the RKF45 method with substepping and error control are used as the exact solution for this simulation. To ensure this solution is sufficiently accurate, the stress error tolerance STOL is set to 10^{-9}.

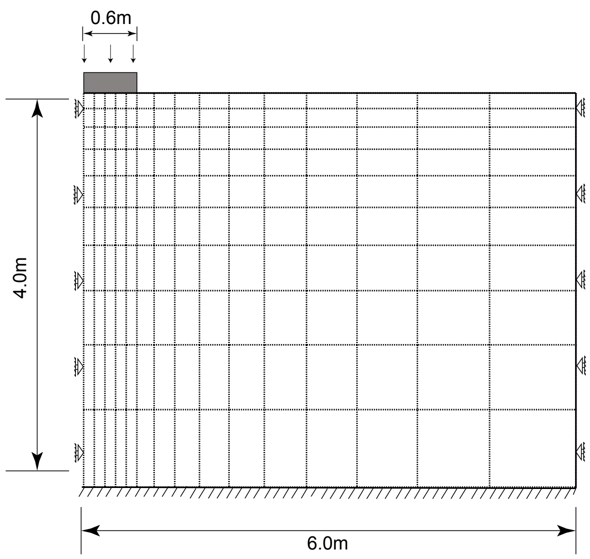

Figure 4.9 Finite element meshes of the rigid footing

Table 4.5 Parameters for Rigid footing test

Para.	C_1	C_2	C_3	C_4	e_0	λ	ξ	α	β	c (kPa)
Value	-50.1	-520.74	-1802.29	-300.57	0.957	0.022	0.061	1.5	1.0	47.6

Table 4.6 Results of different methods for rigid footing test (100 increments.)

Method	CPU time (s)	Total Number of substeps	Maximum Number of substeps	Average error
FE (100 substeps)	22.5	6×10^6	10000	1.928×10^{-4}
FEs (100 substeps)	23.7	6×10^6	10000	-
ME (100 substeps)	41.8	6×10^6	10000	1.293×10^{-4}
MEs (100 substeps)	43.1	6×10^6	10000	
CN method(20 substeps)				
STOL = 10^{-1}	16.8	1.2×10^6	2000	2.886×10^{-4}
STOL = 10^{-2}	15.9	1.2×10^6	2000	2.886×10^{-4}
STOL = 10^{-3}	22	1.2×10^6	2000	2.886×10^{-4}
STOL = 10^{-4}	17.2	1.2×10^6	2000	2.886×10^{-4}
CN method(100 substeps)				
STOL = 10^{-1}	38	6×10^6	10000	1.928×10^{-4}
STOL = 10^{-2}	43.5	6×10^6	10000	1.928×10^{-4}
STOL = 10^{-3}	41.9	6×10^6	10000	1.928×10^{-4}
STOL = 10^{-4}	45.7	6×10^6	10000	1.928×10^{-4}
MEsec method				
STOL = 10^{-1}	16.6	317357	1407	1.525×10^{-4}
STOL = 10^{-2}	16.3	647377	1514	1.983×10^{-5}
STOL = 10^{-3}	16.9	678211	1486	7.647×10^{-6}
STOL = 10^{-4}	18.2	754393	1745	2.884×10^{-6}
RKF23sec method				
STOL = 10^{-1}	24.1	84150	1223	4.076×10^{-5}
STOL = 10^{-2}	29.1	251326	1351	7.550×10^{-6}
STOL = 10^{-3}	29.5	385152	1387	1.252×10^{-6}
STOL = 10^{-4}	30.8	627134	1475	1.914×10^{-7}
RKF45sec method				
STOL = 10^{-9}	29.5	644161	1429	-

The stress integration errors are evaluated from the results of at the end of calculation. Note that the explicit Euler method with stress correction is not involved in the evaluation of stress error. The numerical results can be found in Table 4.6, in which the “Total number of substeps ”is calculated according to the accumulated number of substeps for all Cause points in the whole increments, while the “Maximum number of substeps ”is the substeps of one Cause points with the maximum number of substeps in the whole increments.

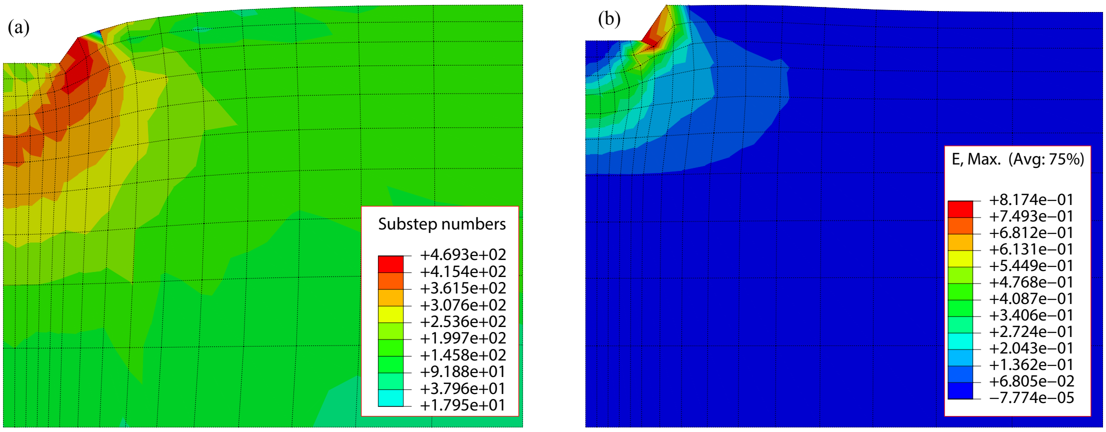

Figure 4.10 (a) The contour of the number of substep at the 3^{th} increament, and (b)Strain contour of of the foundation, and The integration method is RKF45sec method with STOL $= 10^{-9}$

From Table 4.6, we find that the explicit Euler method and the CN method with a total number of substeps of 6.0×10^6 give very close results. While ME method and the CN method cost two times of the CUP time than that of the FE method. The CPU time of the explicit Euler with stress correction is all most the same than that of without stress correction. The CN method with 20 substeps gives wore prediction compared with the CN method with 100 substeps. However, the former takes less time than the later one. As is expected, the adaptive explicit method can control the integration error and CPU time cost effectively for a given STOL. Among the two adaptive methods, the MEsec method is efficient but the RKF23sec method is accurate and both show the very good prediction. Additionally, a color contour plot of the number of substeps for each element is shown in Fig. 4.10(a). As we can see from Fig. 4.10(a), a well-defined the shear band is developed near the loading area tests. The average number of substeps, as expected, is much higher in the region where the shear band emerges. This indicates that the substepping scheme reduces the size of the increments efficiently to acquire the predefined accuracy.

The constant-velocity boundary condition applied to the top surface of the foundation causes the foundation to settle at a constant rate. Theoretically, the foundation pressure can be increased gradually up to the failure point (termed the bearing capacity) at which a failure surface develops. In the present finite element analysis, such a failure surface is evident when the shear strains are plotted for the at-failure condition as shown in Fig. 4.10(b). From this figure, one can immediately notice the presence of a triangular zone directly under the foundation, a radial zone, and a Rankine passive zone resembling the three zones assumed by Terzaghi.

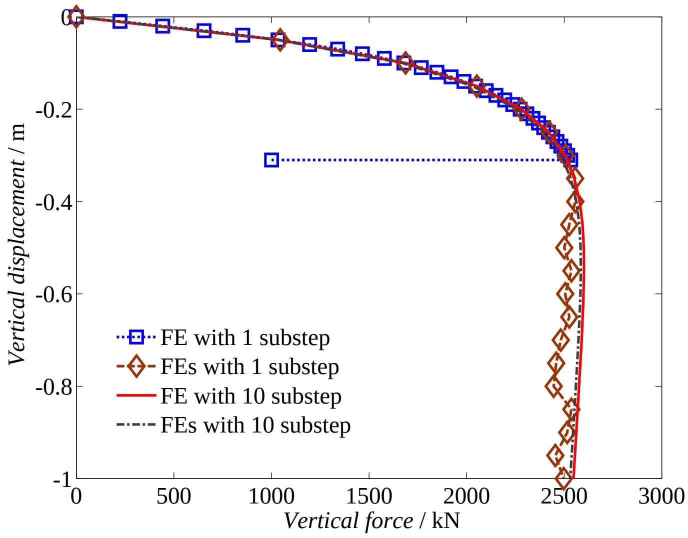

Figure 4.11 Relations of vertical force and vertical displacement(no critical state effect

The relation of vertical force and vertical displacement is shown in Fig.4.11. The vertical force increases non-linearly until the failure point has been achieved, where the bearing capacity of the footing is obtained. As shown in this figure, the FE method with a single substep fails after some steps, however, with stress correction, the FE method finishes all the computation, albeit with an unsatisfying result. The FE method with 10 constant substeps gives better results than the former one. However, it achieves a larger bearing capacity than FE method with 10 constant substeps and stress correction. This indicates that the stress correction, to some extent, can stabilize the numerical computation by avoiding the appearing of too excessive stress states at large increment size.

Tunnel excavation

The model has a height of 60 m and a width of 60 m, which is defined using Abaqus with 446 plate strain elements, the diameter of the tunnel is 8 m in the soil. For the sake of simplicity, an asymmetric model was chosen for the FEM simulation. The material parameters used in this simulation are shown in the following table.

Table 4.7 Parameters for tunnel excavation in soil

Para.	C_1	C_2	C_3	C_4	e_0	λ	ξ	α	β	c (kPa)
Value	-50.1	-541.7	-1135.24	-238.54	0.957	0.022	0.061	1.5	1.0	30

There are two steps to carry out the tunnel excavation: a geostatic step and a tunneling

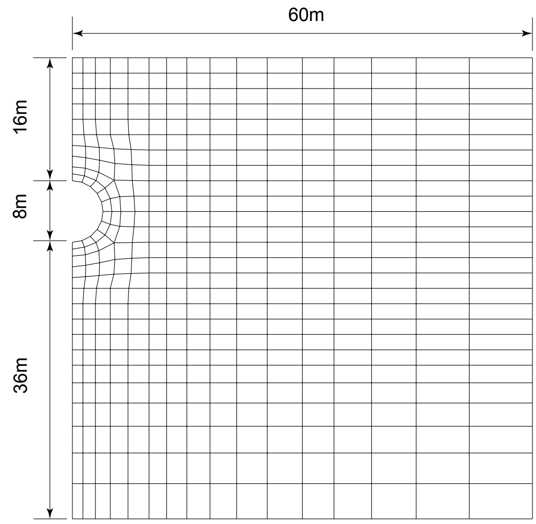

Figure 4.12 Finite element meshes of the excavation in the soil

step. For both steps, appropriate boundary conditions need to be applied. In the geostatic step, the boundary condition for the bottom nodes is given by fixing the vertical displacement. Nodes on lateral boundaries are fixed in the horizontal direction. The moment on all nodes is set to be zero. Gravity load is applied in this step after all boundary conditions are applied. In the second step, the elements of the tunnel is removed to model the excavation process. In the practical tunneling process, however, a tunnel lining will be set up, which is not considered in this simulation, since we are focusing on the effect of different integration methods on the response of the excavation. Three integration methods, the simple Modified Euler method(10 constant substeps), the Modified Euler method(10 constant substeps) with stress correction and RKF45sec method with an error tolerance of STOL = 10^{-9}, have been used in this example.

Fig.4.13(a) and Fig.4.13(b) show the horizontal and vertical displacement after the end of the excavation, respectively. Correspondingly, Fig.4.14(a) shows the surface settlement on the ground surface calculated with different integration methods. As shown in this figure, the largest surface settlement is 10 m distance from the tunnel centreline. Corresponding deformations at the final excavation stage along the vertical cross-section 10 m distance from the tunnel centreline are depicted in Fig. 4.14(b). Differences in the settlement magnitudes are due to different responses of integration method in the model. Overall, The adaptive method with error control and the simply modified Euler method with constant substeps gain the same results, however, the ME method with stress correction owns larger displacement. Since the hypoplastic constitutive model allows some stress state outside of the yield surface whilst bounded by the bound surface. After using the stress correction scheme, some stresses, which are supposed to surpass the yield surface, have been forced back. The means

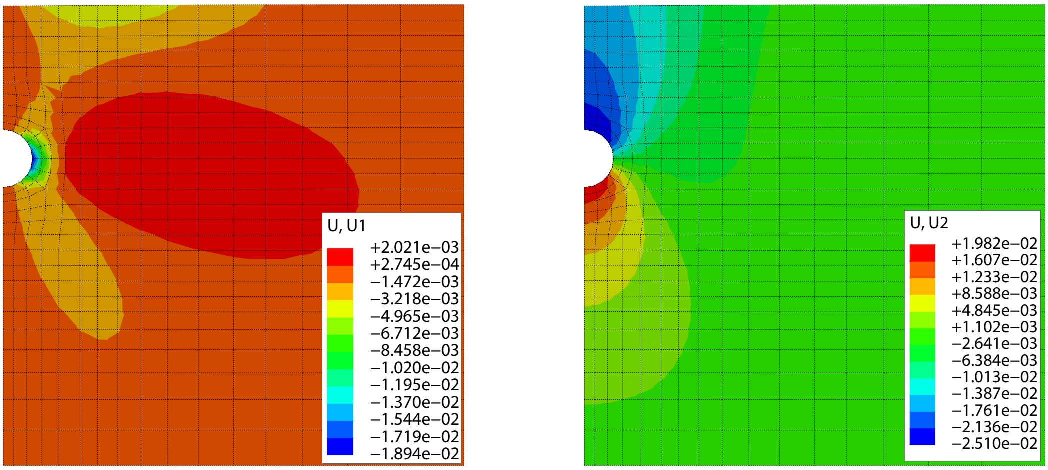

Figure 4.13 The displacement after the excavation (a)horizontal direction U1 (b) vertical direction U2

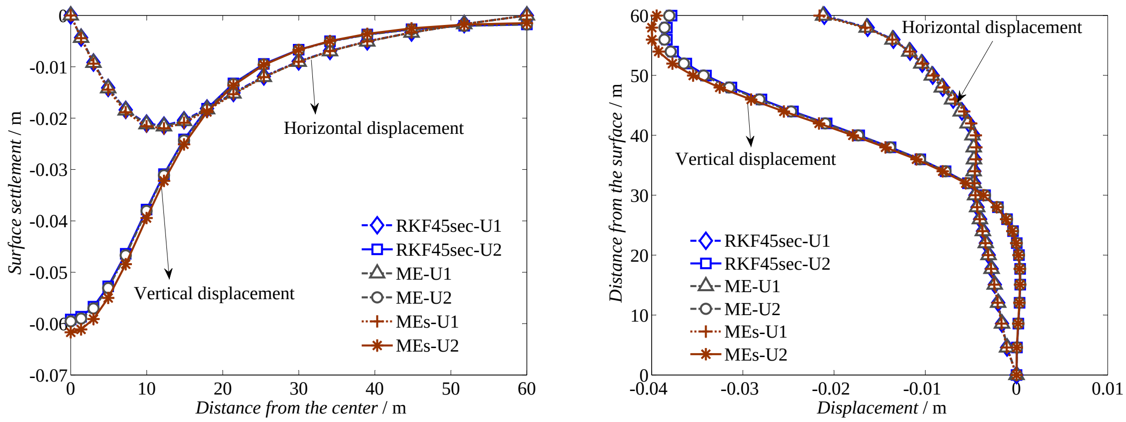

Figure 4.14 (a)Surface settlement above tunnel centreline, (b) Variation of deformations 10 m from tunnel centreline with depth at final stage of excavation

the accessible stress range become smaller and consequently results in larger displacement in the process of excavation.

Safety factor and failure of a homogeneous slope

The stress correction scheme is further validated by evaluating the safety factor of a homogeneous slope and simulating the subsequent failure process. In slope stability analysis, the so-called shear strength reduction technique is usually applied to evaluate the safety (Peng et al., 2015). In the strength reduction technique, the shear strength (friction angle and cohesion) is reduced by a reduction factor until slope failure occurs. The safety factor is defined by this reduction factor. In this section, the safety factor and failure of a homogeneous slope are calculated using the proposed hypoplastic model in Chapter 2. Results from FEM using different integration methods: the implicit CN method, the FE method, the adaptive RKF23 method and those methods with stress correction scheme, are compared.

The geometry and boundary conditions of the considered slope are shown in Fig. 4.15. The slope is assumed to consist of cohesive soil with the material parameters listed in Table 4.8. The initial void ratio of the soil is $e_i = 0.88$. The friction angle / and the cohesion c are the two shear strength parameters subjected to strength reduction. In the searching process, the actual shear strength is reduced by a factor, i.e.,

$$\phi_f = \phi/Fs, \quad c_f = c/Fs, \tag{4.57}$$

The reduced shear strength parameters are then used to compute the corresponding hypoplastic parameters C_1, C_2, C_3, C_4 by the procedure given in Chapter 2.

Table 4.8 Parameters for the homogeneous slope

Para.	E (Mpa)	v	ϕ	ψ	e_0	λ	ξ	α	β	c (kPa)
Value	100	0.35	20^o	0	0.957	0.022	0.061	1.5	1.0	12

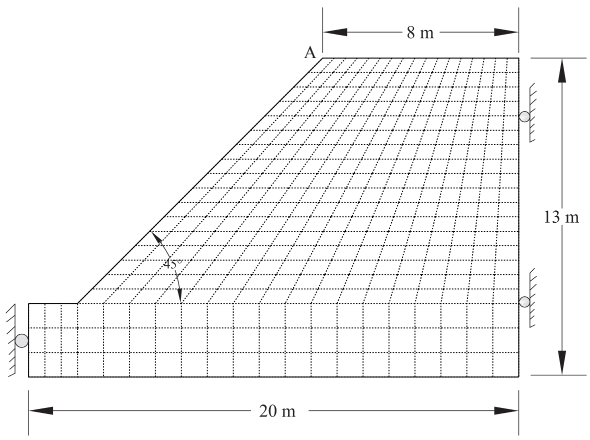

Figure 4.15 Geometry and boundary conditions of the slope

The considered slope is discretized by 349 four node plane strain elements. The bottom of the slope is fixed in horizontal and vertical direction, while the lateral boundaries are fixed in horizontal direction. To obtained the initial stress state, a geostatic step is performed by applying 2 g gravity loading to the soil. In this analysis step, the factor Fs keeps the constant value of 0.5 to avoid failure occurring. In the second step, the shear strength parameters reduced by increasing the factor Fs from 0.5 to 2.0. The initiation of slope failure is defined at which time the computation is not convergent. Therefore, a feasible incrementation is adopted in this simulation. The numerical results are presented in Table 4.9

Table 4.9 Results of different methods for Safety factor of slop(Automatic incrementation)

Method	CPU time (s)	Total Number of increments	Total Number of substeps	Max. Number of substeps	Safety factor
FE (100 substeps)	229.2	488	1.396×10^5	48800	1.2233
FEs (100 substeps)	317.7	482	1.396×10^5	48200	1.2041
CN method (100 substeps)					
STOL = 10^{-1}	363.5	529	1.396×10^5	42900	1.284
STOL = 10^{-2}	477.2	559	1.396×10^5	49300	1.3152
STOL = 10^{-3}	555.8	545	1.396×10^5	54500	1.2404
STOL = 10^{-4}	316.0	535	1.396×10^5	53500	1.2938
CNs method (100 substeps)					
STOL = 10^{-1}		Failed at 1^{st} increment			
STOL = 10^{-2}		Failed at 1^{st} increment			
STOL = 10^{-3}		Failed at 1^{st} increment			
STOL = 10^{-4}		Failed at 1^{st} increment			
RKF23sec method					
STOL = 10^{-1}	195.6	547	7714296	5526	1.3071
STOL = 10^{-2}	194.5	488	6908804	4949	1.2233
STOL = 10^{-3}	221.4	542	7630232	6108	1.2992
STOL = 10^{-4}	218.4	531	7425739	6050	1.2535
RKF23secs method					
STOL = 10^{-1}	113.0	354	4943236	3541	1.0223
STOL = 10^{-2}	135.5	510	7211736	5166	1.2563
STOL = 10^{-3}	141.9	510	7243457	5966	1.2563
STOL = 10^{-4}	135.0	510	7308777	6071	1.2563

It can be observed from Table 4.9 that all explicit methods with or without stress correction scheme give rise to a safety factor approximate 1.2, This means that the slope becomes unstable for the shear parameters of about $\phi = 16.7^o$ and c = 10 kPa. However, the various integration methods show very different performance. The forward Euler (FE) and forward Euler with stress correction (FEs) methods finish about 480 increments of the computation with every loading increment being divided into 100 equal substeps. However, the FE method with stress correction cost approximate 100 s much than the forward Euler method and gives rise to a less safety factor.

The implicit CN method with 100 equal substeps takes more than 500 increments to obtain the safety factor. It is noted that Increasing of the error tolerances does not correspondingly increase the computational time of the analysis for the CN method. The CN method with stress correction scheme fails in the 1^{th} increment as convergence is not obtained during the local iterations. This implies the local iteration is very sensitive to the stress state. Obviously, correction of the stresses may result in a large difference between the current and the last substep of the local iterations. Similarly, the adaptive explicit method with or without stress correction finishes more than 500 increments to get the safety factor. The total number of substeps for all Gauss points is much more than the forward Euler method and implicit CN method, while the total CPU times is less than the other methods without substepping schemes. This further indicates that the adaptive explicit methods can effectively save CPU time due to their adaptive nature. It is also noted that the adaptive explicit method with the stress correction (e.g.the RKF23secs method) cost less time than the RKF23sec method without stress correction.

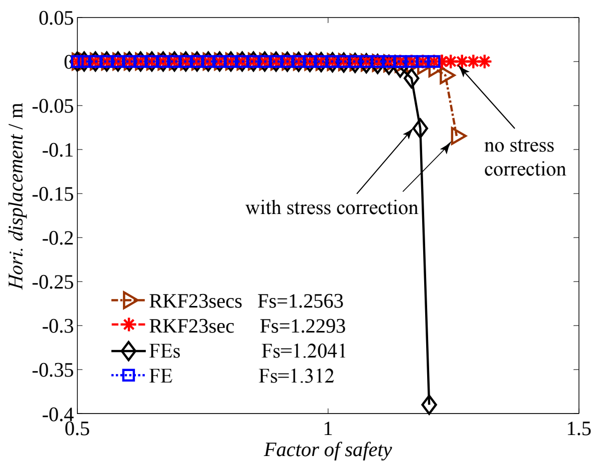

Figure 4.16 Change of the horizontal displacement at the top of the slope under different reduction factors using different integration strategies

The above results imply that, for numerical computation with a hypoplastic model, the stress correction scheme can significantly influence the computation. Fig. 4.16 presents the change of the horizontal displacement at the top of the slope (point A in Fig. 4.15) under different reduction factors using different integration strategies. It is observed that the computations with stress correction scheme can achieve a horizontal displacement of 0.1 m and 0.4 m for the adaptive explicit method and the forward Euler method, respectively.

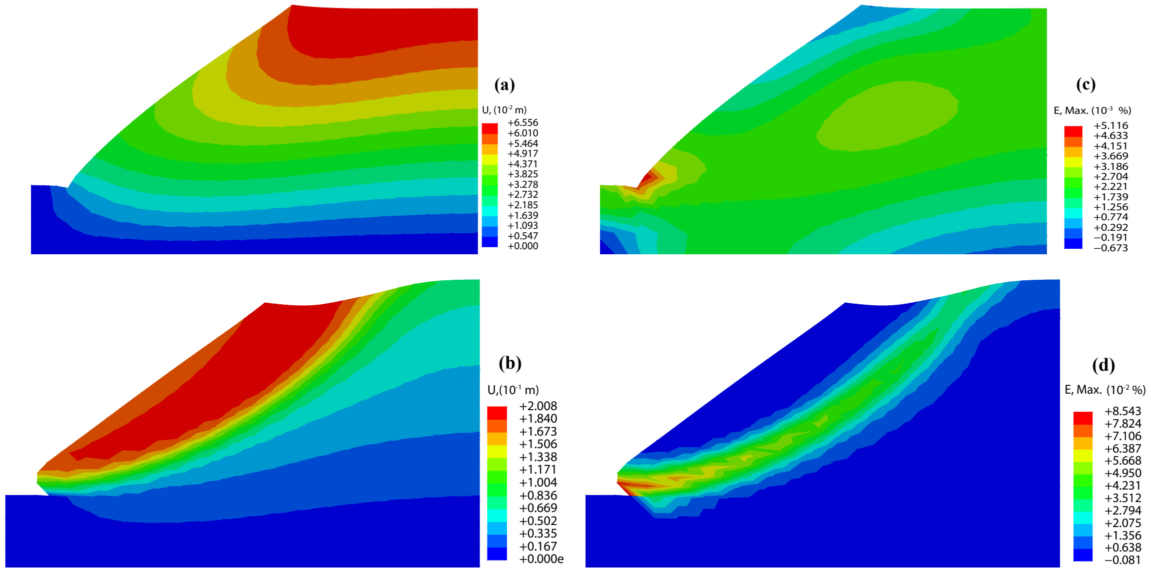

Figure 4.17 The failure surface depicted by the displacement (a,b) and the total equivalent strain (c,d) obtained from the RKF23sec (STOL= 10^{-4}) method no stress correction scheme (a, c) and with stress correction scheme (b,d)

However, the same methods without stress correction scheme obtain no convergence with negligible displacement. The effect of the stress correction scheme can be interpreted by the shear surface of the slope. Fig. 4.17(a),(b) shows the contour plots of the displacement at the final increment. It reveals that a failure surface depicted by the displacement can be observed in the computation with stress correction scheme, while there is no failure surface generated in the computation without stress correction scheme. Correspondingly, Fig. 4.17(c),(d) shows a shear band depicted by the equivalent strain in the computation with stress correction scheme. Therefore, the failure process can be captured by the computation using a hypoplastic constitutive model with stress correction scheme.

4.5 Conclusion

Some important aspects in solving local problems for the implementation of the updated hypoplastic models have been investigated. The influence of factors such as the load increment size, the initial state, the load directions, and the specified error tolerance, and stress correction on the performance of different integration strategies have been studied using triaxial compression tests, stress response envelopes and boundary value problems. The main conclusions of our studies with the hypoplastic model are summarized in the following:

(1) Hypoplastic models are quite sensitive to the increment size, the loading direction, and

the integration algorithm. Inaccurate integration methods can easily lead to unreliable results and thus may result in computation failure. In terms of accuracy, efficiency and robustness, adaptive explicit methods have better performance than implicit methods

(2) The implicit integration methods is sensitive to the loading direction and increment size. A significant error can be produced for the extension loading direction, even though convergence is achieved. On the other hand, the implicit integration methods are not sensitive to the error tolerance compared to the Adaptive explicit methods.

(3) Adaptive explicit methods can effectively avoid many of the shortcomings of implicit methods. They are less sensitive to the loading direction and increment size as they can automatically reduce the step size according to the prescribed accuracy requirement. The latter feature ensures that the step size is reduced in highly nonlinear regions. Not surprisingly, these techniques are quite sensitive to the specified error tolerance due to the strong nonlinearity of the hypoplastic model. The accuracy can be effectively improved by tightening the error tolerance, but this does not obviously increase the number of sub-steps and the CPU time.

(4) Although the adaptive explicit method can achieve adequate numerical results, the intrinsic shortcoming of a hypoplastic model that some stresses can lie outside the yield surface can not be solved. This may result in inaccuracy results. To avoid this shortcoming, stress correction technique must be employed. On one hand, the stress correction can guarantee all stresses lying inside the yield surface. On the other hand, it can stabilize the numerical computation of hypoplasticity in the condition of large increment size.

Chapter 5

Numerical implementation and simulation of the visco-hypoplastic model

5.1 Introduction

In engineering industry, the *Finite element method* incorporating with hypoplasticity has been developed, thus allowing geotechnical engineer, as well as researchers, to solve some complex boundary value problems. One of the first finite element implementation of hypoplastic constitutive model dates back to Sikora (Sikora, 1992). Few of early numerical applications of hypoplasticity to soil mechanical analysis are focused on numerical investigation of soil behavior, for example, generation of shear zone in sands (Tejchman and Bauer, 1996; Tejchman and Górski, 2010; Tejchman and Niemunis, 2006; Tejchman et al., 2007b), soil pressure with respect to void changing (Tejchman et al., 2007a), and deformation analysis of weathered rockfill materials (Bauer, 2009; Bauer et al., 2010). Nowadays, an increasing number of them have been found in practical geotechnical aspects, such as tunnel design (Mašín and Herle, 2005), pile installation process (Henke and Grabe, 2008), shallow foundations (Salciarini and Tamagnini, 2009; Sturm, 2009) and so on, but few of them are considering the time-dependent problems.

Recently, the theory of hypoplasticity has been extended to describe time-dependent behavior of soils according to the over-stress theory (Perzyna, 1963, 1966). A noteworthy visco-hypoplastic constitutive model by Niemunis (1996) has been widely used to describe the viscous effects (including strain-rate effects and rheological behavior) of soil. Later on, the capabilities of the visco-hypoplastic model have been numerically expanded to even more complex applications, such as footing penetration (Qiu and Grabe, 2011) and creeping movement of a natural slope (Van Den Ham et al., 2009). On the other hand, some viscous-hypoplastic models have been proposed based on the fluid theory, such as rheology, have been developed to describe the creep of frozen soil (Xu et al., 2016), debris flow (Guo et al., 2016; Peng et al., 2016). However, no numerical implementation of this kind of hypoplastic models has been reported by using the finite element method. One possible reason is that the visco-hypoplastic models based on the fluid theory usually contains a rheological part, which brings unpredictable risk into the numerical computation. Especially, the model by Xu et al. (2016) is assumed unable to implement into FEM code, because this model contains a higher order term.

In any numerical scheme employed for the analysis of the boundary value problems it eventually becomes necessary to integrate the constitutive equations governing the material behavior. Whereas the numerical performance relies highly on the methods we choose and inappropriate choices can easily lead to unsuccessful computations, unreliable results or unacceptably long analysis times. In most cases, the implementation of a constitutive law requires the resolution of systems of differential equations, thus requiring robust numerical integration algorithms which stem from the theory of differential calculus. Such numerical methods can be summarized in explicit and implicit methods: either an explicit or an implicit method can be employed and each one of the two methods has its advantages and shortcomings: in particular, for the integration of the elastoplastic model, the return mapping algorithm was formulated following an implicit scheme. Explicit methods have the advantages of being simple and straightforward to implement. Low-order explicit methods, such as the forward Euler method and the modified Euler method, however, often give results of low accuracy. This can lead to significant error in the numerical solutions or unexpected failure, especially for highly non-linear models such as those involving non-associated plastic flow. To overcome this shortcoming, Sloan (1987) introduced a substepping scheme which divides an increment of strain into several substeps automatically, based on an estimation of the local truncation error. This kind of integration method can be called the adaptive explicit method, which will be adopted for the implementation of the proposed visco-hypoplastic model. As is discussed in chapter 4, the stress correction scheme is of importance to guarantee the numerical accuracy of the hypoplastic constitutive model. Hence, a new stress correction strategy is applied in the implementation.

The present chapter is organized in the following. In section 5.2, the detailed numerical equation and integration method of the visco-hypoplastic model for creep is outlined. A stress correction scheme has been adopted to avoid numerical error in the integration of the creep model. In section 5.3, the predictive capabilities of the visco-hypoplastic model are examined by performing a series of numerical tests: e.g., a triaxial creep tests, and a gravity-induced creep of a homogeneous slope. In section 5.4, an in-situ direct shear creep test is presented. Then this test is examined by using FEM simulation with the proposed visco-hypoplastic model. Finally, some concluding remarks and suggestions for further studies are given in section 5.5.

5.2 Numerical implementation of the creep model

5.2.1 Numerical equation

The creep model is constructed in terms of creep acceleration components, which are used as the independent state variables in Umat (User defined material in Abaqus). To differentiate the creep constitutive equation (3.21), we evaluate all strain rates and state variables at time t with Eq. (4.32). Hence the acceleration equation can be recast in the following:

$$\ddot{\boldsymbol{\varepsilon}} = -\frac{-I_{se}\|\dot{\boldsymbol{\varepsilon}}\|^{-m}}{k_v}\left[C_1(\mathrm{tr}\boldsymbol{\sigma}_h)\dot{\boldsymbol{\varepsilon}} + C_2(\mathrm{tr}\dot{\boldsymbol{\varepsilon}})\boldsymbol{\sigma}_h + C_3\frac{\mathrm{tr}(\boldsymbol{\sigma}_h\cdot\dot{\boldsymbol{\varepsilon}})}{\mathrm{tr}\boldsymbol{\sigma}_h}\boldsymbol{\sigma}_h + C_4(\boldsymbol{\sigma}_h+\boldsymbol{\sigma}_h^*)\|\dot{\boldsymbol{\varepsilon}}\|I_e\right]. \quad (5.1)$$

Noted that the stresses are constant in creep process, thus the strain rates can be obtained by integration of the acceleration Eq. (5.1). The problem can be solved in the same way as adopted for the hypoplastic constitutive equation in chapter 4. For integration the creep equation, the following tangent is numerically evaluated (the subscript h is dropped as well for brevity)

$$\frac{\partial\ddot{\varepsilon}_{ij}}{\partial\dot{\varepsilon}_{mn}} = \frac{I_{se}\|\dot{\boldsymbol{\varepsilon}}\|^{-m}}{k_v}\left[C_1\Theta\boldsymbol{I}_{ijmn} + C_2\sigma_{ij}\delta_{mn} + C_3\frac{\sigma_{ij}\sigma_{mn}}{\Theta} + C_4(\sigma_{ij}+\sigma_{ij}^*)\dot{\mathscr{E}}_{mn}I_e\right] = h_{ijmn} \quad (5.2)$$

where $\boldsymbol{I}_{ijmn}$ is a rank-four symmetric identity tensor with components

$$\boldsymbol{I}_{ijmn} = \frac{1}{2}(\delta_{im}\delta_{jn} + \delta_{jm}\delta_{in}) \quad (5.3)$$

and $\Theta = \mathrm{tr}\boldsymbol{\sigma}$, $\quad \dot{\mathscr{E}}_{mn} = \dot{\varepsilon}_{mn}/\|\dot{\varepsilon}\|$. Then the constitutive equation can be recast in the following form:

$$\ddot{\varepsilon}_{ij} = h_{ijmn}\dot{\varepsilon}_{mn}, \quad (5.4)$$

Let $\boldsymbol{H}$ denotes the creep strain tangential tensor generated by $h_{ijmn} \to \boldsymbol{H}$, then the creep constitutive equation can be regarded as an ordinary differential equation, for which the general time integration over an increment step $t \in [t_n, t_{n+1}]$ can be written as:

$$\dot{\boldsymbol{\varepsilon}}_{n+1} = \dot{\boldsymbol{\varepsilon}}_n + \int_{t_n}^{t_{n+1}} h(\boldsymbol{\sigma}_h, \boldsymbol{\sigma}_v, e, \dot{\boldsymbol{\varepsilon}})d\tau = \dot{\boldsymbol{\varepsilon}}_n + \boldsymbol{H}\Delta\boldsymbol{\varepsilon}, \quad n = 1,2,... \quad (5.5)$$

where the subscript n denotes the n^{th} step of the analysis. The evolution of the void ratio is related to the volumetric strain $\dot{\varepsilon}_v = \mathrm{tr}(\dot{\boldsymbol{\varepsilon}})$ and $\dot{e} = (1+e)\cdot\dot{\varepsilon}_v$. A closed form of integration for the void ratio is therefore available:

$$e_{n+1} = (1+e_n)\cdot\exp(\Delta\varepsilon_v) - 1 \tag{5.6}$$

The stress-strain integration of the basic hypoplastic model has been studied in the last chapter. The main conclusion is that the explicit method with substepping and error control schemes give the best performance. Herein, the adaptive method for time integration of Eq. (5.5) will be adopted to obtain the creep strain step by step. Theologically, the strain increment obtained from Eq. (5.5) will keep the stresses constant at the creep, i.e., the creep strain increment should vanish the stress increment at step n:

$$||\Delta\boldsymbol{\sigma}_n|| = Tiny, \tag{5.7}$$

Due to the numerical error, the creep strain rate obtained from Eq. (5.5) may not always equal to the trailed strain rate in Abaqus, which may lead to numerical failure in the FEM computation. In order to make these two strain rates equal, a stress correction algorithm presented by Haj-Ali and Muliana (2004), as shown in subsection 5.2.2, is adopted to numerically remedy the shortcoming.

5.2.2 Adaptive integration algorithm with stress correction

To implement the creep constitutive model in a numerical algorithm, Eq. (5.1) needs to be recast in incremental form. A numerical integration method for a three-dimensional viscoelastic ULDB balloons has been presented by Gerngross et al. (2008). We follow the same approach for our creep constitutive equation. This method can be readily extended to any displacement-based FEM code, where the strain components are used as independent state variables.

At the time t_m, the Umat (Abaqus interface for a user defined material) passes a time increment Δt and a trial strain increment $\Delta\boldsymbol{\varepsilon}_h^{tr}$, which is determined by the Jacobian matrix computed at the end of the previous time increment. Likewise, the frictional stresses $\boldsymbol{\sigma}_f$ as well as the creep strain increment $\Delta\boldsymbol{\varepsilon}_m^{cr}$ are initialized based on the integration at the end of the previous time step. The difference between the trial and calculated creep strain increment can be obtained, and thus its scalar measure of relative error reads:

$$R_n = \frac{||\Delta\boldsymbol{\varepsilon}_n^{tr} - \Delta\boldsymbol{\varepsilon}_n^{cr}||}{||\Delta\boldsymbol{\varepsilon}_n^{tr}||} \tag{5.8}$$

The current integration over the n^{th} time step is accepted if the relative error is less than a given error tolerance TOL:

$$R_n \leqslant \mathrm{TOL}, \tag{5.9}$$

Box 1. Stress correction algorithm

1. Initialize stress, trial strain increment, time increment :
$$\boldsymbol{\sigma}_n = \boldsymbol{\sigma}, \quad \Delta\boldsymbol{\varepsilon}_n^{tr} = \Delta\boldsymbol{\varepsilon}^{tr}, \quad \Delta t_n = \Delta t$$
2. Computer frictional stress and creep strain increment with Δt_n:
$$\boldsymbol{\sigma}_n = \boldsymbol{\sigma}_n - \boldsymbol{\sigma}_{n-1}, \quad \Delta\boldsymbol{\varepsilon}_n^{cr} = \dot{\boldsymbol{\varepsilon}}_n^{cr}\Delta t_n$$
3. Compute relative error:
$$R_n = \frac{\|\boldsymbol{R}_n\|}{\|\Delta\boldsymbol{\varepsilon}_n^{tr}\|} = \frac{\|\Delta\boldsymbol{\varepsilon}_n^{tr} - \Delta\boldsymbol{\varepsilon}_n^{cr}\|}{\|\Delta\boldsymbol{\varepsilon}_n^{tr}\|}$$
4. Skip if the step failed:
$$\mathrm{IF} \quad R_n > \mathrm{TOL} \quad \mathrm{GO\ TO\ 7}$$
5. Integrate Eq. (5.1) to obtain creep strain rate for next time step :
$$\dot{\boldsymbol{\varepsilon}}_{n+1}^{cr} = \dot{\boldsymbol{\varepsilon}}_k^{cr} \quad \text{(subscript } k \text{ denotes RKF algorithms)}$$
6. Computer stress increment according to equation:
$$\Delta\boldsymbol{\sigma}_n = \boldsymbol{H}\Delta\boldsymbol{\varepsilon}_n^{tr} + \boldsymbol{D}\Delta\dot{\boldsymbol{\varepsilon}}_n^{tr}$$
7. If step has failed, correct the stress increment according to equation:
$$\Delta\boldsymbol{\sigma}_n = \left[\frac{\partial \boldsymbol{R}_n}{\partial \Delta\boldsymbol{\sigma}_n}\right]^{-1}\boldsymbol{R}_n$$
8. Integration process is complete, return finial stress tensor and Jacobian matrix:
$$\boldsymbol{\sigma}_{n+1} = \boldsymbol{\sigma}_n + \Delta\boldsymbol{\sigma}_n, \qquad \boldsymbol{J} = \left[\frac{\partial \boldsymbol{R}_n}{\partial \Delta\boldsymbol{\sigma}_n}\right]^{-1}, \quad \mathrm{EXIT}$$

Then the RKF algorithm has been used to solve equation (5.1) before all the stresses and state variables being updated. For integration of the acceleration equation, we first collect all the creep strain rate components and state variables in the super-vector $\boldsymbol{y}$

$$\boldsymbol{y} = \{\dot{\varepsilon}_{11}, \dot{\varepsilon}_{22}, \dot{\varepsilon}_{33}, \dot{\varepsilon}_{12}, \dot{\varepsilon}_{13}, \dot{\varepsilon}_{23}, e\}^{\mathrm{T}} \tag{5.10}$$

where $\dot{\varepsilon}_{ij}$ are creep rate components. Integration of Eq. (5.10) yields the creep strain rate for the next time step .

$$\dot{\boldsymbol{\varepsilon}}^{cr}_{n+1}, e_{n+1} \leftarrow \boldsymbol{y}' \tag{5.11}$$

Making use of tangential tensor $\boldsymbol{H}$ and $\boldsymbol{D}$, the stress increment $\Delta\boldsymbol{\sigma}_n$ can be obtained in the following:

$$\Delta\boldsymbol{\sigma}_n = \boldsymbol{D}\Delta\boldsymbol{\varepsilon}^{tr}_n + \boldsymbol{H}\Delta\dot{\boldsymbol{\varepsilon}}^{tr}_n \tag{5.12}$$

However, the integration process would be skipped if relative error is larger than the accuracy requirement. In this case, we get the stress correction.

$$\Delta\boldsymbol{\sigma}_n := \left[\frac{\partial \boldsymbol{R}_n}{\partial \Delta\boldsymbol{\sigma}_n}\right]^{-1} \boldsymbol{R}_n \tag{5.13}$$

After the integration process is complete, UMAT exits and return the stress tensor $\boldsymbol{\sigma}$ as well as the Jacobian matrix $\boldsymbol{J}$.

$$\boldsymbol{\sigma}_{n+1} = \boldsymbol{\sigma}_n + \Delta\boldsymbol{\sigma}_n, \qquad \boldsymbol{J} = \left[\frac{\partial \boldsymbol{R}_n}{\partial \Delta\boldsymbol{\sigma}_n}\right]^{-1} \tag{5.14}$$

Also, at the end of the increment, the history for creep strain rate and viscous stress components are stored using the state array. The complete structure of the stress correction algorithm is given in Box 1.

5.3 Numerical examples

In this section, two numerical simulations, e.g., triaxial creep test and gravity induced slope creep, are examined using the visco-hypoplastic model. In this simulation, the explicit adaptive method with a stress correction is used to integrate the constitutive equation (5.1). It should be noted that there is no attempt to match the simulation results with the experimental data since we only focus on the performance of the proposed model on multiple elements modeling.

5.3.1 Triaxial creep test

The first example is a triaxial creep test simulated using the visco-hypoplastic mode in FEM. The model has a height of 100 mm and a width of 50 mm. For the sake of simplicity, the asymmetric element is chosen for the FEM simulation, see Fig.5.1. The material parameters for modelling of the triaxial creep test are shown in the Table 5.1, and the initial void ratio is set to e_i = 0.92.

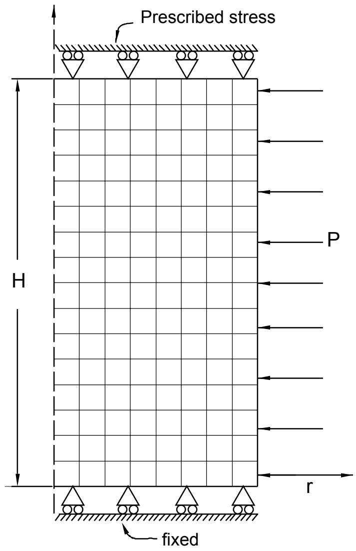

Figure 5.1 The finite element model and meshes of the triaxial test sample(unit:mm)

Table 5.1 Constitutive parameters for the simulation of the triaxial creep test

Para.	C_1	C_2	C_3	C_4	e_{co}	λ	ξ	α	β	k_v	m	χ
Value	-101.2	-962.1	-877.3	1229.2	0.947	0.022	0.51	1.0	10	350.5	0.5	1.08

There are two steps to conduct the creep test: Isotropic loading and creep loading. In the isotropic loading step, an initial isotropic stress state with $\sigma_{11} = \sigma_{22} = \sigma_{33} = 100$ kPa is assumed. For both steps, appropriate boundary conditions are needed to be applied. Since asymmetric elements are included, the nodes on the left side are fixed in the horizontal direction. and the bottom nodes are fixing in the vertical direction. In the creep loading step, a maximum axial (vertical) loading of $\sigma_{22} = 280$ kPa, which is greater than the creep threshold of this material, is applied on the top surface. In what follows, the creeping stage is automatically carried out for a creep time of 100000 min. As is depicted in the chapter 4, the initial conditions of strain rates, as well as the initial viscous stresses, are of significance for the simulation result. Therefore, care should be taken for setting these initial conditions. For an isotopically loaded model, the strain rates and viscous stresses are set to be the same for all integration points in this model. The initial condition of strain rates and viscous stress are shown in Table 5.2.

Table 5.2 Initial conditions and creeping load for the simulation of triaxial creep test

Index	$\dot{\varepsilon}_{11}$ (%/min)	$\dot{\varepsilon}_{22}$ (%/min)	σ_{v11} (kPa)	σ_{v22} (kPa)	σ_{11} (kPa)	σ_{22} (kPa)
Value	-0.142×10^{-4}	6.11×10^{-6}	-100	10	-280	100

The results of creep test are shown in Fig.5.2. Fig.5.2 (a) represent the contour plot of the total displacement, and the corresponding displacement components are shown in Fig.5.2 (b). It is observed that the sample experiences a short period of primary creep, which is followed by a very long time of second creep. It is also noted that the displacement rate is increasing after approximate 40000 hours both in the horizontal and vertical direction.

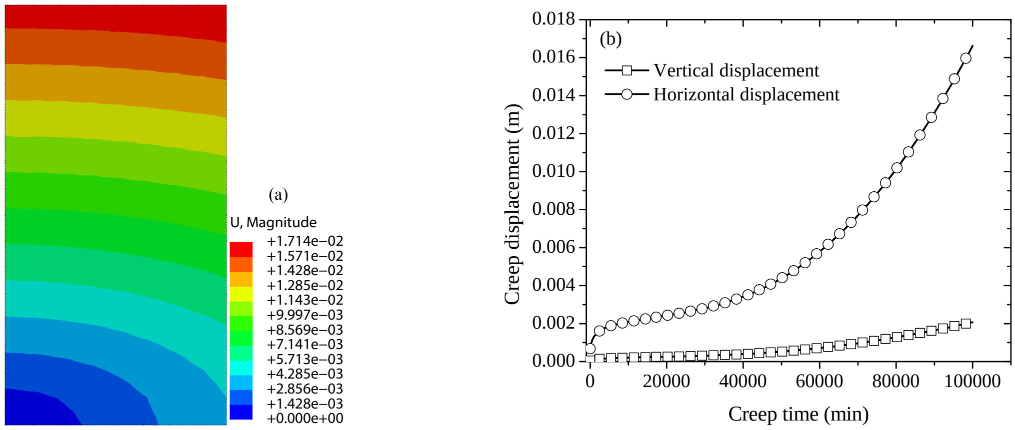

Figure 5.2 (a) The contour plot of the total displacement of the sample, and (b)the horizontal and vertical displacement at the node M

The strain rate and strain acceleration are presented in Fig.5.3. As can be observed from Fig.5.3(a), the strain rate decreases dramatically at the primary creep stage, and remains nearly constant in the second creep stage. In the third creep stage, the strain rate gradually increases. Correspondingly, the strain acceleration is positive at the beginning of creep. The positive acceleration leads to a reduction of the strain rate. Additionally, the absolute value of the acceleration rate in a log-log scale plot is presented in Fig.5.3(b). It reveals that the acceleration reaches zero at 18000 min, where the minimum strain rate is reached. This point can be characterized as the creep failure point. In the fowling time, the strain acceleration turns to negative and remains nearly constant. This negative strain acceleration constantly increases the strain rate in the third creep stage. From the above analysis, it can be concluded that the evaluation of the strain acceleration leads to the generation of the three stages of creep.

Two different types of creep strain, i.e., the integrated creep strain and the trial creep strain, are are presented in Fig.5.4(a). Both strain strains exhibit similar trend to the development of the creep displacement. It should be noted that integrated creep strain and the trial strain are compared, a very good agreement is achieved in this simulation. This implies that the stress correction scheme takes effect in this implementation.

The evolution of the viscous, the frictional, and the total stresses are presented in Fig.5.4(b). It can be observed from this figure that the total stress remains constant at the value of σ_{22}=

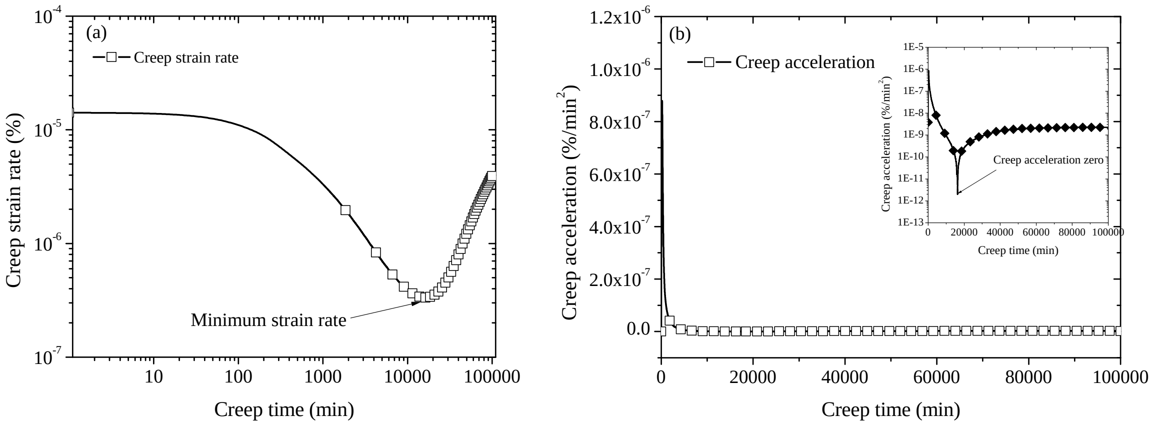

Figure 5.3 (a) log-log plot of the creep strain rate, and (b)Semi-log plot of the strain acceleration

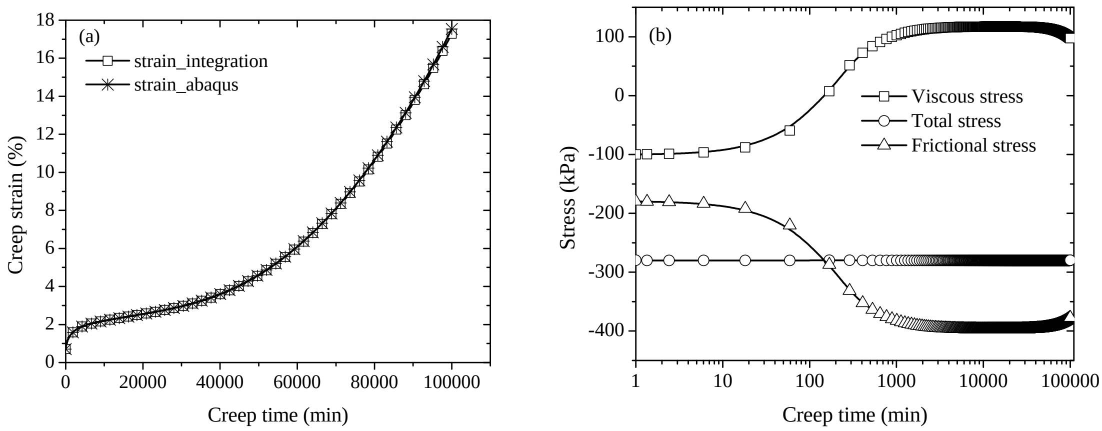

Figure 5.4 (a) The creep strain obtained from integration of the creep equation and the trial strain rate of Abaqus, and (b) the viscous, total, and frictional stresses

-280 kPa during the whole creep process. Although the viscous stress is initially set to be -100 kPa, it increases to 120 kPa in the primary creep stage, and then remains constant until the strain acceleration surpasses zero. Correspondingly, the frictional stress decreases from -180 kPa to -400 kPa. It can be observed, albeit very slowly, the viscous stress begins to decrease after the creep failure.

5.3.2 Gravity induced creep for a homogeneous slope

In the geotechnical engineering, some new-built slope may experience long-term deformation. Usually, the evaluation of the long-term stability of slops requires of the in-situ monitoring work, which is tedious and time-consuming. Therefore, numerical simulation of the creep slope is necessary for both economic and time consideration. In this study, the gravity-induced creep of a homogeneous slope is investigated using the proposed model. The slope model has a height of 30 m , and an angel of 45°. To present the simulation results, five positions at different depth of the slope are selected, as shown in Fig. 5.5. The parameters is presented as Table 5.3 and the slope soil has an initial void ratio of $e_i = 0.88$.

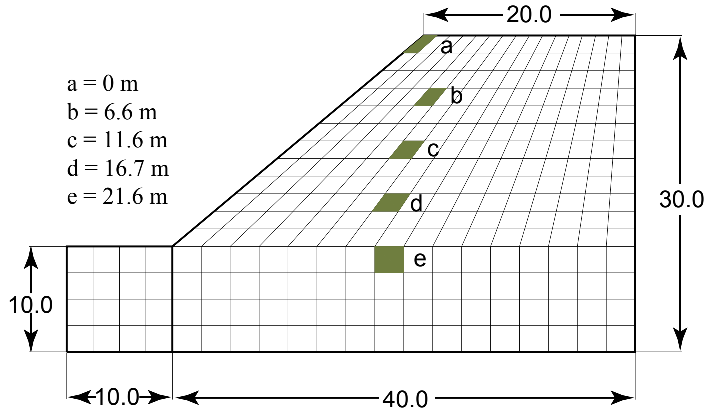

Figure 5.5 The finite element model and meshes of the slope(unit:m)

Table 5.3 Constitutive parameters for the simulation of the slope creep

Para.	C_1	C_2	C_3	C_4	e_{co}	λ	ξ	α	β	k_v	m	χ
Value	-47.2	-81.4	-692.8	-153.1	0.927	0.012	0.61	1.5	10	45.5	-0.5	1.68

Table 5.4 Initial condition of the slope modeling

Index	$\dot{\varepsilon}_{11}$ (%/min)	$\dot{\varepsilon}_{22}$	$\dot{\varepsilon}_{33}$	σ_{v11} (kPa)	σ_{v22}	σ_{v33}	gravity
Value	-0.182×10^{-4}	0.811×10^{-6}	0.111×10^{-8}	5	-10	5	2 g

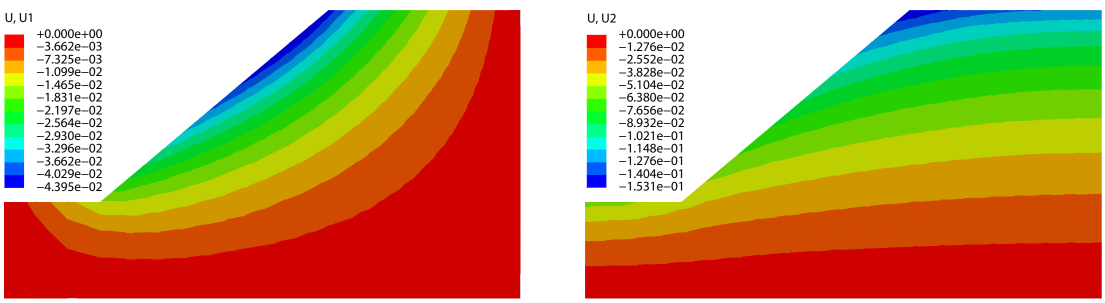

Figure 5.6 The contour plot of creep displacement of the slope: (U1) horizontal displacement, and (U2) vertical displacement

Similar to the previous test, this simulation also includes two steps. Before the creep process, a geostatic step is performed obtain the initial geostatic stress. In this step, a 2 g gravity load is imposed on the slope. After the initial equilibrium state is obtained, the slope begins to creep under the gravity load.During the simulation, the bottom boundary is fixed in both horizontal and vertical direction, and the lateral boundary is fixed in the vertical direction.The top of the slope is set to be free. The same initial viscous stress and initial strain rate are assigned to all slope element, which is presented in the Table 5.4. The contour plot of the horizontal and vertical displacements of the slope after 5000 hours' creep are presented in Fig.5.6. It reveals that all creep displacements increase gradually and then remain constant over the creep time. In addition, the creep deformation of the slope decreases with increasing the slope depth.

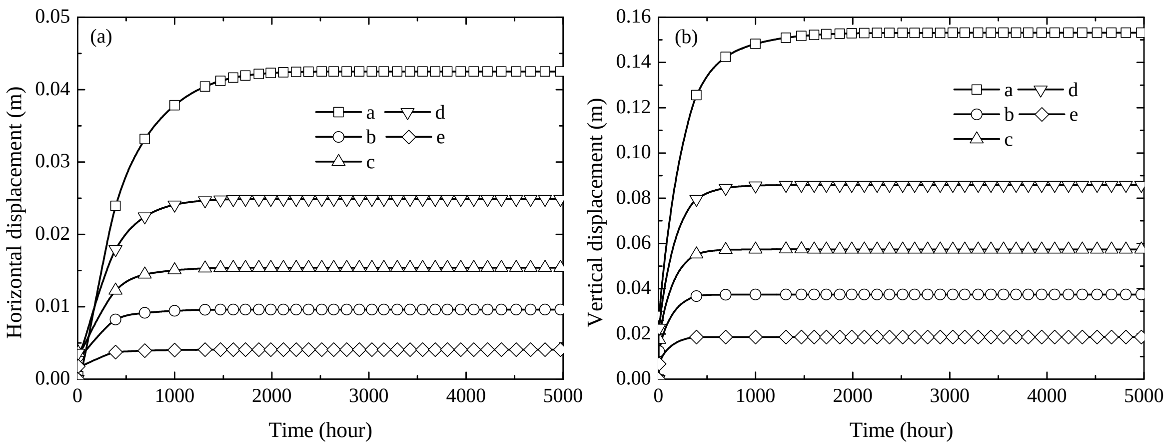

Figure 5.7 (a) The horizontal creep displacement, and (b)the vertical creep displacement at different depth of the slope

The creep strain rates at different slopes depth over creep time are presented in Fig. 5.8(a). Similar to the development of the creep displacement, all strain rates decrease gradually at the primary creep stage, and then remain constant during the rest creep time. Likewise, the largest strain rate in the slope is seen at the top of the slope, and the strain rate decreases with increasing the slope depth. Correspondingly, the strain accelerations at slope depth of 21.6 m, 16.7 m, 11.6 m and 6.6 m, as shown in Fig. 5.8(b), sequentially vanish at creep time of 1100 hour, 1500 hour, 1300 hour and 5000 hours, respectively. However, the strain acceleration at the top of the slope is still greater than zero at the end of the creep time. This implies the creep of the slope is non-stop.

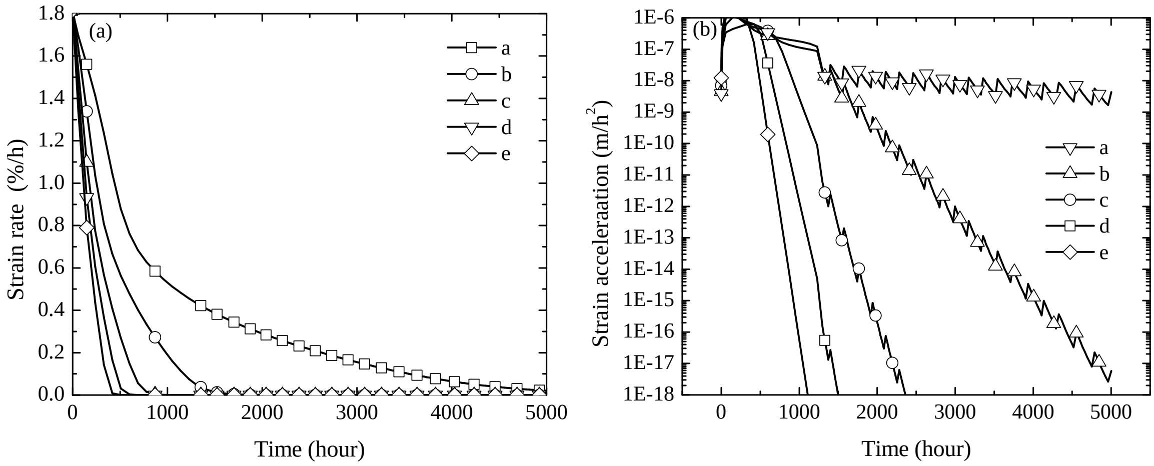

Figure 5.8 (a)Creep strain rate and (b)Creep acceleration at different depth of the slope

5.4 Modeling direct shear box creep test

In the direct shear test, the top half of the specimen is translated relative to the bottom half of the specimen in order to create a shear band/plane across the mid-height of the specimen (Zhang and Thornton, 2007). This test is widely used to measure the shear strength of soil. In geotechnical engineering, the test is performed in a Casagrande shear box (square cross-section). Usually, the direct shear box test is displacement-controlled, in which the externally applied vertical and horizontal forces are measured, and the ratio of horizontal to vertical load is assumed to provide an estimation of the average ratio of shear to normal stress acting in the shear band, and thereby provide a direct measure of the angle of internal friction. Owing to its reliability and simplicity, the direct shear box text is extended to investigate the viscous behavior of cohesive soil by modifying the displacement-control mode to force-control mode. The direct shear creep test has advantages in mimicking the creeping movement of a slope with a pre-existing shear surface. In this section, a force-controlled shear device is designed to perform an in-situ creep test. Then this test is examined by using FEM simulations with the proposed visco-hypoplastic model.

5.4.1 In-situ shear box creep test

To investigate the mechanism of slow-moving landslides, a testing tunnel was excavated beneath the sliding mass of the Huangtupo landslide by Three Gorges Research Center (China) in 2012. The in-situ creep test aimed to investigate the viscous behavior of the sliding zone soil, which is usually a composition of a large proportion of gravels and bounded by soil. The test tunnel was excavated along nearly the strike direction of the slip surface, exposing a sliding zone, on which the direct shear test was carried out.

The direct shear apparatus is made of steel for reliability and comprises a reaction frame, two servo-controlled, oil-actuated hydraulic jacks, a circulation cooling device and the box. The shear box consists two part, i.e., a upper and a lower box. The upper box has the dimensions $0.5 \times 0.5 \times 0.25$ m, while the low box is $0.5 \times 0.5 \times 0.10$ m. The The hydraulic jacks can produce an maximal shear force of 500 kN and normal force of 1000 kN. Both hydraulic jack has a 100 mm's stroke. This implies that the maximal shear and normal displacement is 100 mm. The configuration of the shear box, transducer valves, reaction frame and the loading cylinders are shown in Fig. 5.9.

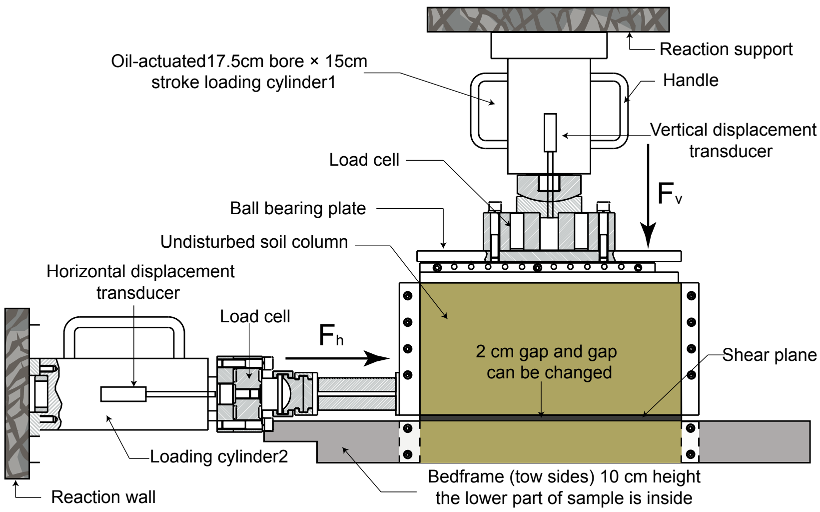

Figure 5.9 Configuration of large direct shear creep box

The in-situ creep test involved the assembly of the shear box and the application of the forces. To as real as possible to mimic the shear movement of the landslide, a block of sample, with near-vertical sides to the slipping surface, was prepared to approximate dimensions of 0.5 m $\times$ 0.5 m $\times$ 0.35 m on the inclined shear surface. Then the exposed interface was grouted flatly before the bedframe was fixed. The bedframe had a height of 0.10 m, and was used as the lower shear box, which accommodated the lower part of the soil sample. The upper shear box was centered over the upper part of the block sample, and stabilized by two adjustable support legs connecting with the bedframe. The gap between the box and the block was filled with wet coarse sand. Afterwards, the loading cylinders, transducers, and data acquisition system were instrumented.

The application of normal and shear forces were of crucial importance for the creep test. To apply the normal and shear forces, two reaction walls in the shear direction and the normal direction were built on the top the inclined slip surface and the left side of the tunnel lining, respectively. The shear force was applied directly to the upper box, at an offset to the plane of shear. The normal load was applied through a rigid pipe supported by the tunnel lining, which imposed a normal stress on the block. During testing, the shear and normal force were servo controlled; and the shear displacement of the upper shear box, vertical displacement of the loading plate, and air temperature were monitored by high-precision transducers. The test was terminated at a horizontal displacement of approximately 100 mm, or the failure occurs in the block sample. The field set-up of the shear box and physical dimensions are shown in Fig. 5.10.

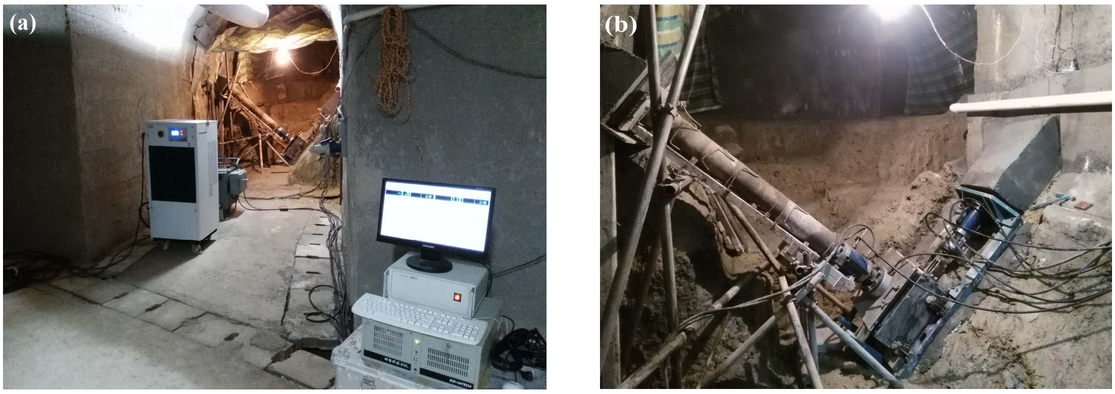

Figure 5.10 (a) Field set-up of the test, and (b) the inclined fixed shear box

Before starting the long-term shear creep test in the test tunnel, several displacement-control shear tests were conducted in the testing tunnel to investigate the general strength range of creep, using the same size of intact samples. Three normal effective stresses (e.g. 100 kPa, 300 kPa and 600 kPa) are applied for the direct shear box tests. The samples were sheared under a shear-rate controlled model with a shearing rate of 0.05 mm/min until the shear residence become constant. Usually, 30 - 40 mm shear displacement was needed to obtain the constant shear strength. The displacement-control shear tests gave a friction angle of about $\phi = 19.6°$, and cohesion of about $c = 30.5$ kPa, which was used as a reference for the assignation of the shear force in the in-situ creep test.

The in-situ shear creep test is so-called multistage creep test which is used commonly in the current creep test. In the test process, the shear force was brought rapidly up to an initial creep level and then was increased to the limit in several equal stress increments under constant normal effective stress, each kept constant for 15 days. Four in-situ creep tests were planned to conducted on the sliding surface. The first test took 34 days from July, 2015 to August 2015. Unfortunately, after two stages of creep test, a technical problem discontinued the test. Therefore, we carried out some short-term creep tests (two days for each stage) instead of long-term creep test after the malfunction was resolved. In consideration of the difficulties in maintaining the device on the inclined surface, only one test in-situ creep test was conducted finally. Improvement of the device is needed to make it more stable for the current test, and afterward, more in-situ tests will be carried out in the test tunnel. Therefore, numerical simulations of the direct shear creep tests are necessary to predict the rest tests at the present time.

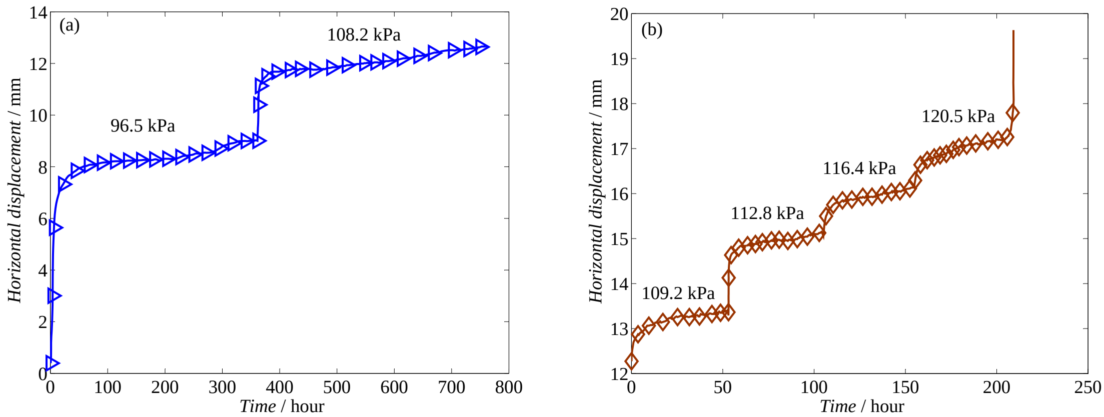

Figure 5.11 Creep displacement against creep time in (a) long-term creep test, and (b)short-term creep test ($\sigma' = 255$kPa)

The in-situ creep test was carried out under effect normal stress of 255 kPa. According to the Mohr-Coulomb criteria, the peak strength of the soil was 123 kPa under $\sigma_n = 255$ kPa. As interpreted in subsection 5.4.1, this test was divided into two part: the long-term creep test and the short-term creep test. The experimental results are presented in Fig.5.11. It can be observed that each stage of creep test starts with a rapid primary creep phase, which is followed by a long-term secondary creep phase with nearly constant horizontal creep displacement rate. The sample block experienced more than 12 mm shear displacement in the long-term creep test. In the short-term creep test, the shear stress increment was very small ($\Delta\tau$ = 3-4 kPa). Each stage of creep test might lead to more than 1.0 mm shear displacement. The sample block failed after 4 mm shear displacement at a shear stress of 120.5 kPa, which is very close to the assumed peak assumed peak strength.

5.4.2 Numerical simulation

Direct shear test

Two-dimensional simulations of the direct shear test using the finite element method (FEM) have been performed on the sling zone soil. Before the simulation of the shear creep test, a simulation of the displacement-control shear test is performed. This numerical simulation aims to study the basic strength parameters of the sliding zone soil. In this simulation, the mesh size is selected in accordance with the expected shear band width (i.e. 2 cm). The soil in a vertical cross section is discretized into 350 plane strain elements. Drained behavior is assumed for the soil. The interface between soil and box walls is assumed non-frictional, and the lateral walls are assumed by smooth rigid surfaces. Additionally, the steel cap of the shear box is assumed rigid and its rotation is prevented. Hence, the interactions between the soil and the shear box cannot be taken into account. Instead, the upper box is constrained in the horizontal direction to have the same displacement. Meanwhile, the top surface is constrained in the vertical direction. The lower box is fixed in the horizontal direction, and the bottom of the model is fixed in both direction. The shear box test is simulated by giving the upper half of the shear box a small displacement, and the corresponding horizontal shear load is obtained by summing the appropriate horizontal reaction force $\boldsymbol{F}$. In presenting the results of the analyses, the mean shear stress τ_{xy} is obtained by dividing the reaction force of the upper box by the initial length of the shear box (i.e. 50 cm).

$$\tau_{xy} = \frac{F}{L} \tag{5.15}$$

where $\boldsymbol{F}$ and L are the reaction force and the length of the shear box, respectively. A very small isotropic initial stress was giving as the initial stress in the sample before shearing, and the vertical load was applied as a distributed pressure on the top of the sample. The finite element grids and the boundary conditions are shown in Fig. 5.12. The initial void ratio of the soil is 0.48 and the rest of the parameters are presented in Table 5.5.

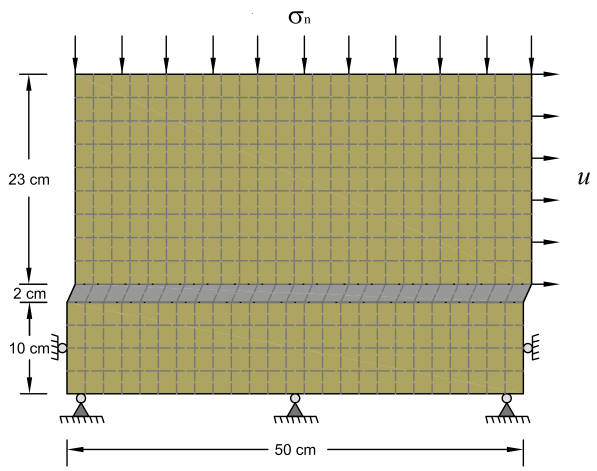

Figure 5.12 Finite element model of the direct shear test

The numerical predictions are shown in Fig. 5.13. The experimental results of the displacement-control shear box test are also shown for comparison. There is close agreement between the numerical predictions and experimental results. The same peak shear

Table 5.5 Constitutive parameters for the simulation of the direct shear test

Para.	C_1	C_2	C_3	C_4	e_{co}	λ	ξ	α	β	c
Value	-7.52	-74.6	-317.6	-48.8	0.55	0.032	0.51	1.2	1	30.5 kPa

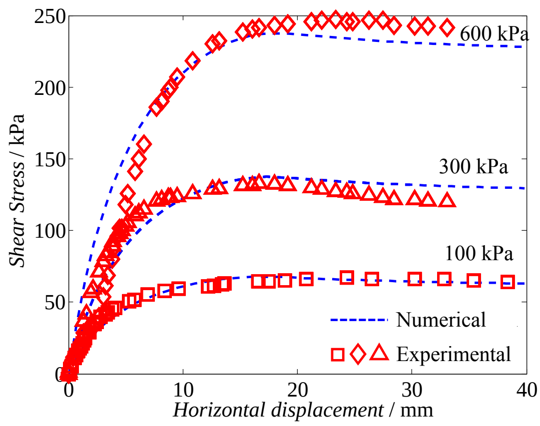

Figure 5.13 Comparison of the numerical predictions and experimental results in the direct shear box test under various normal effective stresses

strength is obtained in all normal stress level. However, the strain-softening behavior for high normal stress level is not well depicted. Despite this, the proposed hypoplastic constitutive model and the numerical simulation can perfectly capture the load - displacement behavior of the sliding zone soil in the shear box test.

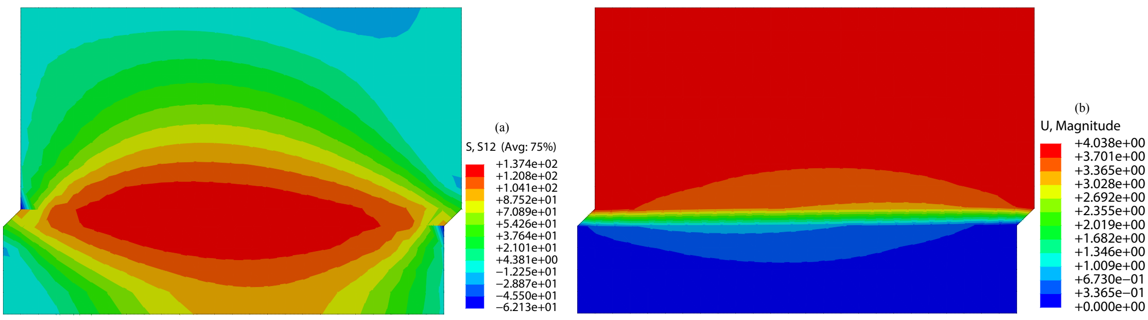

Figure 5.14 (a) Contour plot of the shear stress , and (b) shear displacement in direct shear box test under normal effect stress of 300 kPa

The last increment of the shear stress under the the normal effective stress of 300 kPa is presented in Fig. 5.14(a). As is shown in this figure, an elliptical stress concentrated zone is depicted in the area of the shear band. The magnitude of the largest shear stress in the shear band is very close to the shear stress in Fig.5.13. Meanwhile, the shear displacement is mainly concentrated in the shear zone as well, see 5.14(b). The numerical results have validated the hypoplastic constitutive model in the simulation of the direct shear box test, and further efforts will be made in the simulation of the direct shear creep test.

Direct shear creep test

The direct shear creep tests follow the same procedure as the direct shear box tests while using stress-control mode. Contrary to the experimental creep test, the numerical creep test is carried out using a single stage procedure instead of the multistage procedure. In the creep test simulation, the horizontal force is applied at the middle of the upper box after the vertical pressure is applied. The forces are sustained for a prescribed creep time.

The basic strength parameters of the soil were obtained from displacement-control shear test, as shown in Table 5.12. The viscous parameters were obtained from viscometer test, which gave the $k_v = 35.5$ and $m = -0.38$. The experimental results of the direct shear creep test in Fig. 5.11 are presented according to the multistage creep, while a superposition method is used to separately present the experimental and numerical results at each creep stage, see Fig.5.15.

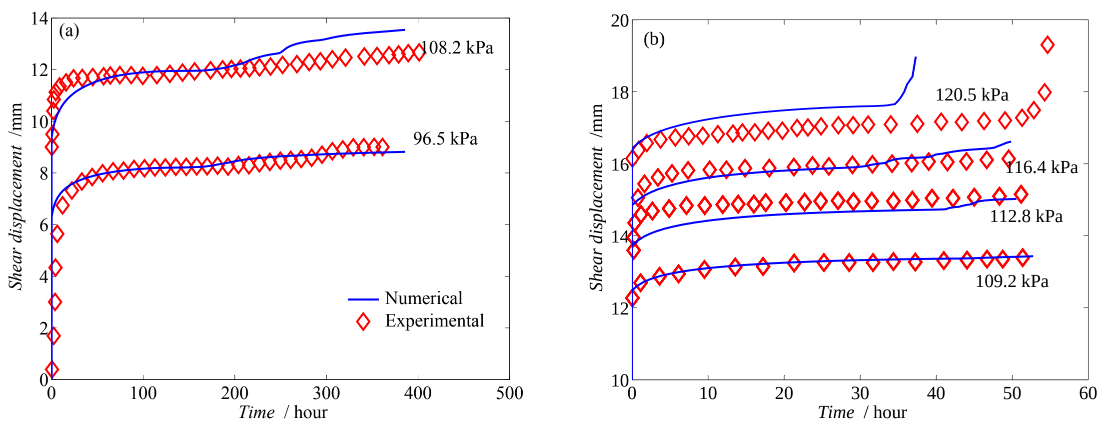

Figure 5.15 The numerical result of the direct shear box creep test, (a) long-term creep test, and (b) short-term creep test

Likewise, six levels of shear stress were applied to model the direct shear creep test, which includes two long-term creep tests (400 hours) and four short-term creep tests (50 hours). The simulation gave a very close prediction to the first stage of creep experiment with shear stress $\tau_{xy} = 96.5$ kPa. In the last stage of creep test, however, the numerical predilection of the failure time was much shorter than the experimental test. The contour plot of the shear stress is presented in Fig. 5.16, in which both the equivalent shear stress and the viscous shear stress after failure, are shown. Fig. 5.16(a) reveals that the shear stress in the soil sample is non-uniform. Specifically, the shear stress is mainly concentrated in the shear zone, which is oriented at approximately 10° to the horizontal. This might be induced by the dilation of the shear zone.

Fig. 5.16(b) presents the contour plot of the viscous shear stress at the last increment of the creep test. It reveals that the largest viscous shear stress is concentrated near the rupture areas. This implies these areas may significantly influence the viscous behavior of the soil in this simulation.

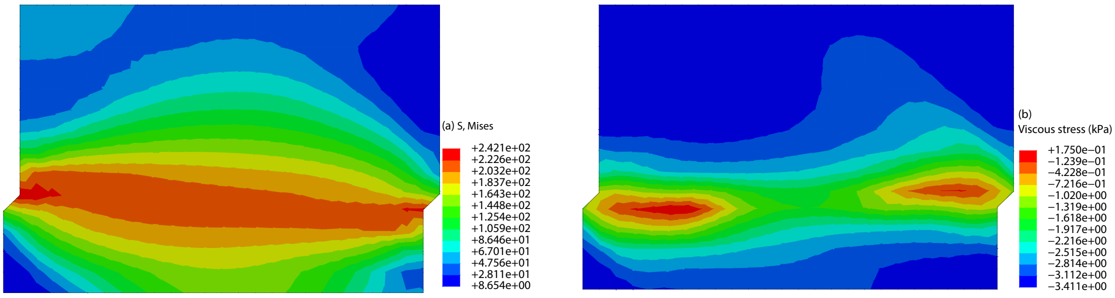

Figure 5.16 Contour plot of (a) the equivalent shear stress , and (b) viscous shear stress in direct shear box test under normal effect stress of 255 kPa

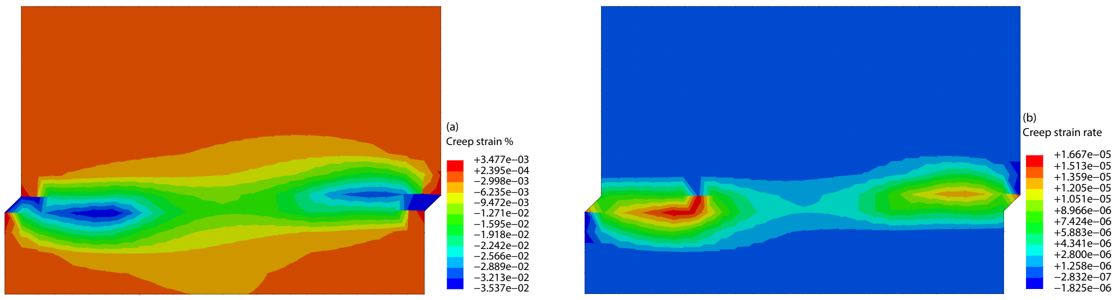

Figure 5.17 Contour plot of (a) the shear strain , and (b) shear strain rate in direct shear box test under normal effect stress of 255 kPa

The contour plot of the shear strain and the shear strain rate are shown in Fig. 5.17. Corresponding to the viscous shear stress in Fig. 5.16(b), the rupture areas have the largest shear strain and shear strain rate, since these areas experienced the largest shear displacement.

5.5 Conclusion

In this chapter, the visco-hypoplastic constitutive model has been successfully implemented into FEM code. The implementation has been validated by performing some simple boundary value problems, such as a triaxial creep test and a gravity induced slope creep. Finally, a numerical simulation of shear box creep test is performed using the proposed model. Some key conclusions can be drawn in the following:

Owing to the high order term (strain acceleration)in the visco-hypoplastic constitutive model, the numerical implementation of this model is not straightforward. However, this aim can be achieved by integrating the strain acceleration instead of the stress integration. An adaptive explicit method with a stress correction scheme is adopted, which can significantly reduce the integration error produced over accumulated time. The numerical model is validated by modeling some simple boundary value problems. Finally, a direct shear box creep experiment and numerical simulation using the proposed visco-hypoplastic model are carried out. The comparison of the experimental results and the results from finite element analysis shows that the visco-hypoplastic model is able to predict the behavior of soils. However, difficulties in determination of the parameters and assignation of the initial conditions are still challenges for practical application. Therefore, further investigations are required.

Chapter 6

Conclusion and further works

6.1 Main work

Modeling of viscous behavior of soils with finite element method is a challenging topic. It has been studied in many different disciplines by many researchers, but there are still many open-ended questions. In this dissertation, a new model is developed to describe the viscous behavior of the granular material. This model combines a simple critical state hypoplastic model and rheological model. The main work and conclusions of this study can be summarized as:

1. A simple critical state hypoplastic constitutive model is introduced for granular and cohesive soils, as shown in chapter 2. To incorporate the critical state behavior of soil, a newly critical function is adopted. Additionally, this model can take the cohesion into account, and thus can model some salient behavior of cohesive soil. It should be noted that this model is rate-independent, therefore cannot take into account the rheological properties of granular soil.

2. Based on the rate-independent hypoplastic constitutive model in chapter 2, a rate-dependent hypoplastic constitutive model, named as visco-hypoplastic the constitutive model is developed in chapter 3 to account for the rheological behaviors, such as acceleration effect and creep behavior, of granular materials. This viscous model is obtained by dividing the stress rate into a frictional and a viscous part, which is represented by the rate-independent model in chapter 2 and a high-order model with the term of strain acceleration, respectively. This model can describe not only the acceleration effect but also the creep behavior in granular material.

3. In order to implement the proposed visco-hypoplastic model, a comprehensive study

of the numerical integration method for the rare independent model in chapter 4 has been carried out. Several explicit and implicit integration methods together with a stress correction scheme have been discussed. The performance of different integration methods has been examined by performing triaxial compression tests, stress response tests, and some boundary value problems. In order to get proper results in numerical computation, the stress correction scheme is necessary for the implementation of the hypoplastic model.

4. On the basis of the numerical study of the rate-independent model, an adaptive method with stress correction scheme is proposed in chapter 5 to implement the visco-hypoplastic model into Finite Element method. The performance of this integration scheme has been examined by performing triaxial creep tests. Furthermore, some boundary value problems have been analyzed using the visco-hypoplastic model.

6.2 Open-ended questions and discussion

This study proposes a new approach to incorporate the time-dependent behavior of granular soil. Some concepts, such as acceleration effect in granular soils, accelerated loading, and creep acceleration have been outlined. Although this new model can describe some salient viscous behavior of granular materials, there are still some problems worthy of attention and need to be declared, such as the limitation of the models, feasible extension or reasonable improvement to the models. These problems are presented in below.

1. The hypoplastic model in chapter 2 possesses a Drucker-Prager type yield surface. This feature has enabled the implementation of this model much easier. Hence it has the same yield limit for both compression and extension. Additionally, this model is not able to correctly model the stress path at the undrained condition. Therefore, some modifications are needed to improve the prediction ability of this model.

2. The visco-hypoplastic constitutive model in chapter 3 has been proved to have a good performance. It can describe not only creep tests at different stresses, but also stepwise compression tests at different loading rates. However, the calibration of the model is a challenge. In the simulations in chapter 3, the model parameters are obtained by fitting experimental data. Hence, some effective methods for determining the parameters are still in need.

3. The viso-hypoplastic model is a combination of a frictional part and a viscous part. In this study, the frictional part of the visco-hypoplastic model is a simple hypoplastic

model for granular materials, but in general, the viscous behavior of clay soils is much more obvious than that of sands. Therefore, an advanced hypoplastic model for clay, such as the model by Mašín (2005), could be considered as a proper candidate to represent the frictional part of clay. With this combination, a new high-order hypoplastic model for clay creep can be proposed.

4. The initial viscous stress and initial strain rate in the application of the visco-hypoplastic constitutive model, owing to the existence of a high order term of strain, can not be obtained in a straightforward way. One approach is to perform an accelerated-control numerical test. Then the accumulated viscous stress can be used as the initial viscous stress. However, this sophisticated way primarily limits the practical application of the visco-hypoplastic.

References

AJ Abbo. *Finite element algorithms for elastoplasticity and consolidation*. PhD thesis, University of Newcastle Upon Tyne, 1997.

T Adachi and F Oka. Constitutive equations for normally consolidated clay based on elasto-viscoplasticity. *Soils and Foundations*, 22(4):57–70, 1982.

LQ AnhDan, F Tatsuoka, and J Koseki. Viscous effects on the stress-strain behavior of gravelly soil in drained triaxial compression. *Soils and Foundations*, 2006.

DD Atapattu, RP Chhabra, and PHT Uhlherr. Creeping sphere motion in herschel-bulkley fluids: flow field and drag. *Journal of non-newtonian fluid mechanics*, 59(2):245–265, 1995.

A Augustesen, M Liingaard, and PV Lade. Evaluation of time-dependent behavior of soils. *International Journal of Geomechanics*, 4(3):137–156, 2004.

JP Bardet. Lode dependences for isotropic pressure-sensitive elastoplastic materials. *Journal of Applied Mechanics*, 57(3):498–506, 1990.

E Bauer. Calibration of a comprehensive hypoplastic model for granular materials. *Soils and Foundations*, 36(1):13–26, 1996.

E Bauer. Hypoplastic modelling of moisture-sensitive weathered rockfill materials. *Acta Geotechnica*, 4(4):261–272, 2009.

E Bauer and W Wu. A hypoplastic constitutive model for cohesive powders. *Powder Technology*, 85(1):1–9, 1995.

E Bauer, ZZ Fu, and SH Liu. Hypoplastic constitutive modeling of wetting deformation of weathered rockfill materials. *Frontiers of Architecture and Civil Engineering in China*, 4 (1):78–91, 2010.

L Bjerrum. Problems of soil mechanics and construction on soft clays and structurally unstable soils (collapsible, expansive and others). In *Proc. of 8th Int. Conf. on SMFE*, volume 3, pages 111–159, 1973.

ET Bowman and K Soga. Mechanisms of setup of displacement piles in sand: laboratory creep tests. *Canadian Geotechnical Journal*, 42(5):1391–1407, 2005.

JB Burland and MC Burbridge. Settlement of foundations on sand and gravel. In *Institution of Civil Engineers, Proceedings, Pt 1*, volume 76, 1985.

R Chambon, J Desrues, W Hammad, and R Charlier. Cloe, a new rate-type constitutive model for geomaterials theoretical basis and implementation. *International Journal for Numerical and Analytical Methods in Geomechanics*, 18(4):253–278, 1994.

H Chen and CF Lee. Runout analysis of slurry flows with bingham model. *Journal of Geotechnical and Geoenvironmental Engineering*, 128(12):1032–1042, 2002.

H Chen, RH Chen, FC Yu, WS Chen, and JJ Hung. The inspection of the triggering mechanism for a hazardous mudflow in an urbanized territory. *Environmental Geology*, 45(7): 899–906, 2004.

FC Chow, RJ Jardine, F Brucy, and JF Nauroy. Effects of time on capacity of pipe piles in dense marine sand. *Journal of Geotechnical and Geoenvironmental Engineering*, 124(3): 254–264, 1998.

YF Dafalias and LR Herrmann. Bounding surface plasticity. ii: Application to isotropic cohesive soils. *Journal of Engineering Mechanics*, 112(12):1263–1291, 1986.

CS Desai and D Zhang. Viscoplastic model for geologic materials with generalized flow rule. *International Journal for Numerical and Analytical Methods in Geomechanics*, 11 (6):603–620, 1987.

H Di Benedetto, Tatsuoka F, and Masanori I. Time-dependent compression deformation characteristics of geomaterials and their simulation. *Soils and Foundations*, 42(2):1–22, 2002. doi: 10.3208/sandf.42.2_1.

C Di Prisco and S Imposimato. Time dependent mechanical behaviour of loose sands. *Mechanics of Cohesive-frictional Materials*, 1(1):45–73, 1996.

C Di Prisco, S Imposimato, and I Vardoulakis. Mechanical modelling of drained creep triaxial tests on loose sand. *Géotechnique*, 50(1):73–82, 2000.

YT Ding, WX Huang, DC Sheng, and SW Sloan. Numerical study on finite element implementation of hypoplastic models. *Computers and Geotechnics*, 68:78–90, 2015.

A Dragon and Z Mróz. A model for plastic creep of rock-like materials accounting for the kinetics of fracture. *International Journal of Rock Mechanics and Mining Sciences & Geomechanics Abstracts*, 16(4):253–259, 1979.

C Fang. Modeling dry granular mass flows as elasto-visco-hypoplastic continua with microstructural effects. ii. numerical simulations of benchmark flow problems. *Acta Mechanica*, 197(3-4):191–209, 2008.

W Fellin and A Ostermann. Consistent tangent operators for constitutive rate equations. *International Journal for Numerical and Analytical Methods in Geomechanics*, 26(12): 1213–1233, 2002.

W Fellin, M Mittendorfer, and A Ostermann. Adaptive integration of constitutive rate equations. *Computers and Geotechnics*, 36(5):698–708, 2009.

A Fodil, W Aloulou, and P Y Hicher. Viscoplastic behaviour of soft clay. *Géotechnique*, 47 (3):581–591, 1998.

H Fröhlich and R Sack. Theory of the rheological properties of dispersions. In *Proceedings of the Royal Society of London A: Mathematical, Physical and Engineering Sciences*, volume 185, pages 415–430. The Royal Society, 1946.

WM Fuentes, A Lizcano, D Fratta, AJ Puppala, B Munhunthan, et al. Visco-hypoplastic model for structured soils. In *Proceedings of GeoFlorida 2010: advances in analysis, modeling and design, West Palm Beach, Florida, USA, 20-24 February 2010.*, pages 452–460. American Society of Civil Engineers (ASCE), 2010.

A Gajo, L Piffer, and F De Polo. Analysis of certain factors affecting the unstable behaviour of saturated loose sand. *Mechanics of Cohesive-frictional Materials*, 5(3):215–237, 2000.

T Gerngross, YX Xu, and S Pellegrino. Viscoelastic behaviour of pumpkin balloons. *Advances in space research*, 42(10):1683–1690, 2008.

H Ghiabi and AP Selvadurai. Time-dependent mechanical behavior of a granular medium used in laboratory investigations. *International Journal of Geomechanics*, 9(1):1–8, 2009.

M Goldscheider. True triaxial tests on dense sand. In *International workshop on constitutive relations for soils*, pages 11–54, 1984.

G Gudehus. A comprehensive constitutive equation for granular materials. *TASK Quarterly: scientific bulletin of Academic Computer Centre in Gdansk*, 4(3):319–342, 2000.

G Gudehus. A visco-hypoplastic constitutive relation for soft soils. *Soils and Foundations*, 44(4):11–25, 2004.

XG Guo, C Peng, W Wu, and YQ Wang. A hypoplastic constitutive model for debris materials. *Acta Geotechnica*, 11(6):1217–1229, 2016.

RM Haj-Ali and AH Muliana. Numerical finite element formulation of the schapery non-linear viscoelastic material model. *International Journal for Numerical Methods in Engineering*, 59(1):25–45, 2004.

OM Heeres and R de Borst. Implicit integration of hypoplastic models. In *Constitutive Modelling of Granular Materials*, pages 457–470. Springer, 2000.

S Henke and J Grabe. Numerical investigation of soil plugging inside open-ended piles with respect to the installation method. *Acta Geotechnica*, 3(3):215–223, 2008.

I Herle and D Kolymbas. Hypoplasticity for soils with low friction angles. *Computers and Geotechnics*, 31(5):365–373, 2004.

SD Hinchberger and RK Rowe. Evaluation of the predictive ability of two elastic-viscoplastic constitutive models. *Canadian Geotechnical Journal*, 42(6):1675–1694, 2005.

WX Huang, W Wu, DA Sun, and S Sloan. A simple hypoplastic model for normally consolidated clay. *Acta Geotechnica*, 1(1):15–27, 2006.

X Huang and MH Garcia. A herschel-bulkley model for mud flow down a slope. *Journal of fluid mechanics*, 374:305–333, 1998.

RJ Jardine, JR Standing, and FC Chow. Some observations of the effects of time on the capacity of piles driven in sand. *Géotechnique*, 56(4):227–244, 2006.

P Jop, Y Forterre, and O Pouliquen. A constitutive law for dense granular flows. *Nature*, 441(7094):727–730, 2006.

H Karimpour and PV Lade. Time effects relate to crushing in sand. *Journal of Geotechnical and Geoenvironmental Engineering*, 136(9):1209–1219, 2010.

M Karstunen and ZY Yin. Modelling time-dependent behaviour of murro test embankment. *Géotechnique*, 60(10):735–749, 2010.

MG Katona. Evaluation of viscoplastic cap model. *Journal of Geotechnical Engineering*, 110(8):1106–1125, 1984.

MG Katona and MA Mulert. *A viscoplastic cap model for soils and rock*. Wiley, 1984.

E Kavazanjian and JK Mitchell. *A general stress-strain-time formulation for soils*. Place of publication not identified, 1977.

YT Kim and S Leroueil. Modeling the viscoplastic behaviour of clays during consolidation: application to berthierville clay in both laboratory and field conditions. *Canadian Geotechnical Journal*, 38(3):484–497, 2001.

S Kimoto and F Oka. An elasto-viscoplastic model for clay considering destructuralization and consolidation analysis of unstable behavior. *Soils and Foundations*, 45(2):29–42, 2005.

T Kiyota and F Tatsuoka. Viscous property of loose sand in triaxial compression, extension and cyclic loading. *Soils and Foundations*, 46(5):665–684, 2006.

D Kolymbas. A rate-dependent constitutive equation for soils. *Mechanics Research Communications*, 4(6):367–372, 1977.

D Kolymbas. A generalized hypoelastic constitutive law. In *Proceedings of XI International Conference Soil Mechanics and Foundation Engineering. AA Balkema, San Francisco*, 1985.

A Komornik, G Wiseman, and JG Zeitlen. Building settlement on end-bearing driven piles. In *Performance of Earth and Earth-Supported Structures*, page 1135. ASCE, 1972.

R Kuwano and RJ Jardine. On measuring creep behaviour in granular materials through triaxial testing. *Canadian Geotechnical Journal*, 39(5):1061–1074, 2002.

WA Lacerda and WN Houston. Stress relaxation in soils. In *Proceedings of 8th International Conference on Soil Mech. Found. Eng*, volume 2, pages 221–227, 1973.

PV Lade. Elasto-plastic stress-strain theory for cohesionless soil with curved yield surfaces. *International Journal of Solids and Structures*, 13(11):1019–1035, 1977.

PV Lade and JM Duncan. Elastoplastic stress-strain theory for cohesionless soil. *Journal of the Geotechnical Engineering Division*, 101(10):1037–1053, 1975.

PV Lade and CT Liu. Experimental study of drained creep behavior of sand. *Journal of Engineering Mechanics*, 124(8):912–920, 1998.

PV Lade, JA Yamamuro, and PA Bopp. Influence of time effects on instability of granular materials. *Computers and Geotechnics*, 20(3):179 – 193, 1997. ISSN 0266-352X. URL http://www.sciencedirect.com/science/article/pii/S0266352X97000025.

PV Lade, CD Liggio Jr, and J Nam. Strain rate, creep, and stress drop-creep experiments on crushed coral sand. *Journal of Geotechnical and Geoenvironmental Engineering*, 135 (7):941–953, 2009.

R Lal and MK Shukla. *Principles of soil physics*. CRC Press, 2004.

J Lee and GL Fenves. A return-mapping algorithm for plastic-damage models: 3-d and plane stress formulation. *International Journal for Numerical Methods in Engineering*, 50(2):487–506, 2001.

S Leroueil, M Kabbaj, F Tavenas, and R Bouchard. Stress-strain-strain rate relation for the of sensitive natural clays compressibility of sensitive natural clays. *Géotechnique*, 1985.

PI Lewin and John B Burland. Stress-probe experiments on saturated normally consolidated clay. *Géotechnique*, 20(1):38–56, 1970.

XS Li and Y Wang. Linear representation of steady-state line for sand. *Journal of Geotechnical and Geoenvironmental Engineering*, 124(12):1215–1217, 1998.

M Liingaard, A Augustesen, and PV Lade. Characterization of models for time-dependent behavior of soils. *International Journal of Geomechanics*, 4(3):157–177, 2004.

J Lin, W Wu, and RI Borja. Micropolar hypoplasticity for persistent shear band in heterogeneous granular materials. *Computer Methods in Applied Mechanics and Engineering*, 289:24–43, 2015.

A Lizcano, V Rinaldi, and WM Fuentes. Visco-hypoplastic model for pampean loess. *Mecánica Computacional, XXVI, Córdoba, Argentina*, 26:2646–2655, 2007.

D Mašín. A hypoplastic constitutive model for clays. *International Journal for Numerical and Analytical Methods in Geomechanics*, 29(4):311–336, 2005.

D Mašín and I Herle. Numerical analyses of a tunnel in london clay using different constitutive models. In *In Proc. 5th Int. Symposium TC28 Geotechnical Aspects of Underground Construction in Soft Ground. Amsterdam, The Netherlands*, 2005.

D Mašín and N Khalili. Modelling of the collapsible behaviour of unsaturated soils in hypoplasticity. In *1st European Conference on Unsaturated Soils, Durham, UK*, pages 659–665, 2008a.

D Mašín and N Khalili. A hypoplastic model for mechanical response of unsaturated soils. *International Journal for Numerical and Analytical Methods in Geomechanics*, 32(15): 1903–1926, 2008b.

H Matsuoka and T Nakai. Stress-deformation and strength characteristics of soil under three different principal stresses. In *Proc. JSCE*, volume 232, pages 59–70, 1974.

M Matsushita. Time effects on the prepeak deformation properties of sands. In *Proc. Second Int. Conf. on Pre-Failure Deformation Characteristics of Geomaterials, IS Torino'99*, volume 1, pages 681–689. Balkema, 1999.

CA Mejia, YP Vaid, and D Negussey. *Time dependent behaviour of sand*. 1988.

N Miura and T Yamanoucm. Effect of water on the behavior of a quartz-rich sand under high stresses. *Soils and Foundations*, 15(4):23–34, 1975.

MM Morsy, NR Morgenstern, and DH Chan. Simulation of creep deformation in the foundation of tar island dyke. *Canadian Geotechnical Journal*, 32(6):1002–1023, 1995.

S Murayama. Formulation of stress-strain-time behavior of soils under deviatoric stress condition. *Soils and Foundations*, 23(2):43–57, 1983.

S Murayama, K Michihiro, and T Sakagami. Creep characteristics of sands. *Soils and Foundations*, 24(2):1–15, 1984.

PM Naghdi and SA Murch. On the mechanical behavior of viscoelastic/plastic solids. *Journal of Applied Mechanics*, 30(3):321, 1962.

A Niemunis. A visco-plastic model for clay and its fe-implementation. *Recent results in mechanics of soils and rocks*, pages 151–162, 1996.

A Niemunis. Anisotropic effects in hypoplasticity. In *Proc. Int. Symp. on Deformation Characteristics of Geomaterials, Lyon, France*, volume 1, pages 1211–1217, 2003a.

A Niemunis. *Extended hypoplastic models for soils*, volume 34. Inst. für Grundbau und Bodenmechanik, 2003b.

A Niemunis and S Krieg. Viscous behaviour of soil under oedometric conditions. *Canadian Geotechnical Journal*, 33(1):159–168, 1996.

A Niemunis, CE Grandas-Tavera, and LF Prada-Sarmiento. Anisotropic visco-hypoplasticity. *Acta Geotechnica*, 4(4):293–314, 2009.

M Norihiko, M Hidekazu, and Y Noririyvkr. Stress-strain characteristics of sand in a particle-crushing region. *Soils and Foundations*, 24(1):77–89, 1984.

R Nova. A viscoplastic constitutive model for normally consolidated clay. In *Proceedings of the IUTAM symposium on deformation and failure of granular materials*, volume 1, pages 287–95, 1982.

S Nushimura, I Towhata, and T Honda. Laboratory shear tests on viscous nature of liquefied sand. *Soils and Foundations*, 42(4):89–98, 2002.

JG Oldroyd. The elastic and viscous properties of emulsions and suspensions. In *Proceedings of the Royal Society of London A: Mathematical, Physical and Engineering Sciences*, volume 218, pages 122–132. The Royal Society, 1953.

W Olszak and P Perzyna. *The constitutive equations of the flow theory for a non-stationary yield condition*. Springer Berlin Heidelberg, 1966a.

W Olszak and P Perzyna. The constitutive equations of the flow theory for a non-stationary yield condition. In *Applied Mechanics*, pages 545–553. Springer, 1966b.

M Pastor, OC Zienkiewicz, and AHC Chan. Generalized plasticity and the modelling of soil behaviour. *International Journal for Numerical and Analytical Methods in Geomechanics*, 14(3):151–190, 1990.

C Peng, W Wu, HS Yu, and C Wang. A sph approach for large deformation analysis with hypoplastic constitutive model. *Acta Geotechnica*, pages 1–15, 2015.

C Peng, XG Guo, W Wu, and YQ Wang. Unified modelling of granular media with smoothed particle hydrodynamics. *Acta Geotechnica*, 11(6):1231–1247, 2016.

P Perzyna. The constitutive equations for rate sensitive plastic materials. *Quarterly of applied mathematics*, pages 321–332, 1963.

P Perzyna. Fundamental problems in viscoplasticity. *Advances in applied mechanics*, 9: 243–377, 1966.

JH Prevost. Undrained stress-strain-time behavior of clays. *Journal of Geotechnical and Geoenvironmental Engineering*, 102(ASCE# 12644), 1976.

G Qiu and J Grabe. Explicit modeling of cone and strip footing penetration under drained and undrained conditions using a visco-hypoplastic model. *geotechnik*, 34(3):205–217, 2011.

D Roddeman. "fem-implementation of hypoplasticity" european union project (erbchbgct 940554). *Institut für Geotechnik und Tunnelbau, Baufakultät, Universität Innsbruck*, 1997.

RK Rowe and SD Hinchberger. Significance of rate effects in modelling the sackville test embankments. *Canadian Geotechnical Journal*, 35(3):500–516, 1998.

D Salciarini and C Tamagnini. A hypoplastic macroelement model for shallow foundations under monotonic and cyclic loads. *Acta Geotechnica*, 4(3):163–176, 2009.

H Sekiguchi. Induced anisotropy and time dependency in clays. *Proc Specialty Session Icsmfe*, pages 229–239, 1977.

I Shahrour and Y Meimon. Calculation of marine foundations subjected to repeated loads by means of the homogenization method. *Computers and Geotechnics*, 17(1):93–106, 1995.

Z Sikora. *Hypoplastic flow of granular materials: A numerical approach*. Publication Series of the Institute of Soil Mechanics and Rock Mechanics, Karlsrnhe University, No. 123, 1992.

A Sing and JK Mitchell. General stress–strain-time functions for soils. *Journal of the Soil Mechanics and Foundations Division*, 94(1):21–46, 1968.

SW Sloan. Substepping schemes for the numerical integration of elastoplastic stress–strain relations. *International Journal for Numerical Methods in Engineering*, 24(5):893–911, 1987.

H Sturm. Numerical investigation of the stabilisation behaviour of shallow foundations under alternate loading. *Acta Geotechnica*, 4(4):283–292, 2009.

C Tamagnini, G Viggiani, and R Chambon. A review of two different approaches to hypoplasticity. In *Constitutive modelling of granular materials*, pages 107–145. Springer, 2000.

M Tankeo, Patrick Richard, and É Canot. Analytical solution of the mu (i)-rheology for fully developed granular flows in simple configurations. *Granular Matter*, 15(6):881–891, 2013.

F Tatsuoka, F Santucci de Magistris, K Hayano, J Koseki, and Y Momoya. Some new aspects of time effects on the stress-strain behaviour of stiff geomaterials. In *2nd Int. Conf. Hard Soils and Soft Rock*, volume 3, pages 1285–1371, 2000.

F Tatsuoka, T Uchimura, K Hayano, H Di Benedetto, J Koseki, and MSA Siddiquee. Time-dependent deformation characteristics of stiff geomaterials in engineering practice. In *Proceedings of 2nd International Conference on Pre-failure Deform. Charact. of Geomat*, volume 2, pages 1161–1262, 2001.

F Tatsuoka, M Ishihara, H Di Benedetto, and R Kuwano. Time-dependent compression deformation characteristics of geomaterials and their simulation. *Soils and Foundations*, 42(2):103–129, 2002.

F Tatsuoka, H Di Benedetto, T Enomoto, and W Kongkitkul. Various viscosity types of geomaterials in shear and their mathematical expression. *Soils and Foundations*, 48(1): 41–60, 2008.

F Tavenas, S Leroueil, P La Rochelle, and M Roy. Creep behaviour of an undisturbed lightly overconsolidated clay. *Canadian Geotechnical Journal*, 15(3):402–423, 1978.

J Tejchman and E Bauer. Numerical simulation of shear band formation with a polar hypoplastic constitutive model. *Computers and Geotechnics*, 19(3):221–244, 1996.

J Tejchman and J Górski. Finite element study of patterns of shear zones in granular bodies during plane strain compression. *Acta Geotechnica*, 5(2):95–112, 2010.

J Tejchman and A Niemunis. Fe-studies on shear localization in an anistropic micro-polar hypoplastic granular material. *Granular matter*, 8(3-4):205–220, 2006.

J Tejchman, I Herle, and J Wehr. Fe-studies on the influence of initial void ratio, pressure level and mean grain diameter on shear localization. *International Journal for Numerical and Analytical Methods in Geomechanics*, 23(15):2045–2074, 1999.

J Tejchman, E Bauer, and SF Tantono. Influence of initial density of cohesionless soil on evolution of passive earth pressure. *Acta Geotechnica*, 2(1):53–63, 2007a.

J Tejchman, E Bauer, and W Wu. Effect of fabric anisotropy on shear localization in sand during plane strain compression. *Acta Mechanica*, 189(1-4):23–51, 2007b.

G Van Den Ham, J Rohn, T Meier, and K Czurda. A method for modeling of a creeping slope with a visco-hypoplastic material law. *Mathematical Geology*, 38(6):711–719, 2006.

G Van Den Ham, J Rohn, T Meier, and K Czurda. Finite element simulation of a slow moving natural slope in the upper-austrian alps using a visco-hypoplastic constitutive model. *Geomorphology*, 103(1):136–142, 2009.

R Verdugo and Ishihara K. The steady state of sandy soils. *Soils and Foundations*, 36(2): 81–91, 1996.

PA Von Wolffersdorff. A hypoplastic relation for granular materials with a predefined limit state surface. *Mechanics of Cohesive-frictional Materials*, 1(3):251–271, 1996.

M Wallin, M Ristinmaa, and NS Ottosen. Kinematic hardening in large strain plasticity. *European Journal of Mechanics - A/Solids*, 22(3):341–356, 2003.

CC Wang. A new representation theorem for isotropic functions. *Archive for rational mechanics and analysis*, 36(3):166–233, 1970.

XT Wang. *An updated hypoplastic model, its implementation and its application in tunelling*. PhD thesis, PhD thesis, Institute of Geotechnical engineering, University of Natural Resources and Life Sciences, Vienna, 2009.

T Weifner and D Kolymbas. A hypoplastic model for clay and sand. *Acta Geotechnica*, 2 (2):103–112, 2007.

J W Wissmann and C Hauck. Efficient elastic-plastic finite element analysis with higher order stress-point algorithms. *Computers and Structures*, 17(1):89–95, 1983.

W Wu. A unified numerical integration formula for the perfectly plastic von mises model. *International Journal for Numerical Methods in Engineering*, 30(3):491–504, 1990.

W Wu. On a simple critical state model for sand. *Proc. 7th Int, Symp. Numerical Models in Geomechanics*, 1999.

W Wu. On high-order hypoplastic models for granular materials. *Journal of Engineering Mechanics*, 56(1):23–34, 2006.

W Wu and E Bauer. A hypoplastic model for barotropy and pyknotropy of granular soils. *Modern Approaches to Plasticity*, 383, 1993.

W Wu and E Bauer. A simple hypoplastic constitutive model for sand. *International Journal for Numerical and Analytical Methods in Geomechanics*, 18(12):833–862, 1994.

W Wu and D Kolymbas. Numerical testing of the stability criterion for hypoplastic constitutive equations. *Mechanics of Materials*, 9(3):245–253, 1990.

W Wu and D Kolymbas. Hypoplasticity then and now. In *Constitutive modelling of granular materials*, pages 57–105. Springer, 2000.

W Wu and A Niemunis. Failure criterion, flow rule and dissipation function derived from hypoplasticity. *Mechanics of Cohesive-frictional Materials*, 1(2):145–163, 1996.

W Wu and A Niemunis. Beyond failure in granular materials. *International Journal for Numerical and Analytical Methods in Geomechanics*, 21(3):153–174, 1997.

W Wu, E Bauer, A Niemunis, and I Herle. Visco-hypoplastic models for cohesive soils. *Modern Approaches to Plasticity*, pages 365–383, 1993.

W Wu, E Bauer, and D Kolymbas. Hypoplastic constitutive model with critical state for granular materials. *Mechanics of Materials*, 23(1):45–69, 1996.

GF Xu, W Wu, and JL Qi. Modeling the viscous behavior of frozen soil with hypoplasticity. *International Journal for Numerical and Analytical Methods in Geomechanics*, 2016.

JA Yamamuro and PV Lade. Effects of strain rate on instability of granular soils. 1993.

JH Yin. Non-linear creep of soils in oedometer tests. *Géotechnique*, 49(5):699–707, 1999.

JH Yin and J Graham. Viscous–elastic–plastic modelling of one-dimensional time-dependent behaviour of clays. *Canadian Geotechnical Journal*, 26(2):199–209, 1989.

JH Yin, J Graham, JI Clark, and L Gao. Modelling unanticipated pore-water pressures in soft clays. *Canadian Geotechnical Journal*, 31(5):773–778, 1994.

ZY Yin and PY Hicher. Identifying parameters controlling soil delayed behaviour from laboratory and in situ pressuremeter testing. *International Journal for Numerical and Analytical Methods in Geomechanics*, 32(12):1515–1535, 2008.

ZY Yin, M Karstunen, and PY Hicher. Evaluation of the influence of elasto-viscoplastic scaling functions on modelling time-dependent behaviour of natural clays. *Soils and Foundations*, 50(6):203–214, 2010a.

ZY Yin, M Karstunen, CS Chang, M Koskinen, and M Lojander. Modeling time-dependent behavior of soft sensitive clay. *Journal of Geotechnical and Geoenvironmental Engineering*, 137(11):1103–1113, 2011.

ZYu Yin, CS Chang, M Karstunen, and PY Hicher. An anisotropic elastic–viscoplastic model for soft clays. *International Journal of Solids and Structures*, 47(5):665–677, 2010b.

L Zhang and C Thornton. A numerical examination of the direct shear test. *Géotechnique*, 57(4):343–354, 2007.

Appendendix I

Matrices $[\mathscr{L}]$ and $[N]$ for Eq.(2.14)

The fourth-order tensor $[\mathscr{L}]$ and the second-order tensor $[N]$ in Eq. (2.9) can be written as a 6×6 and a 6×1 matrices, respectively. The constitutive equation (2.14) can be recast in the following matrix form:

$$\begin{bmatrix}\mathring{\sigma}_{11}\\ \mathring{\sigma}_{22}\\ \mathring{\sigma}_{33}\\ \mathring{\sigma}_{12}\\ \mathring{\sigma}_{13}\\ \mathring{\sigma}_{23}\end{bmatrix} = \begin{bmatrix}\mathscr{L}_{11} & \mathscr{L}_{12} & \mathscr{L}_{13} & \mathscr{L}_{14} & \mathscr{L}_{15} & \mathscr{L}_{16}\\ \mathscr{L}_{21} & \mathscr{L}_{22} & \mathscr{L}_{23} & \mathscr{L}_{24} & \mathscr{L}_{25} & \mathscr{L}_{26}\\ \mathscr{L}_{31} & \mathscr{L}_{32} & \mathscr{L}_{33} & \mathscr{L}_{34} & \mathscr{L}_{35} & \mathscr{L}_{36}\\ \mathscr{L}_{41} & \mathscr{L}_{42} & \mathscr{L}_{43} & \mathscr{L}_{44} & \mathscr{L}_{45} & \mathscr{L}_{46}\\ \mathscr{L}_{51} & \mathscr{L}_{52} & \mathscr{L}_{53} & \mathscr{L}_{54} & \mathscr{L}_{55} & \mathscr{L}_{56}\\ \mathscr{L}_{61} & \mathscr{L}_{62} & \mathscr{L}_{63} & \mathscr{L}_{64} & \mathscr{L}_{65} & \mathscr{L}_{66}\end{bmatrix} \times \begin{bmatrix}\dot{\varepsilon}_{11}\\ \dot{\varepsilon}_{22}\\ \dot{\varepsilon}_{33}\\ \dot{\varepsilon}_{12}\\ \dot{\varepsilon}_{13}\\ \dot{\varepsilon}_{23}\end{bmatrix} - \begin{bmatrix}N_{11}\\ N_{22}\\ N_{33}\\ N_{12}\\ N_{13}\\ N_{23}\end{bmatrix} \|\dot{\boldsymbol{\varepsilon}}\|$$

Since the existence of the second term $\mathrm{tr}(\dot{\boldsymbol{\varepsilon}})\boldsymbol{\sigma}$ in the constitutive equation (2.14), the matrix $[\mathscr{L}]$ is shown to be unsymmetric. Therefore, it is suffices to provide the independent components for $[\mathscr{L}]$:

$$\mathscr{L}_{11} = C_1\bar{\sigma} + C_2\sigma_{11} + C_3\frac{\sigma_{11}\sigma_{11}}{\bar{\sigma}} \quad \mathscr{L}_{12} = C_2\sigma_{11} + C_3\frac{\sigma_{11}\sigma_{22}}{\bar{\sigma}} \quad \mathscr{L}_{13} = C_2\sigma_{11} + C_3\frac{\sigma_{11}\sigma_{33}}{\bar{\sigma}}$$

$$\mathscr{L}_{14} = C_3\frac{\sigma_{11}\sigma_{12}}{\bar{\sigma}} \quad \mathscr{L}_{15} = C_3\frac{\sigma_{11}\sigma_{13}}{\bar{\sigma}} \quad \mathscr{L}_{16} = C_3\frac{\sigma_{11}\sigma_{23}}{\bar{\sigma}}$$

$$\mathscr{L}_{21} = C_2\sigma_{22} + C_3\frac{\sigma_{22}\sigma_{11}}{\bar{\sigma}} \quad \mathscr{L}_{22} = C_1\bar{\sigma} + C_2\sigma_{22} + C_3\frac{\sigma_{22}\sigma_{22}}{\bar{\sigma}} \quad \mathscr{L}_{23} = C_2\sigma_{22} + C_3\frac{\sigma_{22}\sigma_{33}}{\bar{\sigma}}$$

$$\mathscr{L}_{24} = C_3\frac{\sigma_{22}\sigma_{12}}{\bar{\sigma}} \quad \mathscr{L}_{25} = C_3\frac{\sigma_{22}\sigma_{13}}{\bar{\sigma}} \quad \mathscr{L}_{26} = C_3\frac{\sigma_{22}\sigma_{23}}{\bar{\sigma}}$$

$$\mathscr{L}_{31} = C_2\sigma_{33} + C_3\frac{\sigma_{33}\sigma_{11}}{\bar{\sigma}} \quad \mathscr{L}_{32} = C_2\sigma_{33} + C_3\frac{\sigma_{33}\sigma_{22}}{\bar{\sigma}} \quad \mathscr{L}_{33} = C_1\bar{\sigma} + C_2\sigma_{33} + C_3\frac{\sigma_{33}\sigma_{33}}{\bar{\sigma}}$$

$$\mathscr{L}_{34} = C_3\frac{\sigma_{33}\sigma_{12}}{\bar{\sigma}} \quad \mathscr{L}_{35} = C_3\frac{\sigma_{33}\sigma_{13}}{\bar{\sigma}} \quad \mathscr{L}_{36} = C_3\frac{\sigma_{33}\sigma_{23}}{\bar{\sigma}}$$

$$
\begin{array}{lll}
\mathscr{L}_{41} = C_2\sigma_{12} + C_3\dfrac{\sigma_{12}\sigma_{11}}{\bar{\sigma}} & \mathscr{L}_{42} = C_2\sigma_{12} + C_3\dfrac{\sigma_{12}\sigma_{22}}{\bar{\sigma}} & \mathscr{L}_{43} = C_2\sigma_{12} + C_3\dfrac{\sigma_{12}\sigma_{33}}{\bar{\sigma}} \\
\mathscr{L}_{44} = C_1\bar{\sigma} + C_3\dfrac{\sigma_{12}\sigma_{12}}{\bar{\sigma}} & \mathscr{L}_{45} = C_3\dfrac{\sigma_{12}\sigma_{13}}{\bar{\sigma}} & \mathscr{L}_{46} = C_3\dfrac{\sigma_{12}\sigma_{23}}{\bar{\sigma}} \\
\mathscr{L}_{51} = C_2\sigma_{13} + C_3\dfrac{\sigma_{13}\sigma_{11}}{\bar{\sigma}} & \mathscr{L}_{52} = C_2\sigma_{13} + C_3\dfrac{\sigma_{13}\sigma_{22}}{\bar{\sigma}} & \mathscr{L}_{53} = C_2\sigma_{13} + C_3\dfrac{\sigma_{13}\sigma_{33}}{\bar{\sigma}} \\
\mathscr{L}_{54} = C_3\dfrac{\sigma_{13}\sigma_{12}}{\bar{\sigma}} & \mathscr{L}_{55} = C_1\bar{\sigma} + C_3\dfrac{\sigma_{13}\sigma_{13}}{\bar{\sigma}} & \mathscr{L}_{56} = C_3\dfrac{\sigma_{13}\sigma_{23}}{\bar{\sigma}} \\
\mathscr{L}_{61} = C_2\sigma_{23} + C_3\dfrac{\sigma_{23}\sigma_{11}}{\bar{\sigma}} & \mathscr{L}_{62} = C_2\sigma_{23} + C_3\dfrac{\sigma_{23}\sigma_{22}}{\bar{\sigma}} & \mathscr{L}_{63} = C_2\sigma_{23} + C_3\dfrac{\sigma_{23}\sigma_{33}}{\bar{\sigma}} \\
\mathscr{L}_{64} = C_3\dfrac{\sigma_{23}\sigma_{12}}{\bar{\sigma}} & \mathscr{L}_{65} = C_3\dfrac{\sigma_{23}\sigma_{13}}{\bar{\sigma}} & \mathscr{L}_{66} = C_1\bar{\sigma} + C_3\dfrac{\sigma_{23}\sigma_{23}}{\bar{\sigma}}
\end{array}
$$

and we obtain the following components for $[N]$:

$$
\begin{array}{lll}
N_{11} = C_4(\sigma_{11} + \sigma_{11}^*) & N_{22} = C_4(\sigma_{22} + \sigma_{22}^*) & N_{33} = C_4(\sigma_{33} + \sigma_{33}^*) \\
N_{12} = C_4(\sigma_{12} + \sigma_{12}^*) & N_{13} = C_4(\sigma_{13} + \sigma_{13}^*) & N_{23} = C_4(\sigma_{23} + \sigma_{23}^*)
\end{array}
$$

$\|\dot{\boldsymbol{\varepsilon}}\|$ and $\bar{\sigma}$ in the above expressions are defined by

$$
\begin{aligned}
\|\dot{\boldsymbol{\varepsilon}}\| &= \sqrt{\dot{\varepsilon}_{11}^2 + \dot{\varepsilon}_{22}^2 + \dot{\varepsilon}_{33}^2 + 2\dot{\varepsilon}_{12}^2 + 2\dot{\varepsilon}_{13}^2 + 2\dot{\varepsilon}_{23}^2} \\
\bar{\sigma} &= \sigma_{11} + \sigma_{22} + \sigma_{33}
\end{aligned}
$$

Appendendix II

Incremental form in Abaqus

The constitutive equation (2.14) can be integrated by assuming a time step Δt:

$$\Delta\sigma_{11} = C_1\mathrm{tr}(\boldsymbol{\sigma})\Delta\varepsilon_{11} + C_2\mathrm{tr}(\Delta\boldsymbol{\varepsilon})\sigma_{11} + C_3\frac{\mathrm{tr}(\boldsymbol{\sigma}\Delta e)}{\mathrm{tr}\boldsymbol{\sigma}}\sigma_{11} + C_4(\sigma_{11} + \sigma_{11}^*)\|\Delta\boldsymbol{\varepsilon}\|$$
$$\Delta\sigma_{22} = C_1\mathrm{tr}(\boldsymbol{\sigma})\Delta\varepsilon_{22} + C_2\mathrm{tr}(\Delta\boldsymbol{\varepsilon})\sigma_{22} + C_3\frac{\mathrm{tr}(\boldsymbol{\sigma}\Delta\boldsymbol{\varepsilon})}{\mathrm{tr}\boldsymbol{\sigma}}\sigma_{22} + C_4(\sigma_{22} + \sigma_{22}^*)\|\Delta\boldsymbol{\varepsilon}\|$$
$$\Delta\sigma_{33} = C_1\mathrm{tr}(\boldsymbol{\sigma})\Delta\varepsilon_{33} + C_2\mathrm{tr}(\Delta\boldsymbol{\varepsilon})\sigma_{33} + C_3\frac{\mathrm{tr}(\boldsymbol{\sigma}\Delta\boldsymbol{\varepsilon})}{\mathrm{tr}\boldsymbol{\sigma}}\sigma_{33} + C_4(\sigma_{33} + \sigma_{33}^*)\|\Delta\boldsymbol{\varepsilon}\|$$
$$\Delta\sigma_{12} = C_1\mathrm{tr}(\boldsymbol{\sigma})\Delta\varepsilon_{12} + C_2\mathrm{tr}(\Delta\boldsymbol{\varepsilon})\sigma_{12} + C_3\frac{\mathrm{tr}(\boldsymbol{\sigma}\Delta\boldsymbol{\varepsilon})}{\mathrm{tr}\boldsymbol{\sigma}}\sigma_{12} + C_4(\sigma_{12} + \sigma_{12}^*)\|\Delta\boldsymbol{\varepsilon}\|$$
$$\Delta\sigma_{13} = C_1\mathrm{tr}(\boldsymbol{\sigma})\Delta\varepsilon_{13} + C_2\mathrm{tr}(\Delta\boldsymbol{\varepsilon})\sigma_{33} + C_3\frac{\mathrm{tr}(\boldsymbol{\sigma}\Delta\boldsymbol{\varepsilon})}{\mathrm{tr}\boldsymbol{\sigma}}\sigma_{13} + C_4(\sigma_{13} + \sigma_{13}^*)\|\Delta\boldsymbol{\varepsilon}\|$$
$$\Delta\sigma_{23} = C_1\mathrm{tr}(\boldsymbol{\sigma})\Delta\varepsilon_{23} + C_2\mathrm{tr}(\Delta\boldsymbol{\varepsilon})\sigma_{23} + C_3\frac{\mathrm{tr}(\boldsymbol{\sigma}\Delta\boldsymbol{\varepsilon})}{\mathrm{tr}\boldsymbol{\sigma}}\sigma_{23} + C_4(\sigma_{23} + \sigma_{23}^*)\|\Delta\boldsymbol{\varepsilon}\|$$

We recast the equations in a more convenient form by virtue of Euller's theorem for homegeneous functions, then the integral form is:

$$\Delta\boldsymbol{\sigma} = (\boldsymbol{\mathscr{L}} - \boldsymbol{N}\otimes\Delta\vec{\boldsymbol{\varepsilon}}) : \Delta\boldsymbol{\varepsilon} = \boldsymbol{D} : \Delta\boldsymbol{\varepsilon} \tag{1}$$

By using the components of the matrices $[\mathscr{L}]$ and $[N]$, the tangential matrix $[D]$ can be obtained, for instance, $D_{1j}(j = 1 \ddots 6)$:

$$D_{11} = \mathscr{L}_{11} + N_{11}\Delta\varepsilon_{11}/\|\Delta\boldsymbol{\varepsilon}\|, \quad D_{12} = \mathscr{L}_{12} + N_{11}\Delta\varepsilon_{22}/\|\Delta\boldsymbol{\varepsilon}\|$$
$$D_{13} = \mathscr{L}_{13} + N_{11}\Delta\varepsilon_{33}/\|\Delta\boldsymbol{\varepsilon}\|, \quad D_{14} = \mathscr{L}_{14} + N_{11}\Delta\varepsilon_{12}/\|\Delta\boldsymbol{\varepsilon}\|$$
$$D_{15} = \mathscr{L}_{15} + N_{11}\Delta\varepsilon_{13}/\|\Delta\boldsymbol{\varepsilon}\|, \quad D_{16} = \mathscr{L}_{16} + N_{11}\Delta\varepsilon_{23}/\|\Delta\boldsymbol{\varepsilon}\|$$

We have the incremental form of the constitutive equation:

$$\Delta\sigma_{11} = C_1(\sigma_{11}+\sigma_{22}+\sigma_{33})\Delta\varepsilon_{11} + C_2(\Delta\varepsilon_{11}+\Delta\varepsilon_{22}+\Delta\varepsilon_{33})\sigma_{11} + C_3\frac{\sigma_{11}\Delta\varepsilon_{11}+\sigma_{22}\Delta\varepsilon_{22}+\sigma_{33}\Delta\varepsilon_{33}+\sigma_{12}\Delta\varepsilon_{12}+\sigma_{13}\Delta\varepsilon_{13}+\sigma_{23}\Delta\varepsilon_{23}}{\sigma_{11}+\sigma_{22}+\sigma_{33}}\sigma_{11} + C_4(\sigma_{11}+\sigma_{11}^*)\sqrt{\Delta\varepsilon_{11}^2+\Delta\varepsilon_{22}^2+\Delta\varepsilon_{33}^2+2\Delta\varepsilon_{12}^2+2\Delta\varepsilon_{13}^2+2\Delta\varepsilon_{23}^2}$$

$$\Delta\sigma_{22} = C_1(\sigma_{11}+\sigma_{22}+\sigma_{33})\Delta\varepsilon_{22} + C_2(\Delta\varepsilon_{11}+\Delta\varepsilon_{22}+\Delta\varepsilon_{33})\sigma_{22} + C_3\frac{\sigma_{11}\Delta\varepsilon_{11}+\sigma_{22}\Delta\varepsilon_{22}+\sigma_{33}\Delta\varepsilon_{33}+\sigma_{12}\Delta\varepsilon_{12}+\sigma_{13}\Delta\varepsilon_{13}+\sigma_{23}\Delta\varepsilon_{23}}{\sigma_{11}+\sigma_{22}+\sigma_{33}}\sigma_{22} + C_4(\sigma_{22}+\sigma_{22}^*)\sqrt{\Delta\varepsilon_{11}^2+\Delta\varepsilon_{22}^2+\Delta\varepsilon_{33}^2+2\Delta\varepsilon_{12}^2+2\Delta\varepsilon_{13}^2+2\Delta\varepsilon_{23}^2}$$

$$\Delta\sigma_{33} = C_1(\sigma_{11}+\sigma_{22}+\sigma_{33})\Delta\varepsilon_{33} + C_2(\Delta\varepsilon_{11}+\Delta\varepsilon_{22}+\Delta\varepsilon_{33})\sigma_{33} + C_3\frac{\sigma_{11}\Delta\varepsilon_{11}+\sigma_{22}\Delta\varepsilon_{22}+\sigma_{33}\Delta\varepsilon_{33}+\sigma_{12}\Delta\varepsilon_{12}+\sigma_{13}\Delta\varepsilon_{13}+\sigma_{23}\Delta\varepsilon_{23}}{\sigma_{11}+\sigma_{22}+\sigma_{33}}\sigma_{33} + C_4(\sigma_{33}+\sigma_{33}^*)\sqrt{\Delta\varepsilon_{11}^2+\Delta\varepsilon_{22}^2+\Delta\varepsilon_{33}^2+2\Delta\varepsilon_{12}^2+2\Delta\varepsilon_{13}^2+2\Delta\varepsilon_{23}^2}$$

$$\Delta\sigma_{12} = C_1(\sigma_{11}+\sigma_{22}+\sigma_{33})\Delta\varepsilon_{12} + C_2(\Delta\varepsilon_{11}+\Delta\varepsilon_{22}+\Delta\varepsilon_{33})\sigma_{12} + C_3\frac{\sigma_{11}\Delta\varepsilon_{11}+\sigma_{22}\Delta\varepsilon_{22}+\sigma_{33}\Delta\varepsilon_{33}+\sigma_{12}\Delta\varepsilon_{12}+\sigma_{13}\Delta\varepsilon_{13}+\sigma_{23}\Delta\varepsilon_{23}}{\sigma_{11}+\sigma_{22}+\sigma_{33}}\sigma_{12} + C_4(\sigma_{12}+\sigma_{12}^*)\sqrt{\Delta\varepsilon_{11}^2+\Delta\varepsilon_{22}^2+\Delta\varepsilon_{33}^2+2\Delta\varepsilon_{12}^2+2\Delta\varepsilon_{13}^2+2\Delta\varepsilon_{23}^2}$$

$$\Delta\sigma_{13} = C_1(\sigma_{11}+\sigma_{22}+\sigma_{33})\Delta\varepsilon_{13} + C_2(\Delta\varepsilon_{11}+\Delta\varepsilon_{22}+\Delta\varepsilon_{33})\sigma_{33} + C_3\frac{\sigma_{11}\Delta\varepsilon_{11}+\sigma_{22}\Delta\varepsilon_{22}+\sigma_{33}\Delta\varepsilon_{33}+\sigma_{12}\Delta\varepsilon_{12}+\sigma_{13}\Delta\varepsilon_{13}+\sigma_{23}\Delta\varepsilon_{23}}{\sigma_{11}+\sigma_{22}+\sigma_{33}}\sigma_{13} + C_4(\sigma_{13}+\sigma_{13}^*)\sqrt{\Delta\varepsilon_{11}^2+\Delta\varepsilon_{22}^2+\Delta\varepsilon_{33}^2+2\Delta\varepsilon_{12}^2+2\Delta\varepsilon_{13}^2+2\Delta\varepsilon_{23}^2}$$

$$\Delta\sigma_{23} = C_1(\sigma_{11}+\sigma_{22}+\sigma_{33})\Delta\varepsilon_{23} + C_2(\Delta\varepsilon_{11}+\Delta\varepsilon_{22}+\Delta\varepsilon_{33})\sigma_{23} + C_3\frac{\sigma_{11}\Delta\varepsilon_{11}+\sigma_{22}\Delta\varepsilon_{22}+\sigma_{33}\Delta\varepsilon_{33}+\sigma_{12}\Delta\varepsilon_{12}+\sigma_{13}\Delta\varepsilon_{13}+\sigma_{23}\Delta\varepsilon_{23}}{\sigma_{11}+\sigma_{22}+\sigma_{33}}\sigma_{23} + C_4(\sigma_{23}+\sigma_{23}^*)\sqrt{\Delta\varepsilon_{11}^2+\Delta\varepsilon_{22}^2+\Delta\varepsilon_{33}^2+2\Delta\varepsilon_{12}^2+2\Delta\varepsilon_{13}^2+2\Delta\varepsilon_{23}^2}$$

Since the shear strain is stored as engineering shear strain, $\Delta\gamma_{12} = 2\Delta\varepsilon_{12}$ in finite element package Abaqus, so care must be taken when dealing with the shear strain. A good way to eliminate this influence is to change the the engineering shear strain to tensor shear strains at the beginning of programming in Umat.

Appendendix III

Different versions of hypoplastic constitutive model

For the complete of the thesis, some mostly used hypoplascit models are presented in the following. These model are mostly developed based on the reference model presented in chapter 2. The introduction of these model is presented in chronological order. Normally, the later versions of the hypoplastic model is a process of inheritance and development of the earlier versions.

1. **Gudehus and Bauer 1996**

Gudehus(Gudehus, 2000) and Bauer (Bauer, 1996) proposed a model. In this model, the fourth-order tensor $\mathscr{L}$ and the second-order tensor $\boldsymbol{N}$ have the following representations:

$$\mathscr{L} = f_s(\hat{a}^2\mathscr{I} + \hat{\boldsymbol{\sigma}} \otimes \hat{\boldsymbol{\sigma}}), \quad \boldsymbol{N} = f_s f_d \hat{a}(\hat{\boldsymbol{\sigma}} + \hat{\boldsymbol{\sigma}}^*) \tag{2}$$

where $\boldsymbol{I}$ is a second-order unity tensor, $\mathscr{I}_{ijkl} = 0.5(\boldsymbol{I}_{ik}\boldsymbol{I}_{jl} + \boldsymbol{I}_{il}\boldsymbol{I}_{jk})$. and $\hat{\boldsymbol{\sigma}} = \frac{\boldsymbol{\sigma}}{\mathrm{tr}\boldsymbol{\sigma}}$ is the normalized stress tensor. The scalar factors are functions of the mean pressure $p = -\mathrm{tr}\boldsymbol{\sigma}/3$ and the void ratio e:

$$f_s = \Big(\frac{e_i}{e}\Big)^{\beta} \frac{1+e_i}{e_i} \frac{h_s}{n h_i(\hat{\boldsymbol{\sigma}} : \hat{\boldsymbol{\sigma}})} \Big(\frac{-\mathrm{tr}\boldsymbol{\sigma}}{h_s}\Big)^{1-n}, \text{and} \quad f_d = \Big(\frac{e-e_d}{e_c-e_d}\Big)^{\alpha} \tag{3}$$

where e_i, e_c and e_d are the pressure-dependent loosest, densest and the critical void ratios, as given by

$$\frac{e_i}{e_{i0}} = \frac{e_d}{e_{d0}} = \frac{e_c}{e_{c0}} = \exp\Big[-\Big(\frac{-\mathrm{tr}\boldsymbol{\sigma}}{h_s}\Big)^n\Big] \tag{4}$$

and h_i is another scalar factor given by

$$h_i = \frac{8\sin^2\phi}{3-\sin\phi} + 1 - \frac{2\sqrt{2}\sin\phi}{3-\sin\phi}\Big(\frac{e_{i0}-e_{d0}}{e_{c0}-e_{d0}}\Big)^{\alpha} \tag{5}$$

The strength parameter $\hat{a}$ depends basically on the critical friction angle ϕ_c. It is also related to the Lode angle θ by

$$\hat{a} = \hat{a}_0\left(\sqrt{\frac{3}{8}\|\boldsymbol{\sigma}^*\|^2 + \frac{1-(3/2)\|\boldsymbol{\sigma}^*\|^2}{1-\sqrt{3/2}\|\boldsymbol{\sigma}^*\|\cos 3\theta}} - \sqrt{\frac{3}{8}}|\boldsymbol{\sigma}^*\|\right) \tag{6}$$

where

$$\hat{a}_0 = \frac{\sqrt{\frac{8}{3}}\sin\phi_c}{3-\sin\phi_c}, \quad \cos 3\theta = -\frac{\sqrt{6}\hat{\boldsymbol{\sigma}}^{*3}}{\left(\mathrm{tr}\hat{\boldsymbol{\sigma}}^{*2}\right)^{3/2}} \tag{7}$$

The model consists of 8 parameters, which are listed in Table 4 with values used in the numerical investigations.

Table 1 Constitutive parameters used in the calculations for Bauer and Gudehus's model

Para.	ϕ_c	h_s	n	e_{i0}	e_{d0}	e_{c0}	α	β
Value	30	190 MPa	0.4	1.20	0.82	0.51	0.14	1.05

2. **Von wolffersdoff 1996**

The version of Bauer led to the so-called version of Von Wolffersdorff (1996), in which the limit surface was explicitly defined in this version, and pressure dependent limits for the void ratio were also introduced: a minimum, a maximum and a critical void ratio. With this version, laboratory tests with sand could be successfully simulated, as it enables us to model the material behavior of sand irrespective of its state of compaction, and different parameters are not needed for different initial densities like the previous models of Wu and Kolymbas

The model proposed by Von Wolffersdorff (1996) is outlined as follows

$$\mathring{\boldsymbol{\sigma}} = \mathscr{L}(\boldsymbol{\sigma}, e) : \dot{\boldsymbol{\varepsilon}} - \boldsymbol{N}(\boldsymbol{\sigma}, e)\|\dot{\boldsymbol{\varepsilon}}\| \tag{8}$$

with the linear term

$$\mathscr{L} = f_s \frac{1}{\mathrm{tr}(\hat{\boldsymbol{\sigma}}^2)}\left(F^2 \mathscr{I} + a^2 \hat{\boldsymbol{\sigma}} \otimes \hat{\boldsymbol{\sigma}}\right) \tag{9}$$

and the non-linear term

$$\boldsymbol{N} = f_s f_d \frac{aF}{\mathrm{tr}(\hat{\boldsymbol{\sigma}}^2)}\left(\hat{\boldsymbol{\sigma}} + \hat{\boldsymbol{\sigma}}^*\right) \tag{10}$$

where $\boldsymbol{I}$ is a second-order unity tensor $\mathscr{I}_{ijkl} = 0.5(\boldsymbol{I}_{ik}\boldsymbol{I}_{jl} + \boldsymbol{I}_{il}\boldsymbol{I}_{jk})$

The factors for pressure and density dependency (barotropy and pyknotropy) are given by

$$a = \frac{\sqrt{3}(3-\sin\phi_c)}{2\sqrt{2}\sin\phi_c}, \quad f_d = \left(\frac{e-e_d}{e_c-e_d}\right)^{\alpha}, \text{and} \tag{11}$$

$$f_s = \frac{h_s}{n}\left(\frac{e_i}{e}\right)^{\beta}\frac{1+e_i}{e_i}\left(\frac{-\mathrm{tr}\boldsymbol{\sigma}}{h_s}\right)^{1-n}\left[3+a^2-a\sqrt{3}\left(\frac{e_{i0}-e_{d0}}{e_{c0}-e_{d0}}\right)^{\alpha}\right]^{-1} \tag{12}$$

The factor F for adapting the deviatoric yield curve to Matsuoka–Nakai is

$$F = \sqrt{\frac{1}{8}\tan^2\psi + \frac{2-\tan^2\psi}{2+\sqrt{2}\tan\psi\cos3\theta}} - \frac{1}{2\sqrt{2}}\tan\psi \tag{13}$$

with

$$\tan\psi = \sqrt{3}\|\hat{\boldsymbol{\sigma}}^*\|, \text{and} \quad \cos3\theta = -\frac{\sqrt{6}\hat{\boldsymbol{\sigma}}^{*3}}{\left(\mathrm{tr}\hat{\boldsymbol{\sigma}}^{*2}\right)^{3/2}} \tag{14}$$

The void ratios must fulfill the compression law

$$\frac{e_i}{e_{i0}} = \frac{e_d}{e_{d0}} = \frac{e_c}{e_{c0}} = \exp\left[-\left(\frac{-\mathrm{tr}\boldsymbol{\sigma}}{h_s}\right)^n\right] \tag{15}$$

This hypoplastic law has eight parameters: the critical friction angle ϕ_c; the granular hardness h_s; the void ratios e_{i0}; e_{c0} and e_{d0}; and the exponents n and β They can be easily determined from simple index and element tests, see Table 2.

Table 2 Constitutive parameters used in the calculations for Von Wolffersdorff's model

Para.	ϕ_c	h_s	n	e_{i0}	e_{d0}	e_{c0}	α	β
Value	30	190 MPa	0.45	1.18	0.4	0.8	0.15	1.0

3. **Herle Kolymbas 2004**

The Von wolffersdoff's version was used as the basis for further modifications. Based onVon wolffersdoff's model, Herle and Kolymbas (2004) proposed a hypoplastic model for soil with low friction angle.

The model assumes the following stress–strain relation

$$\mathring{\boldsymbol{\sigma}} = f_s\mathscr{L}(\boldsymbol{\sigma}, e) : \dot{\boldsymbol{\varepsilon}} - f_s f_d \boldsymbol{N}(\boldsymbol{\sigma}, e)\|\dot{\boldsymbol{\varepsilon}}\| \tag{16}$$

with the linear term

$$\mathscr{L} = \frac{1}{\hat{\boldsymbol{\sigma}} : \hat{\boldsymbol{\sigma}}}(c_1 F^2 \mathscr{I} + c_2 a^2 \hat{\boldsymbol{\sigma}} \otimes \hat{\boldsymbol{\sigma}}) \tag{17}$$

and the non-linear term

$$\boldsymbol{N} = \frac{Fa}{\hat{\boldsymbol{\sigma}} : \hat{\boldsymbol{\sigma}}}(\hat{\boldsymbol{\sigma}} + \hat{\boldsymbol{\sigma}}^*) \tag{18}$$

where $\boldsymbol{I}$ is a second-order unity tensor $\mathscr{I}_{ijkl} = 0.5(\boldsymbol{I}_{ik}\boldsymbol{I}_{jl} + \boldsymbol{I}_{il}\boldsymbol{I}_{jk})$

The factors for pressure and density dependency (barotropy and pyknotropy) are given by

$$a = \frac{\sqrt{3}(3 - \sin\phi_c)}{2\sqrt{2}\sin\phi_c}, \quad f_d = (\frac{e - e_d}{e_c - e_d})^\alpha \tag{19}$$

and

$$f_s = \frac{h_s}{n}(\frac{e_i}{e})^\beta \frac{1 + e_i}{e_i}(\frac{-\mathrm{tr}\boldsymbol{\sigma}}{h_s})^{1-n}\left[3c_1 + a^2 c_2 - a\sqrt{3}(\frac{e_{i0} - e_{d0}}{e_{c0} - e_{d0}})^\alpha\right]^{-1} \tag{20}$$

The factor F for adapting the deviatoric yield curve to Matsuoka–Nakai is

$$F = \sqrt{\frac{1}{8}\tan^2\psi + \frac{2 - \tan^2\psi}{2 + \sqrt{2}\tan\psi\cos3\theta}} - \frac{1}{2\sqrt{2}}\tan\psi \tag{21}$$

with

$$\tan\psi = \sqrt{3}\|\hat{\boldsymbol{\sigma}}^*\|, \text{and} \quad \cos3\theta = -\frac{\sqrt{6}\hat{\boldsymbol{\sigma}}^{*3}}{\left(\mathrm{tr}\hat{\boldsymbol{\sigma}}^{*2}\right)^{3/2}} \tag{22}$$

The void ratios must fulfill the compression law

$$\frac{e_i}{e_{i0}} = \frac{e_d}{e_{d0}} = \frac{e_c}{e_{c0}} = \exp\left[-(\frac{-\mathrm{tr}\boldsymbol{\sigma}}{h_s})^n\right] \tag{23}$$

The scalar factors c_1 and c_2 are calculated using

$$c_1 = \left(\frac{1 + 1/3a^2 - 1/\sqrt{3}a}{1.5r}\right)^\xi, \quad c_2 = 1 + (1 - c_1)\frac{3}{a^2} \tag{24}$$

with

$$\xi = \left\langle \frac{\sin\phi_c - \sin\phi_{mob}}{\sin\phi_c} \right\rangle, \text{where} \quad \sin\phi_{mob} = \frac{\sigma_1 - \sigma_3}{\sigma_1 + \sigma_3} \tag{25}$$

σ_1 and σ_3 are the maximal and minimal principal stresses, $\sin\phi_{mob}$ is a mobilized friction angle and $\langle\rangle$ are Macauley brackets: $< x >= (x + |x|)/2$

The model requires nine parameters: $\phi_c, h_s, n, e_{d0}, e_{c0}, e_{i0}, \alpha, \beta$ and r,see Table 3.

Table 3 Constitutive parameters used in the calculations for Herle and Kolymbas's model

Para.	ϕ_c	h_s	n	e_{i0}	e_{d0}	e_{c0}	α	β	r
Value	22	627 kPa	0.24	5.65	1.84	3.35	0.15	1.0	1.0

4. **D.Mašín version 2005**

On the basic of Herle and Kolymbas's version, Mašín (2005) modified the linear term and the factors for pressure and density dependency (barotropy and pyknotropy) to describe the basic behavior of clay.

Mathematical formulation of the proposed hypoplastic constitutive model for clays: The general stress–strain relation reads

$$\mathring{\hat{\boldsymbol{\sigma}}} = f_s \mathscr{L}(\boldsymbol{\sigma}, e) : \dot{\boldsymbol{\varepsilon}} - f_s f_d \boldsymbol{N}(\boldsymbol{\sigma}, e)\|\dot{\boldsymbol{\varepsilon}}\| \tag{26}$$

with

$$\boldsymbol{N} = \mathscr{L} : \left(-Y \frac{\boldsymbol{m}}{\|\boldsymbol{m}\|}\right) \tag{27}$$

The hypoelastic tensor $\mathscr{L}$ is

$$\mathscr{L} = 3(c_1 \mathscr{I} + c_2 a^2 \hat{\boldsymbol{\sigma}} \otimes \hat{\boldsymbol{\sigma}}) \tag{28}$$

where $\boldsymbol{I}$ is a second-order unity tensor $\mathscr{I}_{ijkl} = 0.5(\boldsymbol{I}_{ik}\boldsymbol{I}_{jl} + \boldsymbol{I}_{il}\boldsymbol{I}_{jk})$ and

$$a = \frac{\sqrt{3}(3 - \sin\phi_c)}{2\sqrt{2}\sin\phi_c} \tag{29}$$

The degree of non-linearity Y; with the limit value $Y = 1$ at Matsuoka–Nakai failure surface, is calculated by

$$Y = \left(\frac{\sqrt{3}a}{3 + a^2} - 1\right) \frac{(I_1 I_2 + 9I_3)(1 - \sin^2\phi_c)}{8I_3 \sin^2\phi_c} + \frac{\sqrt{3}a}{3 + a^2} \tag{30}$$

with stress invariants I_1; I_2 and I_3;

$$I_1 = \mathrm{tr}\boldsymbol{\sigma}, \quad I_2 = 0.5[\boldsymbol{\sigma} : \boldsymbol{\sigma} - (I_1)^2], \quad I_s = \det\boldsymbol{\sigma} \tag{31}$$

The tensorial quantity m defining the hypoplastic flow rule has the following formulation:

$$\boldsymbol{m} = -\frac{a}{F}\left[\hat{\boldsymbol{\sigma}} + \hat{\boldsymbol{\sigma}}^* - \frac{\hat{\boldsymbol{\sigma}}}{3}\left(\frac{6\hat{\boldsymbol{\sigma}} : \hat{\boldsymbol{\sigma}} - 1}{(F/a)^2 + \hat{\boldsymbol{\sigma}} : \hat{\boldsymbol{\sigma}}}\right)\right] \tag{32}$$

with factor F given by

$$F = \sqrt{\frac{1}{8}\tan^2\psi + \frac{2-\tan^2\psi}{2+\sqrt{2}\tan\psi\cos3\theta}} - \frac{1}{2\sqrt{2}}\tan\psi \tag{33}$$

with

$$\tan\psi = \sqrt{3}\|\hat{\boldsymbol{\sigma}}^*\|, \text{and} \quad \cos3\theta = -\frac{\sqrt{6}\hat{\boldsymbol{\sigma}}^{*3}}{\left(\mathrm{tr}\hat{\boldsymbol{\sigma}}^{*2}\right)^{3/2}} \tag{34}$$

The void ratios must fulfill the compression law

$$\frac{e_i}{e_{i0}} = \frac{e_d}{e_{d0}} = \frac{e_c}{e_{c0}} = \exp\big[-\big(\frac{-\mathrm{tr}\boldsymbol{\sigma}}{h_s}\big)^n\big] \tag{35}$$

Barotropy and pyknotropy factors f_s and f_d read

$$f_s = -\frac{\mathrm{tr}\boldsymbol{\sigma}}{\lambda^*}(3+a^2-2^\alpha a\sqrt{3})^{-1}, \text{and} \quad f_d = \Big[-\frac{2\mathrm{tr}\boldsymbol{\sigma}}{3p_r}\exp\Big(\frac{\mathrm{In}(1+e)-N}{\lambda^*}\Big)\Big]^\alpha \tag{36}$$

where p_r is the reference stress 1 kPa and the scalar quantity α is calculated by

$$\alpha = \frac{1}{\mathrm{In}2}\mathrm{In}\Big[\frac{\lambda^*-\kappa^*}{\lambda^*+\kappa^*}\Big(\frac{3+a^2}{a\sqrt{3}}\Big)\Big] \tag{37}$$

The scalar factors c_1 and c_2 are calculated using

$$c_1 = \frac{2(3+a^2-2^\alpha/\sqrt{3}a)}{9r}, \quad c_2 = 1+(1-c_1)\frac{3}{a^2} \tag{38}$$

with The model requires five constitutive parameters: ϕ_c; λ^*; κ^* ;n and r

Table 4 Constitutive parameters used in the calculations for Mašín D.'s model

Para.	ϕ_c	λ^*	κ^*	n	r
Value	22.6	0.11	0.016	1.375	0.4